Spring 2015

Mechanism and kinetics of homogeneous catalysis

Silei Xiong
Purdue University

Graduate School Form 30
Updated 1/15/2015

PURDUE UNIVERSITY
GRADUATE SCHOOL
Thesis/Dissertation Acceptance

This is to certify that the thesis/dissertation prepared

By Silei Xiong

Entitled

Mechanism and Kinetics of Homogeneous Catalysis

For the degree of Doctor of Philosophy

Is approved by the final examining committee:

James M. Caruthers
Chair

W. Nicholas Delgass

Kendall T. Thomson

Mahdi M. Abu-Omar

To the best of my knowledge and as understood by the student in the Thesis/Dissertation Agreement, Publication Delay, and Certification Disclaimer (Graduate School Form 32), this thesis/dissertation adheres to the provisions of Purdue University's "Policy of Integrity in Research" and the use of copyright material.

Approved by Major Professor(s): James M. Caruthers

Approved by: John Morgan 4/17/2015

Head of the Departmental Graduate Program Date

MECHANISM AND KINETICS OF HOMOGENEOUS CATALYSIS

A Dissertation

Submitted to the Faculty

of

Purdue University

by

Silei Xiong

In Partial Fulfillment of the

Requirements for the Degree

of

Doctor of Philosophy

May 2015

Purdue University

West Lafayette, Indiana

For my parents

ACKNOWLEDGEMENTS

I would like to thank my research advisors, Professor James M. Caruthers, Professor W. Nicholas Delgass, and Professor Kendall T. Thomson for their tremendous support and guidance over the years.

Thanks must also be given to the single-site polymerization group from the School of Chemical Engineering: Dr. Grigori A. Medvedev and Jeffrey Switzer, as well as, my collaborators from the Chemistry Department: David Keith Steelman, Thilina N. Gunasekara, and Paul D. Pletcher.

This research was financially supported by grants from the United States Department of Energy.

TABLE OF CONTENTS

Page

Page

LIST OF TABLES

Table Page

Table Page

Appendix Table

LIST OF FIGURES

Figure Page

Figure Page

Figure Page

Figure Page

Figure Page

Figure Page

Figure Page

Figure Page

Figure Page

Figure Page

Figure Page

Figure Page

Figure Page

Figure Page

Appendix Figure

Figure Page

Figure Page

Figure Page

Figure Page

Figure Page

Figure Page

Figure Page

Figure Page

Figure Page

Figure Page

Figure Page

Figure Page

Figure Page

Figure Page

ABSTRACT

Xiong, Silei. Ph.D., Purdue University, May 2015. Mechanism and Kinetics of Homogeneous Catalysis. Professor: James M. Caruthers, W. Nicholas Delgass and Kendall T. Thomson.

A model-based approach using a diverse set of data including monomer consumption, evolution of molecular weight, and end-group analysis was employed to determine each of the reaction specific rate constants involved in 1-hexene polymerization catalyzed by a family of group IV single-site catalysts. The primary set of elementary reaction steps included initiation, normal propagation, misinsertion, recovery from misinsertion, monomer independent and dependent chain transfer. Robust determination of kinetic constants and reaction mechanisms for a series of Group IV amine bis-phenolate complexes led to the development of several structure−activity relationships.

For some of the catalysts of the bis-phenolate family the primary set of elementary reactions had proven inadequate and further investigation using the analysis developed here revealed the presence of additional key reaction steps. The kinetic study of the Zr[tBu-$ON^{THF}O$]Bn_2/$B(C_6F_5)_3$ system under sub-stoichiometric activator conditions uncovered the formation of a binuclear complex (BNC) consisting of the neutral catalytic species and an active site connected via degenerative transfer of benzyl ligand. The kinetic study of the Zr[tBu-$ON^{NEt2}O$]Bn_2/$B(C_6F_5)_3$ system showed that a special polymeric site was formed

which was capable to incorporate the growing oligomer chains attached to the normal active site to form branched polymer.

The approach was also used to study the kinetics of other catalytic systems, including the zwitterionic ring-opening polymerization using N-heterocyclic carbine. In that study several new reaction steps were proposed and then experimentally validated, including the attack of active zwitterions on cyclic chains that leads to high molecular weight cyclic poly(caprolactones).

CHAPTER 1. INTRODUCTION

While high-throughput screening has accelerated discovery and lead to Dow's catalysts for olefin block copolymer synthesis,[1] combinatorial catalysis does not always translate to "insight' that can lead to rational catalyst design. A major obstacle is the lack of robust rate constants for the elementary reaction steps involved in polymerization; well-defined rate constants can be used to develop descriptors, which can be deployed subsequently to search for improved catalysts and reaction conditions (temperature, initial concentrations, etc.) We have embarked on defining and illustrating what it takes to obtain robust rate constants for single-site olefin polymerization catalysts and how to extract descriptors that can lead to catalyst design.

In Chapter 2 we illustrate how the methodology of using mathematical modeling and computer simulation was firstly employed to study the mechanism and kinetics of single-site olefin polymerization catalyzed by a family of five zirconium amine bis-phenolate complexes, Zr[tBu-ON$_X$O]Bn$_2$ (where X = THF (1), pyridine (2), NMe$_2$ (3), furan (4), and SMe (5)). The mechanism of polymerization usually includes initiation, propagation, misinsertion, recovery from misinsertion, and chain transfer. The results uncover the mechanistic effect of varying the pendant ligand on the rate constant of chain transfer. In Chapter 3 we further extend this relationship to hafnium based catalysts, and the difference between hafnium and zirconium metal center was discussed. In Chapter 4, a

new structure-activity relationship is discovered from the study of four zirconium amine bis-phenolate catalysts, Zr[tBu-ON^{X}O]Bn$_2$ (where, X = pyr-CF$_3$ (**1**), pyr (**2**), pyr-CH$_3$ (**3**), pyr-OMe (**4**). It was observed that the electronic nature of the pendant pyridine ligand affects each monomer insertion event (propagation, misinsertion, and recovery) in a similar fashion.

In addition to obtaining robust rate constants, the kinetics analysis was also used to illuminate key reaction steps. In Chapter 5, the kinetics of 1-hexene polymerization was investigated using a previously studied zirconium amine bis-phenolate catalyst, Zr[tBu-ON^{THF}O]Bn$_2$, where the effect of sub-stoichiometric amounts of activator on the polymerization was studied to more clearly elucidate the mechanism of degenerative benzyl-group transfer via the formation of a binuclear complex (BNC) intermediate. In Chapter 6, the chemistry and kinetic behavior of a special catalyst Zr[tBu-ON^{NEt2}O]Bn$_2$ capable to produce both oligomers and polymer was uncovered and discussed.

The methodology developed from the study of single-site olefin polymerization was so powerful that later on we applied it to other systems through collaborations with different chemistry groups. In Chapter 7, we investigated the kinetics of zwitterionic ring-opening polymerization of ε-caprolactone mediated by N-heterocyclic carbenes (NHC) and illuminated the key reaction steps responsible for the formation of high molecular weight cyclic poly(caprolactones): the re-activation of cyclized chains by active zwitterions. In Chapter 8 where two non-heme manganese complexes were used in the catalytic formation of chlorine dioxide from chlorite under ambient temperature at pH = 5.00, qantitative kinetic modeling enabled the deduction of a mechanism that accounted for all experimental observations.

Finally in Chapter 9, a conclusion of my research is provided.

REFERENCES

(1) Arriola, D. J.; Carnahan, E. M.; Hustad, P. D.; Kuhlman, R. L.; Wenzel, T. T. *Science* **2006**, *312*, 714-719.

CHAPTER 2. EFFECTS OF PENDANT LIGAND BINDING AFFINITY ON CHAIN TRANSFER FOR 1-HEXENE POLYMERIZATION CATALYZED BY SINGLE-SITE ZIRCONIUM AMINE BIS-PHENOLATE COMPLEXES

This chapter contains published work. It is reproduced with permission from *J. Am. Chem. Soc.*, **2013**, *135* (16), pp 6280–6288; Copyright © 2013, American Chemical Society.

In this paper, I performed GPC measurements of polymer samples and kinetics analysis on three of the five catalyst systems: Zr-THF catalyst 1, Zr-Pyridine catalyst 2, Zr-Furan catalyst 4. Jeffrey M. Switzer performed GPC measurements and kinetics analysis on the other two catalyst systems: Zr-NMe_2 catalyst 3, Zr-SMe catalyst 5. D. Keith Steelman, Paul D. Pletcher, and Erin Smith did the experimental part including catalyst synthesis, 1-hexene polymerization, and NMR measurements, etc.

2.1 Introduction

Production of polyolefins is a major industrial process with a current capacity of ca. 110 billion kg per year globally.[1] While polyolefins are primarily produced using heterogeneous Ziegler catalysts, homogeneous single-site catalysts, the so called metallocenes, have attracted attention because they offer potential control of the various kinetic steps, which in turn can be manipulated by "catalyst design."[2,3,4] One of the drawbacks of metallocenes, beside sensitivity to polar functional groups, is their thermal

sensitivity. Beyond metallocenes, the next-generation of thermally stable catalysts includes group 4 coordination complexes featuring phenolate amine ligands.[5] While high-throughput screening has accelerated the discovery process with group 4 coordination complexes leading to Dow's catalysts for olefin block copolymer synthesis,[6] the promise of directly correlating kinetic constants to descriptors of the catalyst has not yet been realized. A major obstacle in the way of rational catalyst design is the lack of proper quantitative kinetic analysis of all the relevant processes (i.e. kinetic steps) that are involved in catalytic olefin polymerization.[7, 8] Nevertheless, the study of single-site catalysts for olefin polymerization is particularly attractive because of the potential of correlating directly the physical properties of the resulting polymer to structural features of the catalyst based on first principles.[9] This correlation allows one to draw conclusions on how a catalyst structure may be manipulated to yield specific polymeric architectures.

One specific family of non-metallocene catalysts, first pioneered by Kol and co-workers, that has sparked interest utilizes an amine bis-phenolate (Salan) ligand system (see Figure 1).[10, 11] The reason for choosing this particular family of ligands as part of our detailed kinetic studies is the relative ease of synthesis and the ability to tune the catalyst's coordination environment.[12] Furthermore, these catalysts exhibit high activity, comparable to metallocene catalysts, with 1-hexene in conventional organic solvents such as toluene. This feature enables the collection of kinetic data in the condensed phase and eliminates mass transfer limitations that are inherent with gaseous substrates. Following up on Kol's earlier qualitative observations that the nature of the pendant ligand (X) and its distance from the metal center (Zr-X) influence chain transfer,[13] we have undertaken a comprehensive kinetic study of the five catalysts shown in Figure 1. We will show in the

following sections the minimally required set of rate constants needed to describe completely the rich data set for each catalyst including the molecular weight evolution. The rate constant affected the most by changing the pendant ligand (X) is that for chain transfer that results in vinyl terminated polymer.

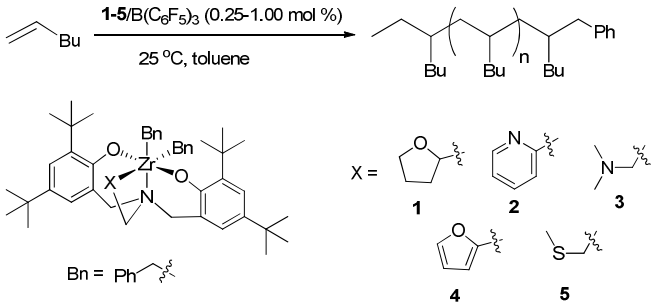

Figure 2-1. 1-hexene polymerization catalyzed by zirconium salan-type catalysts 1-5 when combined with the activator $B(C_6F_5)_3$.

Four chemical mechanisms have been noted for chain transfer in single-site homogeneous olefin polymerization catalysts. Normally chain transfer occurs via β-H elimination to give vinylidene terminated polymer chains. This process is independent of monomer concentration and the resulting metal hydride undergoes re-initiation. If the catalyst is susceptible to 2,1-misinsertion (which results in regio-errors), the resulting polymeryl chain can undergo unimolecular β-H elimination to give vinylene terminated polymer chains.[14] In some cases for propylene, a second mechanism has been recognized in which β-methyl instead of β-H elimination occurs to give M-CH_3, which can reinitiate by inserting a monomer.[15] It should be noted that ethyl or higher alkane elimination has not been observed. A third mechanism is second-order chain transfer in which vinylidene and vinylene end groups result from H-transfer to a monomer.[7, 8] In this mechanism the chain transfer rate constant is second-order and the rate is dependent on the monomer

concentration. The last recognized chemical mechanism for chain transfer is that to the activator. This is usually a minor pathway observed with aluminum alkyl activators, although exceptions where it is dominant have been noted in the literature.[16]

Suppression of chain transfer while maintaining high propagation rate can provide easy access to new block copolymers via controlled sequential addition of monomer.[17] Therefore, quantitative understanding of factors that control the rate of chain transfer exclusively is valuable from fundamental standpoint as well as for practical applications. In semi-quantitative studies, two parameters, catalyst activity (TOF or g polymer mol^{-1} catalyst h^{-1}) that is taken as indicative of the propagation rate constant and the molecular weight average of the resulting polymer (M_w), have been used to infer how catalyst structure influences the chain transfer rate. The consensus from these studies pointed to steric bulk as the major contributor to retardation of chain transfer as long as there is a weakly coordinating ligand or an available coordination site for monomer docking.[18] Bercaw and co-workers observed that the use of a more open metal center leads to faster propagation by allowing more space for a more facile monomer insertion and an increase in the propensity for β-H elimination due to more available space to accommodate the β-H agostic bonding interactions necessary for β-H elimination.[19] This empirical insight has been responsible for the development of late transition metal catalysts based on Fe, Co, and Ni that can effect ethylene polymerization rather than producing oligomers.[18]

Ziegler and co-workers performed a detailed computational study of ethylene polymerization using a wide range of d^0 metal catalysts,[20] finding that the energy barrier for chain transfer is strongly influenced by sterically bulky ligands and, to some degree, the identity of the metal. They also observed that, for the systems studied, β-H transfer to

monomer, a second-order chain transfer process, is preferred over β-H elimination, except when monomer concentration is small or when monomer coordination to the metal is severely hindered. This observation was used successfully by Busico and co-workers to design catalysts that were shown experimentally to have hindered chain transfer reactions.[21] In addition, Camacho and Guan have attributed the steric blocks present in their cyclophane-based nickel catalyst to its ability to polymerize olefins even at high temperatures where chain transfer typically dominates,[22] and Rieger and co-workers have used sterically hindered nickel and palladium catalysts to produce high molecular weight polyethylene rather than α-olefin oligomers.[23]

Earlier work by Doi and co-workers showed that for $V(acac)_3$–$Al(C_2H_5)_2Cl$ the identity of the alkylaluminum co-catalyst influences the amount of chain transfer.[24] Later work by Naga and Mizunuma showed similar activator effects on the amount of chain transfer using zirconium metallocenes, with an additional observation that the β-H chain transfer pathway was preferred with one alkylaluminum activator while chain transfer to activator was dominant with another.[25] More recently, Marks and co-workers have studied the effects of ion pair structure and dynamics on polymerization activity, stereoselectivity, and chain transfer in C_s-symmetric zirconium metallocene precatalysts using various fluorinated aryl borane and aluminum activators.[26] They found that ion pairing dictates the relative rate of termination to propagation as well as the preferred termination pathway.

In this study, we describe a detailed kinetic analysis for catalysts 1-5, culminating in Table 1 which contains all of the rate constants for each system. The following sections will discuss observations and trends that only become apparent through the generation and examination of the full kinetic constants presented in Table 1. These kinetic constants

represent the minimal number of necessary reaction steps needed to describe the entire data set for each of the catalysts, which includes monomer consumption kinetics, molecular weight evolution as determined by GPC (gel permeation chromatography), active-site count, and analysis of terminated end groups in the resulting polymer. The mechanism of chain transfer and its corresponding rate constants as the pendant ligand (X) changes have been pinpointed. A linear quantitative structure-activity relationship (QSAR) between the logarithm of the chain transfer rate constant and the Zr-X bond length will be shown and discussed.

2.2 Experimental Procedure

General Procedure. All manipulations were performed under dry inert atmosphere in a glove box or at a vacuum manifold using air sensitive techniques under N_2 or Ar atmosphere. Toluene and pentane were distilled over activated alumina and a copper catalyst using a solvent purification system (Anhydrous Technologies) and degassed through freeze-pump-thaw cycles. Both solvents were stored over activated molecular sieves. Tetrabenzylzirconium was purchased from STREM and used as received. The monomer 1-hexene was purchased from Aldrich and purified by distillation over a small amount of dimethyl bis(cyclopentadienyl)zirconium and stored over molecular sieves. Tris(pentafluorophenyl)boron was purchased from STREM and purified by sublimation. Diphenylmethane was purchased from Aldrich and stored over molecular sieves. CH_3OD was purchased from Cambridge Isotopes and used as received. D_8-toluene was used as received and stored over molecular sieves. ^1H and ^2H NMR experiments were performed on a Varian INOVA600 MHz or Bruker DRX500 MHz spectrometer.

The ligands and precatalysts (**1**-**5**) were prepared following modified literature procedures.[12, 26, 27] We describe herein the details for one representative procedure and provide the others in the Supporting Information.

Synthesis of 6,6'-((((tetrahydrofuran-2-yl)methyl)-azanediyl)bis(methylene))bis(2,4-di-tert-butyl-phenol), tBu-ON^{THF}O ligand. In a typical synthesis, an 80 mL reaction vessel was charged with 2,4-di-tert-butylphenol (6.19 g, 30.0 mmol), 2-(aminomethyl) tetrahydrofuran (1.55 mL, 15 mmol) and 37% histological grade formaldehyde (6.00 mL, 80 mmol), distilled water, and a stir bar while maintaining a maximum volume of 80 mL. The biphasic reaction mixture was placed in a CEM microwave reactor and allowed to warm to 100 ºC over 5 min while stirring. The reaction was allowed to stand at 100 ºC for 30 min, and then cooled to room temperature. The aqueous layer was removed, and cold, dry methanol was added to the organic phase. This mixture was shaken for 30 min, and the resulting solid isolated by vacuum filtration. The crude ligand product was purified by crystallization from ethanol (28% yield).

Synthesis of Zr[tBu-ON^{THF}O]Bn$_2$ (1). In a typical synthesis, a 100 mL flask was charged with tetrabenzylzirconium (0.557 g, 1.22 mmol), 20 mL toluene, and a stir bar and fitted with a rubber septum. A second 100 mL flask was charged with the ^{t}Bu-ON^{THF}O ligand (0.609 g, 1.13 mmol) and 20 mL of toluene. The two flasks were placed under an inert atmosphere, and the ligand solution was added to the tetrabenzylzirconium solution via a cannula. The reaction was allowed to warm to 60 ºC and stir for 2 h resulting in a bright yellow solution. The solution was concentrated to about 10 mL and placed into a -10 ºC freezer. Yellow crystals formed within 2 days and the mother liquor was removed via a

cannula. The crystals were dried under vacuum (84% yield). The precatalyst was recrystallized by vapor diffusion of pentane into a precatalyst/toluene solution to afford an analytically pure complex.

NMR scale polymerization of 1-hexene. The procedure for NMR scale polymerization is based on literature.[29] For a typical polymerization, Zr[tBu-ON^{THF}O]Bn$_2$ (**1**) (6.1 mg, 0.0075 mmol) was dissolved in 0.5 mL toluene in a small vial and sealed with a screw-cap septum. The vial containing the precatalyst solution was pierced with a 1 mL syringe. The vial and syringe were placed in an N_2 bag and allowed to equilibrate to 25 ºC. Tris(pentafluorophenyl)boron (4.3 mg, 0.0084 mmol), 1-hexene (0.1265 grams, 1.50 mmol), and diphenylmethane (9.5 mg 0.056 mmol) were added to a 2 mL volumetric flask and diluted to the mark with d^8-toluene. This solution was placed in an NMR tube and sealed with a septum. The monomer/activator solution was placed in the spectrometer and allowed to equilibrate to 25 ºC using a VT controller. A measurement was taken to determine the initial concentration of monomer relative to the internal standard. The NMR tube was removed from the spectrometer, and the catalyst precursor solution was added to the activator/monomer solution by piercing the septum while the syringe remained in the N_2 bag. The reaction mixture was shaken for ca. 30 seconds and placed back into the spectrometer. Spectra were acquired at predetermined time intervals until the reaction reached completion. Each sample was prepared for GPC analysis by evaporation over mild heat before dissolution in hexanes and filtration through an alumina plug to remove the quenched catalyst. Evaporation of solvent yielded clear, colorless poly(1-hexene). The

array of ^{1}H spectra was collected on an INOVA 600 MHz spectrometer and analyzed using MestReNova.

Batch polymerization of 1-hexene. The procedure for Manual Quench is based on literature.[30] For a typical polymerization, Zr[tBu-ON^{THF}O]Bn_2 (0.073 g, 0.090 mmol) was dissolved in 5.0 mL toluene in a small vial that was sealed with a screw-cap septum. The vial containing the precatalyst solution was pierced with a 10 mL syringe. The vial and syringe were placed in an N_2 bag and allowed to equilibrate to 25 ºC. Tris(pentafluorophenyl)boron (0.053 grams, 0.099 mmol), and 1-hexene (1.575 g, 18.71 mmol) were added to a 25 mL flask and diluted to the mark with toluene. This solution was diluted to 26 mL with 1 mL of toluene, and 1 mL of the resulting solution was removed for quantification of the initial monomer concentration through NMR analysis. The flask was sealed with a septum and moved from an N_2 filled glovebox to a vacuum manifold and placed under argon. The monomer/activator solution was allowed to equilibrate to 25 ºC using a temperature-controlled silicone oil bath. The catalyst precursor solution was added to the activator/monomer solution by piercing the septum while the syringe remained in the N2 bag. The resulting yellow solution was allowed to stir while aliquots were removed at selected times and each was injected into a 10 mL volumetric flask containing 1 mL of deutero-methanol. A 1 mL aliquot from the quenched solutions was removed and a 0.5 mL solution of d-toluene spiked with diphenylmethane as an internal standard for quantification of 1-hexene consumption (via ^{1}H NMR on Varian Inova600). Each sample was prepared for GPC analysis by evaporation over mild heat before dissolution in hexanes

and filtration through an alumina plug to remove the quenched catalyst. Evaporation of solvent yielded clear, colorless poly(1-hexene).

In the case of vinyl end group analysis, a 1 mL aliquot was worked up as described above. The resulting polymer was dissolved in $CDCl_3$, and diluted to the mark in a 2 mL volumetric flask. Diphenylmethane was used as an internal standard and the method of standard additions was used in quantification of the end groups by 1H NMR. All end-group analysis measurements were taken on a Bruker DRX500 spectrometer at 25 ºC.

In the case of ^2H analysis for active-site counting, the remaining quenched reaction solution (8 mL) was worked up as described above. The resulting polymer was dissolved in CH_2Cl_2, and diluted to the mark in a 2 mL volumetric flask. d_6-benzene was used as an internal standard and the method of standard additions was used in quantification of active sites by ^2H NMR. All active site measurements were taken on a Bruker DRX500 spectrometer at 25 ºC.

Gel Permeation Chromatography (GPC) Analysis. The procedure used to analyze polymer samples using GPC methods was taken from Novstrup et al.,[7] and it is summarized below. Poly(1-hexene) samples were added to THF at room temperature and allowed to dissolve for 4 h. Solutions were then passed through a 0.2 μm filter to remove any particulate matter. The GPC analysis was performed on a Waters GPCV 2000 for system **1** and **3**, and on a Viscotek GPCmax VE 2001 for system **2**, **4**, and **5**. On the Waters GPCV 2000, samples were injected through a 101.3 μL injection loop and passed through two Polymer Laboratories PLGel 5 μm Mixed-C columns in series in a 45 °C oven at a flow rate of 1.0 mL min-1. On Viscotek GPCmax VE 2001, samples were injected through a

200 μL injection loop and passed through three Viscotek T6000M 10 μm General Mixed Org columns in series in a 35 °C oven at a flow rate of 1.0 mL min^{-1}. The analysis made use of the differential RI detector and a capillary viscometer. Molecular weights were assigned by way of a universal calibration curve created with polystyrene standards ranging from 580 g mol-1 to 3,114,000 g mol-1. The calibration was verified through the analysis of a broad standard, SRM 706a, provided by the National Institute of Standards and Technology.

2.3 Results

Here we present a complete kinetic analysis for 1-hexene polymerization by catalysts **1**-**5**. In approaching each system, we followed our previously developed kinetic modeling method[7, 29] based on the analysis of multi-response data that includes GPC traces where we did not make any a priori assumptions about the elementary reaction steps taking place. However, when this independent analysis was completed for each catalyst system, it emerged that all five systems described herein follow a similar kinetic mechanism including initiation, propagation via normal insertion, 2,1-misinsertion, recovery from misinsertion, and two types of chain transfer resulting in the formation of vinylidene and vinylene species. The kinetic steps are illustrated in Scheme 1. The activation step is fast on the timescale of polymerization and as a result was not used in the kinetic modeling. Chain transfer resulting in vinylidene and vinylene follows either unimolecular (monomer independent) β-H elimination or bimolecular β-H transfer to monomer.

Examining the available data, the reasons for the mechanism above (Scheme 1) are as follows:

I. Misinsertion (k_{mis}) and recovery (k_{rec}) are necessary because

1. we observe two types of chains attached to the active sites (primary and secondary) in active-site counting experiments with MeOD quenches (2H NMR of isolated polymer gives δ 0.83 (DH2C—Polymer) and 1.22 (DH(Bu)C—Polymer).
2. when analyzing the produced polymer, there are two types of vinyl end groups are observed: one with a terminal double bond at the end of the chain (vinylidene), and another with an internal double bond inside the chain (vinylene). We believe, in agreement with the literature,30 the latter arises from chain transfer of misinserted chains.
3. the secondary sites (Zr-CH(Bu)-Polymer) do not accumulate over time. We assume this is the case because they are able to recover via normal 1-hexene insertion.
4. although there is an alternative explanation for points 1 through 3, namely, that there are two different sites growing separately, it is expected that such a mechanism would at least under some experimental conditions produce bimodal MWD. The facts that none of the five systems exhibit a bimodal MWD and all yield narrow PDI values strongly suggest that these systems are single-site catalysts.

II. Chain transfer reactions are necessary because we observe polymer chains with vinyl end groups. It should be noted that there are two possible mechanisms through monomer dependent and monomer independent pathways. The monomer dependent pathway (β-H transfer to monomer) results in an active site with one repeat unit, while the monomer independent pathway (β-H elimination) results in the formation of a zirconium hydride. There is an ongoing discussion in the literature whether the insertion of a monomer in the zirconium hydride i.e. re-initiation ($k_{reinitiation}$) is facile or hindered as compared to

the normal initiation (k_i) for a given catalyst system.[31] If the rate constant of re-initiation ($k_{reinitiation}$) of the zirconium hydride is slow, it effectively renders affected catalyst sites inactive, which in turn has an effect on the monomer consumption curve, active sites count, and the MWDs. As a result the value of the re-initiation rate constant ($k_{reinitiation}$) can be determined. On the other hand, when the rate constant of the re-initiation of zirconium hydride is fast, the data are usually not sensitive enough to determine its value precisely, similarly to how the data are not sensitive enough to determine the normal initiation rate when it is not significantly slower than the propagation rate. In practice we have set the re-initiation rate to be equal to the propagation rate in cases when the re-initiation rate is determined to be fast.

An important caveat is that the catalyst participation for each system may vary and not be 100%. The catalyst participation can be estimated from the active site counting experiments (quench with MeOD followed by ^{2}H NMR analysis polymer chains). Also, for the systems where the chain transfer is low (catalysts 1 and 5) the catalyst participation is readily estimated from the slope of M_w vs. conversion plot, which is linear in these cases. When applicable, these two methods give consistent results. The catalyst participation information for 1-5 is provided in the Supporting Information.

For each system we simultaneously fit the following: (1) monomer consumption, (2) MWD, (3) active site counts, and (4) end group counts. The data set usually includes several initial conditions of different $[C]_0$ (C = precatalyst/$B(C_6F_5)_3$) and $[M]_0$ (M = 1-hexene). For some conditions, multiple repeats were carried out, and the results were consistent when small variation in active-site catalyst participation was accounted for; however, only one repeat is shown in the figures below.

In determining error margins of the estimates for the six rate constants for each catalyst system (see Scheme 1), the following considerations apply: (1) the experimental data has an inherent error resulting from the measurement procedure. Specifically, the NMR spectrum is characterized by the uncertainty of roughly 5% for the peak integration; the GPC trace is characterized by the uncertainty of the weight average, M_w, of approximately 3%, where the uncertainty in the shape of the distribution is more difficult to ascertain (see discussion in reference 29). However, these estimates are based on the best experimental conditions, such sufficient concentration of the species of interest in the case of NMR, which holds for the monomer concentration. (2) In the case of the active sites and vinyl end group analyses, the concentrations are relatively low, causing the uncertainty to increase. Three separate measurements were performed for each sample, where the concentration varied slightly from measurement to measurement. The standard deviation calculated on the basis of these three measurements is compared to the inherent NMR integration error, and the larger error is chosen. (3) In the case of the GPC measurements, repeat runs result in minimal scatter such that the GPC curves appear overlapping. This, however, should not be taken as an actual estimate of the experimental error, since the error in the GPC measurements may be systematic rather than random due to various reasons described in the literature.[29] Instead, we assumed that the potential error in the GPC outputs caused by the uncertainty in the *dn/dc* values, inter-detector time, etc., amounts to at most a 10% up or down shift of each slice molecular weight and hence the shift of the entire MWD. (This actually translates in the -0.05/+0.04 shifts on log scale).[7] For most of the studied systems, error from the GPC measurements were determined to

cause the largest uncertainty in the rate constants, and therefore this method was used to generate the uncertainty reported in this paper.

In the rest of this section we provide first the detailed analysis including fits to the data for each catalyst system, and then a summary of all the rate constants in Table 1.

Activation

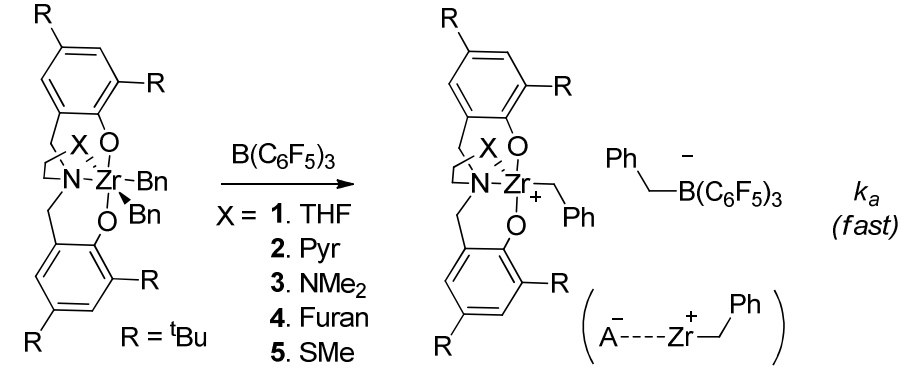

Initiation

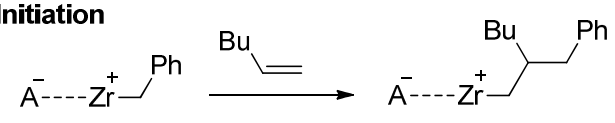

Propagation

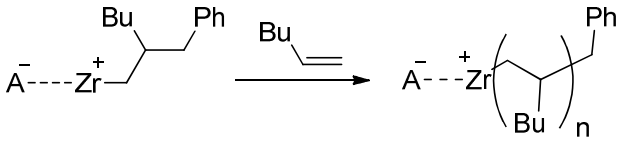

Misinsertion

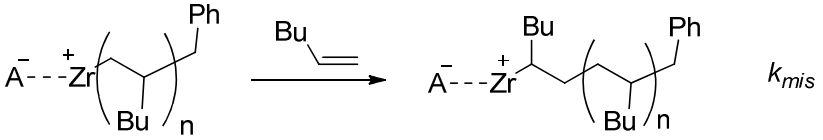

Recovery

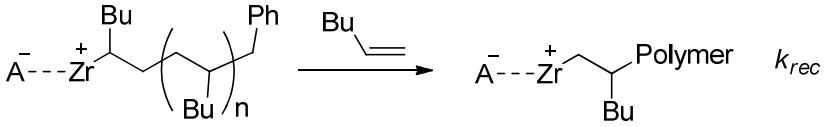

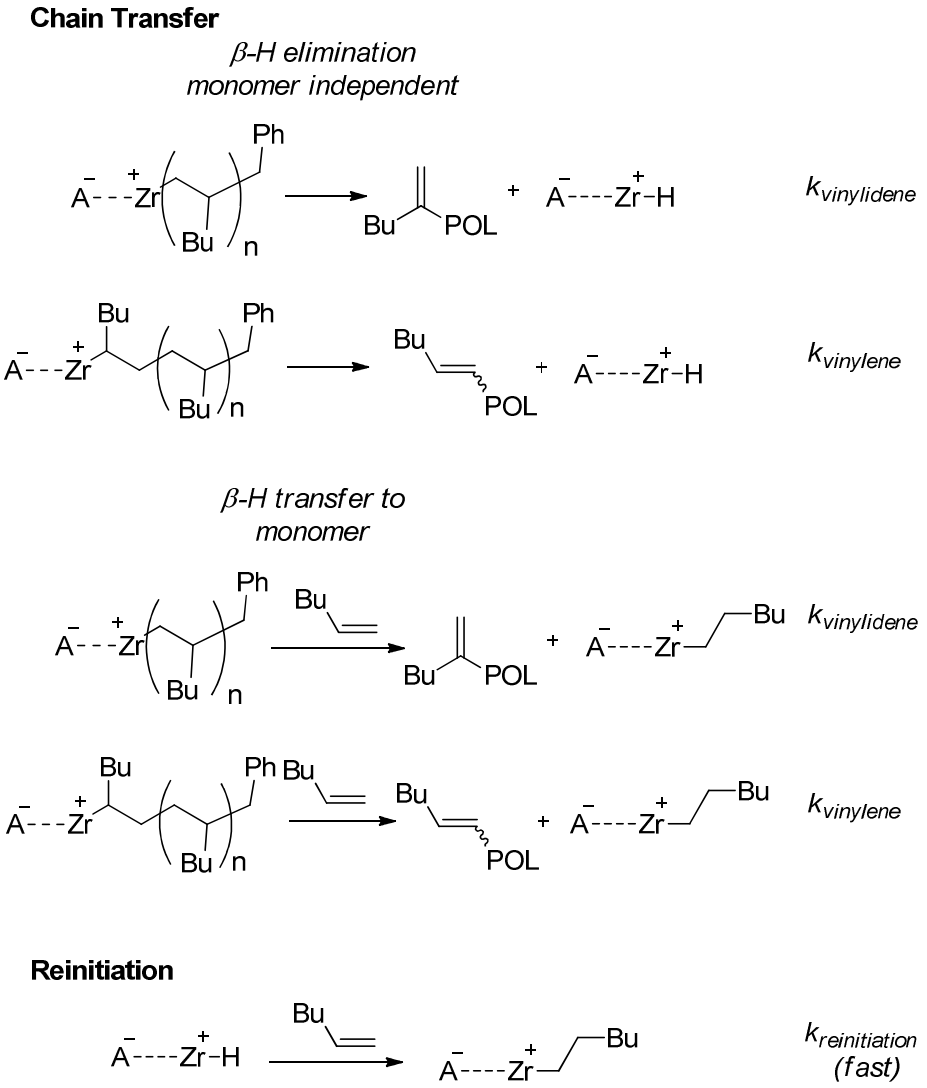

Scheme 2-1. The elementary kinetic steps used in fitting the data for catalysts 1-5. The ordinary differential equations (ODEs) that describe the mass-action kinetics associated with this mechanism are provided in the Supporting Information.

Zr-THF catalyst 1. The experimental data along with the kinetic modeling fits are presented in Figure 2.

The specific features of this system are:

(1) very few chain transfer events;

(2) catalyst participation is around 50%;

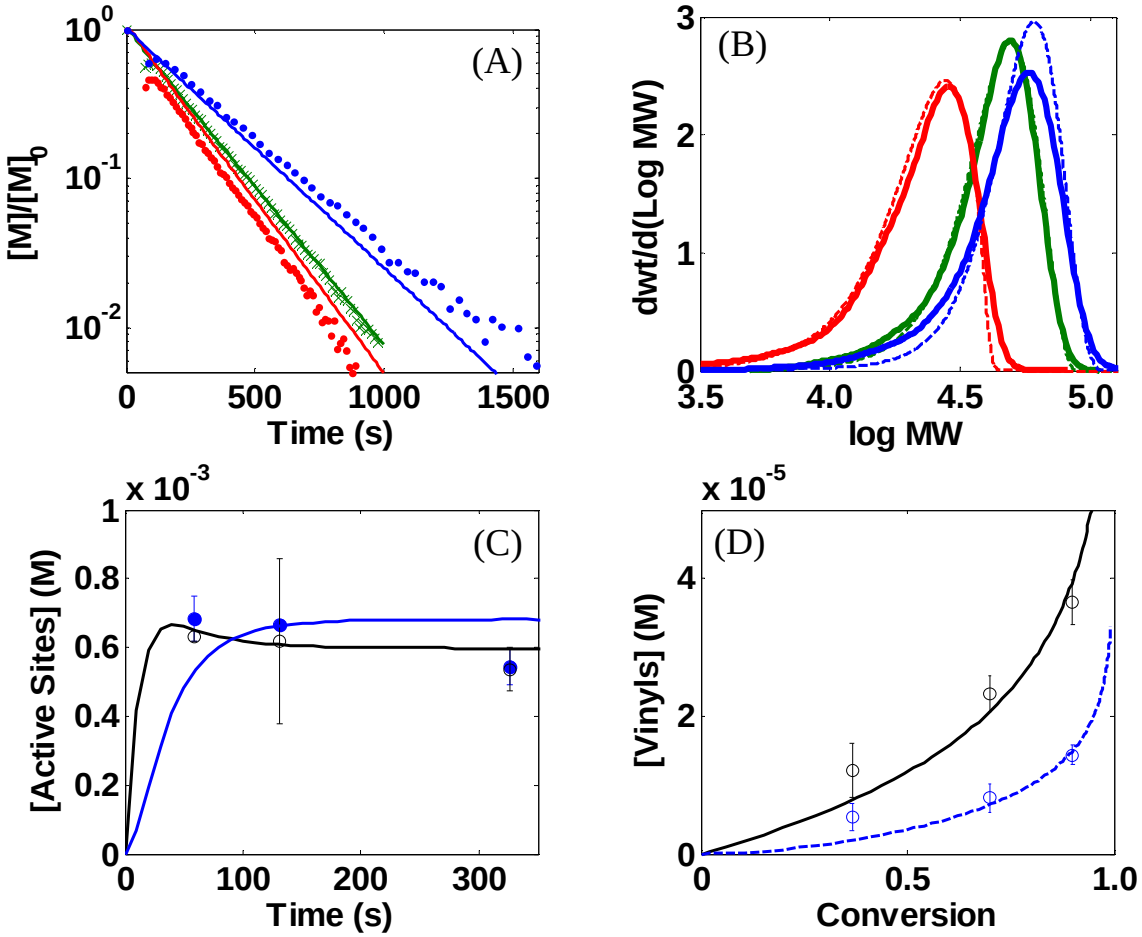

Figure 2-2. Multi-response data set with fits for Zr[^{t}Bu-ON^{THF}O]Bn$_2$/B(C$_6$F$_5$)$_3$ catalyst 1. (A) Monomer consumption of selected NMR scale reactions having catalyst to monomer ratios of 1:100 (red, $[C]_0$ = 3.0 mM, $[M]_0$ = 0.30 M), 1:200 (green, $[C]_0$ = 3.0 mM, $[M]_0$ = 0.60 M), and 1:400 (blue, $[C]_0$ = 1.5 mM, $[M]_0$ = 0.60 M). Symbols are data, solid lines are modeling fits. (B) MWDs of the polymer resulting from the reactions shown in (A). Solid curves are data, dashed curves are fits. (C) Active site counts of selected batch scale reaction with three quenches using MeOD at different reaction times. $[C]_0$ = 3.0 mM, $[M]_0$ = 0.60 M. Black symbols: primary active-site count; blue symbols: secondary active-site count. Solid curves are modeling fits. (D) Vinyls analyses of selected batch scale reaction with three quenches at different reaction time. $[C]_0$ = 3.0 mM, $[M]_0$ = 0.60 M. Black symbols: vinylidene count; blue symbols: vinylene count. Lines represent kinetic modeling fits.

Zr-Pyridine catalyst 2. The experimental data along with the kinetic modeling fits are presented in Figure 3.

The specific features of this system are:

(1) catalyst participation around 50%;

(2) initiation is fast, i.e. no more than 40 times slower than propagation;

(3) the monomer consumption, i.e. the logarithm of the normalized monomer concentration vs. time (Figure 3a) appears bent downward. The explanation for this effect is that the overall rate of consumption is controlled by the primary sites, while the secondary sites are dormant. The exit from the secondary sites can happen via two pathways: (1) recovery by normal monomer insertion, and (2) monomer independent chain transfer resulting in an activated catalyst ready to initiate a new chain and start consuming monomers. Toward the end of the reaction, when the monomer concentration becomes low, the rate of misinsertion slows down but the second recovery pathway (chain transfer) does not (since it's independent of monomer). As a result, the number of primary sites increases and the number of secondary sites decreases (Figure 3c), producing the apparent acceleration of monomer consumption.

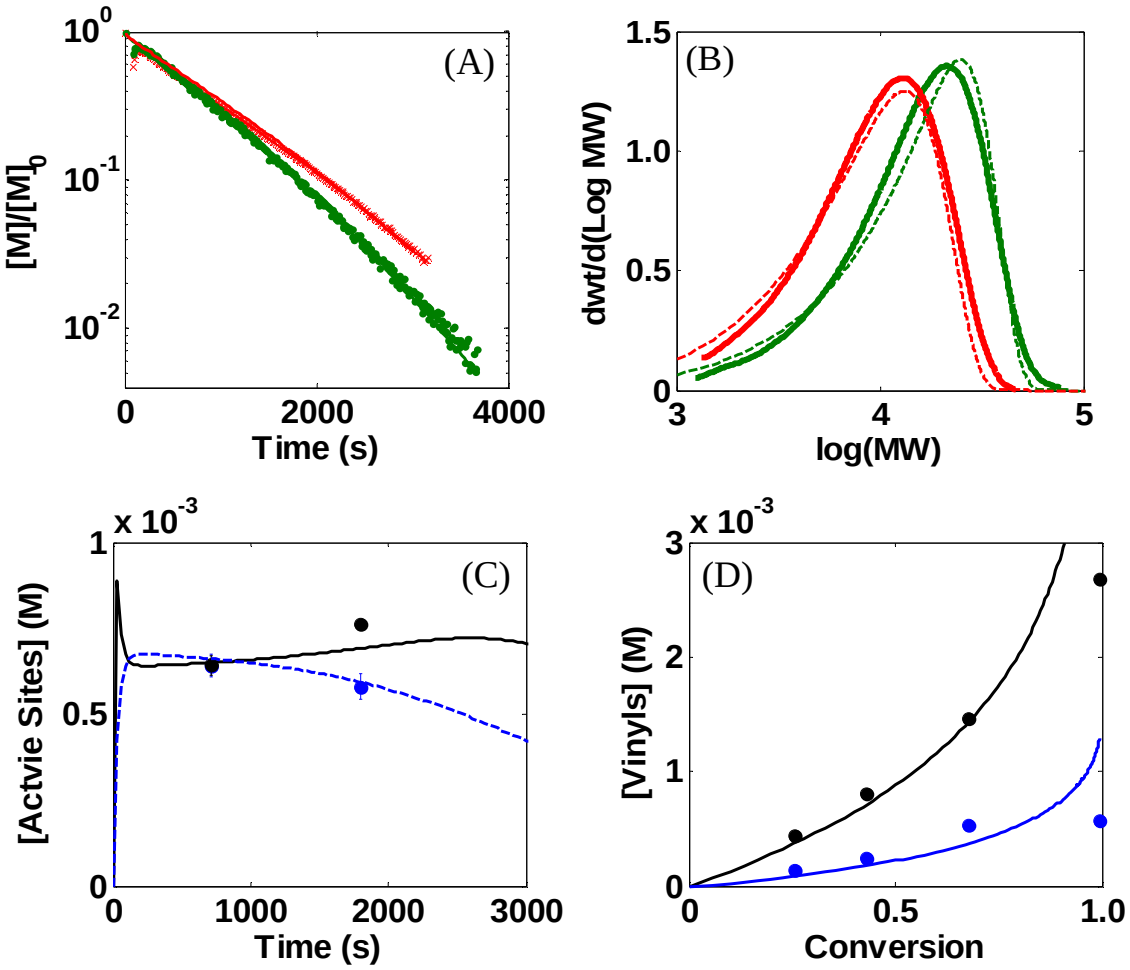

Figure 2-3. Multi-response data set with fits for Zr[^{t}Bu-ON^{Py}O]Bn$_2$/B(C$_6$F$_5$)$_3$ catalyst 2. (A) Monomer consumption of selected NMR scale reactions having catalyst to monomer ratios of 1:100 (red, $[C]_0$ = 3.0 mM, $[M]_0$ = 0.30 M), and 1:200 (green, $[C]_0$ = 3.0 mM, $[M]_0$ = 0.60 M). Symbols are data, solid lines are modeling fits. (B) MWDs of the polymer resulting from the reactions shown in (A). Solid curves are data, dashed curves are fits. (C) Active site counts from three selected NMR scale reactions. Each reaction is quenched using MeOD at different reaction time. $[C]_0$ = 3.0 mM, $[M]_0$ = 0.60 M. Black symbols: primary active-site count; blue symbols: secondary active-site count. Solid curves are modeling fits. (D) Vinyls analyses of three selected NMR scale reactions quenched at different reaction time. $[C]_0$ = 3.0 mM, $[M]_0$ = 0.60 M. Black symbols: vinylidene count; blue symbols: vinylene count. Lines represent kinetic modeling fits.

Zr-NMe$_2$ catalyst 3. The data and model fits for this catalyst have been published in a previous article.[29] The specific features of this system are:

(1) Catalyst participation is generally around 45%, although the exact value varied from 20 - 60% depending on the experiment;[29]

(2) Initiation is roughly 70 times slower than propagation;

(3) Chain transfer occurred moderately frequently, with both vinylidene and vinylene end groups detected. The data suggest that monomer independent pathways, β-H elimination, lead to both types of the observed vinyl end groups;

(4) The error estimation in the referenced work[29] was calculated via a different method than the one used here. For consistency, the current method has been applied to the data to produce error estimates for the rate constants shown in Table 1. The error estimation is based on the error from the GPC measurement.

Zr-Furan catalyst 4. The experimental data along with the kinetic modeling fits are presented in Figure 4.

The specific features of this system are:

(1) catalyst participation around 50%;

(2) initiation is slow, evidenced by the apparent induction period on the monomer consumption curve (Figure 4a);

(3) chain transfer reactions are monomer dependent, β-H transfer to monomer, supported by the following arguments: (a) under different initial catalyst and monomer concentrations, the MWD does not change significantly (Figure 4b); and (b) the relationship between the end group concentrations and monomer conversion during most of the reaction is linear. These two features indicate that the ratio of the chain transfer rate to the propagation rate is a constant independent of the initial

concentrations, and that monomer dependent chain transfer reactions control the MW in this system.

(4) There is a continuous increase in the end group counts when the batch system is allowed to run overnight after the monomer has already been fully consumed (Figure 4d). It is, hence, concluded that monomer independent chain transfer reaction must take place when there is no monomer, and this chain transfer reaction most likely arises from normal insertion. As mentioned before, this type of chain transfer results in formation of zirconium hydride. However, in order to model the monomer consumption data for this catalyst system, it is necessary for the re-initiation rate constant to be zero, which effectively creates a deactivation pathway that is responsible for the bending observed in the monomer consumption curve (Figure 4a) and the drop in primary site count (Figure 4c). It is known that for some systems, the re-initiation rate is slow for metal hydride.[31]

(5) Given that the primary active-site count drops and the secondary active-sites accumulate, we believe there is no recovery from misinsertion in this system ($k_{reinitiation} \sim 0$).

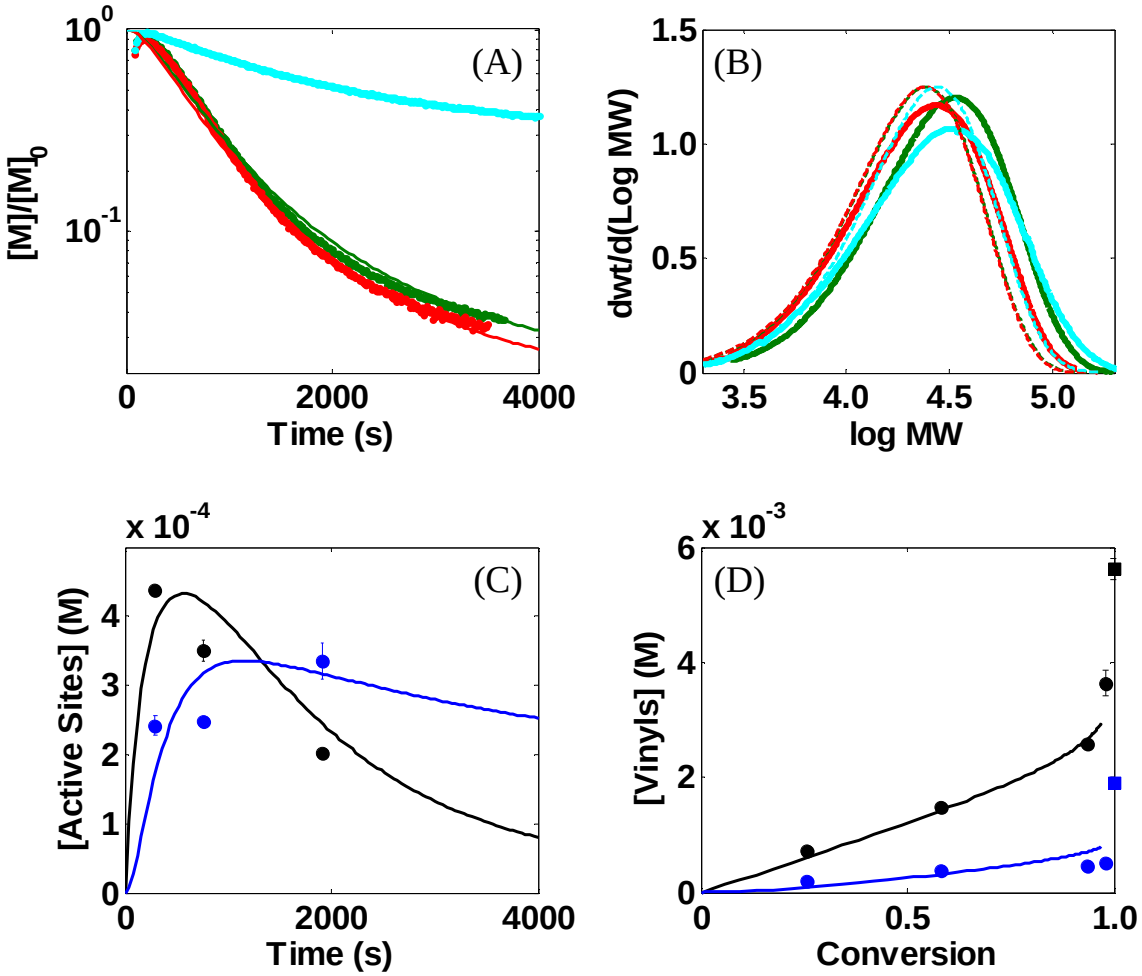

Figure 2-4. Multi-response data set with fits for Zr[^{t}Bu-ON^{furan}O]Bn$_2$/B(C_6F_5)$_3$ catalyst 4. (A) Monomer consumption of selected NMR scale reactions having catalyst to monomer ratios of 1:100 (red, $[C]_0$ = 3.0 mM, $[M]_0$ = 0.30 M), 1:200 (green, $[C]_0$ = 3.0 mM, $[M]_0$ = 0.60 M), and 1:400 (cyan, $[C]_0$ = 1.5 mM, $[M]_0$ = 0.60 M). Symbols are data, solid lines are modeling fits. (B) MWDs of the polymer resulting from the reactions shown in (A). Solid curves are data, dashed curves are fits. (C) Active site counts of selected batch scale reaction with three quenches using MeOD at different reaction time. $[C]_0$ = 3.0 mM, $[M]_0$ = 0.60 M. Black symbols: primary active-site count; blue symbols: secondary active-site count. Solid curves are modeling fits. (D) Vinyls analyses of selected batch scale reaction with three quenches at different reaction time. $[C]_0$ = 3.0 mM, $[M]_0$ = 0.60 M. Black symbols: vinylidene count; blue symbols: vinylene count. Squares are vinyls counts taken after 12 h. Lines represent kinetic modeling fits.

Zr-SMe catalyst 5. The experimental data along with the kinetic modeling fits are presented in Figure 5.

The specific features of this system are:

(1) secondary Zr-polymer sites (Zr-CH(Bu)-Polymer) resulting from misinsertion dominate over primary active-sites (Zr-CH2-Polymer). The model-based explanation is that the k_{mis}/k_p ratio is high while k_{rec}/k_p is low. These values for this catalyst are similar to those for catalyst 1, where secondary sites are roughly equal to primary sites.

(2) vinylene end groups, which are formed from chain transfer of secondary sites, are more abundant than vinylidene end groups. This is because of the higher concentration of secondary sites rather than a larger $k_{vinylene}$ rate constant.

(3) vinyl groups form via chain transfer to monomer, affording second-order rate constants. The data, however, is not definitive, and a first-order reaction (β-H elimination) cannot be definitively ruled out. In either case, the vinyl concentrations are relatively small, and the effect of the chain transfer rate constants on the responses other than the vinyl end group analysis data (e.g. the MWDs) is small.

(4) the total active site concentration (primary plus secondary) decreases over the course of the reaction. In addition, the monomer consumption slows late in the reaction. These behaviors imply a first order (in catalyst) deactivation reaction. The deactivation rate constant is approximately half of the initiation rate constant, with the result that the total active site concentration remains low throughout the reaction.

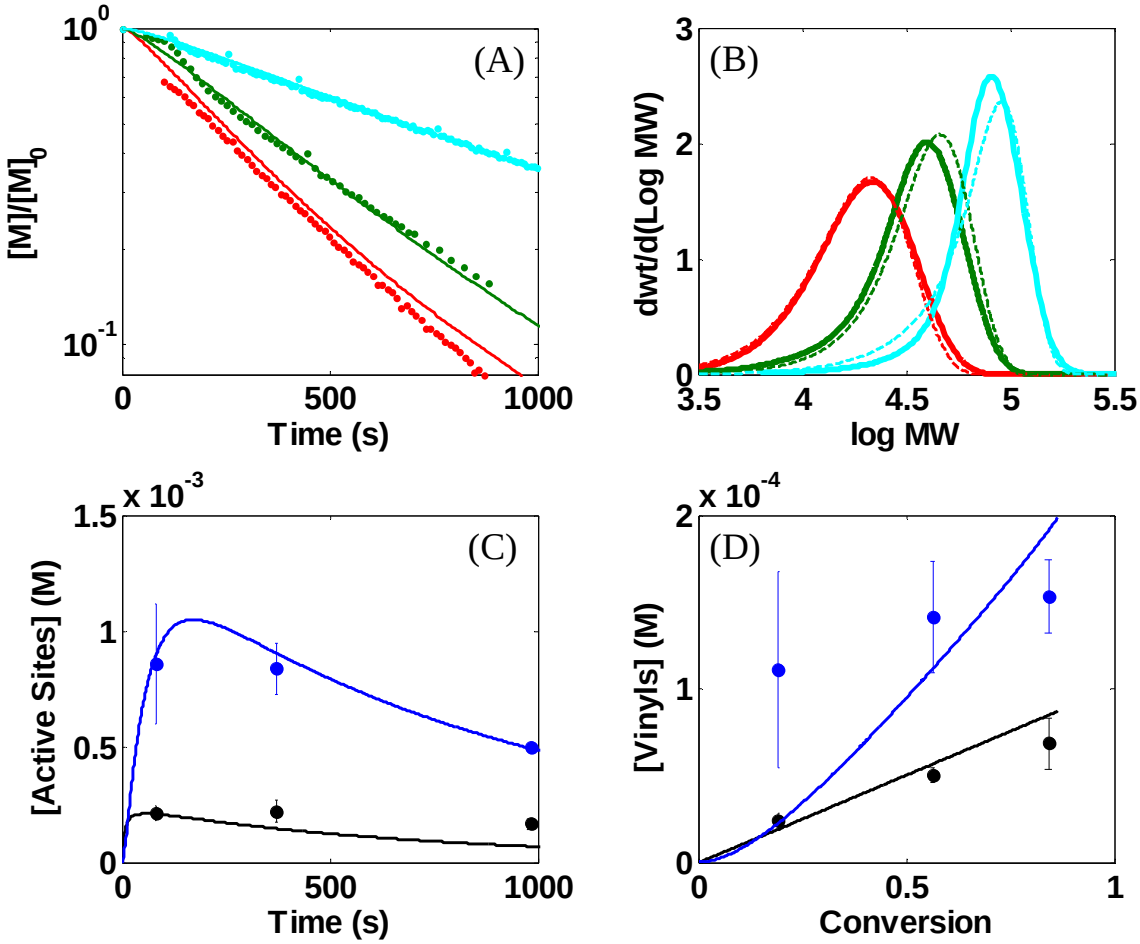

Figure 2-5. Multi-response data set with fits for Zr[^{t}Bu-ON^{SMe}O]Bn$_2$/B(C_6F_5)$_3$ catalyst 5. (A) Monomer consumption of selected NMR scale reactions having catalyst to monomer ratios of 1:100 (red, $[C]_0$ = 3.0 mM, $[M]_0$ = 0.30 M), 1:200 (green, $[C]_0$ = 3.0 mM, $[M]_0$ = 0.60 M), and 1:400 (cyan, $[C]_0$ = 1.5 mM, $[M]_0$ = 0.60 M). Symbols are data, solid lines are modeling fits. (B) MWDs of the polymer resulting from the reactions shown in (A). Solid curves are data, dashed curves are fits. (C) Active site counts of selected batch scale reaction with three quenches using MeOD at different reaction time. $[C]_0$ = 3.0 mM, $[M]_0$ = 0.60 M. Black symbols: primary active-site count; blue symbols: secondary active-site count. Solid curves are modeling fits. (D) Vinyls analyses of selected batch scale reaction with three quenches at different reaction time. $[C]_0$ = 3.0 mM, $[M]_0$ = 0.60 M. Black symbols: vinylidene count; blue symbols: vinylene count. Squares are vinyls counts taken after 12 h. Lines represent kinetic modeling fits.

(5) while 100% of the catalyst is available to initiate (in contrast to the other systems where only a fraction participates), no more than about one third (ca. 33%) of the zirconium active sites contain a growing polymer chain at any given time.

2.4 Discussion

In this study, the complete set of kinetic rate constants for five zirconium amine bis-phenolate catalyst systems have been presented. For each system, a rich data set including MWD has been collected and successfully fitted by comprehensive kinetic modeling. The mechanism of 1-hexene polymerization for these catalysts (1-5) consists of the following elementary reaction steps: initiation, normal propagation, misinsertion, recovery, and chain transfer. The values of the rate constants are shown in Table 1.

Table 2-1. Rate constants for 1-hexene polymerization with the Zr[tBu-ON^{X}O]Bn$_2$/B(C_6F_5)$_3$ catalysts **1**-**5**.[a]

X	THF (1)	Pyridine (2)	NMe2 (3)	Furan (4)	SMe[b] (5)
Zr—X/ Å	2.37	2.51	2.59	2.69	2.89
k_i/ M^{-1} s^{-1}	0.08 (+0.02/ -0.01)	> 0.05	0.16 (+0.04/-0.02)	0.0031 (+0.0003/-0.0004)	0.017 (+0.002/-0.001)
k_p/ M^{-1} s^{-1}	8.0 (+0.8/ -0.2)	1.8 (+0.2/-0.1)	11 (+1/-1)	3.52 (+0.03/-0.04)	12 (+5/-4)
k_{mis}/ M^{-1} s^{-1}	0.054 (+0.026/-0.003)	0.031 (+0.004/-0.005)	0.055 (+0.007/-0.004)	0.0064 (+0.0002/-0.0004)	0.20 (+0.08/-0.06)
k_{rec}/ M^{-1} s^{-1}	0.047 (+0.021/-0.002)	0.028 (+0.004/-0.005)	0.04 (+0.03/-0.02)	0[c]	0.036 (+0.001/-0.001)
$k_{vinylidene}$ (10^{-3}) / s^{-1}	0.14 (+0.014/ -0.02)	2.4 (+0.1/-0.1)	12.2 (+0.8/-0.6)	1.00 (+0.07/-0.08)	0
$k_{vinylene}$ (10^{-3})/ s^{-1}	0.051 (+0.002/ -0.003)	0.65 (+0.06/ -0.05)	8.72 (+0.07/ -0.04)	0	0
$k_{vinylidene}$ (10^{-3}) / M^{-1} s^{-1}	0	0	0	12.1 (+0.7/-0.6)	2.2 (+0.6/-0.4)
$k_{vinylene}$ (10^{-3})/ M^{-1} s^{-1}	0	0	0	6.9 (+0.07/-0.06)	0.95 (+0.06/-0.04)

[a] In toluene at 25 °C. See Figure 1 for precatalyst structures and Scheme 1 for reactions steps. Errors are in parentheses. [b] In toluene at 22 °C. [c] A value of zero means the fit did not require the inclusion of this reaction step.

In the first row in Table 1, the Zr-X bond distance as determined by single crystal X-ray crystallography is shown for each catalyst precursor.[10, 11, 13] Catalysts 1-5 are characterized by a progressively longer Zr-X bond distance. Examining the data given in Table 1, the chain transfer reaction rates (chain transfer following normal insertion, $k_{vinylidene}$, and chain transfer following misinsertion, $k_{vinylene}$) for systems 1, 2, and 3 are monomer independent, whereas, for systems 4 and 5, the predominant chain transfer reactions are monomer dependent. We speculate that once a certain Zr-X bond distance has

been reached, there is enough steric freedom to accommodate monomer dependent chain transfer processes as is the case for systems 4 and 5. As shown in Figure 4d (see caption), when left overnight, system 4 shows an increase in chain transfer products even after all available monomer has been consumed within 1 h suggesting that there is some amount of monomer independent chain transfer (β-H elimination) events taking place. It follows that although monomer dependent chain transfer is the preferred pathway for systems containing a longer Zr-X bond distance, the possibility of monomer independent chain transfer events remains.

While the literature has ample support from empirical observations and semi-quantitative measurements that steric constraints of the ligand contribute significantly to chain transfer rates and the mechanism by which chain transfer occurs, i.e. unimolecular β-H elimination versus transfer to monomer,[18] we present a quantitative measure of the rate constants and illustrate at what point a cross-over in the chain transfer mechanism occurs. An important point that should not be passed over lightly is that in the analysis of systems 1-5 the chain transfer rate constants presented in this work are not obtained just by analysis of vinyl end groups in isolation from all the other rate constants that are pertinent to the catalytic cycle, but rather the full suite of rate constants describing the entire data set for each of the catalyst systems. It is only when this level of quantitative analysis has been employed that one can make definitive QSAR describing how catalyst structure affects properties of the resulting polymer. For example, often in the literature observation of changes in M_w is taken as a direct measure of chain transfer rates as long as activity (TOF) of the catalysts under study remained comparable.[5, 18] The assumption in such comparisons is that TOF is a direct measure of k_p and that all other constants did not change. By applying

our quantitative analysis methods such assumptions and pitfalls that arise from comparing activities rather than rate constants can be eliminated.

A close examination of the unimolecular (β-H elimination) chain transfer rate constants $k_{vinylidene}$ and $k_{vinylene}$ for systems 1, 2, and 3 revealed a very intriguing trend. There appears to be a direct correlation between the length of the Zr-X bond distance and $k_{vinylidene}$ and $k_{vinylene}$ (Figure 6). Remarkably, the logarithms of both chain transfer rate constants appear to depend linearly on the aforementioned bond length. It can be speculated that this increase in bond distance allows for more steric freedom to accommodate the β-hydride agostic interaction necessary for chain transfer to occur, causing an increase in $k_{vinylidene}$ and $k_{vinylene}$ for catalysts 1, 2, and 3. This observation implies that the activation energy, which is proportional to the logarithms of the rate constants at constant temperature, is linearly related to the Zr-X bond length at least for the three systems investigated. Although $k_{vinylidene}$ is always larger than $k_{vinylene}$, as seen in Figure 6, both rate constants are affected in a similar way by the increase of the Zr-X bond length as evidenced by their similar slopes.

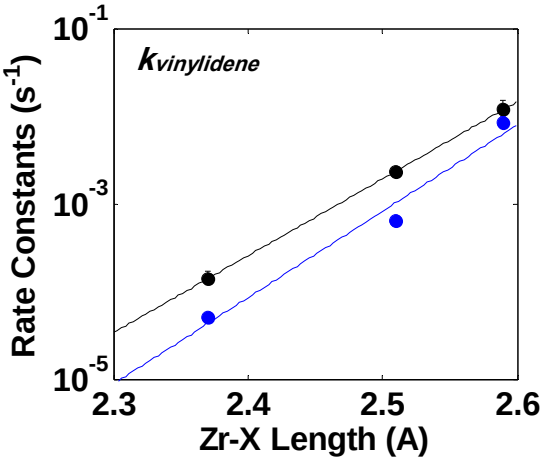

Figure 2-6. Plot of monomer independent chain transfer rate constants ($k_{vinylidene}$ and $k_{vinylene}$) versus Zr-X bond length for catalysts 1, 2, and 3. Black symbols: chain transfer rate constants from primary sites ($k_{vinylidene}$); blue symbols: chain transfer rate constants from secondary sites ($k_{vinylene}$).

Marks and co-workers have probed the effects of using different activators in Zr-based metallocene systems and showed that ion pairing does modulate chain transfer among other rates of polymerization and stereodefects.[26] The work presented in this study has been able to elucidate the role of variations have on the rates of chain transfer in a way that can be quantified in terms of the simple Zr-X bond distance. The QSAR presented in Figure 6 is useful because it establishes a relationship for this catalyst family that is based on robust rate constants rather than a relative trend or estimated ordering of rates that represents a composite of elementary reaction steps. Of course, robustly establishing a QSAR model will require the analysis of more systems than just the five reported in this paper; however, these results are the start towards developing a fundamental understanding of the relationship between chemical structure and catalytic activity.

However, in systems 4 and 5 the further increase in the Zr-X bond length does not result in the expected increase in vinyl terminated chains, breaking the aforementioned trend and, moreover, leads to a different chain transfer mechanism: a monomer dependent β-H transfer. To illustrate that this change in the trend is quite significant, we show in Figure 7 the predicted vinyl concentrations for system 4 when it is assumed that the trend would continue. Specifically, the hypothetical values $k_{vinylidene}$ = 0.093 s^{-1} and $k_{vinylene}$ = 0.063 s^{-1} are obtained by extrapolating linearly to the Zr-X bond length for system 4, which is 2.69 Å. The predicted vinylidene concentration is more than one order of magnitude higher than the measured experimental value at the end of the reaction. It should be noted that the monomer independent chain transfer is not eliminated completely. As mentioned above, when system 4 was allowed to run for 12 hours after the monomer had been consumed an increase in vinyl concentrations were detected.

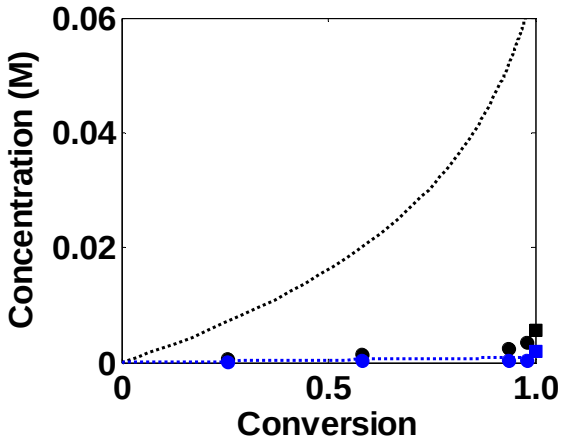

Figure 2-7. Predicted vinyls formation (dashed curves) using rate constants: k_i = 0.08 $M^{-1}s^{-1}$, k_p = 8 $M^{-1}s^{-1}$ $k_{misinsertion}$ = 0.054 $M^{-1}s^{-1}$, k_{rec} = 0.047 $M^{-1}s^{-1}$, $k_{vinylidene}$ = 0.093 s^{-1}, and $k_{vinylene}$ = 0.063 s^{-1} for catalyst 4. Black symbols: measured vinylidene counts; blue symbols: measured vinylene counts. $[C]_0$ = 3.0 mM, $[M]_0$ = 0.60 M.

In the above, we attributed the emergence of the monomer dependent chain transfer mechanism in systems 4 and 5 to increased steric freedom availed by greater Zr-X bond distance. While this may explain the greater ease with which monomer can coordinate to effect chain transfer, it by itself does not explain why the monomer independent reaction should become hindered. We speculate that once the Zr-X distance is large enough (or alternatively the pendent zirconium interaction is weak enough), some other agent, most likely the counter ion, may occupy the spot thereby precluding the β-H agostic bond from forming.[26]

Catalyst 5 also exhibits monomer dependent chain transfer with fairly low rate constants. This result is less surprising than that of system 4 as the sulfur atom of the pendant group in 5 is significantly different than the second row pendant ligand atoms (N

or O) in 1-4 according to HSAB theory. It is speculated that this effect accounts for the mechanistic change observed in system 5.

The rest of the rate constants shown in Table 1 do not seem to exhibit clear trends with respect to Zr-X bond length. Specifically, k_p is large for systems 1, 3 and 5, and several times lower for catalysts 2 and 4. This effect alludes to the fact that other catalyst descriptors, i.e. electronic effects, derived from the sp^2 nature of the donor, are perhaps responsible.[10]

Rate constants for misinsertion (k_{mis}) are similar for systems 1, 2, and 3; whereas, in the case of 4, k_{mis} is an order of magnitude slower. For System 5, k_{mis} is an order of magnitude faster. It stands to reason that the longer Zr-X bond distance would allow for more steric freedom for the misinsertion of monomer resulting in an increased misinsertion rate. However, this line of logic fails to describe catalyst 4, which appears, yet again, to be an outlier.

Rate of recovery from misinsertion (k_{rec}) is similar for systems 1, 2, 3, and 5. For system 4, k_{rec} is zero within the uncertainty of the kinetic analysis. This suggests that the recovery rate for these systems is not governed by sterics.

As discussed in the literature[10,11], these catalysts produce atactic poly(1-hexene); so, it is not clear if the change in the nature of the pendant effects the degree of tacticity in the resulting polymer product in a way that is easily defined.

2.5 Conclusions

A comprehensive kinetic study of five catalytic systems based on Zr amine bis-phenolate complexes has been completed, and the relevant rate constants and elementary

reaction steps were robustly determined for each system. The mechanism includes initiation, normal propagation, misinsertion, recovery, and chain transfer. The most significant finding was an apparent correlation between the zirconium pendant ligand (Zr-X) bond distance and the rate constants of chain transfer. Specifically, for catalysts 1-3, the logarithm of the chain transfer rate constants ($k_{vinylidene}$ and $k_{vinylene}$) increase linearly with the Zr-X bond distance. Once a certain Zr-X bond distance is reached, the chain transfer mechanism changes from monomer independent β-H elimination to monomer dependent β-H transfer (to monomer), as observed for systems 4 and 5. This study has also shown that, with the exception of 4, the rate of misinsertion (k_{mis}) increases for a longer Zr-X bond distance, which is most likely due to an increase in the steric freedom allowing for an increase in misinsertion events, regio errors.

REFERENCES

(1) Chemical Market Associates, Inc. (CMAI), **2005** *World Polyolefins Analysis,* www.cmaiglobal.com.

(2) (a) Chen, E. Y-X.; Marks, T. J. *Chem. Rev.* **2000**, *100*, 1391-1434. (b) Li, H.; Marks, T. J. *Proc. Natl. Acad. Sci. USA* **2006**, *103*, 15295-15302.

(3) Manz, T. A.; Phomphrai, K.; Medvedev, G. A.; Krishnamurthy, B. B.; Sharma, S.; Haq, J.; Novstrup, K. A.; Thomson, K. T.; Delgass, W. N.; Caruthers, J. M.; Abu-Omar, M. M. *J. Am. Chem. Soc.* **2007**, *129*, 3776-3777.

(4) (a) Krauledat, H.; Brintzinger, H. H. *Angew. Chem. Int. Ed.* **1990**, *29*, 1412-1413. (b) Piers, W. E.; Bercaw, J. E. *J. Am. Chem. Soc.* **1990**, *112*, 9406-9707. (c) Coates, G. W.; Waymouth, R. M. *J. Am. Chem. Soc.* **1991**, *113*, 6270-6271.

(5) Britovsek, G. J. P.; Gibson, V. C.; Wass, D. F. *Angew. Chem. Int. Ed.* **1999**, *38*, 428-447.

(6) Arriola, D. J.; Carnahan, E. M.; Hustad, P. D.; Kuhlman, R. L.; Wenzel, T. T. *Science* **2006**, *312*, 714-719

(7) Novstrup, K. A.; Travia, N. E.; Medvedev, G. A.; Stanciu, C.; Switzer, J. M.; Thomson, K. T.; Delgass, W. N.; Abu-Omar, M. M.; Caruthers, J. M. *J. Am. Chem. Soc.* **2010**, *132*, 558-566.

(8) Liu, Z. X.; Somsook, E.; White, C. B.; Rosaaen, K. A.; Landis, C. R. *J. Am. Chem. Soc.* **2001,** *123*, 11193-11207.

(9) (a) Angermund, K.; Fink, G.; Jensen, V. R.; Kleinschmidt, R. *Chem. Rev.* **2000**, *100*, 1457–1470. (b) Bochmann, M. *J. Organomet. Chem.* **2004**, *689*, 3982–3998. (c) Mohring, P. C.; Coville, N. J. *Coord. Chem. Re*v. **2006**, *250*, 18–35. (d) Wang, B. *Coord. Chem. Re*v. **2006**, *250*, 242–258.

(10) Tshuva, E.Y.; Goldberg, I.; Kol, M.; Goldschmidt, Z. *Organometallics*, **2001**, *20*, 3017-3028.

(11) Tshuva, E.Y.; Groysman, S.; Goldberg, I.; Kol, M.; Goldschmidt, Z. *Organometallics*, **2002**, *21*, 662-670.

(12) Kerton, F.M.; Holloway, S.; Power, A.; Soper, R.G.; Sheridan, K.; Lynam, J.M.; Whitwood, A.C.; Willans, C. E. *Can. J. Chem.* **2008**, *86*, 435-443.

(13) Groysman, S.; Goldberg, I.; Kol, M.; Genizi, E.; Goldschmidt, Z. *Organometallics*, **2003**, *22*, 3013-3015.

(14) a) Gahleitner, M.; Severn, J. R., *Designing Polymer Properties.* In *Tailor-Made Polymers*; Wiley-VCH Verlag GmbH & Co., 2008. b) Resconi, L.; Cavallo, L.; Fait, A.; Piemontesi, F., *Chem. Rev.* **2000**, *100*, 1253-1346.

(15) Resconi, L.; Piemontesi, F.; Franciscono, G.; Abis, L.; Fiorani, T. *J. Am.Chem. Soc.* **1992**, *114*, 1025-1032.

(16) Mogstad, A-L.; Waymouth, R. M. *Macromolecules.* **1992**, *25*, 2282-2284.

(17) Coates, G. W.; Hustad, P. D.; Reinartz, S. *Angew. Chem. Int. Ed.* **2002**, *41*, 2236-2257.

(18) Mecking, S. *Angew. Chem. Int. Ed.* **2001**, *40*, 534-540, and references therein.

(19) Agapie, T.; Henling, L. M.; DiPasquale, A. G.; Rheingold, A. L.; Bercaw, J. E. *Organometallics*, **2008**, *27*, 6245-6256.

(20) Margl, P.; Deng, L. Q.; Ziegler, T. *J. Am. Chem. Soc.* **1999**, *121*, 154-162.

(21) Busico, V.; Cipullo, R.; Friederichs, N.; Ronca, S.; Talarico, G.; Togrou, M.; Wang, B. *Macromolecules* **2004**, *37*, 8201-8203.

(22) Camacho, D. H.; Guan, Z. B. *Macromolecules* **2005**, *38*, 2544-2546.

(23) (a) Meinhard, D.; Wegner, M.; Kipiani, G.; Hearley, A.; Reuter, P.; Fischer, S.; Marti, O.; Rieger, B.*J. Am. Chem. Soc.*, **2007**, *129*, 9182-9191. (b) Anselment, T. M. J.; Wichmann, C.; Anderson, C. E.; Herdtweck, E.; Rieger, B. *Organometallics*, **2011**, *30*, 6602-6611.

(24) Doi, Y.; Ueki, S.; Keii, T. *Macromolecules* **1979**, *12*, 814-819.

(25) Naga, N.; Mizunuma, K. *Polymer* **1998**, *39*, 5059-5067.

(26) Chen, M-C.; Roberts, J. A. S.; Marks, T. J. *J. Am. Chem. Soc.* **2004**, *126*, 4605-4625.

(27) Groysman, S.; Goldberg, I.; Kol, M.; Genizi, E.; Goldschmidt, Z. *Inorg. Chim. Acta* **2003**, *345*, 137-144.

(28) Tshuva, E. Y.; Gendeziuk, N.; Kol, M. *Tetrahedron Lett.* **2001,** *42*, 6405-6407.

(29) Switzer, J. M.; Travia, N. E.; Steelman, D. K.; Medvedev, G. A.; Thomson, K. T.; Delgass, W. N.; Abu-Omar, M. M.; Caruthers, J. M. *Macromolecules*, **2012**, *45*, 4978-4988.

(30) Liu, Z.; Somsook, E.; Landis, C. R. *J. Am. Chem. Soc.*, **2001**, *123*, 2915-2916.

(31) Christianson, M.D.; Tan, E. H. P.; Landis, C.R. *J. Am. Chem. Soc.* **2010**, *132*, 11461-11463.

CHAPTER 3. COMPARISON OF SELECTED ZIRCONIUM AND HAFNIUM AMINE BIS(PHENOLATE) CATALYSTS FOR 1-HEXENE POLYMERIZATION

In this paper, I performed GPC measurements of polymer samples and kinetics analysis on Hf-THF catalyst 1b system. Jeffrey M. Switzer performed GPC measurements and kinetics analysis on the other two catalyst systems: Hf-Pyridine catalyst 2b and Hf-NMe_2 catalyst 3b. D. Keith Steelman and Paul D. Pletcher did the experimental part including catalyst synthesis, 1-hexene polymerization, and NMR measurements, etc.

3.1 Introduction

Production of polyolefins is a major industrial process with a current capacity of ca. 110 billion kg per year globally.[1] Today polyolefins are produced primarily using heterogeneous Ziegler catalysts; however, in recent years, homogeneous single-site catalysts, specifically metallocene-type catalysts, have attracted attention because they offer potential control of the various kinetic steps, which in turn can be manipulated by "catalyst design."[2-4] While high-throughput screening has accelerated the discovery process with group 4 coordination complexes leading to Dow's catalysts for olefin block copolymer synthesis,[5] the promise of directly correlating kinetic constants to descriptors of

the catalyst has not yet been realized. A major obstacle in the way of rational catalyst design is the lack of proper quantitative kinetic analysis of all the relevant processes (i.e. kinetic steps) that are involved in catalytic olefin polymerization.[6,7] Nevertheless, the study of single-site catalysts for olefin polymerization is particularly attractive because of the potential to directly correlate the physical properties of the resulting polymer to structural features of the catalyst based on first principles.[8] These types of correlations enable one to draw conclusions on how a catalyst structure may be manipulated to yield specific polymeric architectures. One particular avenue of interest is to investigate the effect that changing the metal center will have on the polymerization process.

Of the group IV elements, the metal that has received the most attention as a homogeneous polymerization catalyst is zirconium. Another group IV element that is known to act as a homogenous polymerization catalyst is found by dropping down one row in the periodic chart to hafnium. Zirconium and hafnium in the +4 oxidation state are remarkably similar, having the same number of outer shell d-electrons and the same ionic radii due to the lanthanide contraction. Many of the analogous zirconium and hafnium complexes reported in the literature have virtually identical crystal structures.[9-11] Despite their similarities, these two metals behave drastically different as polymerization catalysts. When studying β-Me elimination chain transfer pathways in propylene oligomers, Fiorani et. al. observed that as a general rule zirconocene type catalysts have increased activity over their hafnocene type catalysts; however, for bis(Cp*)-metallocenes, hafnium has a significantly larger activity than its zirconium analog, making it one of the few examples where the general rule is broken.[10] Further studies by Collins and Ferrara showed the same

phenomena with an additional note that the hafnium analogs produce polymers with a significantly larger molecular weight, M_w.[9,11]

One specific family of non-metallocene catalysts, first pioneered by Kol and co-workers that has sparked interest utilizes an amine bis-phenolate (salan) ligand system (see Figure 1).[12,13] The reason for choosing this particular family of ligands as part of our detailed kinetic studies is the relative ease of synthesis and the ability to tune the catalyst's coordination environment.[14] Furthermore, these catalysts exhibit high activity, comparable to metallocene catalysts, with 1-hexene in conventional organic solvents such as toluene. This feature enables the investigation of kinetic data in the condensed phase thereby eliminating mass transfer limitations that are inherent in gas phase polymerization reactions. Following up on Kol's earlier qualitative observations that the nature of the pendant ligand (X) and its distance from the metal center (Zr-X) influence chain transfer,[15] we have shown a linear correlation between the logarithm of the chain transfer rate constants, $k_{vinylidene}$ and $k_{vinylene}$, and the Zr-X bond distance, which was probed by quantitative kinetic modeling of a diverse set of multi-response data.[16,17] In this study, we will continue the use of quantitative kinetic modeling of multi-response data for the salan-type catalysts to elucidate the effect of changing the metal center from Zr to Hf on the rate constants that comprise the olefin polymerization mechanism.

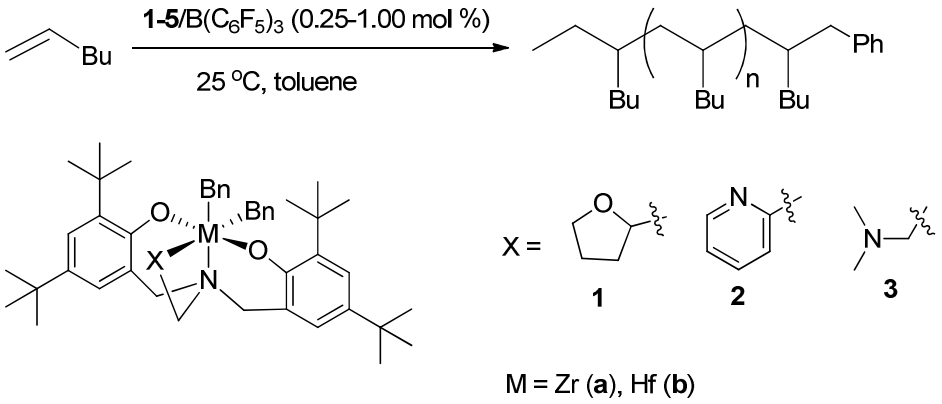

Figure 3-1. 1-hexene polymerization catalyzed by zirconium/hafnium salan-type catalysts **1a**-**3b** when combined with the activator $B(C_6F_5)_3$.

3.2 Experimental Procedure

General Procedure. All manipulations were performed under dry inert atmosphere in a glove box or at a vacuum manifold using air sensitive techniques under N_2 or Ar atmosphere. Toluene and pentane were distilled over activated alumina and a copper catalyst using a solvent purification system (Anhydrous Technologies) and degassed through freeze-pump-thaw cycles. Both solvents were stored over activated molecular sieves. Tetrabenzylzirconium was purchased from STREM and used as received. The monomer 1-hexene was purchased from Aldrich and purified by distillation over a small amount of dimethyl bis(cyclopentadienyl)zirconium and stored over molecular sieves. Tris(pentafluorophenyl)boron was purchased from STREM and purified by sublimation. Diphenylmethane was purchased from Aldrich and stored over molecular sieves. CH_3OD was purchased from Cambridge Isotopes and used as received. D_8-toluene was used as received and stored over molecular sieves. ^1H and ^2H NMR experiments were performed on a Varian INOVA600 MHz or Bruker DRX500 MHz spectrometer.

The ligands and precatalysts (**1a-3b**) were prepared following modified literature procedures.[12,13] We describe herein the details for one representative procedure and provide the others in the Supporting Information.

Synthesis of 6,6'-((((tetrahydrofuran-2-yl)methyl)-azanediyl)bis(methylene))bis(2,4-di-tert-butyl-phenol), tBu-ON^{THF}O ligand (1). In a typical synthesis, an 80 mL reaction vessel was charged with 2,4-di-tert-butylphenol (6.19 g, 30.0 mmol), 2-(aminomethyl) tetrahydrofuran (1.55 mL, 15 mmol) and 37% histological grade formaldehyde (6.00 mL, 80 mmol), distilled water, and a stir bar while maintaining a maximum volume of 80 mL. The biphasic reaction mixture was placed in a CEM microwave reactor and allowed to warm to 100 ºC over 5 min while stirring. The reaction was allowed to stand at 100 ºC for 30 min, and then cooled to room temperature. The aqueous layer was removed, and cold, dry methanol was added to the organic phase. This mixture was shaken for 30 min, and the resulting solid isolated by vacuum filtration. The crude ligand product was purified by crystallization from ethanol (28% yield).

Synthesis of Zr[tBu-ON^{THF}O]Bn$_2$ (1a). In a typical synthesis, a 100 mL flask was charged with tetrabenzylzirconium (0.557 g, 1.22 mmol), 20 mL toluene, and a stir bar and fitted with a rubber septum. A second 100 mL flask was charged with the ^{t}Bu-ON^{THF}O ligand (0.609 g, 1.13 mmol) and 20 mL of toluene. The two flasks were placed under an inert atmosphere, and the ligand solution was added to the tetrabenzylzirconium solution via a cannula. The reaction was allowed to warm to 60 ºC and stir for 2 h resulting in a bright yellow solution. The solution was concentrated to about 10 mL and placed into a -10 ºC freezer. Yellow crystals formed within 2 days and the mother liquor was removed via a

cannula. The crystals were dried under vacuum (84% yield). The precatalyst was recrystallized by vapor diffusion of pentane into a precatalyst/toluene solution to afford an analytically pure complex.

NMR scale polymerization of 1-hexene. The procedure for NMR scale polymerization is based on literature.[17] For a typical polymerization, Zr[tBu-ON^{THF}O]Bn$_2$ (**1**) (6.1 mg, 0.0075 mmol) was dissolved in 0.5 mL toluene in a small vial and sealed with a screw-cap septum. The vial containing the precatalyst solution was pierced with a 1 mL syringe. The vial and syringe were placed in an N_2 bag and allowed to equilibrate to 25 ºC. Tris(pentafluorophenyl)boron (4.3 mg, 0.0084 mmol), 1-hexene (0.1265 grams, 1.50 mmol), and diphenylmethane (9.5 mg 0.056 mmol) were added to a 2 mL volumetric flask and diluted to the mark with d^8-toluene. This solution was placed in an NMR tube and sealed with a septum. The monomer/activator solution was placed in the spectrometer and allowed to equilibrate to 25 ºC using a VT controller. A measurement was taken to determine the initial concentration of monomer relative to the internal standard. The NMR tube was removed from the spectrometer, and the catalyst precursor solution was added to the activator/monomer solution by piercing the septum while the syringe remained in the N_2 bag. The reaction mixture was shaken for ca. 30 seconds and placed back into the spectrometer. Spectra were acquired at predetermined time intervals until the reaction reached completion. Each sample was prepared for GPC analysis by evaporation over mild heat before dissolution in hexanes and filtration through an alumina plug to remove the quenched catalyst. Evaporation of solvent yielded clear, colorless poly(1-hexene). The

array of ^{1}H spectra was collected on an INOVA 600 MHz spectrometer and analyzed using MestReNova.

Batch polymerization of 1-hexene. The procedure for Manual Quench is based on literature.[18] For a typical polymerization, Zr[tBu-ON^{THF}O]Bn_2 (0.073 g, 0.090 mmol) was dissolved in 5.0 mL toluene in a small vial that was sealed with a screw-cap septum. The vial containing the precatalyst solution was pierced with a 10 mL syringe. The vial and syringe were placed in an N_2 bag and allowed to equilibrate to 25 ºC. Tris(pentafluorophenyl)boron (0.053 grams, 0.099 mmol), and 1-hexene (1.575 g, 18.71 mmol) were added to a 25 mL flask and diluted to the mark with toluene. This solution was diluted to 26 mL with 1 mL of toluene, and 1 mL of the resulting solution was removed for quantification of the initial monomer concentration through NMR analysis. The flask was sealed with a septum and moved from an N_2 filled glovebox to a vacuum manifold and placed under argon. The monomer/activator solution was allowed to equilibrate to 25 ºC using a temperature-controlled silicone oil bath. The catalyst precursor solution was added to the activator/monomer solution by piercing the septum while the syringe remained in the N_2 bag. The resulting yellow solution was allowed to stir while aliquots were removed at selected times and each was injected into a 10 mL volumetric flask containing 1 mL of deutero-methanol. A 1 mL aliquot from the quenched solutions was removed and a 0.5 mL solution of d-toluene spiked with diphenylmethane as an internal standard for quantification of 1-hexene consumption (via ^{1}H NMR on Varian Inova600). Each sample was prepared for GPC analysis by evaporation over mild heat before dissolution in hexanes

and filtration through an alumina plug to remove the quenched catalyst. Evaporation of solvent yielded clear, colorless poly(1-hexene).

In the case of vinyl end group analysis, a 1 mL aliquot was worked up as described above. The resulting polymer was dissolved in $CDCl_3$, and diluted to the mark in a 2 mL volumetric flask. Diphenylmethane was used as an internal standard and the method of standard additions was used in quantification of the end groups by 1H NMR. All end-group analysis measurements were taken on a Bruker DRX500 spectrometer at 25 ºC.

In the case of ^2H analysis for active-site counting, the remaining quenched reaction solution (8 mL) was worked up as described above. The resulting polymer was dissolved in CH_2Cl_2, and diluted to the mark in a 2 mL volumetric flask. d_6-benzene was used as an internal standard and the method of standard additions was used in quantification of active sites by ^2H NMR. All active site measurements were taken on a Bruker DRX500 spectrometer at 25 ºC.

Gel Permeation Chromatography (GPC) Analysis. The procedure used to analyze polymer samples using GPC methods was taken from Novstrup et al.,[6] and it is summarized below. Poly(1-hexene) samples were added to THF at room temperature and allowed to dissolve for 4 h. Solutions were then passed through a 0.2 μm filter to remove any particulate matter. The GPC analysis was performed on a Waters GPCV 2000 for system **1a** and **3a**, and on a Viscotek GPCmax VE 2001 for system **1b**, **2a**, **2b**, and **3b**. On the Waters GPCV 2000, samples were injected through a 101.3 μL injection loop and passed through two Polymer Laboratories PLGel 5 μm Mixed-C columns in series in a 45 °C oven at a flow rate of 1.0 mL min-1. On the Viscotek GPCmax VE 2001, samples were injected

through a 200 μL injection loop and passed through three Viscotek T6000M 10 μm General Mixed Org columns in series in a 35 °C oven at a flow rate of 1.0 mL min^{-1}. The analysis made use of the differential RI detector and a viscometer. Molecular weights were assigned by way of a universal calibration curve created with polystyrene standards ranging from 580 g mol-1 to 3,114,000 g mol-1. The calibration was verified through the analysis of a broad standard, SRM 706a, provided by the National Institute of Standards and Technology.

3.3 Results

The complete kinetic analysis for the zirconium based systems **1a**, **2a**, and **3a** has been reported in previous publications.[16, 17] Here we present the experimental data and a complete kinetic analysis for 1-hexene polymerization by hafnium based analogs **1b, 2b,** and **3b**. For each system, we followed our previously developed kinetic modeling method[6,16,17] based on the analysis of multi-response data that includes (1) monomer consumption, (2) MWD, (3) active site counts, and (4) vinyl end group counts. We determine the active site count at any point in the course of the reaction as the number measured by quenching with d_4-methanol and performing ^2H NMR measurement of the concentration of chains with deuterated end groups. The sites that have undergone 1,2-insertion are defined as primary sites, and the sites that have undergone 2,1-misinsertion are defined as secondary sites. Within this analysis, each system is studied independently and no *a priori* assumptions are made with respect to the elementary steps. As explained in detail in the supporting information, the analysis procedure begins with the most basic mechanism, e.g., initiation and propagation, and fitting is attempted to the entire data set;

only after a simple mechanism is shown to fail, new elementary step, e.g. chain transfer, is added and the fitting is attempted again.

Activation

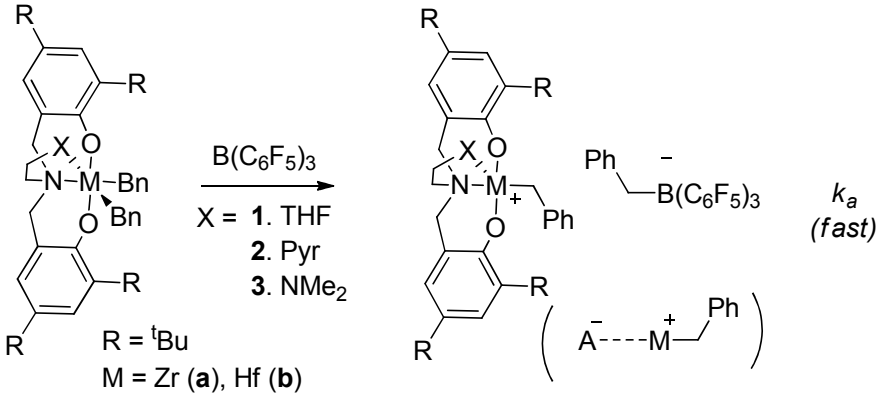

Initiation

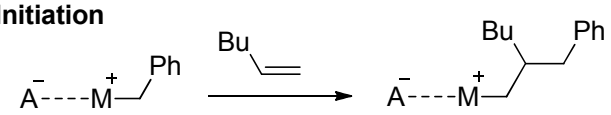

Propagation

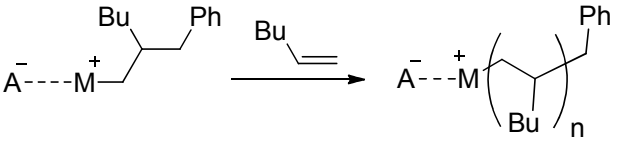

Misinsertion

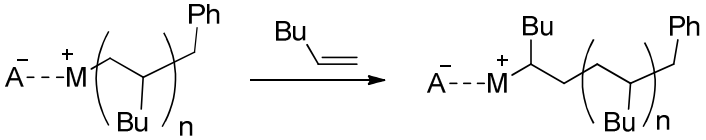

Recovery

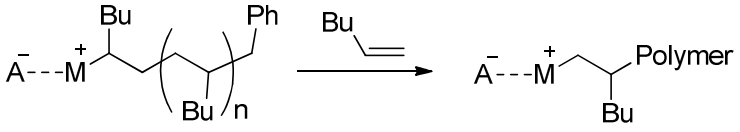

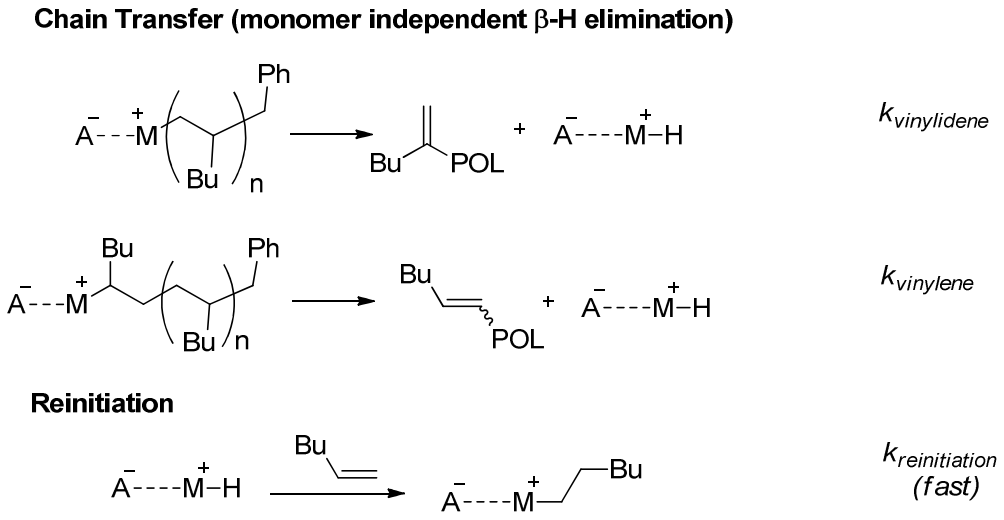

Scheme 3-1. The elementary kinetic steps used in fitting the data for catalysts 1-5. The ordinary differential equations (ODEs) that describe the mass-action kinetics associated with this mechanism are provided in the Supporting Information.

As a result, a minimal set of elementary steps is determined that can fit the multi-response data. For the zirconium based systems **1a**, **2a**, and **3a**, such a minimal set turned out to include initiation, propagation via normal insertion, 2,1-misinsertion, recovery from misinsertion, and chain transfer[16] resulting in the formation of vinylidene and vinylene species (See Scheme 1). Also it is noted that the catalyst participation may not be 100% of the nominal precatalyst amount and it may vary from system to system. By catalyst participation, here we mean the fraction of precatalyst that can be activated and initiated once the reactant species are combined. This is separate from time-dependent deactivation. For the hafnium based systems **1b, 2b,** and **3b**, the results of the kinetic analysis are here presented, where we chose the system **2b** to illustrate the quality of kinetic fitting, where the similar figures for systems **1b** and **3b** are in the Supporting Information. The main

conclusion is that the kinetic mechanism for hafnium based systems is essentially the same as for zirconium analogs.

Hf-Pyridine catalyst 2b. The experimental data along with the kinetic modeling fits are presented in Figure 2.

The specific features of this system are:

(1) Catalyst participation is nearly 100%;

(2) In case of the batch scale experiments, significant catalyst deactivation is observed as evidenced by bending of the monomer consumption curve in Figure 2C and the steep decline in primary active site counts over the course of the reaction in Figure 2E. In case of the NMR scale experiments, the deactivation either does not occur or is much less significant. For that reason, deactivation is not considered as part of the catalytic reactions;

(3) The amount of chain transfer is relatively high as evidenced by the significant vinylidene concentration in Figure 2F and the fact that MWD does not change much after 30% conversion of the monomer. The vinylidene formation is via a monomer independent reaction as evidenced by the upward curvature in the vinylidene concentration versus monomer conversion plot (Figure 2F);

(4) The vinylene end group concentration is much lower than that of vinylidene (Figure 2F), where the vinylene formation is via monomer dependent reaction as evidenced by the linear accumulation in Figure 2F.

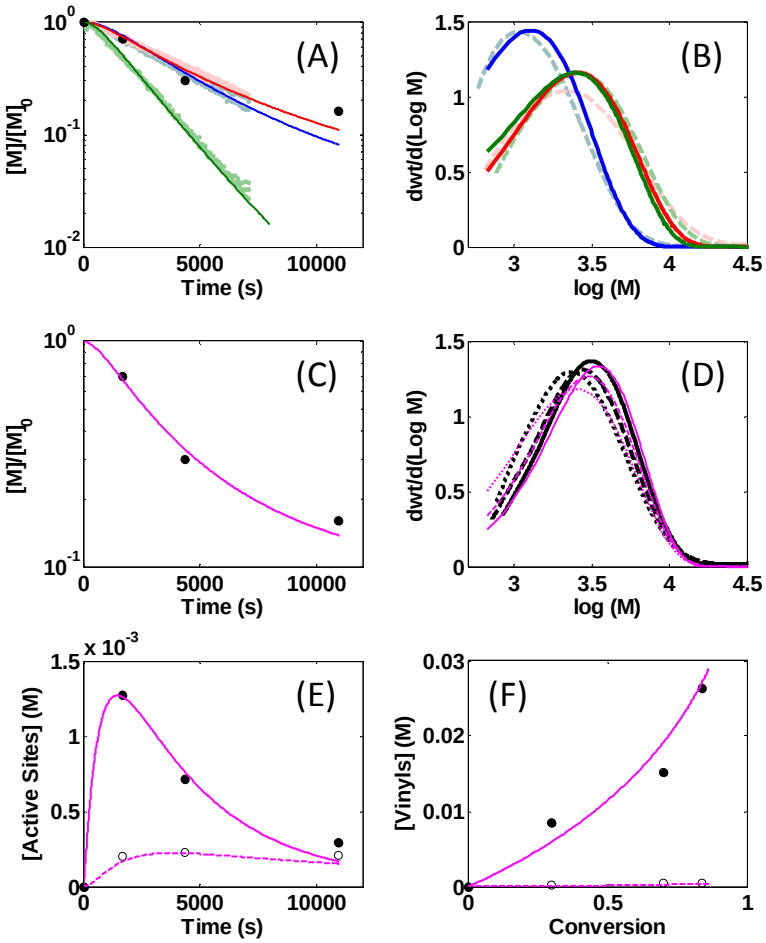

Figure 3-2. Multi-response data set with fits for catalyst 2b. NMR-scale experiments: (A - B); (A) Monomer consumption. Data: symbols, fits: lines. (B) MWDs at the end. {Blue, Red, Green}: $[C]_0$ = {3.0, 3.0, 6.0} mM and $[M]_0$ = {0.30, 0.60, 0.60} M. Data: solid, fits: dashed. Batch scale experiments ($[C]_0$ = 3.0 mM, $[C]_0$ = 0.60 M): (C - F). (C) Monomer consumption. Data: symbols, fit: line. (D) MWDs at: — 1694 s, – – 4352 s, ··· 10963 s. Data: black, fits: magenta. (E) Active site counts. Primary - filled circles (data)/solid line (fit); secondary - open circles (data)/dashed line (fit). (F) End group analysis. Filled circles (data)/solid line (fit): vinylidene; open circles (data)/dashed line (fit): vinylene. In (A), black circles same as in (C) for comparison.

Hf-THF catalyst 1b. The experimental data along with the kinetic modeling fits are presented in the Supporting Information.The specific features of this system are:

(1) Catalyst participation is approximately 50%;

(2) Faster chain transfer rate and slower propagation rate compared to its zirconium analog, which results in a much higher chain transfer frequency (i.e. the measured vinyl terminated groups are 100 times higher at the end of the reaction). However, the chain transfer rate of this catalyst remains the lowest compared to catalyst 2b and 3b.

(3) Fewer secondary sites are formed, meaning there is less dormancy as compared to the zirconium analog. The vinylene count is quite small, indicating that the actual chain transfer rate from secondary site is negligible.

Hf-NMe_2 catalyst 3b. The experimental data along with the kinetic modeling fits are presented in the Supporting Information. The specific features of this system are:

(1) Catalyst participation is approximately 40%;

(2) There is a decline in active catalyst sites over the course of the reaction, although it is not as steep as in Systems 1b and 2b;

(3) No secondary catalyst sites were measured, although a small amount of vinylene end groups were detected. This peculiar behavior was also observed for the EBIZrMe_2/B(C_6F_5)$_3$ catalyst.[6,7] Vinylene is typically expected to form following chain transfer of secondary sites. It is likely in this system that secondary sites do form, but they rapidly undergo either chain transfer or monomer-dependent recovery. Since no secondary sites are observed even late in the reaction when monomer concentration is low, a fast monomer independent chain transfer event is more probable.

3.4 Discussion

In this study, the complete set of kinetic rate constants for three zirconium amine bis-phenolate catalyst systems and three hafnium analogs have been presented. For each system, a rich data set including MWD has been collected and successfully fitted by comprehensive kinetic modeling. With one possible exception, the mechanism of 1-hexene polymerization for these catalysts (**1a**-**3b**) consists of the following elementary reaction steps: initiation, normal propagation, misinsertion, recovery, and chain transfer. For System **3b**, there is not enough information to include or exclude a recovery reaction.

The values of the rate constants are shown in Table 1 including error bounds, which were determined using the methodology for determining error bounds discussed in the previous paper.[16] Examining the summarized kinetic data in Table 1, the following conclusions emerge:

(1) The monomer-dependent rate constants: k_i, k_p, k_{mis}, and k_{rec} are slower for the Hf systems than for the Zr systems. In particular, the propagation rate is one order of magnitude slower in all the hafnium based systems.

(2) $k_{vinylidene}$, which is *not* monomer dependent, is not uniformly slower for Hf. In fact, it is faster for THF, about the same for Py, and slower for NMe_2 ligated metal.

(3) Vinylene formation does not behave consistently across all pendants with Hf as it does for Zr. For Hf-Py it appears 2nd order; for Hf-NMe_2 it is apparently fast (consistent with fast $k_{vinylidene}$). We do not currently have an explanation for this behaviour.

(4) Each hafnium complex exhibits less secondary site formation than its zirconium analogue.

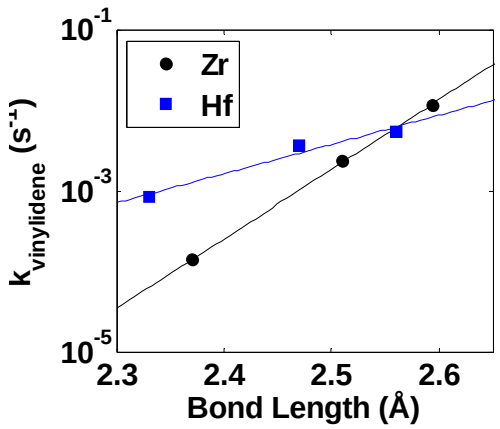

Figure 3-3. Log($k_{vinylidene}$) vs M-X bond length.

A possible reason for the reduction in the rate of all elementary steps that require the insertion of a monomer is due to the larger metal-carbon bond enthalpy of the hafnium systems as compared with the analogous zirconium systems.[19] In our previous paper we pointed out a linear correlation between the logarithm of the rate of monomer independent chain transfer and the bond distance between the zirconium and the pendant group.[16] A similar linear relationship appears to be holding for the monomer independent chain transfer rate for the hafnium based systems as shown in Figure 3. However, the hafnium based system exhibit a much weaker dependence on the bond length as the slope of this correlation is 2.7 times smaller. In our previous study,[16] we speculated that this increase in bond distance allows for more steric freedom to accommodate the β-hydride agostic interaction necessary for chain transfer to occur. Since the effective size of the hafnium metal center is generally believed to be similar to that of zirconium, it is unclear why this correlation is weaker in hafnium based systems. However, it is likely that the exact reason lies with the intrinsic properties of the metal center and how these properties control the β-hydrogen transfer reactions.

3.5 Conclusions

A comprehensive kinetic study of three catalytic systems based on hafnium amine bis-phenolate complexes has been completed, and the relevant rate constants and elementary reaction steps were robustly determined for each system. The mechanism includes initiation, normal propagation, misinsertion, recovery, and chain transfer. In conjunction with the previous study of zirconium analogs, this report allows for the first quantitative comparison between similarly ligated hafnium and zirconium based olefin polymerization catalysts. The most important findings are: the one order of magnitude decrease in k_p for the hafnium catalysts; an overall decrease in all monomer dependent reaction steps; and the correlation between the logarithm of monomer independent chain transfer and the hafnium pendant ligand (Hf-X) bond distance. The last observation is similar to the one previously reported for zirconium systems, but in case of the hafnium catalysts the dependence is 2.7 times weaker.

REFERENCES

(1) Chemical Market Associates, Inc. (CMAI), **2005** *World Polyolefins Analysis*, www.cmaiglobal.com.

(2) (a) Chen, E. Y-X.; Marks, T. *J. Chem. Rev.* **2000**, *100*, 1391-1434. (b) Li, H.; Marks, T. J. *Proc. Natl. Acad. Sci. USA* **2006**, *103*, 15295-15302.

(3) Manz, T. A.; Phomphrai, K.; Medvedev, G. A.; Krishnamurthy, B. B.; Sharma, S.; Haq, J.; Novstrup, K. A.; Thomson, K. T.; Delgass, W. N.; Caruthers, J. M.; Abu-Omar, M. M. *J. Am. Chem. Soc.* **2007**, *129*, 3776-3777.

(4) (a) Krauledat, H.; Brintzinger, H. H. *Angew. Chem. Int. Ed.* **1990**, *29*, 1412-1413. (b) Piers, W. E.; Bercaw, J. E. *J. Am. Chem. Soc.* **1990**, *112*, 9406-9707. (c) Coates, G. W.; Waymouth, R. M. *J. Am. Chem. Soc.* **1991**, *113*, 6270-6271.

(5) Arriola, D. J.; Carnahan, E. M.; Hustad, P. D.; Kuhlman, R. L.; Wenzel, T. T. *Science* **2006**, *312*, 714-719.

(6) Novstrup, K. A.; Travia, N. E.; Medvedev, G. A.; Stanciu, C.; Switzer, J. M.; Thomson, K. T.; Delgass, W. N.; Abu-Omar, M. M.; Caruthers, J. M. *J. Am. Chem. Soc.* **2010**, *132*, 558-566.N.; Caruthers, J. M.; Abu-Omar, M. M. *J. Am. Chem. Soc.* **2007**, *129*, 3776-3777.

(7) Landis, C.R.; Rosaaen, K.A.; Sillars, D.R. *J. Am. Chem. Soc.* **2003**, *125*, 1710-1711.

(8) (a) Angermund, K.; Fink, G.; Jensen, V. R.; Kleinschmidt, R. *Chem. Rev.* **2000**, *100*, 1457–1470. (b) Bochmann, M. *J. Organomet. Chem.* **2004**, *689*, 3982–3998. (c) Mohring, P. C.; Coville, N. J. *Coord. Chem. Re*v. **2006**, *250*, 18–35. (d) Wang, B. *Coord. Chem. Re*v. **2006**, *250*, 242–258.

(9) Hunter, W.E.; Hrncir, D.E.; Bynum, R.V.; Penttila, R.A.; Atwood, J.L *Organometallics*. **1983**, *2*, 750-755.

(10) Resconi, L.; Piemontesi, F.; Franciscono, G.; Abist, L.; Fioranit, T., *J. Am. Chem. Soc*. **1992**, *114*, 1025-1032.

(11) Abbas, R.; Ferrara, J. *Journal of Organometallic Chemistry*. **1992**, *435*, 299-310.

(12) Tshuva, E.Y.; Goldberg, I.; Kol, M.; Goldschmidt, Z. *Organometallics*, **2001**, *20*, 3017-3028.

(13) Tshuva, E.Y.; Groysman, S.; Goldberg, I.; Kol, M.; Goldschmidt, Z. *Organometallics*, **2002**, *21*, 662-670.

(14) Kerton, F.M.; Holloway, S.; Power, A.; Soper, R.G.; Sheridan, K.; Lynam, J.M.; Whitwood, A.C.; Willans, C. E. *Can. J. Chem.* **2008**, *86*, 435-443.

(15) Groysman, S.; Goldberg, I.; Kol, M.; Genizi, E.; Goldschmidt, Z. *Organometallics*, **2003**, *22*, 3013-3015.

(16) Steelman, D.K.; Xiong, S.; Pletcher, P.D.; Smith, E.; Switzer, J.M.; Medvedev, G.A.; Delgass, W.N.; Caruthers, J.M.; Abu-Omar, M.M. *J. Am. Chem. Soc.*, **2013**, *135*, 6280-6288

(17) Switzer, J.M.; Travia, N.E.; Steelman, D.K.; Medvedev, G.A.; Thomson, K.T.; Delgass, W.N.; Abu-Omar, M.M.; Caruthers, J.M. *Macromolecules*, **2012**, *45*, 4978-4988.

(18) Liu, Z.; Somsook, E.; Landis, C. R. *J. Am. Chem. Soc.*, **2001**, *123*, 2915-2916.

(19) Kissounko, D.A.; Zhang, Y.; Harney, M.B.; Sita, L.R. *Adv. Synth. Catal.*, **2005**, *347*, 426-432.

CHAPTER 4. EFFECTS OF ELECTRONIC PERTURBATIONS ON 1-HEXENE POLYMERIZATION CATALYZED BY ZIRCONIUM AMINE BIS-PHENOLATE COMPLEXES

In this paper, I performed GPC measurements of polymer samples and kinetics analysis on all the catalyst systems. D. Keith Steelman did the experimental part including catalyst synthesis, 1-hexene polymerization, and NMR measurements, etc.

4.1 Introduction

A recent review of catalytic C-H functionalization highlights the importance of connecting the rational design of ligands with catalyst architecture to maximize activity and selectivity.[1] This concept is especially relevant to olefin polymerization because homogeneous single-site catalysts are amenable to exquisite control of the various kinetic steps through "catalyst design."[2-7] The demand for polyolefin materials continues to increase as the world's population grows[8,9], where improved structure-activity relationships for single-site polymerization catalysts would have a direct impact on making desired polymer architectures.[10-13] A common view among chemists is that polymerization catalysts are beyond the reach of rational design.[14] This belief is built on the misconception that the promise of directly correlating kinetic constants to descriptors of the catalyst has

not yet been realized, due primarily to the lack of proper quantitative kinetic analysis of all the relevant processes (i.e. kinetic steps) that comprise the olefin polymerization mechanism.[15,16]

A primary example is the obscure role of metal electrophilicity. On one hand, a highly electron deficient complex has been proposed to interact more strongly with an incoming olefin.[17-19] Group IV complexes have shown enhanced activity with increasing electron deficient metal center.[17] Another example is a series of Ni-based complexes bearing α-iminocarboxamide ligands.[20] For this family of catalysts, it was observed that systematically decreasing the electron density of the metal center resulted in increased activity towards ethylene polymerization.

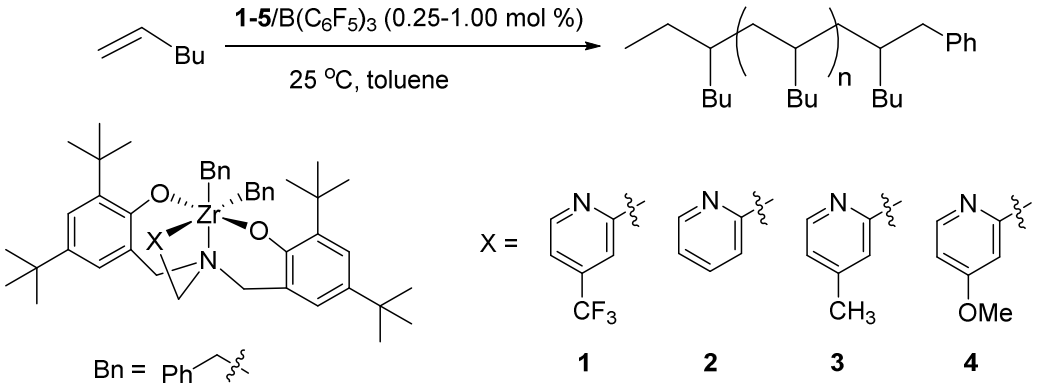

Figure 4-1. 1-hexene polymerization catalyzed by zirconium amine bis-phenolate complexes 1-4 when combined with the activator $B(C_6F_5)_3$.

On the other hand, it has been observed both experimentally[21,22] and theoretically[23,24] that electron donating groups increase catalyst activity. Theoretical studies on a series of zirconium and titanium complexes with chelating alkoxide ligands showed that additional electron density on the metal center lowers the insertion barrier

energy for an incoming olefin.[23,24] Also, for a set of titanium bis(phenolate) catalysts, it was observed that electron donating groups in the ligand increase activity.[21,22]

One specific family of non-metallocene catalysts, pioneered by Kol and co-workers, utilizes an amine bis-phenolate ligand system (see Figure 1).[25,26] The reason for choosing this particular family of ligands as part of our kinetic studies is the relative ease of synthesis and the ability to tune the catalyst's coordination environment.[27] Furthermore, these catalysts exhibit high activity, comparable to metallocene catalysts, for polymerization of 1-hexene in conventional organic solvents such as toluene. This feature enables the collection of kinetic data in the condensed phase and eliminates potential mass transfer limitations that are inherent with gas phase monomers. Following up on Kol's earlier qualitative observations that the nature of the pendant ligand (X) and its distance from the metal center (Zr-X) influence chain transfer,[28] we have shown a correlation between the logarithm of the chain transfer rate constants, $k_{vinylidene}$ and $k_{vinylene}$, and the Zr-X bond distance, which was established via quantitative kinetic modelling.[29] Furthermore, catalytic systems bearing a more electron rich pendant exhibit a k_p several times lower than that for a less electron rich catalyst. In this study, we will use quantitative kinetic modeling for a series of four Zr-based amine bis-phenolate complexes bearing an electronically modified pyridine to elucidate the effect of electronic perturbations on the rate constants that comprise the olefin polymerization mechanism. In addition, we will examine the correlation of the determined rate constants with Hammett Parameters and computational results.

The complete kinetic analysis for system **2** has been reported previously.[29] Here we present a **slightly modified** (as described below) kinetic analysis for system **2** and the

experimental data and complete kinetic analysis for 1-hexene polymerization of the structural analogs **1**, **3**, and **4**. For each system, we followed our previously developed kinetic modeling method[15,29,30] based on the analysis of multi-response data. Within this analysis, each system is studied independently and no a priori assumptions are made with respect to the elementary steps, as explained in detail in the supporting information. Using this procedure, a minimal set of elementary steps emerges providing a fit to the data.

4.2 Experimental Procedure

General Procedure. All manipulations were performed under dry inert atmosphere in a glove box or at a vacuum manifold using air sensitive techniques under N_2 or Ar atmosphere. Toluene and pentane were dried and degassed using a Solvent Drying System (Pure Process Technologies, LLC.) Both solvents were stored over activated molecular sieves. Tetrabenzylzirconium was purchased from STREM and used as received. The monomer 1-hexene was purchased from Aldrich and purified by distillation over a small amount of dimethyl bis(cyclopentadienyl) zirconium and stored over molecular sieves. Tris(pentafluorophenyl) boron was purchased from STREM and purified by sublimation. Diphenylmethane was purchased from Aldrich and stored over molecular sieves. CH_3OD was purchased from Cambridge Isotopes and used as received. D_8-toluene was used as received and stored over molecular sieves. (4-methylpyridin-2-yl)methanamine,(4-(trifluoromethyl) pyridin-2-yl)methanamine, and (4-methoxypyridin-2-yl) methanamine were purchased from Anichem, LLC, and used as received. ^1H and ^2H NMR experiments were performed on a Varian INOVA600 MHz or Bruker DRX500 MHz spectrometer.

The ligands and pre-catalysts (**1**-**4**) were prepared following modified literature procedures.[25,26,29,30] We describe herein the details for one representative procedure and provide the others in the Supporting Information.

NMR scale polymerization of 1-hexene with Zr[tBu-ON^{Pyr}O]Bn$_2$ at 25 ºC. The procedure for NMR scale polymerization is based on literature.[29,30] For a typical polymerization, Zr[tBu-ON^{Pyr}O]Bn$_2$ (6.1 mg, 0.0075 mmol) was dissolved in 0.5 mL toluene in a small vial and sealed with a screw-cap septum. The vial containing the precatalyst solution was pierced with a 1 mL syringe. The vial and syringe were placed in an N_2 bag and allowed to equilibrate to 25 ºC. Tris(pentafluorophenyl)boron (4.2 mg, 0.0083 mmol), 1-hexene (0.126 grams, 1.50 mmol), and diphenylmethane (9.7 mg 0.058 mmol) were added to a 2 mL volumetric flask and diluted to the mark with d^8-toluene. This solution was placed in an NMR tube and sealed with a septum. The monomer/activator solution was placed in the spectrometer and allowed to equilibrate to 25 ºC using a VT controller. A measurement was taken to determine the initial concentration of monomer relative to the internal standard. The NMR tube was removed from the spectrometer, and the catalyst precursor solution was added to the activator/monomer solution by piercing the septum while the syringe remained in the N_2 bag. The reaction mixture was allowed to shaken for 30 seconds and inserted back into the spectrometer. Measurements were taken at predetermined time intervals until the reaction reached completion. This same sample was collected in a vial, cleaned up, and analyzed in accordance with literature procedure.[16,29,30] NMR analysis shows that the resulting polymer produced with this catalyst is atactic.

Quenched NMR scale polymerization of 1-hexene. The catalyst/activator and monomer/internal standard solutions were prepared in the same fashion as the previously described experiments using instead a temperature controlled oil bath at 25 ºC. These reactions were quenched at the the time corresponding to the desired conversion of monomer using 0.75 mL of d_4-methanol. The quench reaction was analyzed by ^{1}H NMR to verify the conversion of monomer. This same sample was collected in a vial, cleaned up, and analyzed in accordance with literature procedure.[16,29,30] The monomer conversion and the MWD of product of each quench reaction are given in Table 1.

Table 4-1. Kinetics Runs for 1-hexene polymerization with the with the Zr[tBu-ON^{X}O]Bn$_2$/B(C_6F_5)$_3$ catalysts 1-4.[a]

X	Conversion (time/s), M_w, M_w/M_n		
	Run 1	Run 2	Run 3
pyr-CF3 (**1**)	25% (80), 10k, 1.17	59% (205), 21k, 1.27	93% (515), 24k, 1.35
pyr (**2**)	47% (490), 16k, 1.34	71% (1259), 22k, 1.53	96% (3225), 20k, 1.87
pyr-Me (**3**)	26% (798), 8.6k, 1.26	55% (2051), 11k, 1.47	87% (5180), 12k, 1.62
pyr-OMe (**4**)	35% (1291), 7.9k, 1.58	44% (2355), 8.4k, 1.63	77% (6039), 8.7k, 1.72

[a] Catalyst = 3.0 mM, activator = 3.3 mM, and 1-hexene = 0.60 M.

4.3 Results

Although the complete kinetic analysis for catalyst **2** has been reported in a previous publication,[29] as explained below, this analysis has been modified slightly in the present paper. Here we present the experimental data and a complete kinetic analysis for 1-hexene polymerization by catalysts **1-4**. For each system, we followed our previously developed kinetic modeling method[6,16,17] based on the analysis of multi-response data that includes (1) monomer consumption, (2) MWDs at different conversions, (3) active site counts, and (4)

vinyl end group counts. We determine the active site count as the number measured by quenching with d_4-methanol and performing ^2H NMR measurement of the concentration of chains with deuterated end groups. The sites that have undergone 1,2-insertion are defined as primary sites, and the sites that have undergone 2,1-misinsertion are defined as secondary sites. Each system is studied independently and no *a priori* assumptions are made with respect to the elementary steps. The analysis procedure begins with the most basic mechanism, e.g., initiation and propagation, and fitting is attempted to the entire data set; only after a simple mechanism is shown to fail is a new elementary step, e.g. chain transfer, added and the fitting is attempted again, etc.

This results in determination of a minimal set of elementary steps to fit the multi-response data. For catalysts **1** - **4**, the minimal set includes:

(1) Initiation, which is generally fast since there is no induction period in the monomer consumption profiles for the monomer-to-catalyst ratios used;

(2) propagation via normal 1,2-insertion;

(3) 2,1-misinsertion and recovery from misinsertion, as supported by the measurement of secondary active site;

(4) chain transfer via β-hydrogen elimination that results in the formation of vinylidene and vinylene end groups.

Also it is noted that the catalyst participation is usually not 100% of the nominal precatalyst amount and may vary from system to system and from experiment to experiment for a given system. By catalyst participation, here we mean the fraction of precatalyst that is activated and initiated once the reactant species are combined. This is

distinct from time-dependent deactivation. Catalyst participation for each system is determined via simultaneous fitting of the complete data set and is determined primarily by the active site counts and the location of the MWD peak. The value of catalyst participation is typically around 50% for the systems considered here. Although the degree of catalyst participation is not part of the catalytic mechanism, it can have an effect on the values of the rate constants obtained as a result of the kinetic modeling.

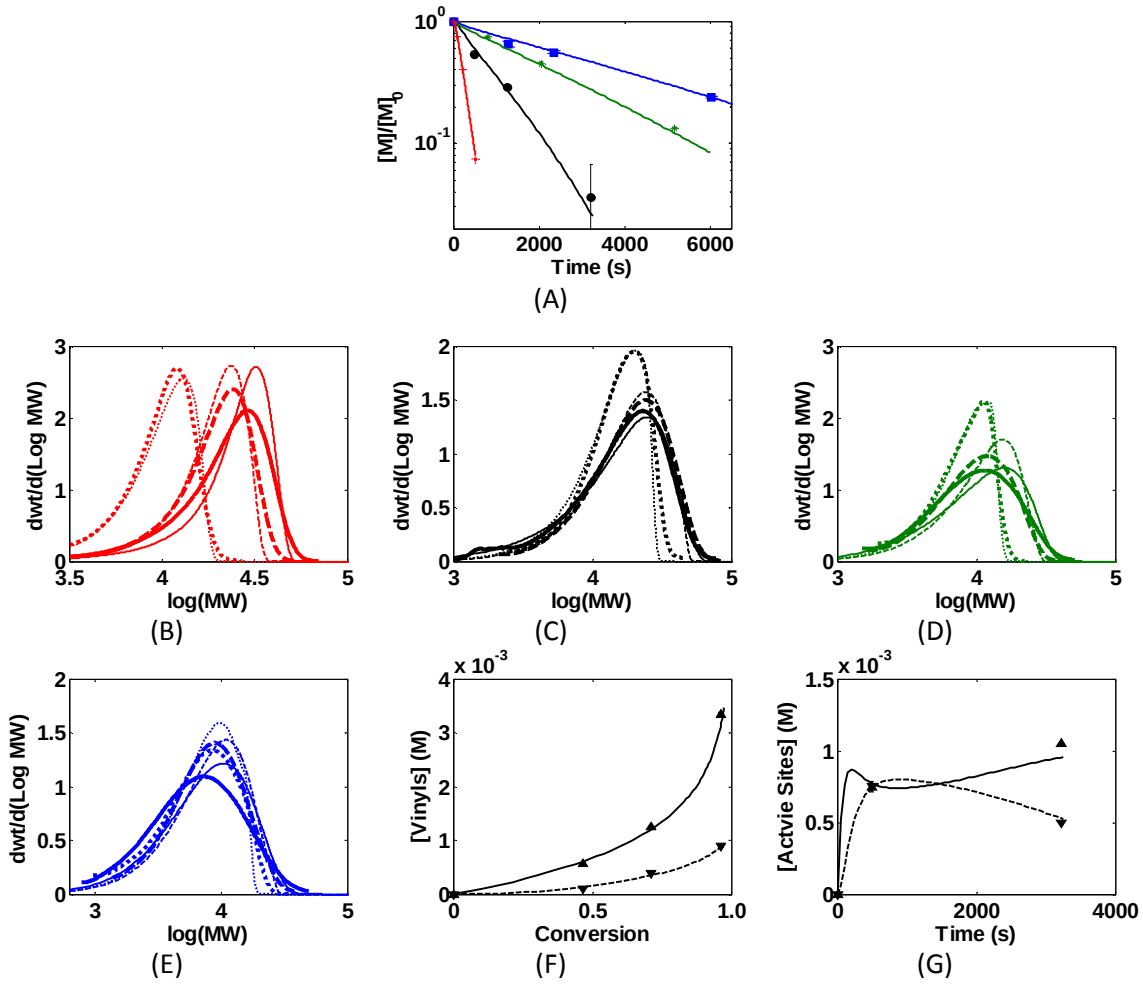

Figure 4-2. Multi-response data set with fits for systems **1** (red), **2** (black), **3** (green), and **4** (blue) in the order of curves with decreasing slope in panel (A). (A) Monomer consumption. Data: symbols, fits: lines. (B) MWDs at 25%, 59%, and 93% conversion for system **1.** (C) MWDs at 47%, 71%, and 96% conversion for system **2.** (D) MWDs at 26%, 55%, and 87% conversion for system **3.** (E) MWDs at 35%, 44%, and 77% conversion for system **4.** From (B) to (E), Data: thicker lines, fits: thinner lines. (F) Active site counts of system **2**. Primary – up triangles (data)/solid line (fit); secondary – lower triangles (data)/dashed line (fit). (G) End group analysis for system **2**. Vinylidene - up triangles (data)/solid line (fit); vinylene - down triangles (data)/dashed line (fit). Initial conditions: $[C]_0$ = 3.0 mM, $[M]_0$ = 0.60 M.

A case in point is catalyst **2** for which we report rate constants that are somewhat different from those reported previously.[29] There are two reasons for the change in the values. Firstly, the active site counts previously obtained for system **2** were based on batch

scale experiments, which tend to be slightly lower thanNMR scale experiments (45% vs. 52%).[29,30] Secondly and more importantly, the vinyl counts reported in the previous paper[29] were scarce and showed significant scatter, resulting in higher uncertainty than desired. In the present study, all experiments for **2** and other systems were conducted on the NMR scale to eliminate inconsistency and abundant data was collected to ascertain robust rate cosntants determination. Comparing the previously published constants[29] and the results in the present analysis herein shown in Table 2, the values of the rate constants have been corrected by the following amounts: k_p -25%, k_{mis} -75%, k_{rec} -80%, $k_{vinylidene}$ -44%, $k_{vinylene}$ 52%. These results are consistent with the well documented[15,16,29,30] observation that not all of the catalyst participates in the polymerization, where the origin of the lack of 100% participation is not fully understood and small differences in reaction conditions (e.g. batch vs. NMR scale) can have some consequences.

The experimental data, along with the kinetic modeling fits of system **1 – 4,** are shown in Figure 2. Additional fits to the active sites and vinyls counts are included in the SI. The values of the rate constants are shown in Table 2 including error bounds, which were determined using the methodology discussed previously[29] and in the SI.

Table 4-2. Rate constants for 1-hexene polymerization with the Zr[tBu-ON^{X}O]Bn$_2$/B(C$_6$F$_5$)$_3$ catalysts 1-4

X	pyr-CF3 (**1**)	pyr (**2**)	pyr-Me (**3**)	pyr-OMe (**4**)
Hammett Parameter (σ)	0.54	0.00	-0.17	-0.27
k_i / M^{-1} s^{-1}	0.035	0.017 (±.02)	Fast	Fast
k_p / M^{-1} s^{-1}	4.5 (±0.4)	1.35 (-0.1/+0.2)	0.40 (±0.03)	0.3 (±0.01)
k_{mis} (10^{-3}) / M^{-1} s^{-1}	39 (-5/+8)	7.7 (-0.4/+0.5)	6.1 (-0.5/+1.0)	3.7 (-0.2/+0.3)
k_{rec} (10^{-3}) / M^{-1} s^{-1}	70 (-10/+20)	5.2 (-0.9/+1.2)	7.4 (-0.8/+1.5)	3.2 (-0.3/+0.4)
$k_{vinylidene}$ (10^{-3}) / s^{-1}	1.24 (±0.02)	1.34 (-0.01/+0)	0.93 (±0.02)	1.24 (±0.01/)
$k_{vinylene}$ (10^{-3}) / s^{-1}	0.99 (-0.02/+0.03)	0.441 (±0.003)	0.37 (±0.01)	0.294 (-0.006/+0.004)
Cat %	58% (-2%/+3%)	52%	58% (-3%/+2%)	47% (-0/+1%)

4.4 Discussion

In this study, the complete set of kinetic rate constants for four zirconium amine bis-phenolate catalyst systems have been determined. The mechanism of 1-hexene polymerization for these catalysts consists of the following elementary reaction steps: initiation, normal propagation, misinsertion, recovery, and chain transfer.

The values of the rate constants are given in Table 2 Examining the summarized kinetic data in Table 2, the following conclusions emerge:

(1) Based on experimental active site counts, in all four systems, the catalyst participation is between 50% and 60%, with significant amounts of primary and misinserted secondary sites, where the former is slightly more prevalent than the latter. None of these systems exhibit a decrease in active site counts with

time, indicating that there is no catalyst deactivation and the re-initiation after chain transfer is not slower than normal initiation.

(2) Examining the rate constants in Table 2, the rate constant for propagation increases with the electron withdrawing capability of the pyridine substituent. This is due to the fact that the para position of the pyridyl pendant is electronically coupled to the active site via conjugation. The rate constants for the other monomer insertion steps, including misinsertion and recovery exhibit similar downward trend, where the increase in the rate constant values for all these three reactions is approximately one order of magnitude from catalyst **4** to catalyst **1**.

(3) According to (2), the rate constant for initiation is expected to decrease from catalyst **1** to **4** if the rate limiting step is a monomer insertion. In systems **1** and **2** the k_p/k_i ratio is 129 and 79, respectively, which is large enough for k_i to be resolved from the MWD data. In systems **3** and **4**, the determination of k_i value is not possible as the data are not sensitive enough to changes in k_i indicating that k_i is not slow enough relative to k_p. This suggests that the trend of decrease in k_i when going from catalyst 1 to 4 by the amount as large as the one observed for the other monomer dependent steps does not hold. Our explanation for this is that the rate limiting step for initiation is probably the displacement of the counter-ion, where in case of propagation the counter-ion has already been displaced.

(4) Both of the rate constants for chain transfer, i.e., $k_{vinylidene}$ and $k_{vinylene}$, are monomer independent for all four systems and have similar magnitude. As

shown in Figure 3a, both the vinylidene and vinylene data for all four systems overlap when plotted versus time. However, because of the decrease in the propagation rate from catalyst **1** to **4**, the frequency of chain transfer with respect to propagation increases, causing the total amount of vinyls to increase and the MWD to become broader as the catalyst changes from **1** to **2** to **3** to **4**.

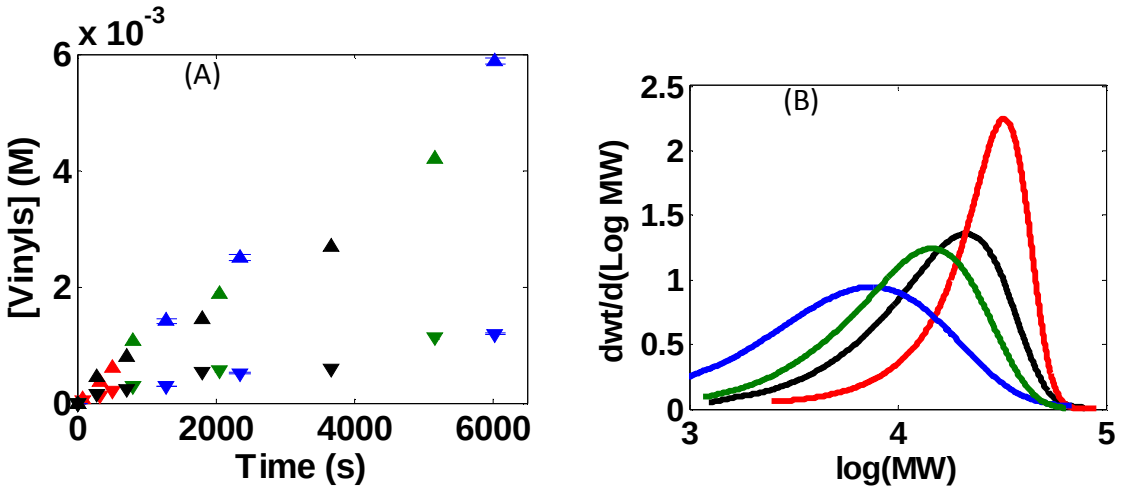

Figure 4-3. Collected data from catalyst **1** (red), catalyst **2** (black), catalyst **3** (green), and catalyst **4** (blue). (A) Concentration of vinyl end groups versus time (vinylidene - up triangles; vinylene - down triangles) (B) MWDs at full conversion.

To summarize, with change in the pyridine substituent group, we observe systematic changes in the rate constants of all the elementary steps involving monomer insertion and no changes in the rate constants of monomer independent steps. Consequently, proper selection of the pyridine ligand enables the rational control of the MWD of the polymer (**Figure 3b)**. To further quantify how the ligand structure affects the reaction rates, Hammett Parameters are determined to quantify the electron withdrawing capabilities of different substituent group. The structure-rate constant relationships are shown in Figure 4. The data presented in Figure 4 shows that electron-withdrawing substituents on the

pyridine pendant increase the rate of all monomer dependent steps with comparable Hammett constants: k_p (ρ = 1.45), k_{mis} (ρ = 1.22), k_{rec} (ρ = 1.57). This is likely the result of further destabilizing the already positive cationic active site by removing additional electron density, thereby, making the active site more apt to react with available monomer. In addition to the correlation with the Hammett Parameter, the rate constants are also correlated with various orbital energies including the HOMO orbital as determined by DFT calculation (see SI).

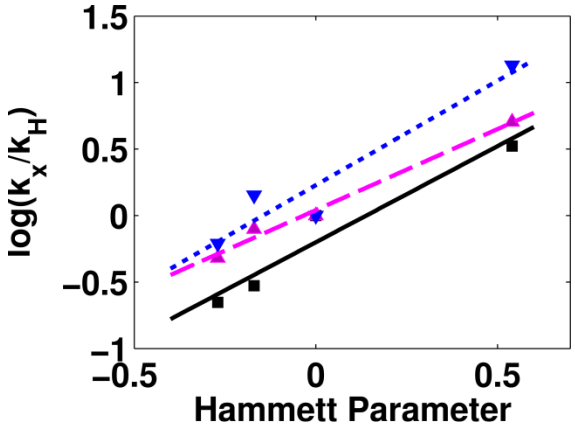

Figure 4-4. Plot of og(k_X/k_H) vs. Hammett Parameter. Squares: log(k_p), up triangles: log(k_{mis}), down triangles: log(k_{rec}). Lines are linear fits.

4.5 Conclusions

A comprehensive kinetic study of four catalytic systems based on Zr amine bis-phenolate complexes has been completed, and the relevant rate constants and elementary reaction steps were determined for each system. The mechanism includes initiation, normal propagation, misinsertion, recovery, and chain transfer. The most significant finding was a correlation between the Hammett Parameter and the rate constants of propagation, misinsertion, and recovery from misinsertion. Specifically, for catalysts 1-4, the logarithm of the rate constants (k_p, k_{mis}, and k_{rec}) decrease with the electron withdrawing capabilities

of different substituent group. This indicates that the systematic addition of electron withdrawing character to the pendant results in a lowering of the energy barrier associated with each monomer insertion event. It was also noted that the chain transfer rates across catalysts 1-4 were relatively unaffected, indicating that the electronic nature of the pendant has little effect on chain transfer. A forthcoming study will explore the effect of steric perturbations on the rate of chain transfer.

REFERENCES

(1) Shul'pin, G. B. *Dalton Trans.* **2013**, *42*, 12794-12818.

(2) Chen, E. Y.-X.; Marks, T. J. *Chem. Rev.* **2000**, *100*, 1391-1434.

(3) Li, H.; Marks, T. J. *Proc. Natl. Acad. Sci. U. S. A.* **2006**, *103*, 15295-15302.

(4) Manz, T. A.; Phomphrai, K.; Medvedev, G.; Krishnamurthy, B. B.; Sharma, S.; Haq, J.; Novstrup, K. A.; Thomson, K. T.; Delgass, W. N.; Caruthers, J. M.; Abu-Omar, M. M. *J. Am. Chem. Soc.* **2007**, *129*, 3776-3777.

(5) Krauledat, H.; Brintzinger, H.-H. *Angew. Chem., Int. Ed. Engl.***1990**, *29*, 1412-1413.

(6) Piers,W.; Bercaw, J. E. *J. Am. Chem. Soc.***1990**, *112*, 9406-9407.

(7) Coates, G. W.; Waymouth, R. M. *J. Am. Chem. Soc.* **1991**, *113*, 6270-6271.

(8) Global Industry Analysts (GIA). *Plastics: A Global Outlook*, **2012**.http://www.prweb.com/releases/plastics_bioplastics/engineered_plastics/prweb9194821.htm.

(9) Sita, L. R. *Angew. Chem., Int. Ed. Engl.* **2011**, *50*, 6963-6965.

(10) Angermund, K.; Fink, G.; Jensen, V. R.; Kleinschmidt, R. *Chem. Rev.*. **2000**, 100, 1457-1470.

(11) Bochmann, M. *J. Organomet. Chem.* **2004**, *689*, 3982-3998.

(12) Mohring, P. C.; Coville, N. J. *Coord. Chem. Rev.* **2006**, *250*, 18-35.

(13) Wang, B. *Coord. Chem. Rev.* **2006**, *250*, 242-258.

(14) Busico, V.; Cipullo, R.; Pellecchia, R.; Rongo, L.; Talarico, G.; Macchioni, A.; Zuccaccia, C.; Froese, R. D. J.; Hustad, P. D. *Macromolecules* **2009**, *42*, 4369-4373.

(15) Novstrup, K. A.; Travia, N. E.; Medvedev, G. A.; Stanciu, C.; Switzer, J. M.; Thomson, K. T.; Delgass, W. N.; Abu-Omar, M. M.; Caruthers, J. M. *J. Am. Chem. Soc.* **2010**, *132*, 558-566.

(16) Liu, Z.; Somsook, E.; Landis, C. R. *J. Am. Chem. Soc.* **2001**, *123*, 2915-2916.

(17) Warren, T. H.; Schrock, R. R.; Davis, W. M. *Organometallics* **1998**, *17*, 308-321.

(18) Ewart, S. W.; Sarsfield, M. J.; Williams, E. F.; Baird, M. C. *J. Organomet. Chem.* **1999**, *579*, 106-113.

(19) Tsukahara, T.; Swenson, D. C.; Jordan, R. F. *Organometallics* **1997**, *16*, 3303-3313.

(20) Azoulay, J. D.; Itigaki, K.; Wu, G.; Bazan, G. C. *Organometallics.* **2008**, *27*, 2273-2280.

(21) Sernetz, F. G.; Mülhaupt, R.; Fokken, S.; Okuda, J. *Macromolecules* **1997**, *30*, 1562-1569.

(22) Porri, L.; Ripa, A.; Colombo, P.; Miano, E.; Capelli, S.; Meille, S. V. *J. Organomet. Chem.***1996**, *514*, 213-217.

(23) Froese, R. D. J.; Musaev, D. G.; Matsubara, T.; Morokuma, K. *J. Am. Chem. Soc.* **1997**, *119*, 7190-7196.

(24) Froese, R. D. J.; Musaev, D. G.; Morokuma, K. *Organometallics* **1999**, *18*, 373-379.

(25) Tshuva, E. Y.; Groysman, S.; Goldberg, I.; Kol, M.; Goldschmidt, Z. *Organometallics* **2002**, *21*, 662-670.

(26) Tshuva, E. Y.; Goldberg, I.; Kol, M.; Goldschmidt, Z. *Organometallics* **2001**, *20*, 3017-3028.

(27) Kerton, F. M.; Holloway, S.; Power, A.; Soper, R. G.; Sheridan, K.; Lynam, J. M.; Whitwood, A. C.; Willans, C. E. *Can. J.Chem.* **2008**, *86*, 435-443.

(28) Groysman, S.; Goldberg, I.; Kol, M.; Genizi, E.; Goldschmidt, Z. *Organometallics* **2003**, *22*, 3013-3015.

(29) Steelman, D. K.; Xiong, S.; Pletcher, P. D.; Smith, E.; Switzer, J. M.; Medvedev, G. A.; Delgass, W. N.; Caruthers, J. M.; Abu-Omar, M. M. *J. Am. Chem. Soc.* **2013**, *135*, 6280-6288.

(30) Switzer, J. M.; Travia, N. E.; Steelman, D. K.; Medvedev, G. A.; Thomson, K. T.; Delgass, W. N.; Abu-Omar, M. M.; Caruthers, J. M. *Macromolecules* **2012**, *45*, 4978-4988.

CHAPTER 5. SELECTIVE DEGENERATIVE BENZYL GROUP TRANSFER IN OLEFIN POLYMERIZATION

This chapter contains published work. It is reproduced with permission from *ACS Catal.*, **2014**, *4* (4), pp 1162–1170; Copyright © 2014, American Chemical Society.

In this paper, I performed GPC measurements of polymer samples and kinetics analysis of the catalyst system. D. Keith Steelman did the experimental part including catalyst synthesis, 1-hexene polymerization, and NMR measurements, etc.

5.1 Introduction

Because of the opportunity for more precise control of the polymer's molecular architecture, homogeneous single-site catalysts have attracted considerable attention.[1,2,3] The pre-catalysts can be activated by a number of activators to generate a coordinately unsaturated cation with an associated counter anion, a zwitterionic catalyst,[4] where the activators include methyl-aluminoxane (MAO), tris-(pentafluoro phenyl) borane ($B(C_6F_5)_3$, and perfluoroarylborate ($[BAr^F{}_4]^-$) and aluminate salts.[5] However, unlike MAO which produces multiple and sometimes ambiguous catalytic species, $B(C_6F_5)_3$ and $[BAr^F{}_4]^-$based activators activate these complexes in a stoichiometrically precise fashion,[6] enabling fundamental kinetic analysis.

The traditional mechanism for single-site polymerization involves activation, initiation, propagation, and finally chain transfer and/or termination.[7] However, the

polymerization may also include degenerative transfer, where an actively polymerizing chain reacts with a dormant chain thereby reactivating the dormant chain for additional polymerization. The concept of degenerative transfer has been previously employed in the analysis of anionic, cationic, group transfer, and controlled/living free radical polymerizations.[8-11] For systems where the exchange between active and "dormant" groups is slow compared to propagation, the resulting molecular weight is broadened compared to analogous systems where degenerative transfer does not occur.[8,9] Conversely, when the rate constant for degenerative transfer is much greater than the rate constant for propagation, i.e. $k_{ex} >> k_p$, the molecular weight distribution of the resulting polymer is narrow and the undesired effect of bimolecular reactions are minimized or eliminated.[12]

It has been shown that under conditions where the activator is limiting, Group IV metallocene complexes have a tendency to form dimeric species due to competition between the $[BAr^F_4]^-$ counter anion and the neutral, unactivated metallocene complex for the highly electrophilic activated metallocene cation.[9,12-14] The mechanistic implication is that cooperativity can provide an additional variable for the control of important aspects of single-site polymerization catalysis, including stereocontrol.[13a] This cooperative effect has been exploited in the development of multi-nuclear single-site catalysts which offer the possibility of creating novel polymeric architectures beyond the reach of conventional mononuclear catalytic systems, including ethylene-styrene copolymerization[13b] and enhanced methyl chain branching.[13c]

Much of the mechanistic work concerning binuclear interactions has focused on the systems containing two non-tethered metal centers. Bochmann and Lancaster observed peak broadening of Zr-Me ^{1}H NMR signal in a series of $[Cp_2MR_2]$ (R = alkyl, M = Ti, Zr, or Hf)/

$[CPh_3][B(C_6F_5)_4]$ systems that they interpreted as a signature of the formation of a binuclear complex (BNC).[15] The BNC arises from the interaction of an actively polymerizing metal center with a neutral metal center from pre-catalyst, where the neutral metal center is, in essence, activated by the active metal-ligand complex, leaving the former in a neutral state with the general structure X-M-P (X = an abstractable group, M = metal, and P = polymer).[9,12] Marks and co-workers reported the formation of BNC by constrained geometry catalysts as indicated by NMR broadening.[14]

Sita and co-workers recently reported a detailed study of the degenerative ligand transfer in olefin polymerization using mixed metallocene acetamidinate catalysts with a sub-stoichiometric amount of activator, where they employed the concept of a BNC.[12] In this study a ^{13}C-enriched catalyst was used to observe the methyl exchange and metal-centered epimerization, which led to the postulate of the BNC. Studying activity and the MWD at the end of the reaction, Sita and co-workers observed that (1) the rate of consumption linearly decreased with increase in the amount of pre-catalyst while keeping the activator concentration constant, (2) the M_n was determined by only the monomer to pre-catalyst ratio and not the amount of the activator, and (3) the PDI was independent of the excess amount of pre-catalyst.[12a] Using the model proposed by Muller and co-workers[9], Sita et al. argued that the mechanism consistent with these observations must include the rate of BNC formation that is much faster than k_p (propagation) and the equilibrium constant for BNC formation that is much larger than the observed consumption rate. It should be pointed out that the work of Sita et al. although containing the aforementioned qualitative conclusions about relative rates of the BNC related reactions did not produce the actual rate constants. The system studied by Sita and coworkers is essentially living,

where the PDI value is less than 1.05. On the other hand, most of the group IV single site catalysts are not living. For example, a significant amount of misinsertion occurs in the Salan catalyst systems.[7] It would be instructive from both practical and fundamental standpoint to study if the BNC formation happens similarly if the polymeric species involved are normally inserted or misinserted. Furthermore, occurrence of the BNC discussed above has been limited until now to methyl or chloride abstractable groups. In fact, it has been stated specifically that the benzyl ligand could not form the BNC.[15]

We have previously studied the polymerization kinetics for a family of group IV amine bis-phenolate (Salan) ligated pre-catalysts which is characterized by high activity, and solubility in conventional organic solvents like toluene.[16,17] The complete kinetic analysis of this system under stoichiometric activator to pre-catalyst ratio has been carried out,[7b] where we have used our previously established techniques[7] to robustly determine the mechanism and rate constants for all of the elementary steps. In particular, we have found that the $Zr[^{t}Bu\text{-}ON^{THF}O]Bn_2/B(C_6F_5)_3$ catalyst system possesses a relatively large amount of misinsertion, where the concentration of the secondary (i.e. 2,1-misinserted) active sites under typical conditions equals the concentration of the primary (i.e. normally 1,2-inserted) active sites. As such this system represents an attractive candidate for a study of BNC formation by different active sites, provided the BNC formation can be effected.

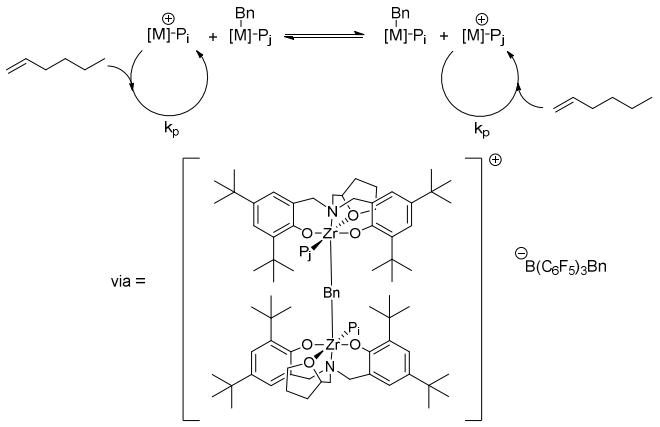

Figure 5-1. 1-hexene polymerization catalyzed by zirconium salan-type catalyst Zr[tBu-ON(THF)OBn$_2$ using sub-stoichiometric amounts of tris(pentafluorophenyl) borane. The structure of pre-catalyst is published in previous work.[7b]

In this study we report the polymerization kinetics of the Zr[^{t}Bu-ON^{THF}O]Bn$_2$/B(C$_6$F$_5$)$_3$ catalyst system under sub-stoichiometric activator conditions in order to elucidate the degenerative transfer process. We will first demonstrate BNC formation for this system via peak broadening of Zr-benzyl ^{1}H NMR signal. Next, we will show that the change in the MWD with decreasing amounts of activator cannot be explained using the mechanism established under the condition of stoichiometric amount of activator. In light of the aforementioned literature claim that the benzyl bridged BNC cannot form,[15] we undertook the task of elucidating the mechanism capable of describing the data. A sequence of increasingly complex kinetic mechanisms have been analyzed, where a minimal mechanism set capable of predicting the data in its entirety has emerged as the one that involves the formation of BNC (Figure 1). In addition to kinetic analysis, we will provide additional experimental evidence for the formation of the BNC via a novel experimental procedure where a labeled catalyst is introduced when the polymerization reaction is approximately 50% completed. Most importantly, the kinetic mechanism

arrived upon in this study implies that the BNC formation is highly selective in that the BNC can only be formed by the coupling between the primary active sites and neutral pre-catalytic species and not by the secondary misinserted active sites. This selectivity has an additional benefit of producing polymer with narrow MWD.

The ability to quantitatively fit the multi-response data provides confidence in that this minimal kinetic model is a robust description of the underlying polymerization process. The comprehensive kinetic modeling of $Zr[^{t}Bu\text{-}ON^{THF}O]Bn_2/B(C_6F_5)_3$ system also enables extraction of the rate constants of association and dissociation of the BNC, which clearly indicate that the actual benzyl-group transfer is rapid. Another interesting feature that results from the kinetic modeling of this system is that the BNC has a faster initiation rate than the zwitterion pair catalyst. This is likely due to the anion being previously displaced by the incoming unactivated pre-catalyst.

In recent years, considerable attention has been paid to the development of novel processes that reduce or eliminate the need for an activator.[12,13,18] As a result of decreasing the amount of activator present in the system, there is an increase in cooperativity between two distinct metal centers which gives rise to new mechanistic possibilities and increased polymerization control.[12,13] The BNC complex has the added benefit of simultaneously activating all neutral pre-catalyst molecules contained in the system using a minimal amount of activator.

5.2 Experimental Procedure

General Procedure. All manipulations were performed under inert atmosphere in a glove box or on a vacuum manifold. Toluene and pentane were purified over activated alumina

and a copper catalyst using a solvent purification system (Anhydrous Technologies), degassed through freeze-pump-thaw cycles, and stored over activated molecular sieves. Tetrabenzylzirconium was purchased from STREM and used as received. 1-hexene was purchased from Aldrich and purified by distillation over a small amount of $CpZrMe_2$ and stored over molecular sieves. $B(C_6F_5)_3$ was purchased from STREM and purified by sublimation. Diphenylmethane was purchased from Aldrich and stored over molecular sieves. CD_3OD was purchased from Cambridge Isotopes and used as received. D_8-toluene was used as received and stored over molecular sieves. ^1H and ^2H NMR experiments were performed on a Varian INOVA600 MHz or Bruker DRX500 MHz spectrometer.

The ligand and unlabeled pre-catalyst were prepared following literature procedures.[7,16,17,19]

Quenched NMR scale polymerization of 1-hexene. To a catalyst/activator solution in an NMR tube at 25 ºC, 1-hexene was added. At the desired monomer conversion, this reactions was quenched with 0.75 mL of d_4-CD_3OD. These reactions were quenched at the desired conversion of monomer using 0.75 mL of d_4-methanol. The quench reaction was analyzed as previously described.[7]

Zr[tBu-ON^{THF}O]Cl$_2$ synthesis. $ZrCl_4$ (3.6141 g, 15.5 mmol) and 25 mL of ether were added to a 100 mL flask. In a separate flask, 25 mL of ether and tBu-ON^{THF}O ligand (8.3408 g, 15.5 mmol) were added. Each flask was allowed to cool to -30 C. The ligand solution was then added to the $ZrCl_4$ slowly. The resulting colorless solution was filtered, and the white solid discarded. The leftover solution was dried under vacuum to yield a

colorless solid (93% yield). The solid is >95% pure, by 1H NMR. No further purification was needed.

Zr[tBu-ON^{THF}O]d$_7$-Bn$_2$ synthesis. Zr[tBu-ON^{THF}O]Cl$_2$ (2.10 g, 3.0 mmol) and 25 mL of d$_8$-toluene were added to a 100 mL flask. This flask was allowed to cool to -30 C. To this flask, solid d$_7$-benzylpotassium (1.65 g, 12.0 mmol) was added. The reaction mixture was allowed to warm up to 25 ºC over 30 min. Then, the reaction mixture was heated to 60 ºC for 2 h. The resulting slurry was treated with 30 mL of dichloromethane and filtered yielding a yellow solution. The solution was dried under vacuum to give a yellow solid (63 % yield). The solid was found by ^{1}H NMR and ^{2}H NMR to be >95% pure product. The solid was recrystallized in d$_8$-toluene to yield an analytically pure complex.

Batch Polymerization of 1-hexene using Zr[tBu-ON^{THF}O]Bn$_2$ with an additional equivalent of labelled Zr[tBu-ON^{THF}O]d$_7$-Bn$_2$. Zr[tBu-ON^{THF}O]Bn$_2$ (0.073 g, 0.90 mmol) dissolved in 5.0 mL toluene was added under Ar to a 25 mL toluene solutions containing 1-hexene (1.58 g, 18.7 mmol) and Tris(pentafluorophenyl)boron (0.024 grams, 0.047 mmol). The reaction mixture was quenched with 3 mL of d4-CD_3OD at a selected time point corresponding to ca. 50% completion. An identical reaction to that described was initiated and at the same selected time for the above reaction quench, here an additional equivalent of labelled Zr[tBu-ON^{THF}O]d^7-Bn$_2$ (0.073 g, 0.90 mmol) in 5 mL was added to the ongoing polymerization reaction. This reaction was quenched with 3 mL of d4-CD_3OD in its entirety at ca. 80% conversion. In a second batch fun with added labelled precatalyst, the polymerization reaction was run until completion before quenching with d4-CD_3OD at

>90% conversion. The quenched solutions from each of the above reactions were worked up and analyzed for monomer consumption by ^{1}H NMR, active site counting by ^{2}H NMR, extent of deuterium incorporation into the poly-hexene by ^{2}H NMR, and MWD of the resulting polymer (GPC) as described previously.[7]

Kinetic Modeling Method. In previous work, we have determined the time-dependent concentrations of all species by solving the set of coupled nonlinear ordinary differential equations (ODEs) that result from mass action kinetics for a given polymerization mechanism.[7] However, ODE methods are significantly more difficult when the number of chemical species is combinatorially large as is the case when there is the association/dissociation of two polymer species that occurs via a BNC mediated reaction. Specifically, the number of distinct BNC species is the number of all possible combinations of all chain lengths – a computationally intractable number even for the massively parallelized ODE solver that we have developed.[20] Thus, we have developed a new solution algorithm based upon Dynamic Monte Carlo (DMC) methods[21] that is mathematically equivalent to the more traditional ODE formulation. The implementation of the DMC method employs the Gillespie's algorithm[21] for which a new computer code has been developed. Determination of the optimal set of the rate constants needed to fit a given mechanism to multi-response experimental data employs the Nelder-Mead's (i.e. simplex) optimization procedure.[22] A complete discussion of the formulation, DMC algorithm, and the Nelder-Mead optimization procedure is given in the Supporting Information.

5.3 Results

The 1-hexene polymerization using zirconium amine bis-phenolate catalyst, Zr[tBu-ON^{THF}O]Bn2 has been investigated previously with stoichiometric amounts of activator[7b]; herein the effect of sub-stoichiometric activator concentration is the primary focus. The conditions studied are listed in Table 1, where Case 1 is the stoichiometric condition. A caveat is that the current experimental procedure involves first mixing activator and the pre-catalyst, and then adding monomer, whereas previously the pre-catalyst was added to the mixture of activator and monomer.

Activation Analysis. The catalyst/activator system under study has been previously shown to activate quickly and cleanly under both stoichiometric and a slight excess activator in neat 1-hexene.[16,17] Under these conditions, polymeryl exchange experiments showed that each catalytic species present in the system acts independently with no communication between different catalytic species.[16] Spectroscopic evidence for this conclusion is furnished by (i) the immediate conversion of the pre-catalyst to two sharp benzylic ^{1}H signals (δ 2.89 and 2.62 ppm) and (ii) the clean conversion of the ^{19}F signals of the borane activator (δ -128.4, -143.2 and 160.6 ppm) into the borate counter-anion (δ -131.6, -164.8 and 167.8 ppm). In situations where the pre-catalyst to activator ratio is more than 1, i.e. the activator is limiting, the conversion of borane to the borate counter-anion remains clean. However, the ^{1}H spectrum of the resulting reaction mixture shows significant line broadening of the two benzyl signals, indicating a dynamic process in which the benzyl groups are rapidly exchanged between two catalytic species (Figure S4).

Kinetics of Polymerization. For every condition in Table 1, six experiments were carried out: three experiments to pre-specified monomer conversions, and three to full conversion. Time dependent monomer consumption was monitored for the three experiments proceeding to full conversion; end point monomer consumption was measured for every experiment. The MWD of polymers was obtained via GPC at the end of all six experiments. The active site counts were obtained at the end of the three reactions to pre-specified monomer conversions as shown in Figure 2. The active site count was determined by quenching with d_4-methanol and performing ^2H NMR measurement of the concentration of chains with deuterated end groups using established methods.[7] The sites that have undergone 1,2-insertion are defined as primary sites, and the sites that have undergone 2,1-misinsertion are defined as secondary sites. Representative examples of the MWD at full monomer conversion are shown in Figure 3. The concentrations of vinyl end groups were shown to be negligible for this catalyst system.[7b]

Table 5-1. Initial Conditions of NMR scale experiments. "C" – pre-catalyst, "A" – activator, "M" – monomer.

Case	$[C]_0$ (mM)	$[A]_0$ (mM)	$[A]_0/[C]_0$	$[M]_0$ (mM)
1	3.0	3.3	1.1	600
2	3.0	1.5	0.5	600
3a	3.0	0.75	0.25	600
3b	6.0	1.5	0.25	1200

When sub-stoichiometric amounts of activator were used, the following features of the polymerization reaction emerged as shown in Figures 2 and 3:

1. The consumption rate decreases with decrease in activator amount.
2. The measured total amounts of active sites are almost the same for Cases 1, 2, and 3a. While the total amount of active sites remains nearly constant, the

amount of secondary sites decreases with decreasing amounts of activator, and the amount of primary sites increases as shown in Figure 2.

3. Despite the measured total amount of active sites being constant, the MWD in the sub-stoichiometric cases surprisingly shifts toward lower molecular weights and becomes narrower (i.e. in Figure 3B the PDIs for Case 2 is 1.17 and 3a is 1.12 vs. PDIs of 1.29 for stoichiometric conditions, Case 1).

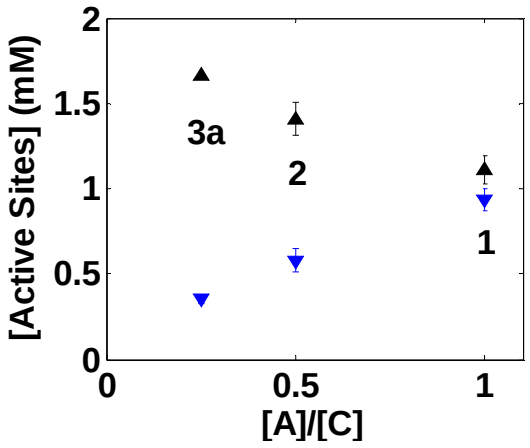

Figure 5-2. Active site counts of quenched NMR scale reactions 1, 2, 3a. Black up-pointing triangles: primary site counts; blue down-pointing triangles: secondary site counts.

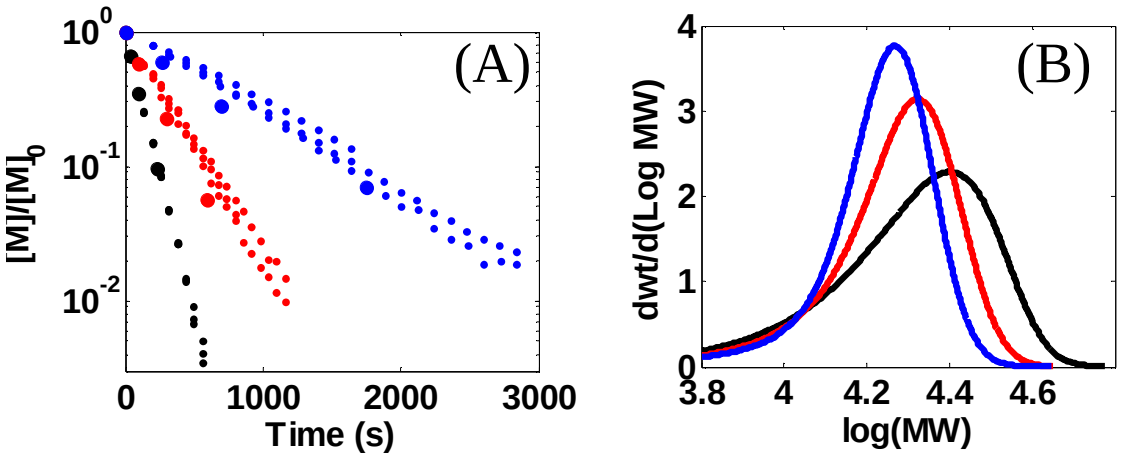

Figure 5-3. A) Comparison of NMR scale and quenched NMR scale reactions 1, 2, 3a. Initial concentrations are shown in Table 1. Black: case 1; red: case 2; blue: case 3. B) Corresponding end point MWDs.

Kinetic Analysis. The natural point of departure for a detailed kinetic model is the set of elementary reactions that was previously developed to describe the polymerization reaction under stoichiometric activator conditions.[7a] The set consists of initiation, propagation, misinsertion and recovery as shown in Scheme 1, where the active catalyst is denoted as C*, primary active site as R_i, secondary active site as P_i and the index i indicates the length of the polymer chain. In what follows this mechanism is referred to as Base Model. In light of Points 1-3 above, the Base Model predicts that when there is less activator, less pre-catalyst is activated, resulting in lower number of active sites and consequently higher molecular weight polymers. However, the experimental data in Figures 2 and 3 clearly contradict these predictions, where experimentally the molecular weight decreases and the number of active sites remains constant as the activator concentration is decreased. Including chain transfer reactions does lower the molecular weight; however, this also

results in significant broadening of the MWD, which is not observed experimentally. *The Base Model cannot describe experiments with sub-stoichiometric activator concentrations*.

Assuming that each activator molecule is responsible for the formation of a single active site, the amount of active sites should not exceed the initial amount of activator. However, in Cases 2 and 3a the amount of active sites measured by NMR (i.e. the sum of the primary and secondary sites) is 2.1 mM in both cases, which is higher than the 1.5 mM or 0.75 mM of activator used in 2 and 3a, respectively. This leads to the idea of *reversible activation*, which allows for activating more pre-catalyst than the nominal amount of activator. The reversible activation model assumes that the activator can transfer between an actively polymerizing catalyst complex and an inactive chain, where the activator transfer reactivates the inactive chain for further polymerization but inactivates the previously growing catalyst-polymer complex. A detailed analysis of the reversible activation model is given in the SI where this model does have some beneficial features. Nevertheless, the fluorine NMR results described in the Activation Analysis section eliminates this model, because the model does not distinguish between stoichiometric and sub-stoichiometric cases whereas the broadening of benzyl ligand NMR lines is observed under the sub-stoichiometric conditions vs. sharp peaks under stoichiometric conditions.

Ligand Transfer Model. The difference between stoichiometric and sub-stoichiometric activator conditions is the presence of unactivated pre-catalyst. The Ligand Transfer Model assumes that the pre-catalyst is activated by direct transfer of the benzyl ligand (Bn) from the pre-catalyst to the active catalyst via the formation of a binuclear complex (BNC).

Unlike the case of reversible activation, ligand transfer will not take place under stoichiometric conditions, because there is no excess pre-catalyst.

BNC formation/dissociation is assumed to take place via Scheme 2, where L_4 denotes the four-fold ligated [tBu-ONTHFO] moiety. A BNC consists of one active catalytic complex (R_i or P_i) and one inactive catalytic complex, denoted here as Bn-R_j or Bn-P_j. When Bn shifts from the inactive catalyst to the active one in the BNC, the inactive catalyst becomes active and vice versa. The mass action equations for the reactions in Scheme 2 are given by

$$R_i + Bn\text{-}R_j \underset{k_{ex}^-}{\overset{k_{ex}^+}{\rightleftharpoons}} R_i\text{-}Bn\text{-}R_j \qquad (1)$$

$$P_i + Bn\text{-}P_j \underset{k_{ex}^-}{\overset{k_{ex}^+}{\rightleftharpoons}} P_i\text{-}Bn\text{-}P_j \qquad (1')$$

$$CC^* \xrightarrow{k_{i\_BNC}} R_1 + C \qquad (2)$$

$$C^*\text{-}Bn\text{-}R_i \xrightarrow{k_{i\_BNC}} R_1 + Bn\text{-}R_i \qquad (3)$$

Eqns. 1 and 1' use a compact notation where the activated catalyst C* is denoted as R_0, and the pre-catalyst C is denoted as Bn-R_0.

Introduction of the BNC complex in the mechanism leads to several questions that need to be addressed: Are both primary and secondary active sites capable of forming the BNC? Is the BNC formation reversible? Does the BNC propagate and what is the propagation rate constant? And, can a BNC that consists of the activated catalyst and a pre-catalyst (i.e. C-C*) be initiated, and if this is possible, what is the rate constant of initiation? The answer to each of these questions will result in different versions of the Ligand Transfer Model. We summarize and eliminate various alternative models, where the detailed analysis is given in the SI.

1. The case that both primary and secondary active sites form BNC can be dismissed, because it is not selective with respect to the primary and secondary sites. As explained in the SI, if the BNC is formed by both primary and secondary sites with equal probability, the ratio of primary to secondary sites will not change with the activator-to-catalyst ratio. This is in obvious contradiction with the experimental observation shown in Figure 2. If on the other hand the BNC is formed predominantly by the primary sites, their relative abundance can be explained. In other words, the secondary site count decreases with the activator amount normally as it would in the absence of BNC formation. The primary site count would have behaved in the same way if not for the additional activation channel afforded by the BNC. In formal terms this implies that Eqn. 1' does not occur and hence the species Bn-P_j do not form.
2. The BNC formation has to be reversible otherwise one activator can only activate two pre-catalysts at most. Specifically if the BNC formation was not reversible then at a 1:4 [A]:[C] ratio (i) only one half (instead of all) of the catalyst would grow chain, hence the active site counts would be lower than the observed value (70%) and (ii) the molecular weight would be much higher in contradiction to the experimental data.
3. If the initiation rate of BNC k_{i_BNC} is no faster than k_i, the shift of the MWD to lower values with decrease in activator-to-catalyst ratio seen in Figure 3B is not fully predicted as explained in the SI. However, when k_{i_BNC} is much faster than k_i, the shift in the MWD is captured.

Thus, the Ligand Transfer Model involving Eqns. 1, 2, and 3 has the appropriate mechanistic structure to describe all the data sets with different activator-to-catalyst ratios. As shown in Figure 4, the agreement between the model predictions and the experimental data is quite good. The optimized rate constants are given in Table 2.

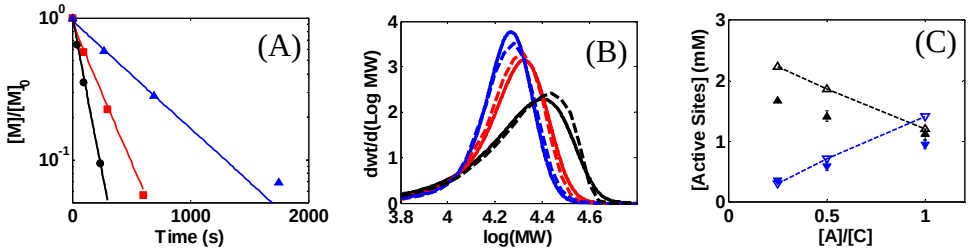

Figure 5-4. Ligand Transfer Model predictions of NMR scale reactions 1 (black), 2 (red), 3a (blue) based on Model 3.3. A) Monomer consumptions. Data: symbols, predictions: lines. B) End-point MWDs. Data: solid, predictions: dashed. C) Active site counts of reactions 1, 2, and 3. Data: black up-pointing triangles: primary site counts; blue down-pointing triangles: secondary site counts, predictions: dashed lines with unfilled triangles.

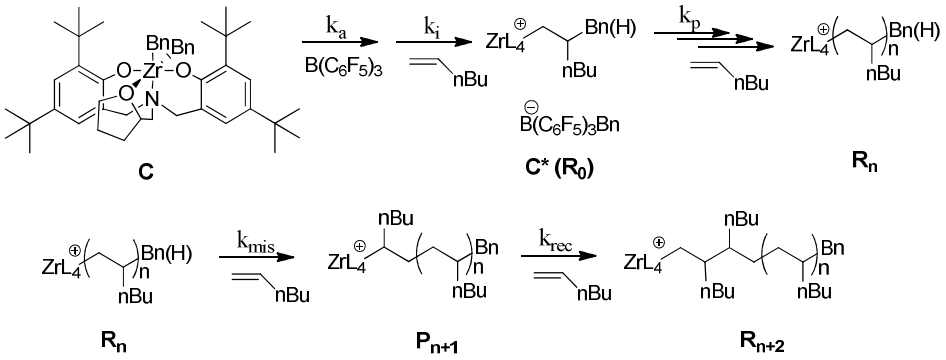

Scheme 5-1. The elementary kinetic steps included in the Base Model.

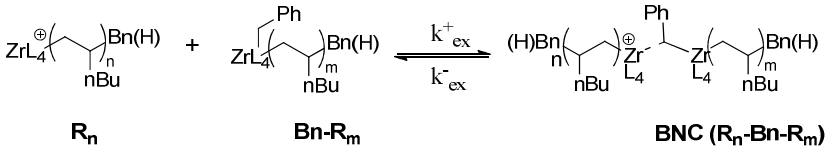

Scheme 5-2. The associated elementary kinetic steps of the BNC formation.

Table 5-2. Optimized rate constants for Ligand Transfer Model.

k_i (M^{-1} s^{-1})	k_p (M^{-1} s^{-1})	k_{mis} (M^{-1} s^{-1})	k_{rec} (M^{-1} s^{-1})	k_{ex}^{+} (M^{-1} s^{-1})
0. 08	8.0	0.054	0.040	400
k_{ex}^{-} (s^{-1})	K_{ex} (M^{-1})	k_{i_BNC} (M^{-1} s^{-1})	$\frac{[BNC]}{[A]_0}$ at $\frac{[A]_0}{[C]_0} = \frac{1}{2}$	$\frac{[BNC]}{[A]_0}$ at $\frac{[A]_0}{[C]_0} = \frac{1}{4}$
20	20	12	3%	4%

Based on the optimized rate constants shown in Table 2, the ratio of BNC concentration to the total catalyst concentration is very low under sub-stoichiometric conditions. Consequently, unless the BNC propagation rate is two orders of magnitude or more higher than k_p, it has little effect on the monomer consumption rate and the MWD. Thus for simplicity we will assume that the propagation rate by BNC was equal to k_p of the zwitterionic catalyst.

In order to experimentally validate the Ligand Transfer Model, a qualitatively different experiment was developed, where a second shot of pre-catalyst was added at 44% conversion (feed at 0 s: $[C]_0$=3.0 mM, $[A]_0$=1.5 mM, $[M]_0$=0.60 M; at 157 s: $[C]_1$=3.0 mM). Deuterated benzyl ligands were used for this second shot of pre-catalyst. It was observed from NMR that a fraction of the final polymer products contained deuterated benzyl, indicating that the added pre-catalyst activates and participates in polymerization despite seemingly having no activator left to be activated by. The number of secondary sites decreases and of primary sites increases after the second pre-catalyst addition is made. And, after the addition of pre-catalysts in the middle of the reaction, a second peak appears in

the MWD as shown in Figure 5. The rate of monomer consumption is not affected by the addition of pre-catalyst.

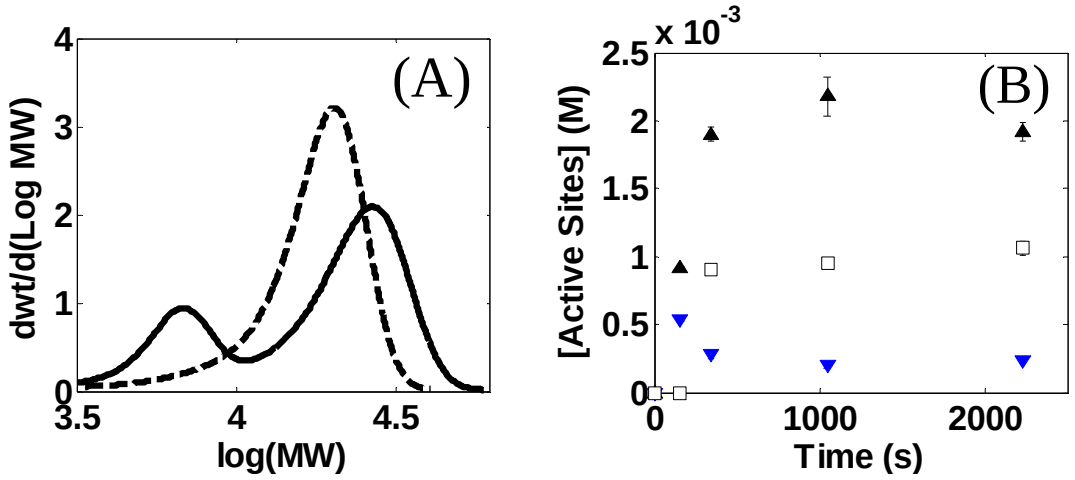

Figure 5-5. Batch scale experiment with additional shot of pre-catalyst (3.0 mM) at 44% conversion. Initial conditions: $[C]_0$ = 3.0 mM, $[A]_0$ = 1.5 mM, $[M]_0$ = 0.60 M. A) Active site counts and d_7-benzyl incorporation (sqares) of catalyst pulse batch scale reactions. Black up-pointing triangles: primary site counts; blue down-pointing triangles: secondary site counts. B) MWDs at 44% (dashed) and at 100% (solid) conversion.

Examining the results in Table 2, the k_{i_BNC} initiation rate constant is significantly higher than the standard initiation rate constant k_i. To validate this prediction of the Ligand Transfer Model, we carried out two polymerization experiments with low monomer-to-activator ratio (5:1) where the activator to pre-catalyst ratio was in one case 1:1 and in the other case 1:4 i.e. sub-stoichiometric. Low monomer-to-activator/catalyst ratio experiments are sensitive to the ratio of the initiation rate to the propagation rate allowing more accurate determination of the initiation rate.[7c] Specifically in a typical case of the k_i to k_p ratio of approximately 1:100 and a monomer-to-catalyst ratio of 100 or higher the initiation is fast on the experimentally accessible time scale, where the number of growing chains reaches a maximum and then remains constant as shown schematically by the dotted

line in Figure 6B. On the other hand, in case of the monomer-to-catalyst ratio of 5:1 the initiation continues in the course of the entire polymerization reaction resulting in a pronounced induction period seen in the monomer consumption curve (solid black curves in Figures 6A and 6B). The data in Figure 6A presents the comparison between the cases of stoichiometric and sub-stoichiometric activator to pre-catalyst ratios (with the activator amount being fixed). In the sub-stoichiometric case the BNC is formed. Now if the BNC did not participate in the initiation, it would effectively act as a de-initiator. This is because when the BNC is formed by an active site and a pre-catalyst and then is dissociated as an uninitiated active site and a neutral catalytic species neither of them can propagate. As a result it is predicted somewhat unexpectedly that if k_{i_BNC} is much slower than k_p then the system with excess amount of pre-catalyst would consume monomer at much slower rate than the one with the lower amount of pre-catalyst. This prediction is shown schematically as dashed blue line in Figure 6. This of course is not observed experimentally as evidenced by Figure 6A, where the consumption in the sub-stoichiometric case is in fact faster than that in the stoichiometric case (blue circles vs. black circles). By the above reasoning this can only be the result of the k_{i_BNC} initiation rate by the BNC being fast, much faster than k_i.

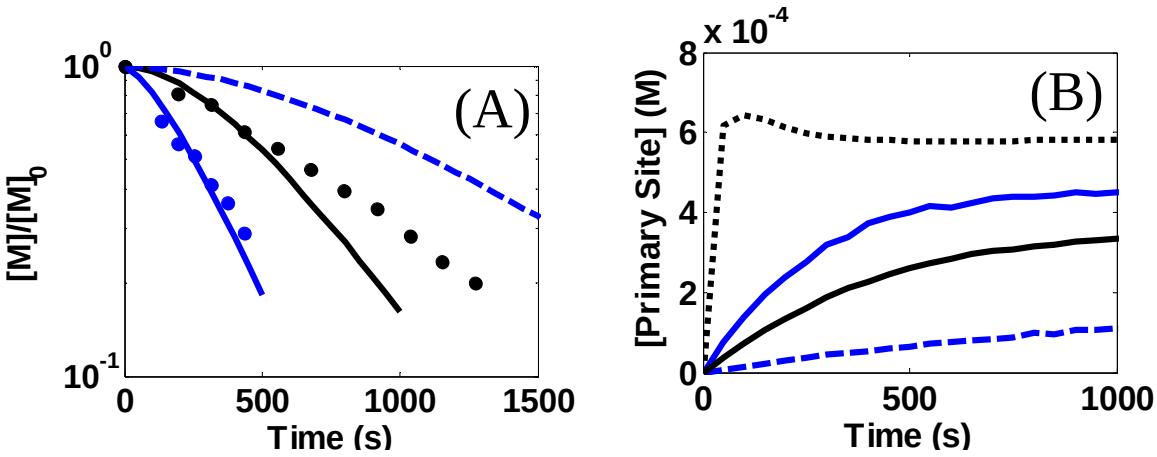

Figure 5-6. Initiation kinetics under low monomer-to-catalyst ratios. Initial conditions: $[A]_0$ = 1.5 mM, $[M]_0$ = 7.5 mM, $[C]_0$ = 1.5 mM (black) and 6.0 mM (blue). (A) Monomer consumptions. Symbols are data, curves are predictions. (B) Predictions of primary site concentration. Rate constants are reported in Table 2 except that $k_{i\_BNC} = 0$ for blue dashed curve.

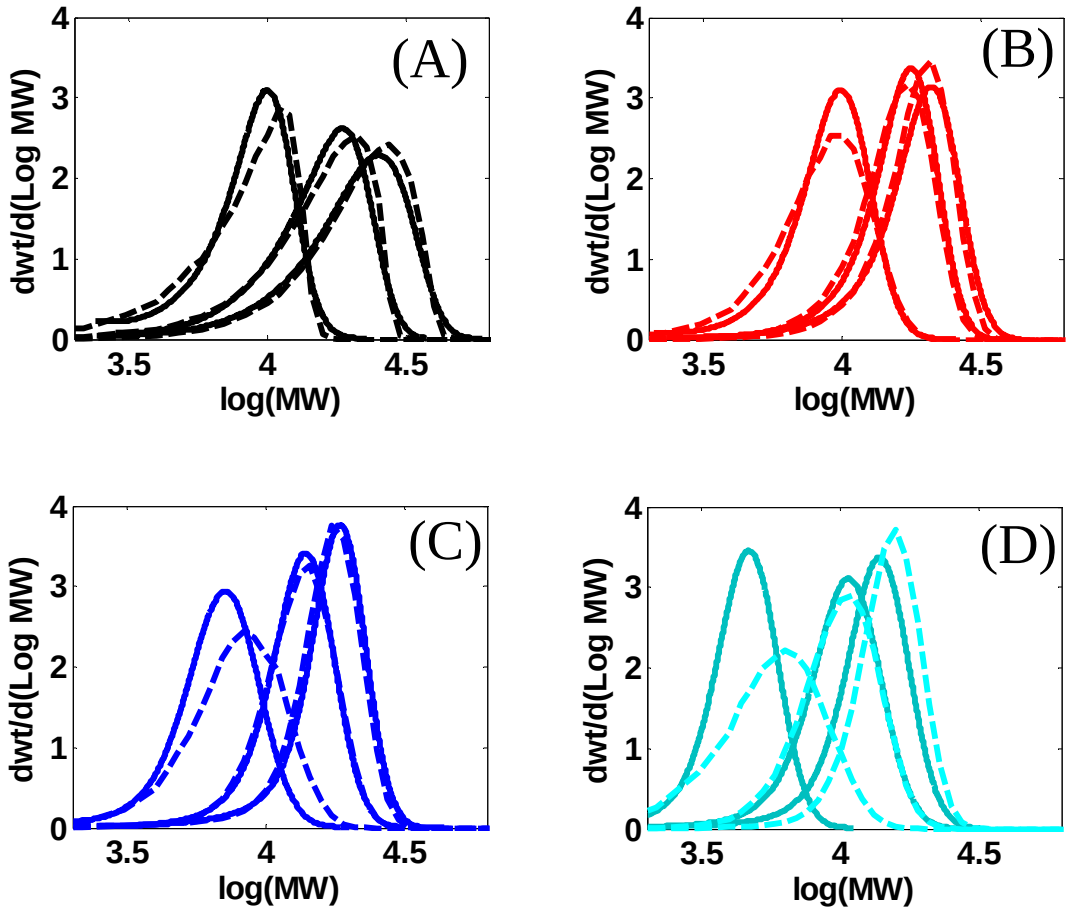

Figure 5-7. Modeling predictions of NMR scale reactions 1 (black), 2 (red), 3a (blue), 3b (cyan) based on Model 3.3. A) MWDs at 35%, 65%, 91% conversion, B) MWDs at 43%, 77%, 94% conversion, C) MWDs at 41%, 72%, 93% conversion, D) MWDs at 29%, 56%, 86% conversion. Data: solid, predictions: dashed.

To summarize, the simplest reaction mechanism capable of accounting for the experimental results was determined to be Schemes 1 and 2. In addition to predicting the data in Figure 4 (Cases 1, 2 and 3a in Table 1), the Ligand Transfer Model successfully describes the rest of the data (including Case 3b) and in particular the time evolution of MWD shown in Figure 7. The only unsatisfactory prediction is for the lowest (29%) conversion in Case 3b (Figure 7D). A possible explanation for this discrepancy is that the

light scattering dn/dc value decreases from the constant value when the molecular weight is low ($M_w \leq 5000$ for the lowest peak in Figures 7C and 7D). The overestimation on this value results in the underestimation of the sample molecular weight. The catalyst participation (i.e. fraction of the of pre-catalyst being active in the reaction) for this system is approximately 90% as determined from fitting the data using the method reported previously.[7] This is attributed to experimental error or small amount of impurities.

5.4 Discussion

A selected zirconium amine bis-phenolate catalyst system has been studied, where a rich kinetic data set including the evolution of MWD has been collected for a wide range of initial conditions with a focus on the sub-stoichiometric amounts of activator. As previously reported,[7b] the mechanism of 1-hexene polymerization for this catalyst using a stoichiometric amount of activator consists of the following elementary reaction steps: initiation, normal propagation, misinsertion, and recovery. However, under sub-stoichiometric amounts of activator, additional elementary steps are needed to describe the data that involve the formation of a binuclear complex (BNC). Validation of the BNC based mechanism was obtained via (i) NMR scale polymerizations listed in Table 1, where the active site counts and MWD both indicate the catalyst participation is the same even as the activator to catalyst ratio is varied and (ii) the use of a novel experimental technique wherein a labeled pre-catalyst was injected into a normal polymerization reaction at approximately ~50% conversion, resulting in instantaneous activation of all incoming pre-catalyst. As the reaction proceeds a second peak appears in the MWD that initially has a

lower molecular weight, which is the result of chains growing on the newly formed active sites.

Comprehensive kinetic modeling yielded values of the rate constants for all the elementary reactions, including the ones involving the BNC, given in Table 2. While the literature has ample support from empirical observations and semi-quantitative measurements that groups such as –Cl and –Me can participate in degenerative transfer,[12] we present a quantitative measure of the rate constants that govern the association and dissociation of the complex leading to degenerative transfer, and for the first time demonstrate ligand transfer with benzyl group.

The ligand exchange process in this system is found to be rapid as evidenced by significant line broadening of the two benzylic signals in the ^{1}H spectrum. By examining the data in Table 2, one can see that the formation rate of BNC, i.e. k_{ex}^{+}, is extremely fast as is the inter-conversion of species R_n and Bn-R_n, on the timescale of the other elementary steps contained within the mechanism. The dissociation rate of BNC, k_{ex}^{-}, is also fast, given that it is a first order rate constant. The rapid dissociation of this complex indicates that it is an unstable complex. Therefore, the concentration of BNC at any moment is much lower than the concentration of R_n. This is in agreement with the literature[12] conclusion that BNC compounds are unstable and no isolated crystal structure has been obtained; consequently, the exchange rate could only be qualitatively estimated in previous work.[12] In contrast the quantitative kinetic modeling methodology presented here provides quantitative analysis of the dynamics of the BNC. Two major conclusions from this work are:

1. With the decrease in activator, there is systematic decrease in misinserted sites and increase in normally inserted sites. To account for this effect, the Ligand

Transfer Model postulates that the secondary active sites P_n (formed by misinsertion) cannot form the BNC. A possible explanation is that the large side group of the misinserted chain hinders the ability of the benzyl ligand to bridge the two zirconium centers. *By effectively shutting down the misinsertion pathway (i.e. the formation of P_n), the use of sub-stoichiometric amounts of activator causes the $Zr[^tBu\text{-}ON^{THF}O]Bn_2/\ B(C_6F_5)_3$ system to approach that of a living polymerization.*

2. Initiation via BNC is much faster than the normal initiation of a single active catalyst. This is likely due to the anion being previously displaced by the incoming pre-catalyst, and the two metal centers present in BNC being not as tightly associated as in the case of a normal zwitterion pair catalyst. *As a result, the MWD of the polymer is systematically lowered with decreasing activator concentration.*
3. Note that the mechanism developed in this paper can be used to analyze the data of Sita et al.[12] with the caveat that misinsertion does not occur in the first place for that system. The details of the analysis are given in the SI and the main results are summarized in Table 3. Catalyst participation is determined to be 68% based on M_n vs. $[M]_0/[Zr]_{tot}$ dependence, which for the case of living polymerization gives the amount of growing chains.

Table 5-3. Modeled results of Sita's $Cp^*ZrMe_2[N(tBu)C(Me)N(Et)]/ [B(C_6F_5)_4]$ system

k_p (M^{-1} s^{-1})	K_{ex} (M^{-1})	k_{ex}^{+} (M^{-1} s^{-1})	$\frac{[BNC]}{[A]_0}$ at $\frac{[A]_0}{[C]_0} = \frac{1}{2}$	$\frac{[BNC]}{[A]_0}$ at $\frac{[A]_0}{[C]_0} = \frac{1}{4}$
19.6	111.5	$>3\times10^3$	10%	25%

Similar to the current system the system of Sita et al.[12] is characterized by association rate of BNC which is much faster than k_p. Sita et al. reasoned that the BNC does not propagate. Specifically, they observed that the rate of monomer consumption linearly decreased with increase in the amount of pre-catalyst when keeping the activator concentration constant. Specifically, assuming that the excess of pre-catalyst results in formation of BNC; if the BNC propagates at the same rate as normal active site, then the consumption rate will not change; since this is not the case, the BNC must be less active. The quantitative kinetic analysis developed in this paper is consistent with this conclusion, where the decrease in the observed consumption rate with increasing pre-catalyst concentration enables determination of the amount of the BNC. It is instructive to evaluate the ratio of the BNC concentration to the total amount of activator used, as this allows comparison across different systems. As shown in Table 3, the ratio of the concentration of BNC to the total cation concentration for the Sita catalyst is 10% and 25% at ½ activator and ¼ activator condition, respectively. These values are significantly higher than their counterparts for our $Zr[tBu\text{-}ON^{THF}O]Bn_2/B(C_6F_5)_3$ system given in Table 2 with 3% and 4% at ½ activator and ¼ activator condition, respectively. Finally, the Ligand Transfer Model shows that the concentration of BNC is not a linear function of the excess amount of pre-

catalyst, where with addition of more pre-catalyst the decrease in consumption rate becomes less significant.

5.5 Conclusions

A comprehensive kinetic study of the Zr[tBu-ON^{THF}O]Bn_2/$B(C_6F_5)_3$ system under sub-stoichiometric activator conditions has been completed, where decreasing the amount of activator causes (i) the rate of monomer consumption to decrease and (ii) the MWD to narrow and shift to lower values. Using quantitative kinetic analysis a Ligand Transfer Model was developed that is capable of describing the diverse data set. This mechanism includes the formation of the binuclear complex (BNC) consisting of the neutral catalytic species and an active site connected via degenerative transfer of benzyl ligand. Bridging via methyl and chloral ligands have been previously postulated[12,15], but not bridging via a benzyl ligand, which has been argued to not be feasible.[15] The BNC can be formed when a pre-catalyst species react with an active catalyst thereby providing a second channel for activation. *The most significant finding of this study was that the BNC is only formed by the normally inserted active sites and not by misinserted sites, resulting in narrowing of the MWD of the polymer as compared to the case of stoichiometric activator where the BNC is not formed*. Although under the conditions studied the BNC concentration is small compared to the concentration of active sites due to the small equilibrium constant of BNC formation, it is shown to play an important role in initiation which is faster via the BNC. This results in the experimentally observed lower and narrower MWD of the resulting polymer.

REFERENCES

(1) (a) Chen, E. Y-X.; Marks, T. J. *Chem. Rev.* 2000, *100*, 1391-1434. (b) Li, H.; Marks, T. J. *Proc. Natl. Acad. Sci. USA* 2006, *103*, 15295-15302.

(2) Manz, T. A.; Phomphrai, K.; Medvedev, G. A.; Krishnamurthy, B. B.; Sharma, S.; Haq, J.; Novstrup, K. A.; Thomson, K. T.; Delgass, W. N.; Caruthers, J. M.; Abu-Omar, M. M. *J. Am. Chem. Soc.*, 2007, *129*, 3776-3777.

(3) (a) Krauledat, H.; Brintzinger, H. H. *Angew. Chem. Int. Ed*., 1990, *29*, 1412-1413. (b) Piers, W. E.; Bercaw, J. E. *J. Am. Chem. Soc.* 1990, *112*, 9406-9707. (c) Coates, G. W.; Waymouth, R. M. *J. Am. Chem. Soc.*, 1991, *113*, 6270-6271.

(4) Brintzinger, H. H.; Fischer, D.; Mullhaupt, R.; Rieger, B.; Waymouth, R.M. *Angew. Chem. Intl. Ed. Engl*., 1995, *34*, 1143-1170.

(5) Chen, Y-X.; Metz, M.V.; Li, L.; Stern, C.L.; Marks, T.J. *J. Am. Chem. Soc*., 1998, *120*, 6287-6305.

(6) (a) Jia, L.; Yang, X.; Stern, C.L.; Marks, T.J. *Organometallics*, 1997, *16*, 842-857. (b) Yang, X.; Stern, C.L.; Marks, T.J. *Organometallics*, 1991, *10*, 840-842.

(7) (a) Switzer, J. M.; Travia, N. E.; Steelman, D. K.; Medvedev, G. A.; Thomson, K. T.; Delgass, W. N.; Abu-Omar, M. M.; Caruthers, J. M. *Macromolecules*, 2012, *45*, 4978-4988. (b) Steelman, D.K.; Xiong, S.; Pletcher, P.D.; Smith, E.; Switzer, J.M.; Medvedev, G.A.; Delgass, W.N.; Caruthers, J.M.; Abu-Omar, M.M. *J. Am. Chem. Soc.*, 2013, *135*, 6280-6288. (c) Liu, Z. X.; Somsook, E.; White, C. B.; Rosaaen, K. A.; Landis, C. R. *J. Am. Chem. Soc.* **2001,** *123*, 11193-11207.

(8) Greszata, D.; Mardare, D.; Matyjasewki, K. *Macromolecules*, 1994, *27*, 638-644.

(9) (a) Muller, A.H.E.; Zhuang, R.; Yan, D.; Litvinenko, G. *Macromolecules*, 1995, *28*, 4326-4333. (b) Muller, A.H.E.; Yan, D.; Litvinenko, G.; Zhuang, R.; Dong, H. *Macromolecules*, 1995, *28*, 7335-7338.

(10) Hawker, C. J. *Acct. Chem. Res.* 1997, *30*, 373-382.

(11) (a) Chong, Y.K.; Le, T. P. T.; Moad, G.; Rizzardo, E.; Thang, S. H. *Macromolecules*, 1999, *32*, 2071-2074. (b) Fukuda, T.; Moad, G.; Rizzardo, E. Thang, S. H. *Macromolecules*, 2001, *34*, 402-408.

(12) (a) Zhang, Y.; Keaton, R.J.; Sita, L.R. *J. Am. Chem. Soc.*, 2003, *125*, 9062-9069. (b) Zhang, Y.; Sita, L.R. *J. Am. Chem. Soc.* 2004, *126*, 7776-7777. (c) Kissounko, D.A.; Zhang, Y.; Harney, M.B.; Sita, L.R. *Adv. Syn. Catal*., 2005, *347*, 426-432.

(13) (a) Chen, M-C.; Roberts, J.A.S.; Marks, T.J. *J. Am. Chem. Soc*., 2004, *126*, 4605-4625. (b) Neng, G.; Stern, C.L.; Marks, T.J. *J. Am. Chem. Soc.* 2008, *130*, 2246-2261. (c) Rodriguez, B.A.; Delferro, M.; Marks, T.J. *Organometallics*, 2008, *27*, 2166-2168.

(14) Chen, Y.-X.; Marks, T.J. *Organometallics*, 1997, *16*, 3649-3657.

(15) Bochmann, M.; Lancaster, S.J. *Angew. Chem. Intl. Ed. Engl.*, 1994, *33*, 1634-1637.

(16) Groysman, S.; Goldberg, I, Kol, M. *Organometallics*, 2003, *22*, 3013-3015.

(17) Groysman, S.; Goldberg, I.; Kol, M.; Genizi, E; Goldschmidt, Z. *Inorg. Chim. Act.*, 2003, *345*, 137-144.

(18) Younkin, T. R.; Connor, E. F.; Henderson, J. I.; Friedrich, S. K.; Grubbs, R.H. *Science*, 2000. *287*, 460-462.

(19) Tshuva, E. Y.; Gendeziuk, N.; Kol, M. *Tetrahedron Letters*, 2001, 42, 6405-6407.

(20) Cao, J.; Goyal, A.; Novstrup, K.; Midkiff, S.; Caruthers, J. *International Journal of Parallel Programming*, 2009, *37*, 127.

(21) Gillespie, D. T. Journal of Computational Physics 1976, *22*, 403.

(22) Nelder, J.; Mead, R. *Computer Journal*, 1965, *7*, 308.

CHAPTER 6. SIMULTANEOUS POLYMERIZATION AND OLIGOMERIZATION OF 1-HEXENE BY A GROUP IV BIS-PHENOLATE AMINE COMPLEX

In this paper, I performed GPC measurements of polymer samples and kinetics analysis of the catalyst system. Thilina N. Gunasekara and D. Keith Steelman did the experimental part including catalyst synthesis, 1-hexene polymerization, and NMR measurements, etc.

6.1 Experimental Results

We've done a series of experiments using Zr-Net2 catalyst varying the concentration of each reactant: catalyst, activator and monomer. Experiment data were collected under different monomer to catalyst ration or activator to monomer ratio. For every condition in Table 1, a minimal set of two measurements were done: time evolution of monomer consumption is monitored through the reaction, MWD was measured when the reaction is quenched in the end. Representative examples of the MWD at full monomer conversion are shown in Figure 1A. The active site count was determined by quenching with d_4-methanol and performing ^2H NMR measurement of the concentration of chains with deuterated end groups using established methods.[7] The sites that have undergone 1,2-insertion are defined as primary sites, and the sites that have undergone 2,1-misinsertion are defined as secondary sites. In addition, for condition of type **1** in Table 1, the

experiments were controlled with various pre-mix time of catalyst and activator (add detail description) before adding monomer to start polymerization.

Table 6-1. Initial Conditions of NMR scale experiments. "C" – pre-catalyst, "A" – activator, "M" – monomer.

Condition		$[C]_0$ (mM)	$[A]_0/[C]_0$	$[M]_0$ (M)	$[M]_0/[C]_0$
1 (reference)		9.0	1.1	4.5	500
	2	9.0	0.5	4.5	500
I	**3**	9.0	0.25	4.5	500
	4	9.0	2	4.5	500
	5	9.0	1.1	2.25	250
II	**6**	9.0	1.1	0.9	100
	7	9.0	1.1	0.45	50
	8	18	1.1	4.5	250
III	**9**	4.5	1.1	4.5	1000
	10	2.25	1.1	4.5	2000

The most distinctive and unexpected feature of this catalyst is the appearance of two well separated peaks on the MWD observed under some conditions where the low MW peak is oligomeric containing chains of the length under 10^3 Daltons and the high MW peak is above 10^5 Daltons. The totality of observed features can be summarized as follows.

1. Two distinct peaks in the MWD are observed when i) the pre-mix time t_p of catalyst and activator is larger than 5 minutes under standard conditions (see experimental section) and ii) activator to catalyst ratio is at least stoichiometric, i.e. greater than one (1.1:1). The representative example of the MWD is shown in Figure 1a (black). The effect of pre-mix time on the polymer fraction is illustrated in Figure 1b. It appears that the polymer weight fraction initially increases rapidly with pre-mix

time and then saturates. Interestingly, whereas the wtp changes with pre-mix time, the MWD does not (Figure 2). More details on the effect of the activation conditions are provided and discussed below.

2. If activator to catalyst ratio is sub-stoichiometric or the pre-mix time is shorter than 5 minutes, only the oligomeric peak is observed (Figure 1 red).

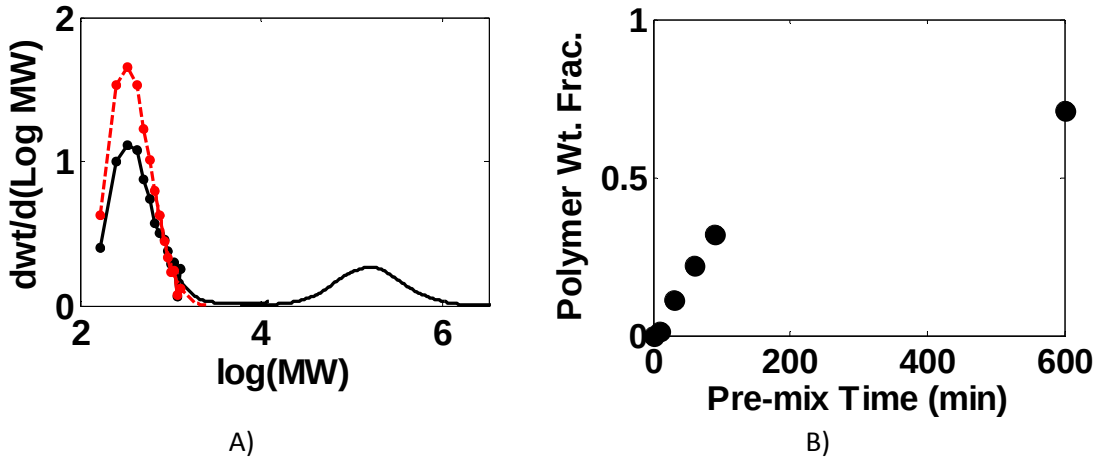

Figure 6-1. A) Signiture MWD of samples polymerized by Zr-Net2 catalyst: blace – Case 1, red – Case 2. B) Effect of the pre-mix time on polymer weight fraction wt_p.

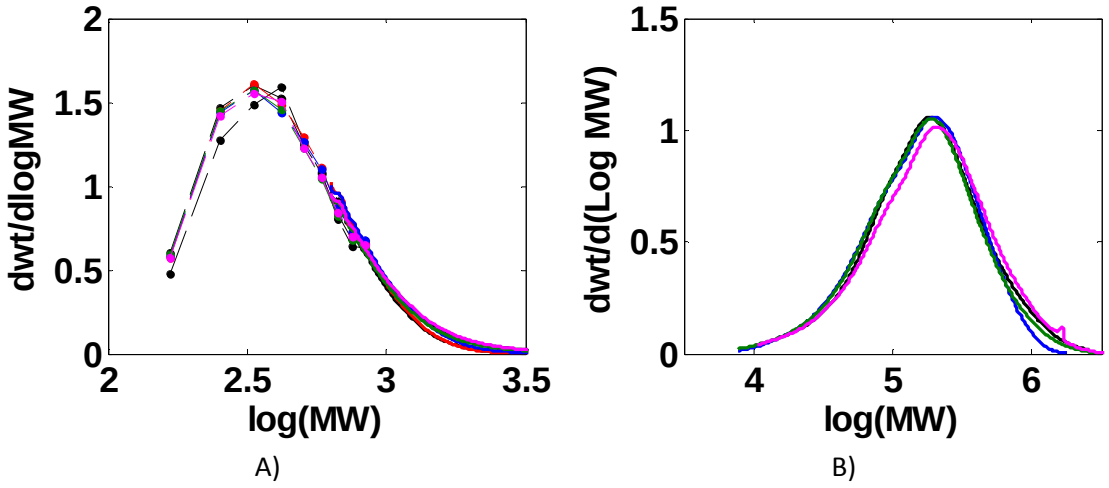

Figure 6-2. MWD of products from case 1 with different pre-mix time: 6 (red), 30 (blue), 60 (green), 90 (magenta) min. MWD of products from case 4: black (2eq. of activator). A) MWD of oligomers fraction, B) MWD of polymer fraction.

3. Conditions that affect wt_p do not change the MWDs of both the oligomer fraction and the polymer fraction.
4. The polymer produced by Zr-Net2 catalyst differs dramatically from the standard linear poly(1-hexene). This is evidenced by two experimental observations: i) the ^{13}C NMR shown in Figure X demonstrates presents of quaternary carbons and ii) the value of dn/dc obtained from the GPC measurements is 0.025 which is 3 times smaller than that of the linear poly(1-hexene) (0.076). Note that the calculation of dn/dc of the polymer required knowing the mass of the polymer. The polymer fraction was separated from the reaction product using the procedure described in the experimental section.
5. Varying initial catalyst concentration $[C]_0$ has no discernable effect on polymer weight fraction wt_p as illustrated in Figure 2a.
6. wt_p does not change with conversion in the course of the reaction (Figure 3b). This has been validated for conversions as low as 15% and as high as 99%.

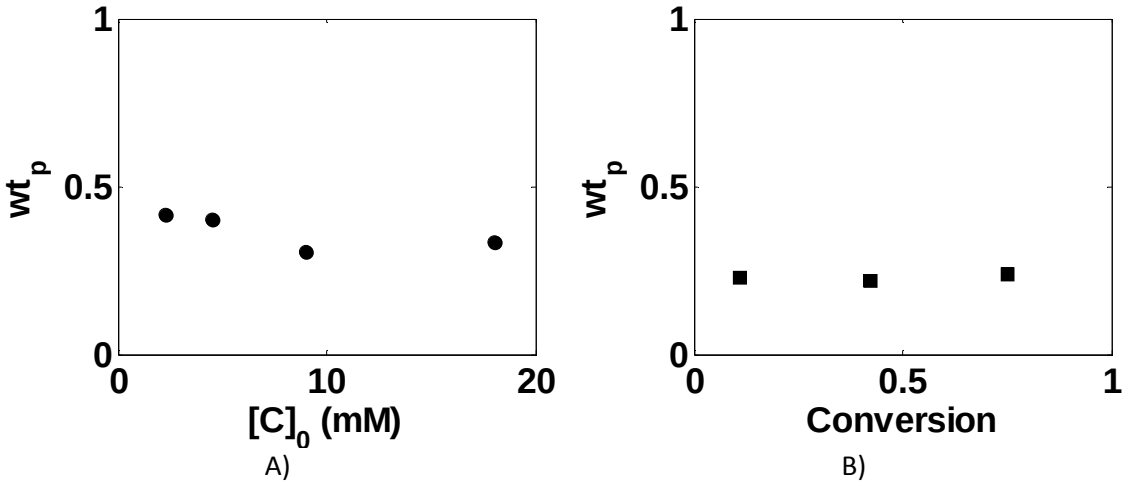

Figure 6-3. A) Effect of conversion on wt_p: case 1, t_p = 65 min. B) Effect of $[C]_0$ on wt_p: case 1, 8 – 10, t_p = 60 min.

7. The MWD of polymer fraction reaches its final shape at as early as at 20% conversion and the peak position is at least an order of magnitude higher than that for “living” poly(1-hexene) under the same catalyst to monomer ratio.

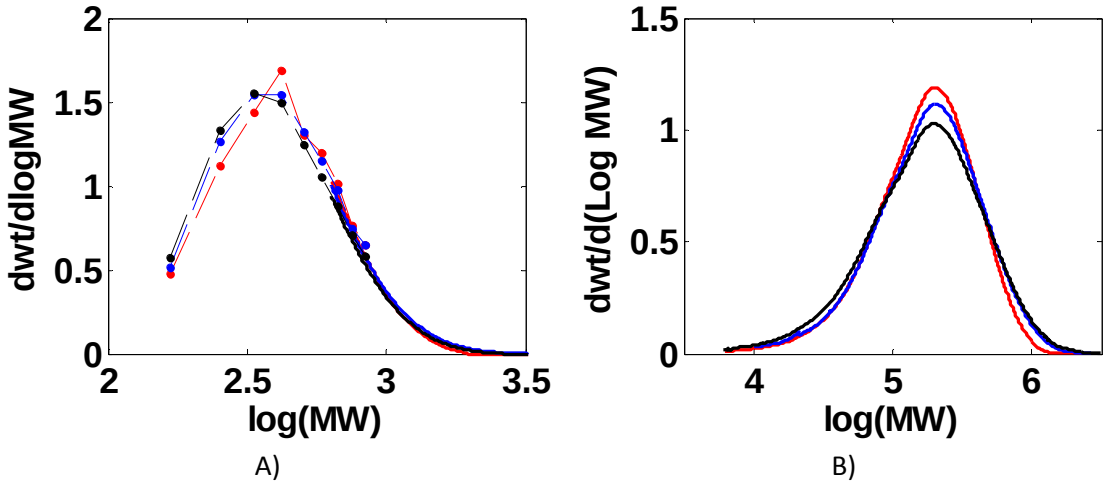

Figure 6-4. MWD of products from case 1 at different conversion: 24% (red), 59% (blue), 74% (black). A) MWD of oligomers fraction, B) MWD of polymer fraction.

8. MWD does not change after all the monomer is consumed, even when the reaction mixture is allowed to “stew” overnight.
9. The monomer consumption rate is 1st order in catalyst (Figure 5A) and monomer (Figure 5C). It does not change with pre-mix time (Figure 5B) even though the wt_p is affected. Of particular significance is the observation that in case of mixing time zero, when no polymer is produced and in case of mixing time of 1 hrs when 30% of the product is polymer, the rate of consumption is the same as illustrated in Figure 5B. The dependence of consumption rate on activator to catalyst ratio is shown in Figure 5D. This rate is proportional to the ratio under sub-stoichiometric conditions and is constant in case of excess activator.

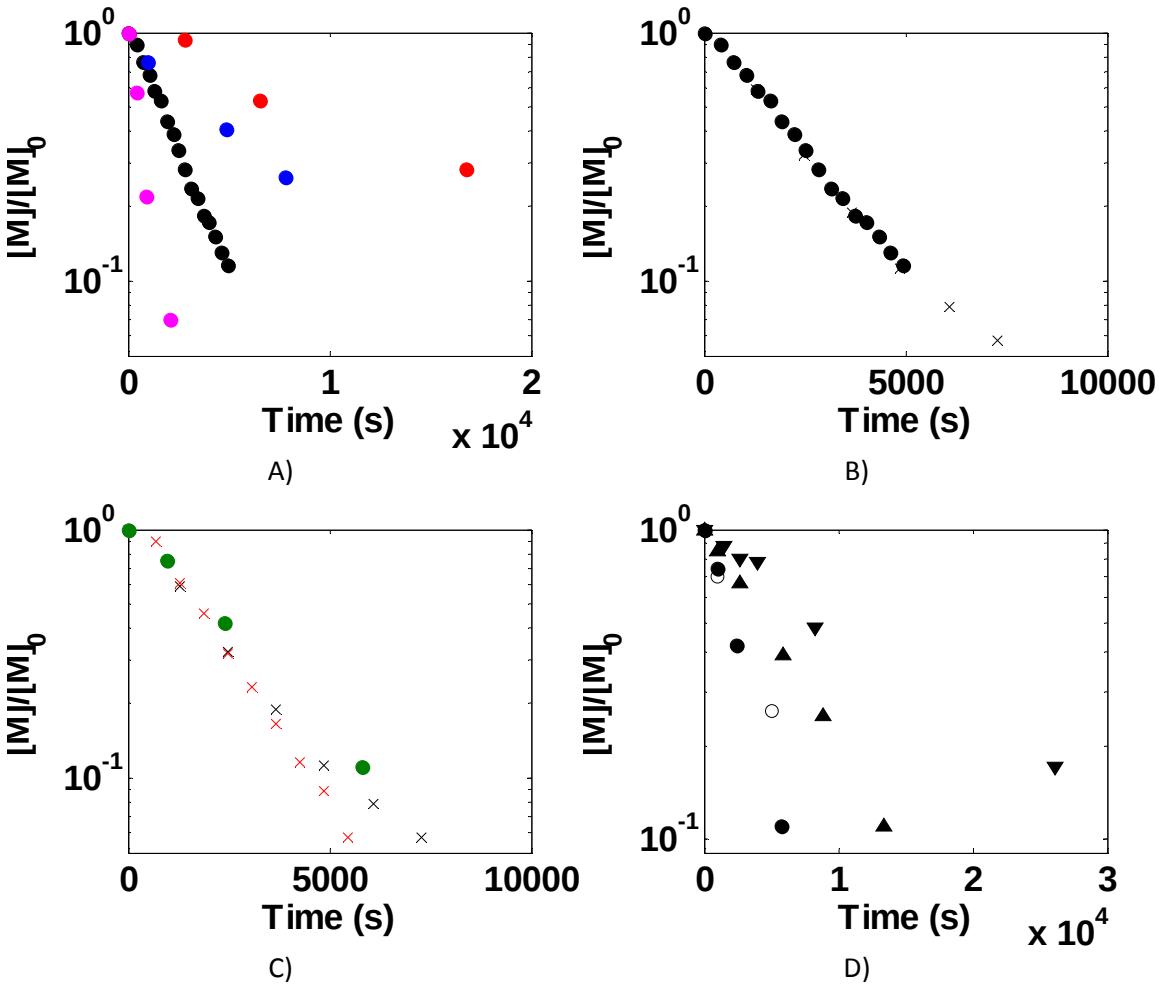

Figure 6-5. Monomer consumptions under different conditions. A) Variation on $[C]_0$: 1 black, 8 magenta, 9 blue, 10 red. B) Variation on t_p (wt_p): 1hrs (30%) circles, 0 (0) crosses. C) Variation on $[M]_0$: 1 black, 6 green, 7 red. D) Varition on $[A]_0$: 1 closed circles, 2 upper triangles, 3 lower triangles, 4 open circles.

10. The MWD of Oligomer is non-Flory-Schulz when $[M]_0$ is low or conversion is low.

It becomes Flory-Schulz at high conversions and higher $[M]_0$ (Figure 6).

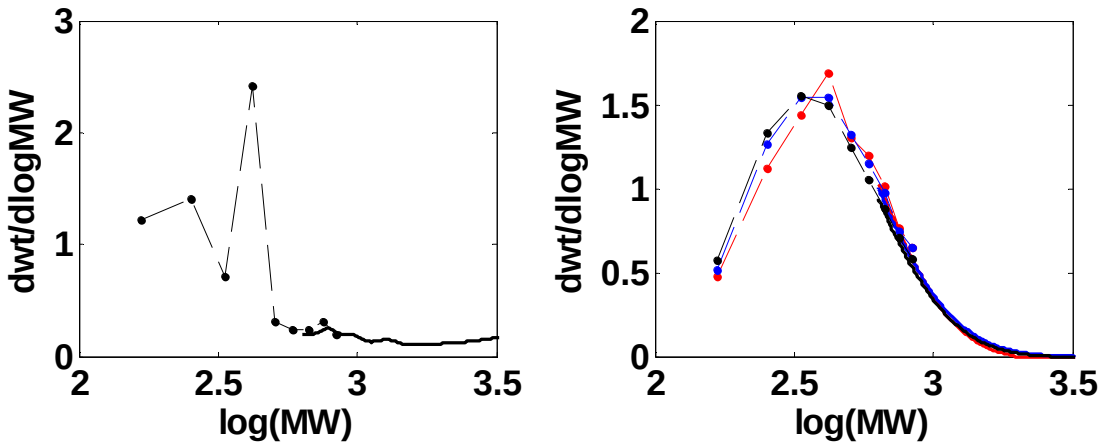

Figure 6-6. MWD of oligomers. A) products at the end of the consumption in Case 6. B) Products in Case 1 at different conversion: 24% (red), 59% (blue), 74% (black).

11. Effect of temperature on pre-mixing.

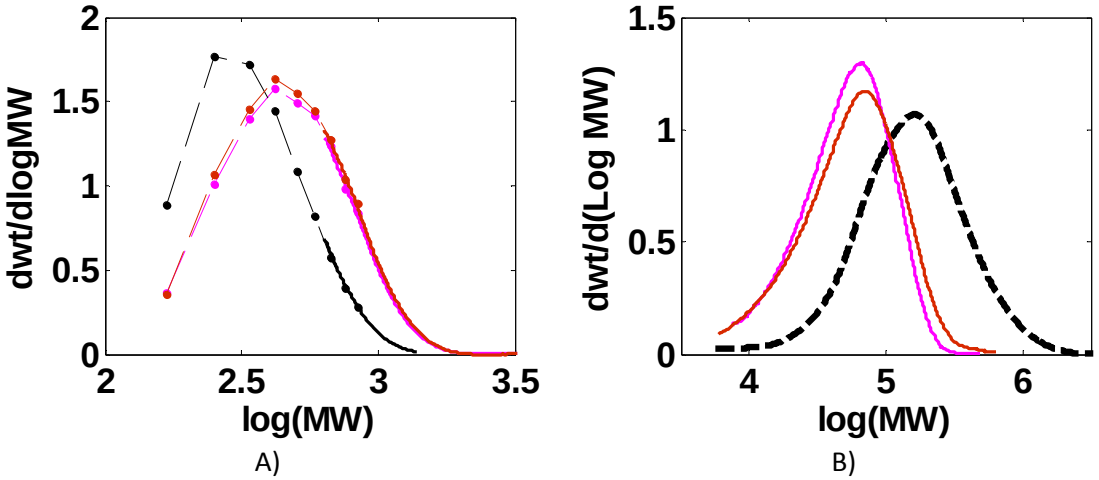

Figure 6-7. MWD of products from case 2 at different pre-mix temperature (tp = 3 hrs): 25C – black solid (95% conversion), 45C – red (28%) and magenta (38%). A) MWD of oligomers fraction, B) MWD of polymer fraction (black dashed is a reference obtained from case 1 at 25C pre-mix temperature).

6.2 Kinetic Analysis.

The acceptable mechanism has to be able to describe all the 1-10 features outlined in the previous section. Clearly a standard set of reaction steps present in single-site polymerization will not result in a bimodal MWD. A natural hypothesis is that at least two different active sites are involved in the reaction. Then the reasonable first step is to focus on the conditions where only single oligomeric peak is produced. After the rate constants for oligomeric site are determined, the polymer producing site can be added and its kinetic behavior analyzed.

6.2.1 Oligomerization

The natural point of departure for a detailed kinetic model is the set of elementary reactions that was previously developed to describe the single-site polymerization reaction that products only has a single MWD peak .[7a] The set consists of initiation, propagation, chain transfer, misinsertion and recovery as shown in Scheme 1, where the active catalyst is denoted as C*, primary active site as O_i, secondary active site as O'_i, vinyls formed after chain transfer as V_i and the index i indicates the length of the polymer chain. In what follows this mechanism is referred to as Base Model. The Base Model predicts that when there is a single oligomer peak formed under certain conditions. Because the chain transfer is so fast that the products are oligomers, MWD is controlled primarily by k_{ctr} and less affected by misinsertion and recovery. Hence although the ratio of k_{mis}/k_{rec} is tightly fixed by the amount of primary site and secondary site, the magnitude of the rate constants cannot be robustly determined.

$$O_0 + M \xrightarrow{k_i} O_1$$
$$O_n + M \xrightarrow{k_p} O_{n+1}$$
$$O_n \xrightarrow{k_{ctr}} V_n + O_0$$
$$O_n + M \xrightarrow{k_{mis}} O'_{n+1}$$
$$O'_n + M \xrightarrow{k_{rec}} O_{n+1}$$

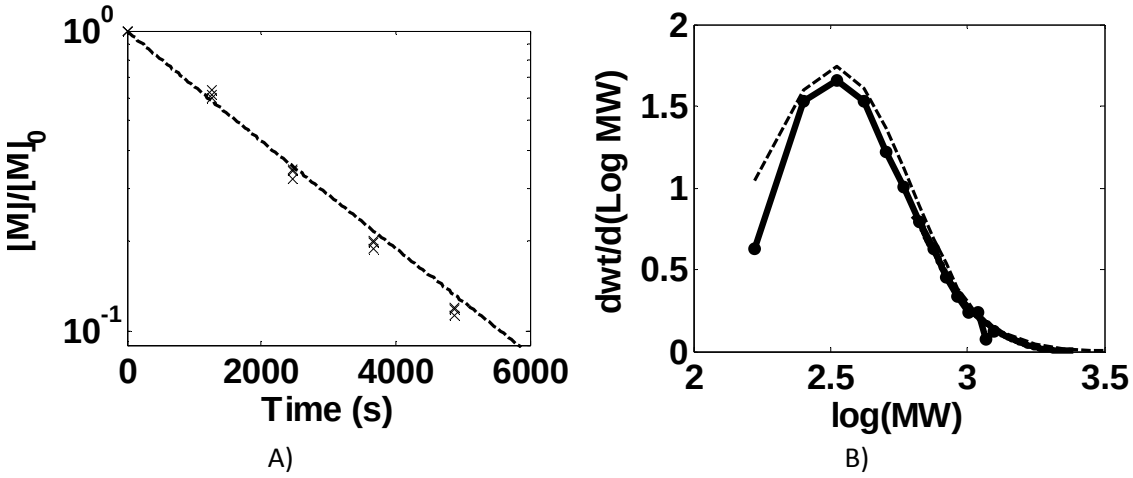

Figure 6-8. Model results of the oligomer formation. (vinyls and active sites (90% of [c]0) to be added)

Table 6-2. Rate constants of the oligomeric site.

ki (M^{-1} s^{-1})	**kp (M^{-1} s^{-1})**	**kctr (s^{-1})**	**k_{mis}/k_{rec}**	**k_{mis} (M^{-1} s^{-1})**
0.07	0.07	0.12	1	Cannot be determined

6.2.2 Polymer Formation

There are two hypotheses about the polymer producing site that can be readily dismissed. I) if the polymer site is similar to oligomeric site such that it has the same propagation rate but slower rate of chain transfer. This would be consistent with Feature 9 (Figure 5b) where the rate of consumption was independent on whether the polymer was produced. However, such mechanism will result in the molecular weight of polymer

significantly lower than measured. This is because even if the chain transfer is absent, i.e., "living" polymerization case, the predicted MWD peak is still at least an order of magnitude lower than measured and the chain transfer can only make it lower. The "living" MW is evaluated as $[M]_0 / [C]_0 * conversion * m_w$, which is 42 k at full conversion under condition 1. At the same time the experimental M_w is 200 k (Figure 1a). The discrepancy is even larger at lower conversions where the experimental Mw is the same but the "living" Mw is lower proportionally to the conversion. II) If the polymer producing site is assumed to have a propagation rate that is significantly higher than that of the oligomer producing site, the polymer MW will be higher. However, under this assumption Feature 9 cannot possibly be fulfilled as the presence/absence of high propagation rate site must have an effect on overall consumption rate.

With the two simple possibilities ruled out we are forced to turn to more complex scenarios. The observation that the structure of polymer product differs from the standard linear poly(1-hexene) and particularly the presence of quaternary carbons suggest that perhaps the polymer is at least partially built from oligomers present in the reaction mixture rather than monomers. The oligomers exist in two forms: the free vinyl terminated species which resulted from chain transfer and the currently growing oligomers attached to the oligomer producing site. Then two distinct mechanisms are possible: i) the free vinyl terminated oligomers are inserted in the polymer producing site; i.e., macromonomer insertion mechanism that has been reported in the literature for a number of systems[ref]; ii) the growing oligomers are incorporated into the polymer producing site as a result of reaction between oligomer producing site and polymer producing site.

The most straightforward way to distinguish between these two mechanisms would be to introduce extra vinyl terminated oligomers into the reaction. If free vinyls are inert, they will not affect the polymer products, on the other hand if they can be inserted the amount of polymer product will increase. Since there is a possibility of contaminating the reaction mixture if the separately purified vinyl species are used, it is preferable to avoid any such step. The following experimental protocol involving vinyl addition and control experiments shown in Table 2 was carried out. In the reference experiment 1, the 9 mM catalyst was prre-mixed for 3 hrs with 1.1 eq. activator, and the 4.5 mM catalyst was pre-mixed for 0 hrs with 1.1 eq. activator. Then two mixtures were combined and 0.9 M monomer was added. The mixing time of 3 hrs has been previously shown to result in approximately 45% polymer in condition 1 in Table 1. On the other hand, the 0 hr mixing time 4.5 mM catalyst is known to make zero polymer. Since no effect of extra catalyst on formation of polymer producing site has been detected previously, it is expected that 9 mM portion of the mixture will produce polymers and oligomers, and the 4.5 mM portion will produce only oligomers. The idea of experiment 2 is to have exactly the same amount of catalyst activator and monomer as in the experiment 1 and in addition significant amount of vinyl terminated oligomers at the beginning of the reaction. It is also important to make sure that the amount of oligomer producing sites and polymer producing sites in experiment 2 be the same as in experiment 1. This is achieved by conducting vinyl producing experiment prior to the experiment 2. The vinyl producing experiment is performed as follows: 4.5 mM catalyst with 0 hr pre-mix time with 1.1 eq. activator is mixed with 2.25 M monomer. This reaction is allowed to run for 3 hrs (90% conversion) resulting in 100% oligomers. The oligomer producing site does not deactivate as evidenced by the monomer

consumption curve remaining linear on log scale (Figure xx). To summarize, at the end of this step we have 4.5 mM oligomer producing sites and 2.25 M vinyl terminated oligomers denoted as portion (A). Separately from the vinyl producing step, 9 mM catalyst with 1.1 eq. activator is allowed to mix for 3 hrs, which is portion (B). Finally, at the beginning of experiment 2 (A) an (B) are combined and also 0.9M monomer is added. This sequence ensures the desired conditions where experiments 1 and 2 are equivalent except for the 2.25 M vinyls in the latter case.

The results of the experiments 1 and 2 are presented in Figure 11 and Table 3.

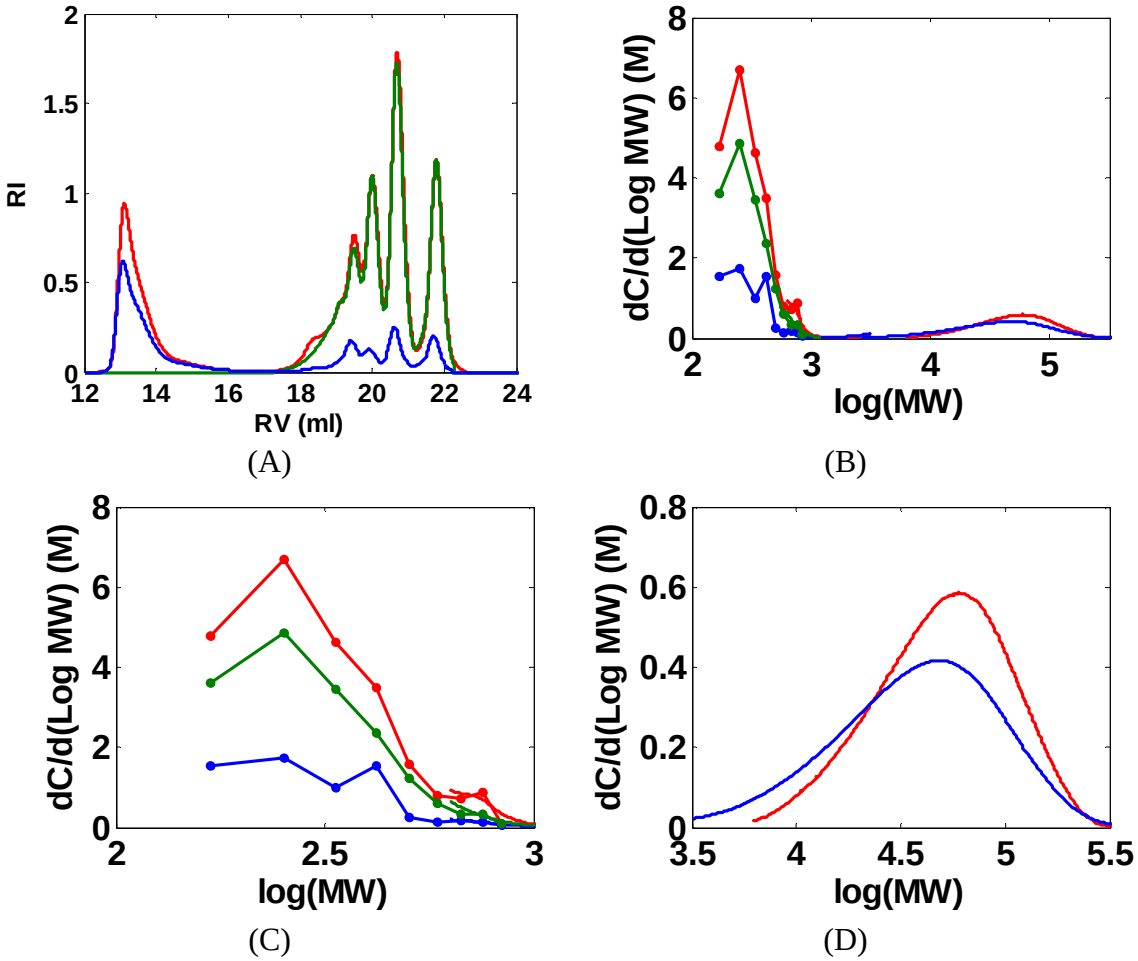

Figure 6-9. (A) RI vs. retention volume of samples measured by GPC. Green: $[C]_0$ = 4.5 mM, $[A]_0$ = 4.95 mM, pre-mix time = 0, $[M]_0$ = 2.25 M. Red: $[C]_0$ = 9 mM, $[A]_0$ = 9.9 mM, pre-mix time = 3 hrs, $[M]_0$ = 0.9 M was added to the final reaction mixture of green. Blue: $[C]_0$ = 9 mM, $[A]_0$ = 9.9 mM, pre-mix time = 3 hrs, $[M]_0$ = 0.9 M was added to $[C]_0$ = 4.5 mM, $[A]_0$ = 4.95 mM, pre-mix time = 0. (B) Full MWDs. (C) Oligomer MWDs. (D) Polymer MWDs.

Table 6-3. Product distribution of validation experiments.

	wt_p	Mass_Polymer (M)	Mass_Oligomer (M)
1 (red)	15%	0.47	2.68
1'(green)	0	0	2.25
2 (blue)	45%	0.41	0.49

The experimental result shows that the polymer mass barely increased even when large amount of vinyls was served in the system. (The model predicts a decreased amount

of oligomers compared to green and increased amount of polymers compared to blue at the end of the reaction) Hence we conclude that vinyls are not reactive species in the system.

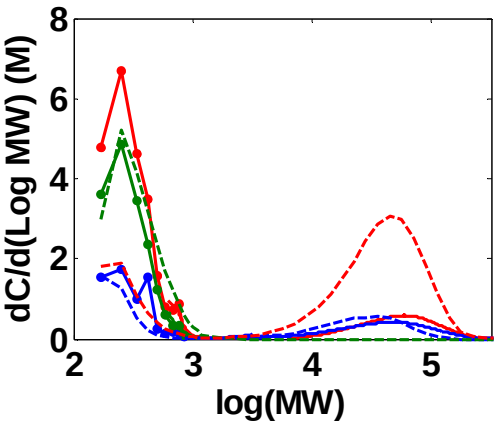

Figure 6-10. Predictions of macromonomer inserstion model (dashed lines).

Incorporation of Active Site Oligomer Model. After excluding the oligomer reinsertion model, we finally come up with this new model: polymer chain growth by incorporation of active site oligomer. So instead of react with a free vinyl, the polymeric site interacts directly with an oligomeric site to allow the oligomeric to transfer and inserted in the polymeric site. This model is capable to explain all the current observations.

$$P_n + O_m \xrightarrow{k_{incorp}} P_{n+m} + O_0$$

$$P_n \xrightarrow{k_{ctr}2} V_n + O_0$$

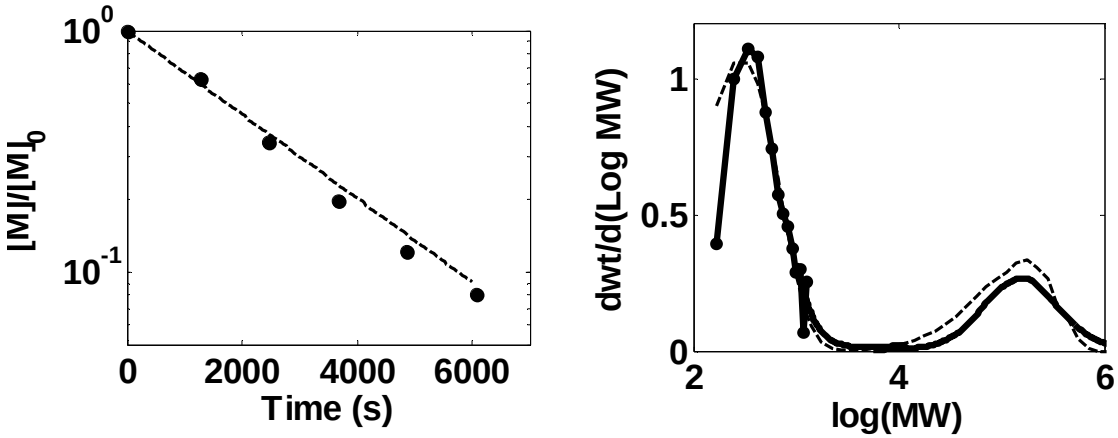

(A) (B)

Figure 6-11. Predictions of Active Site Oligomer Incorporation Model (dashed lines) of Condition 1. (A) Monomer consumption, (B) MWD. Additional rate constants: k_{incorp} = 100 M^{-1} s^{-1}, k_{ctr2} = 0.01 s^{-1}.

6.3 Conclusions

A comprehensive kinetic study of the Zr[tBu-$ON^{NEt2}O$]Bn_2/$B(C_6F_5)_3$ system has been completed, where both oligomers and polymer were produced simultaneously. Using quantitative kinetic analysis a Chain Growth by Incorporation of Active Site Oligomer Model was developed that was capable of describing the diverse data set. The mechanism for oligomerization includes initiation, normal propagation, misinsertion, recovery, and chain transfer, which is similar to that of the other group IV bis-phenolate amine catalysts. The mechanism of polymerization, on the other hand, occurs on a different type of active site, where the chain growth through incorporation of growing oligomer chains attached on normal oligomeric sites. The polymer produced in this way is short-chain branched as evidenced by ^{13}C 2D NMR. The chemistry nature of the polymer formation site and oligomer formation site is currently under investigation.

CHAPTER 7. ZWITTERIONIC RING-OPENING POLYMERIZATION: MODELS FOR KINETICS OF CYCLIC POLY(CAPROLACTONE) SYNTHESIS

In this paper, I performed kinetics analysis on the catalyst system. Hayley A. Brown and Young A. Chang did the experimental part including catalyst synthesis, caprolactone polymerization, etc.

7.1 Introduction

The properties of cyclic polymers differ significantly from their linear topological isomers.[1-3] Cyclic polymers cannot entangle or reptate in the same way as linear chains.[1, 3] The rheology,[4] conformations,[5] and properties[1] of high molecular weight cyclic polymers remains incompletely understood, largely as a consequence of the synthetic challenges in preparing these materials.[6-9] High molecular weight cyclic polymers are challenging to prepare by traditional chain coupling methods.[3, 10] Ring-expansion polymerization[9, 11, 12] and zwitterionic ring-opening polymerization (ZROP)[6, 8, 13-20] have been reported for the generation of high molecular weight cyclic polymers. The nucleophilic zwitterionic[21] ring-opening polymerization of lactide with the N-heterocyclic carbene 1,3-bis(2,4,6-(trimethylphenyl)imidazol-2-ylidene) (IMes) **1** generates cyclic poly(lactides) with

molecular weights $M_n \leq 30{,}000$ Da and molecular weight distributions between $1.14 < M_w/M_n < 1.31$, Scheme 1).[6, 14, 16, 19] In contrast, the zwitterionic ring-opening polymerization of ε-caprolactone with the more nucleophilic[22] carbenes **2-4** generates higher molecular weight cyclic poly(caprolactone)s (up to $M_n = 150{,}000$ Da) with broader polydispersities ($1.29 < M_w/M_n < 2.10$)[6, 17, 18] The ability to generate high molecular weight poly(caprolactones) is an enabling advance to investigate the properties of entangled cyclic polymers,[17] but the factors which control the molecular weights and molecular weight distributions in these zwitterionic polymerizations remain poorly understood.

Kinetics can shed important insights on the factors that control the relative rates of initiation, propagation and chain-transfer in polymerization reactions.[12, 20, 23-25] Mechanistic and kinetics studies of the ZROP of lactide (Scheme I) implicated a complex chain-growth polymerization mechanism[14, 16] characterized by: (1) slow and reversible initiation in the generation of the initial zwitterion, (2) fast propagation in the addition of lactide to the alkoxide terminus of a growing zwitterion, and (3) cyclization to liberate the cyclic poly(lactide). In addition to these steps, a depropagation step (liberating lactide) and a chain-scrambling step[24, 26] between growing zwitterions were invoked; the latter to rationalize the formation of odd-numbered lactide units in the resulting cyclic poly(lactides). These studies indicated that the molecular weights of the cyclic poly(lactides) ($M_n \leq 30{,}000$ Da) were limited by the relative rates of propagation and cyclization (Scheme I).

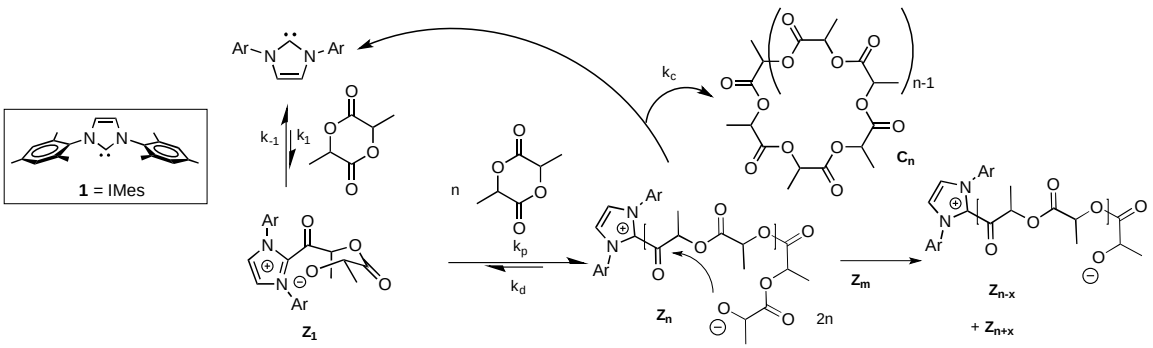

Scheme 7-1. Proposed mechanism for the NHC-mediated generation of cyclic poly(lactide)

Attempts to rationalize the higher molecular weights of the poly(caprolactones) obtained from carbenes **2-4** by the same mechanism as that for lactide were unsuccessful. As the rates, molecular weights and molecular weight distributions of cyclic polymers generated by zwitterionic ring-opening polymerization are sensitive to both the nature of the nucleophile and the monomer,[15, 17, 20, 27, 28] we initiated a detailed kinetics study of the ring-opening polymerization of caprolactone with carbenes **2-4**. Herein, we employ a modeling procedure that simultaneously accounts for time-dependence of the monomer concentration and the evolution of polymer molecular weight and molecular weight distribution to identify a minimal set of elementary reactions that are consistent with the experimental data.[25, 29] Previous studies on the kinetics of olefin polymerization have shown that incorporation of the molecular weights into the kinetics model can illuminate and distinguish rates and mechanisms of initiation, propagation, misinsertion, recovery, and chain-transfer.[25, 29]

7.2 Results and Discussion.

The homopolymerization of ε-caprolactone (CL) was carried out in toluene at 25°C with N-heterocyclic carbenes **2-4** under a variety of conditions. Kinetics runs analyzed by ^{1}H NMR spectroscopy were carried out in toluene-d_8; for batch runs, aliquots were removed at various time points, quenched with nitrophenol and analyzed by ^{1}H NMR to determine the monomer concentration and by gel-permeation chromatography (GPC) to determine the molecular weights and molecular weight distributions.

In the absence of alcohol initiators, the ring-opening polymerization of caprolactone occurs readily with carbenes **2-4**.[17, 27] In toluene, the rate of polymerization depends sensitively on the nature of the carbene: the tetramethyl-substituted carbene **2** is approximately 5 times faster than the isopropyl-substituted carbene **4** (Figure 1). The zwitterionic ring-opening of CL with N-alkyl-substituted carbenes **2-4** generates cyclic poly(caprolactones) with molecular weights that range from M_n = 40,000 to 150,000 Da.[17] The cyclic topology of the poly(CL) was evident from the lack of endgroups in the ^{1}H NMR spectra and lower intrinsic viscosities[1] of the cyclic samples compared to their linear counterparts (see Supporting info).

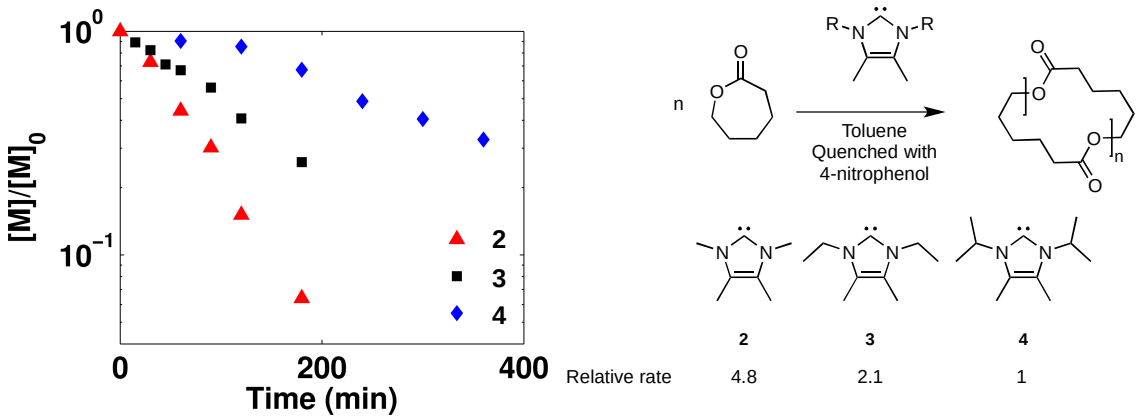

Figure 7-1. Relative rates of polymerization of CL with NHCs **2-4**. Initial conditions: $[M]_0$ = 1.0 M, $[NHC]_0$ = 0.01 M in toluene, 25°C. Monomer consumption determined by ^{1}H NMR spectroscopy.

The kinetics for the ring-opening polymerization of CL was investigated in toluene with carbene **2** at 25 °C under a variety of conditions (Table 1). The ZROP of lactones with NHCs is quite sensitive to trace impurities. The carbenes were recrystallized several times and the monomers were distilled twice over calcium hydride; nevertheless some variation in polymerization behavior was noted between different batches of carbene and CL monomer. The data reported in Table 1 were carried out with two different sets of carbenes and CL monomer: Data set I (runs 1-3abc, 4, 5) was collected within a single batch of monomer and carbene and Data set II (run 3d) was collected using a different batch of monomer and carbene. Monomer consumption was monitored by ^{1}H NMR spectroscopy in d_8-toluene for runs 1-3ab, 4, 5; runs 3c and 3d are batch reactions carried out in an inert-atmosphere glovebox. For these latter runs, aliquots were removed at different time points and analyzed both by ^{1}H NMR and GPC.

Table 7-1. Kinetics Runs for ROP of CL with NHC **2** at 25°C.

Run (Data set)	$[NHC]_0$ (M)	$[M]_0$ (M)	$[M]_0/[I]_0$	conv (t,min)	M_n, M_w/M_n
1 (I)	0.05	2.0	40	75% (25)	
2 (I)	0.01	2.0	200	75% (72)	
3a (I)	0.01	1.0	100	76% (94)	
3b (I)	0.01	1.0	100	76% (110)	
3c (I)	0.01	1.0	100	64% (60)	77K, 2.60
3d (II)	0.01	1.0	100	76% (60)	77K, 1.65
4 (I)	0.01	0.5	50	75% (216)	
5 (I)	0.006	0.3	50	76%(465)	

For the kinetics modeling, we utilized Data set I to evaluate several different models to determine the minimum set of elementary reactions that are consistent with the experimental data. Plotted in Figure 2a is the monomer consumption kinetics and shown in Figure 2b are the GPC traces at different time points for run 3c.

As seen in Figure 2a, the disappearance of monomer does not exhibit a simple exponential decay. A noticeable induction period[30] was observed for the polymerization of CL in d_8-toluene; this is especially evident for run 5. The rate of monomer consumption shows a clear dependence on the initial monomer concentration $[M]_0$ at a fixed initiator concentration (runs 2, 3a, 4).

The molecular weights increase with increasing conversion. Moreover, the molecular weights (M_w) at both low (24%) and high (98%) monomer conversion are significantly higher than the value predicted from $[M]_0/[I]_0$. The molecular weight distributions also increase with increasing conversion; polydispersities range from M_w/M_n = 1.2-2.0 up to approximately 90% conversion. Closer inspection of Figure 2 reveals that even at modest conversions ($[M]/[M]_0$ = 0.3) the molecular weight distributions reveal a

tailing to high molecular weights, suggesting that a considerable fraction of high molecular weight polymers are formed even at early times.

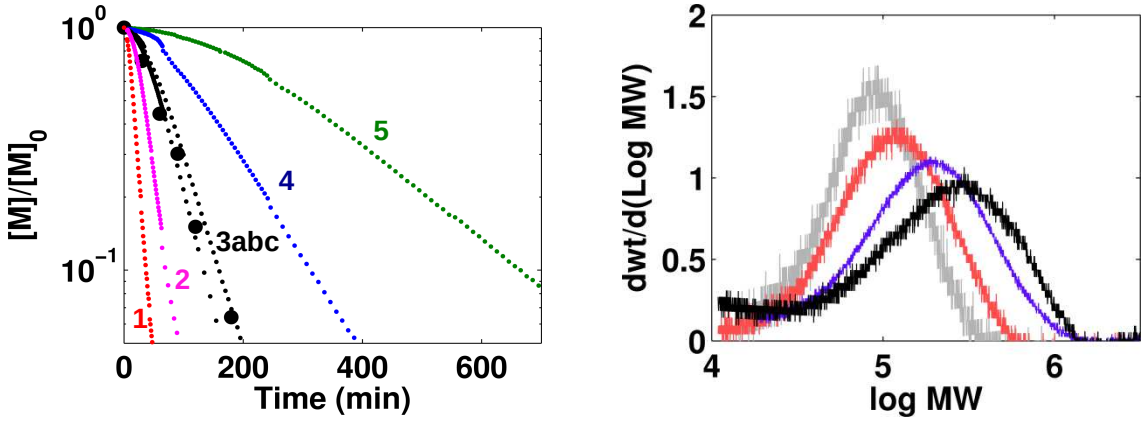

Figure 7-2. Results for Data set I. (a) Monomer consumption versus time measured by ^{1}H NMR: red (run 1), pink (run 2), black (runs 3abc), blue (run 4), green (run 5). (b) MWDs for aliquots of run **3c** in Table 1. Gray 27% (30 min), red 56% (60 min), purple 70% (90 min), and black 94% (180 min).

The observed increase in molecular weights with increasing conversion is suggestive of a chain-growth mechanism. The observed induction periods and the observation that the molecular weights are higher than that predicted from the ratio of $[M]_0/[I]_0$ suggest that the initiation step is significantly (at least two orders of magnitude) slower than propagation, as previously suggested for the ZROP of lactide.[16]

7.3 Kinetics Models.

To model the kinetics of the zwitterionic polymerization of CL with carbene **2**, we consider several models to identify the steps responsible for the rate of enchainment, the evolution of molecular weight and molecular weight distribution. The concentrations of all

the species as a function of time were calculated using the Dynamic Monte Carlo (DMC) method[31, 32] and the rate constants for each step were optimized simultaneously to fit the monomer concentration, the molecular weights and the molecular weight distributions using the Nelder-Mead's (simplex) optimization method.[33] The detailed description of the custom built DMC simulator and its implementation to the case of zwitterionic polymerization is given in the SI.

In the following, we present the results of several different models where we assume a minimal set of chemically reasonable reaction steps and then attempt to fit the data (Data Set I) by simultaneous optimization of the rate constants of each step. If a given model is unable to reproduce the experimental data, additional reactions steps were added until a satisfactory fit was found. Once a reasonable mechanism was found for Data set I, we then re-optimized all the rate constants based on the combined data sets I and II to test the robustness of the model.

Model I. In this model, we considered two elementary steps (Scheme 2): (i) a reversible initiation step involving nucleophilic addition of the carbene to the caprolactone to generate zwitterion Z_1, (associated with rate constants k_i and k_{-i}), and (ii) a propagation step involving nucleophilic attack of the zwitterionic alkoxide on the caprolactone monomer to extend the zwitterion (associated with rate constant k_p).

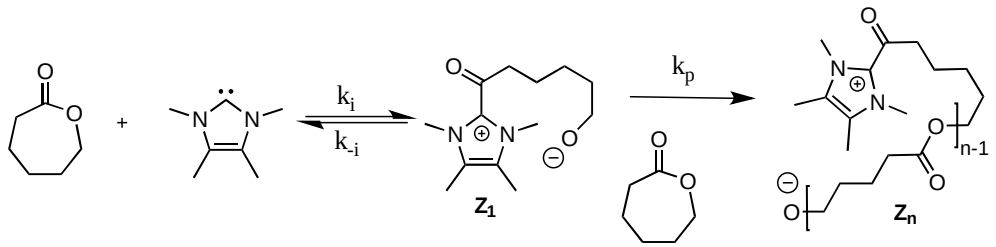

Scheme 7-2. Proposed zwitterionic mechanism for polymerization of CL with NHC **2**: Elementary steps for Model I.

The optimization using Model I was attempted to obtain the best fit to the time evolution of both monomer consumption and the molecular weight distributions. The optimized set of rate constants for this model were $k_i = 0.54\ M^{-1}\ min^{-1}$, $k_{-i} = 1.95\times10^3\ min^{-1}$ and $k_p = 39.6\ M^{-1}\ min^{-1}$. The experimental data (Data set I) and fits to the monomer concentration are shown in Figure 3a, and the molecular weight distributions are shown in Figure 3b. As seen in Figure 3a, this model provides a reasonable fit to the evolution of monomer concentration with time. In particular, this model reproduces the induction period for a slow and reversible initiation step that is coupled with a fast rate of propagation, and the dependence of the rate on both initial monomer and initiator concentrations. Nevertheless, this model does not capture the molecular weight distributions: the predicted polydispersities are significantly narrower than those observed experimentally. These results illustrate the importance of simultaneously fitting all the data to derive an acceptable model; using both criteria, Model I is clearly inadequate.

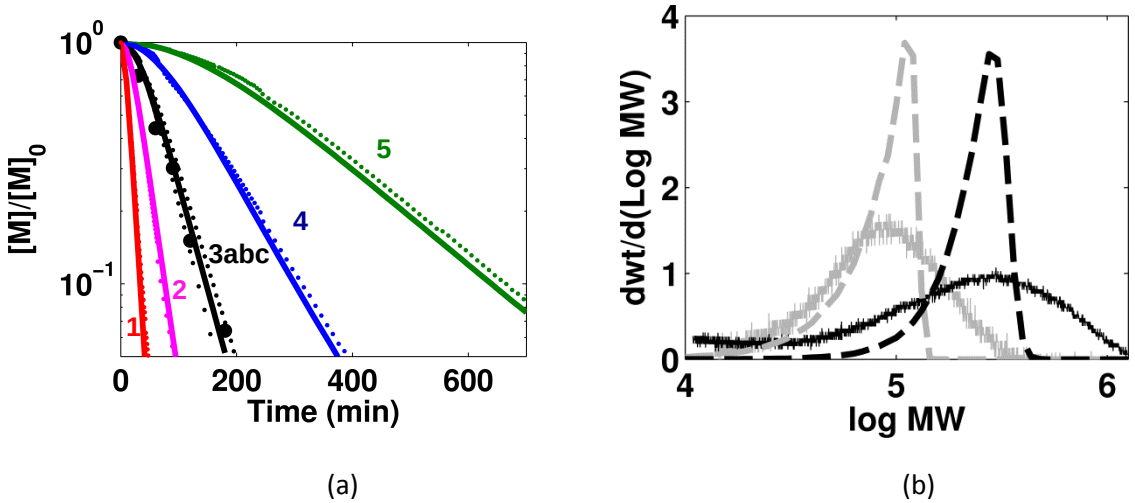

Figure 7-3. Model I: Simulation results based on Data set I. (a) Monomer consumption; conditions from Table 1: red 1, magenta 2, black 3a, b, black circles 3c, blue 4, green 5. Fits are solid lines. (b) MWDs for aliquots of run **3c**: gray 27% (30 min), black 94% (180 min). Data: solid, fits: dashed.

Model II. As Model I was incapable of capturing the molecular weight distributions, in Model II, we considered two additional steps. A cyclization step was added to Model I where the alkoxide of a growing zwitterion Z_n attacks the acylimidazolium terminus to liberate a cyclic chain and the carbene initiator (associated with rate constant k_c, eq (1)). This cyclization step (eq 1) would provide a mechanism for generating cyclic chains, as observed experimentally.[17, 18] As cyclization results in termination of growing zwitterion and liberation of the carbene initiator, addition of only this additional step would lead to a much lower rate than that observed experimentally. Thus, we considered additional steps (both associated with rate constant k_{ca}) where the carbene initiators could attack internal esters of either growing zwitterions Z_n (eq 2), or cyclized chains (eq 3). The latter reaction results in a growing zwitterion thereby effectively re-initiating the free carbene. The reaction steps given by eqs (1-3) in combination with those of Model I constitute Model II.

The nucleophilic attack of carbenes on the growing zwitterions (eq 2) would provide a mechanism for broadening the molecular weight distribution and the attack of the carbene on cyclized chains (eq 3) would provide a mechanism for generating higher molecular weight chains. The optimized rate constants for Model II are given in Table 3 and simulated monomer consumption curves and molecular weight distributions are shown in Figure 4.

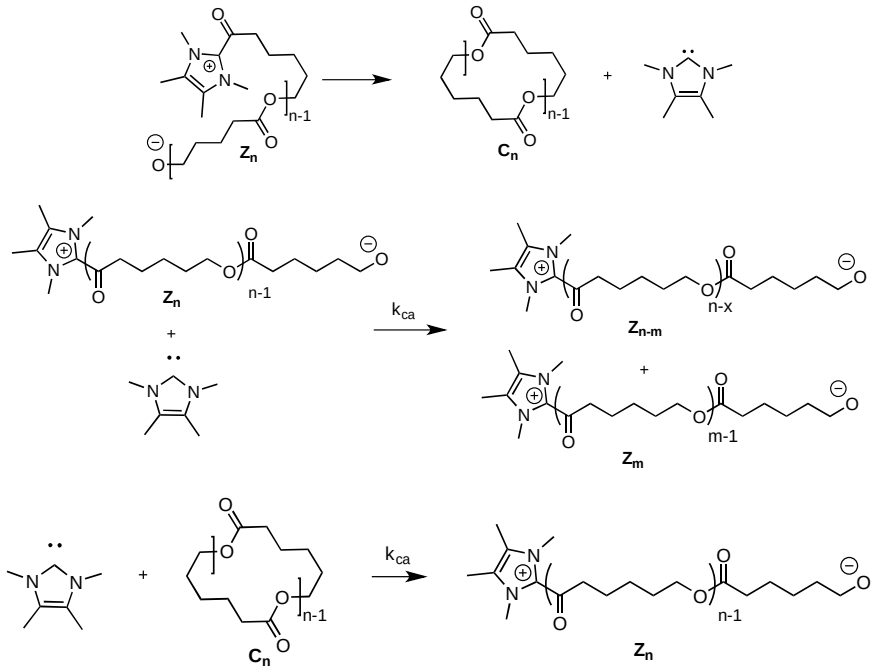

(1)

(2)

(3)

Table 7-2. Rate Constants for Model II.

k_i ($M^{-1}min^{-1}$)	k_{-i} (min^{-1})	k_p ($M^{-1}min^{-1}$)	k_c (min^{-1})	k_{ca} ($M^{-1}min^{-1}$)
0.061	2.0×10^3	63	0.076	0.0039

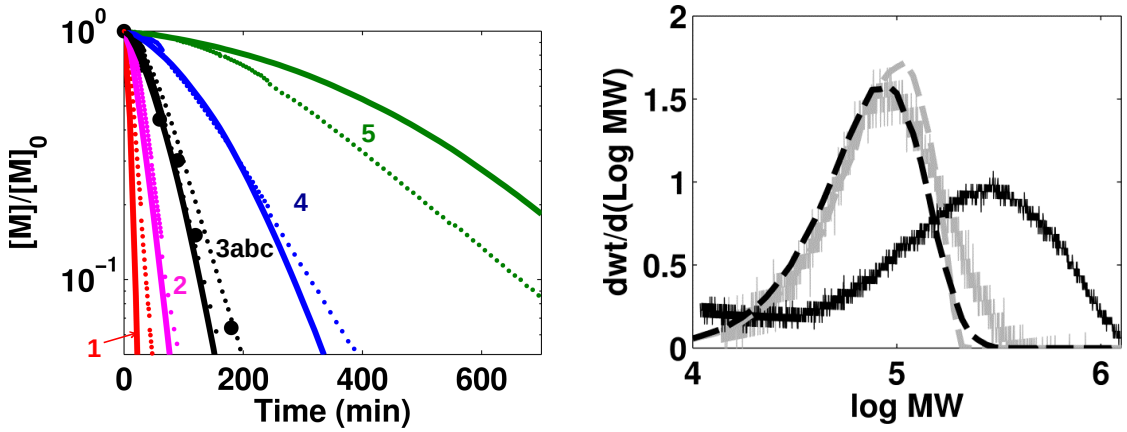

(a) (b)

Figure 7-4. Model II: Simulation results based on Data set I. (a) Monomer consumption; conditions from Table 1: red 1, magenta 2, black 3ab, black circles 3c, blue 4, and green 5. Fits are solid lines. (b) MWDs for aliquots from run **3c**: gray 27% (30 min), black 94% (180 min). Data: solid, fits: dashed.

Incorporating the additional steps of cyclization and carbene attack on growing or cyclized chains leads to a broadening of the molecular weight distribution (Figure 4b), as anticipated. However, Model II does not provide an adequate description of monomer consumption (Fig. 4a) and significantly underestimates the molecular weights at high conversion. While the attack of carbenes on cyclized chains (eq 3) provides a pathway for these chains to grow to higher molecular weight, this process is necessarily accompanied by attack of the carbene on growing zwitterions, resulting in shorter chains. As a result, the combined effect is insufficient to provide a satisfactory fit of the experimentally observed molecular weights.

Model III. In this model we considered, in addition to reversible initiation and propagation, an alternative mechanism for generating cyclic chains; an intramolecular cyclization or "backbiting" reaction[26] where the terminal alkoxide reacts with an internal ester of a

growing zwitterion Z_n to eliminate a cyclic polyester and lower molecular weight zwitterion (eq 4, rate constant k_{bb}). Back-biting reactions have been commonly invoked for many polyesterification reactions.[24, 26, 34, 35]

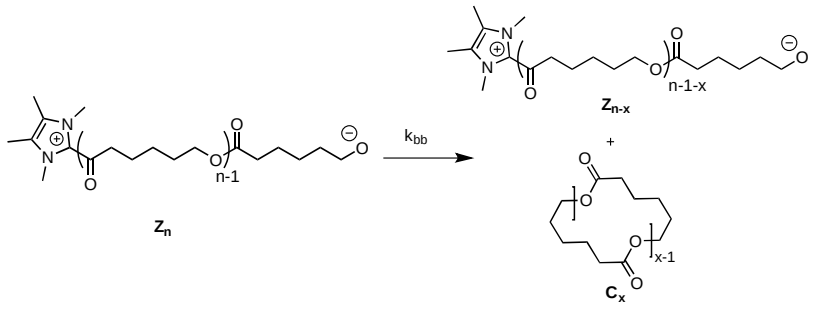

(4)

To accommodate the high molecular weights observed experimentally, we considered additional chain-transfer steps (eq 5, 6) where the terminal alkoxide of a growing zwitterion could react either with the internal esters of another zwitterion (a "chain-scrambling" step, eq 5)[26, 35] or the internal esters of a cyclized chain (eq 6). As the rate of this process would be expected to be independent of whether the internal ester exist on another zwitterion or on a cyclized chain, this step was characterized by a single rate constant $k_{tr(2)}$. [26]

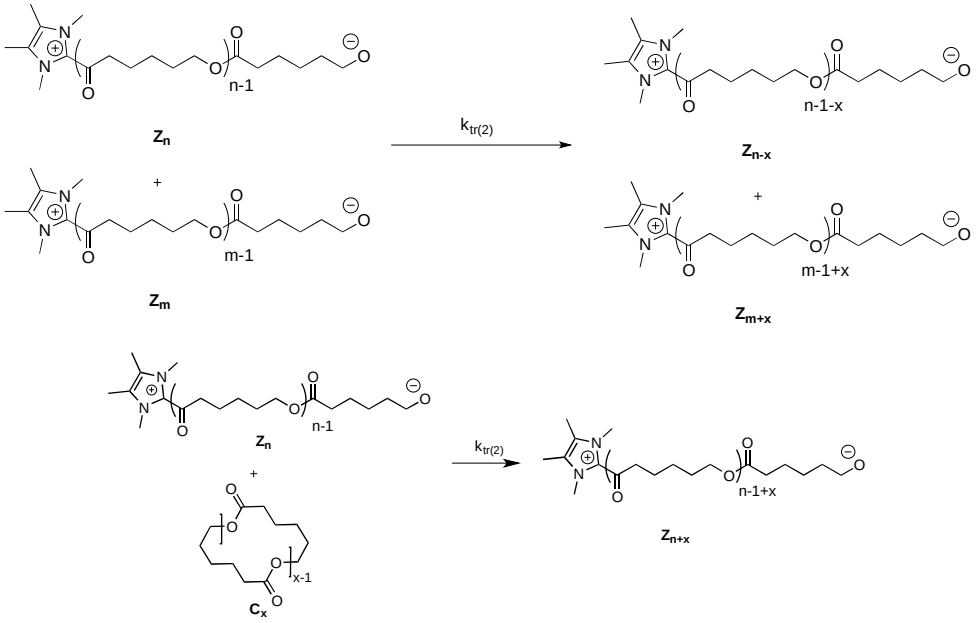

(5)

(6)

The backbiting cyclization step (eq 4) preserves the number of active zwitterions, in contrast to the cyclization mechanism of Model II. In addition, the intermolecular chain-transfer steps (eqs 5, 6) would be expected both to lead to broader molecular weight distributions (eq 5)[26] and the generation of high molecular weight chains (eq 6), once a significant fraction of cyclized chains are present.

Model III incorporates the following elementary steps: reversible initiation (k_i, k_{-i}), propagation (k_p), and intra- (k_{bb}) and intermolecular ($k_{tr(2)}$) chain-transfer reactions. The optimized rate constants for Model III are presented in Table 4 and the simulated monomer consumption curves and molecular weight distributions for Model III are shown in Figure 5.

Table 7-3. Optimized rate constants for Model III (Data set I).

k_i ($M^{-1}min^{-1}$)	k_{-i} (min^{-1})	k_p ($M^{-1}min^{-1}$)	k_{bb} (min^{-1})	$k_{tr(2)}$ ($M^{-1}min^{-1}$)
0.045	3.0×10^3	55	0.051	0.17

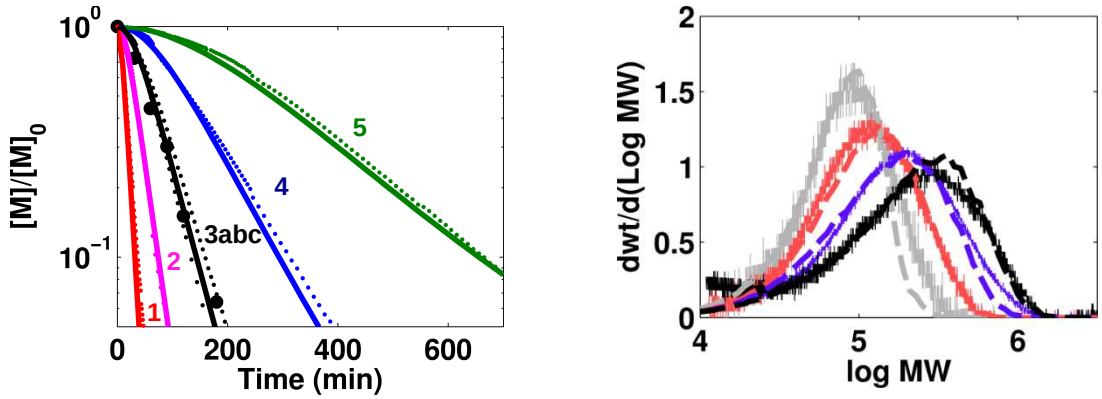

(a) (b)

Figure 7-5. Model III: Simulation results based on Data set I. (a) Monomer consumption; conditions from Table 1: red 1, magenta 2, black 3a, b, black circles 3d, blue 4, and green 5. Fits are solid lines. (b) MWDs for run **3d**: gray 27% (30 min), gray 27% (30 min), red 56% (60 min), purple 70% (90 min), and black 94% (180 min). Data: solid, fits: dashed.

As shown in Figure 5, this model provides an excellent fit to both the time-dependence of monomer consumption as well as the molecular weight distributions. The modeling of Data Set I, comprising 7 different experiments (runs 1-3abc, 4, 5), enabled us to identify one possible mechanism consisting of four elementary steps that are consistent with the kinetics data: (i) a slow and reversible initiation step to generate zwitterion Z_1, (ii) a fast propagation step involving addition of monomer to Z_n, (iii) an intramolecular backbiting reaction to liberate cyclic chains, and (iv) intermolecular chain-transfer reactions where the alkoxides of growing zwitterions react either with internal esters of other zwitterions or cyclized chains.

As Model III provided an excellent fit to all the experimental data of data set I, we utilized the same set of reactions and re-optimized the rate constants to fit the data from both data set I and data set II. Data set II (run 3d, Table 1) were carried out with a different batch of carbene **4** and a different batch of monomer approximately 6 months after data set

I was acquired. As seen in Figure 6, the rate of polymerization in run 3d (data set II) is faster than that observed for run 3c even though the concentrations of all species were identical. As observed for run 3c, the molecular weights and molecular weight distributions for run 3d increase with increasing conversion.

The faster rate of polymerization of run 3d relative to run 3c implies that trace impurities may be contributing to the variability observed in the rates. As noted previously, the NHCs are readily deactivated by trace amounts of water. We observe some batch to batch variability in the rate of polymerization depending on the source of the carbene or monomer, even when both have been purified repeatedly. While the exact nature of the impurities or the mechanism by which they deactivate the carbene are unknown, we hypothesize that protic species present in monomer, catalyst, or even in the glovebox ambient atmosphere are responsible for deactivating the carbene initiator, leading to batch-to-batch variations. Nevertheless, for a given batch of carbene and monomer (Data set I, runs 1-3abc, 4, 5) we observe consistent results, as evidenced by the consistent fits of Model III to the entire data set I.

To accommodate the different rates observed between data set I and data set II, we introduced one additional adjustable parameter in our model, $X_{carbene}$, the mole percent of carbene added that is active for initiation and/or polymerization. We arbitrarily assigned $X_{carbene}$ for data set II to be 100% and then re-optimized the rate constants and $X_{carbene}$ for data set I in an effort to fit all the data from both data sets.

The results of this optimization procedure are presented in Table 4 and Figure 6. As seen in Table 4 and Figure 6, we could adequately model all the data if we assume that

the fraction of active carbene $X_{carbene}$ = 100% for data set II, and $X_{carbene}$ = 30% for data set I (run 3d).

Table 7-4. Optimized rate constants for Model III with combined data sets I and I).

Data Set (runs)	k_i ($M^{-1}min^{-1}$)	k_{-i} (min^{-1})	k_p ($M^{-1}min^{-1}$)	$k_{tr(2)}$ ($M^{-1}min^{-1}$)	k_{bb} (min^{-1})	$X_{carbene}$
I (1-3abc,4,5)	0.17	$4.8x10^3$	68	0.18	0.068	30%
II (3d)	0.17	$4.8x10^3$	68	0.18	0.068	100%

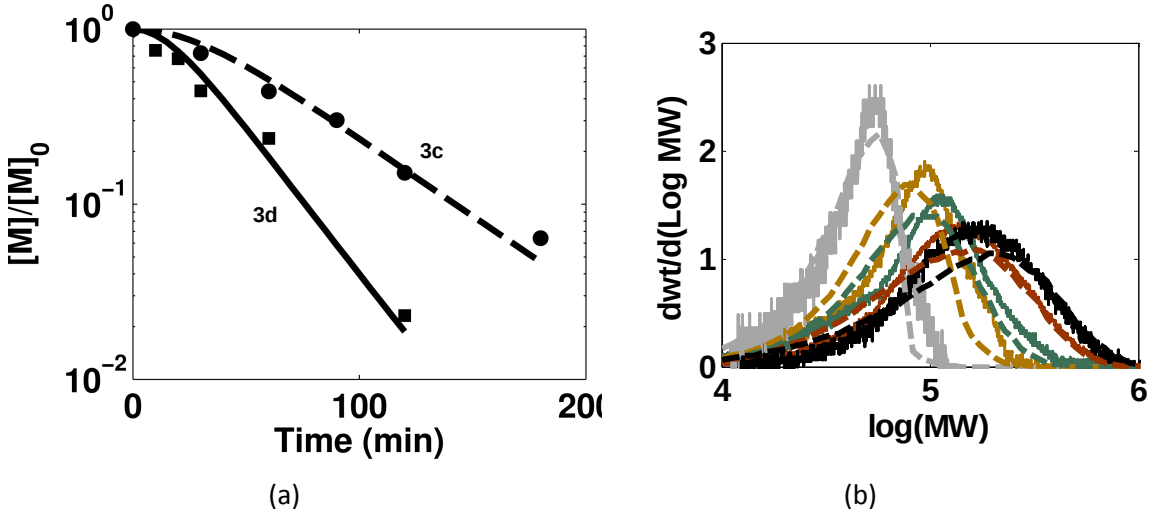

Figure 7-6. Model III: Simulation results based on Data set II. (a) Monomer consumption: circles: data set I (run **3c**), squares: data set II (run **3d**), dashed line: simulation of **3c**, solid line: simulation of **3d**. (b) MWDs for run **3d** in Table 1. Gray 24% (10 min), yellow 32% (20 min), green 56% (30 min), red 76% (60 min), black 98% (120 min). Data: solid, fits: dashed.

The agreement between the simulations and experimental data demonstrates the robustness of Model III across two separate data sets. By adjusting $X_{carbene}$, the percentage of carbene added that is chemically active, the model can account for the batch-to-batch variations in rate and accurately simulate the kinetics of the system. As we currently have no accurate means of estimating $X_{carbene}$ for any given set of experiments, our choice of

$X_{carbene}$ = 100% is an arbitrary choice: the mole percentage of active carbene in run 3d (data set II) may actually be (and most likely is) lower than 100% as trace impurities are likely still present, in which case the optimized rate constants of Table 4 are likely lower bounds to the actual rate constants for the various steps. Our intent for the kinetics modeling is not so much to provide an accurate determination of the rate constants, but rather to identify a minimal set of elementary reactions and a set of *relative rate constants* in a mechanism that is consistent with the rates of polymerization as well as the molecular weights and molecular weight distributions that can be expected for any given set of initial conditions.

An additional insight provided by the kinetics modeling is that the time evolution of concentrations of growing zwitterions (Fig 7, solid line) and cyclized chains (Fig 7, dashed line) can be simulated. These simulations predict that concentration of zwitterions Z_n increases at early times and saturates at approximately 60% conversion (~ 30 min). The concentration of cyclized chains increases more slowly than that of the zwitterions at early times, but continues to increase with increasing conversion. The continuous growth in the number of cycles is due to the back-biting reaction which is monomer independent. At infinite time, if the carbenes remain active, the system would be expected to reach equilibrium,[36] but we have not carried out experiments at these longer times.

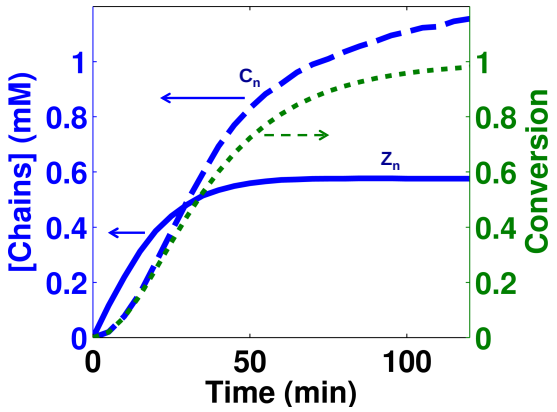

Figure 7-7. Simulated concentrations of growing zwitterions Z_n (solid line) and cyclized chains C_n (dashed line) for run 3 based on Model III. The monomer conversion (green dotted line) is also plotted with a different y-axis.

The prediction that a significant concentration of zwitterions remains even at high conversion was tested by adding a second charge of monomer at roughly 80% conversion (Figure 8). As shown in Figure 8a, an increase in molecular weight was observed upon addition of the second monomer charge at t_a = 90 min, indicating that some fraction of the chains are active and are chain-extended to higher molecular weight. In addition, the rate of monomer consumption following the addition of the second charge of monomer is faster than the initial rate of monomer consumption (Figure 8b). This is evident in Figure 8c where the rate of monomer consumption following the addition of the second charge of monomer (red open triangles) is compared to the rate for run 3d (black squares). That the chains extend and that the rate is faster are consistent with the chain extension of active zwitterions upon addition of more monomer, as the model indicates that monomer should be consumed more rapidly in the presence of active zwitterions than in the case where only the carbene initiator is present.

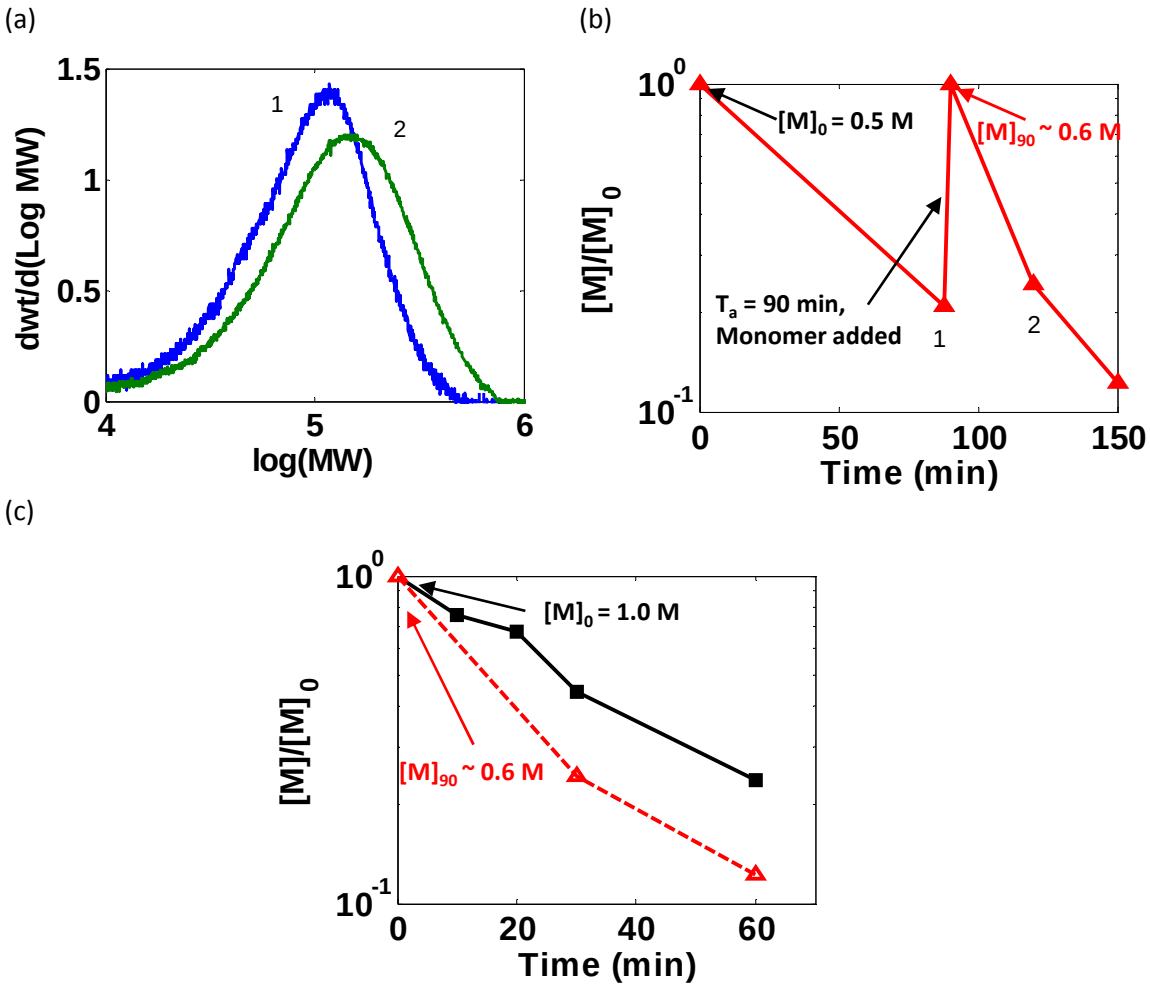

Figure 7-8. Monomer addition experiment using NHC **2**. Initial conditions: $[M]_0$ = 0.5 M, $[NHC]_0$ = 0.01 M in toluene. A second charge of monomer ($[M]_{add}$ = 0.5 M) is added into the reaction at t_a = 90 min (~ 80% conversion). (a) GPC traces at t = 88 min, blue (1), 79% conversion, M_n = 55 kDa, M_w/M_n = 1.801 (PS) and t = 120min (t_a + 30min), green (2), M_n = 70 kDa, M_w/M_n = 2.029 (PS). (b) $[M]/[M]_0$ for monomer addition experiment; t_a = 90 min. (c) Comparison of normalized $[M]/[M]_0$ for run 3d $[M]_0$ = 1.0 M, black squares, and for monomer addition experiment at time t_a = 90 min, $[M]_{90}$ = 0.5 M, open triangles.

To assess whether cyclized chains can be re-activated during the course of the polymerization, as proposed in Models III (eq 6) and II (eq. 3), we carried out an experiment where cyclized chains were added to a zwitterionic polymerization (Figure 9). The polymerization at $[CL]_0$ = 0.5M was carried out with carbene **2** to 84% conversion (t

= 88 min), an aliquot was removed (trace 1, Fig. 9), and to the reaction mixture 0.10 g of a cyclic p(CL) (trace 2, Fig 9) was added. The resulting mixture was stirred for an additional 60 min and analyzed by GPC. As shown in Figure 9, the resulting polymers isolated after a total reaction time of 150 min exhibited a molecular weight intermediate (M_n = 101 kDa, with M_w/M_n = 2.63) between that of the growing chains (trace 1) and added cyclic chains (trace 2, Fig 9).

The decrease in molecular weight of the added cyclic pCL provides clear evidence that the cyclic polymers are not 'dead' chains, but can be reactivated under the reaction conditions and undergo scrambling reactions, either with active zwitterions (eq 6) and/or the unitiated carbenes (eq 3). The increase in molecular weight of the growing chains (peak 1) upon addition of cyclic PCL is most reasonably attributed to the attack of active zwitterions on the cyclized PCL chains, since after addition, the unreacted monomer would have decreased (upon dilution) to a concentration of approx. $[CL]_{90}$ = 0.03M. This latter result provides experimental support for the hypothesis that nucleophilic attack of the growing zwitterions on cyclized chains provides a mechanism for generating high molecular weight cyclic chains (eq 6 of Model III) in the zwitterionic ring-opening polymerization of caprolactone.

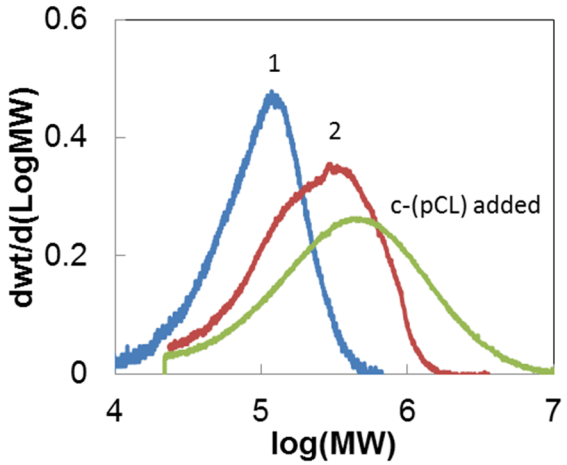

Figure 7-9. GPC traces for the polymer addition experiment using NHC **2**. Initial conditions: $[M]_0$ = 0.5 M, $[NHC]_0$ = 0.01 M in 1. 8 mL toluene, Trace 1 (blue), t = 88 min, 84% conv, M_n = 61 kDa, M_w/M_n = 1.74. At t = 90 min, 0.10 g of cyclic PCL (cPCL added (grey), M_n = 146 kDa, M_w/M_n = 2.58), was added in 3.0 mL of toluene. After stirring for 60 min, the resulting polymer isolated (t = 150 min) is represented in trace 2 M_n = 101 kDa, M_w/M_n = 2.63).

Proposed Mechanism. On the basis of the kinetics and modeling, we propose the mechanism shown in Scheme 3 for the zwitterionic ring-opening polymerization of ε-caprolactone with N-alkyl heterocyclic carbenes. A slow and reversible initiation step to generate zwitterion Z_1 leads to an induction period and a time-dependent initiator efficiency such that at $[M]_0$ = 1.0M, $[NHC]_0$ = 0.01M, only 60% of the active NHC carbenes transform to active propagating zwitterions (Fig 7). The zwitterions Z_n rapidly add monomer, but also undergo several other reactions. Cyclization of Z_n by a backbiting intramolecular transesterification generates cyclized chains C_x and lower molecular weight zwitterions Z_{n-x}. This cyclization event preserves the number of active zwitterions and thus has no effect on the rate.

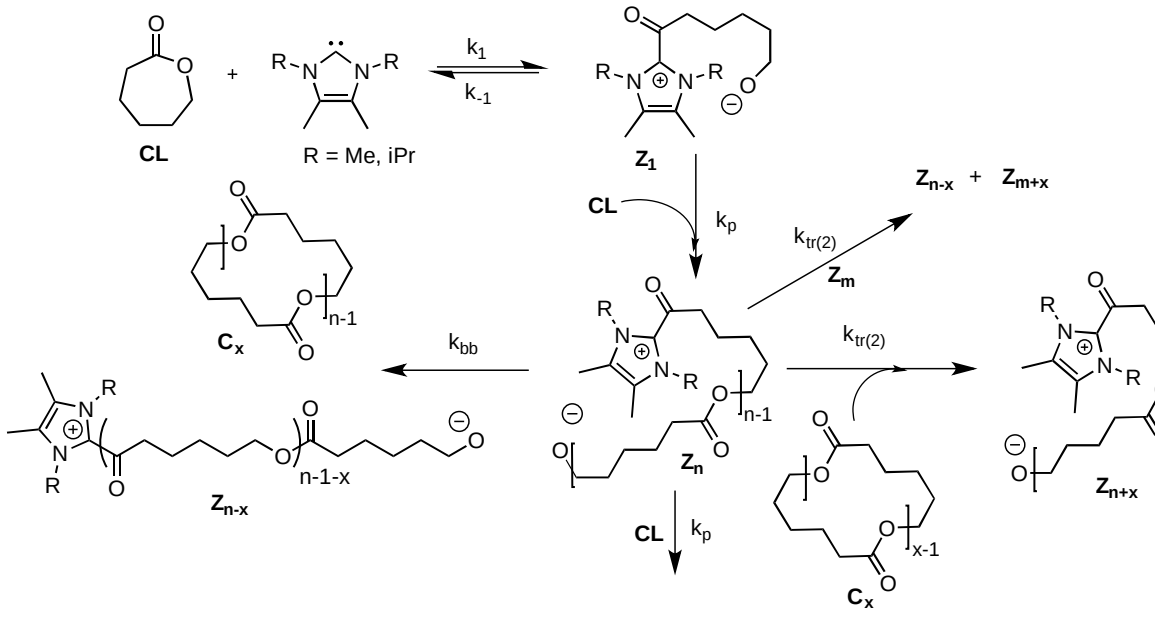

Scheme 7-3. Proposed mechanism for zwitterionic ring-opening polymerization of caprolactone

Chain-transfer events include the reaction of growing zwitterions with each other ($Z_n + Z_m \longrightarrow Z_{n-x} + Z_{m+x}$), which leads to the broadening of the molecular weight distributions. Addition of cyclized chains C_x to the growing zwitterion Z_n is another chain-transfer event that leads to high molecular weight zwitterions Z_{n+x}, once a significant concentrations of cyclized chains are present. This latter step can explain the observed tailing of the molecular weight distributions to higher molecular weights, and is a key step that enables the synthesis of high molecular weight cyclic poly(caprolactones).[17]

The proposed mechanism for the zwitterionic ring-opening polymerization of caprolactone with the N-alkyl heterocyclic carbenes **2-4** differs from that proposed for the ZROP of lactide with the less nucleophilic carbene IMes **1** (Scheme I) in several significant ways. First, for caprolactone, the cyclization step to generate cyclic chains is proposed to be an intramolecular cyclization of growing zwitterions on internal esters of the zwitterion

("backbiting") rather than cyclization at the acyl-imidazolium terminus of the zwitterion (Scheme I, eq (1)). It is likely that such backbiting reactions occur for the zwitterionic polymerization of lactide as well, but this step might be expected to be more probable[37] for poly(caprolactones) as the internal esters of poly(caprolactone) are derived from primary alcohols whereas those from lactide are derived from secondary alcohols. Another key difference is the proposed addition of cyclized poly(caprolactone) chains to growing zwitterions. This step implies that cyclized chains are not "dead" chains, but can be reactivated by growing zwitterions. This combination of chain-growth and step-growth mechanisms[34] leads to high molecular weight zwitterions and ultimately high molecular weight cyclic poly(caprolactones), that was not evident in the zwitterionic polymerization of lactide.[14, 16]

The mechanism proposed in Scheme 3 (Model III) represents the only minimal set of reaction steps that are consistent with kinetics data, as well as the time evolution of molecular weight and polydispersity. It is likely that other reactions occur, including a cyclization step (eq (1)), steps corresponding to eqs (2) and (3) or a depropagation step. Several of these steps were considered and added to kinetics Model III (see Supporting information), but did not provide significantly better fits to the data. Thus, Scheme 3 provides one mechanism that is consistent with the currently available kinetics data that can both rationalize the rates and molecular weights of the cyclic poly(caprolactones) generated with NHC initiators.

7.4 Conclusion

In summary, these investigations revealed several key insights on the rate of zwitterionic ring-opening polymerization of caprolactone and the reaction steps responsible for the time evolution of molecular weights and polydispersities. Simultaneous modeling of both the evolution of monomer conversion, molecular weights and molecular weight distributions were necessary to rule out several likely scenarios, as several models were adequate to model the rate of monomer conversion alone. On the basis of modeling, a minimal set of reaction steps were identified that could rationalize both the rates and molecular weights of the resulting cyclic poly(caprolactones), as well as the variations in rate caused by trace impurities. These studies reveal that the generation of reactive zwitterions by a slow and reversible initiation step is followed by the rapid growth of zwitterions. Initiation and propagation is accompanied by several chain-transfer and chain-scrambling steps, including the intramolecular backbiting of the alkoxide chain-ends on internal esters of the growing zwitterions to liberate cyclic chains, and the attack of active zwitterions on the internal esters of other zwitterions as well as cyclized chains. The attack of active zwitterions on cyclized chains is proposed as a key step that leads to high molecular weight cyclic poly(caprolactones).

7.5 Experimental

General Information. All reactions and polymerizations were performed in a drybox or with Schlenk techniques under nitrogen. ^{1}H nuclear magnetic resonance (NMR) spectra were recorded at room temperature on Varian 400 MHz, Unity/Inova Varian 500 MHz, or Unity/Inova Varian 600 MHz spectrometers. The chemical shifts are reported in parts per

million (δ) downfield from tetramethylsilane and referenced to the residual solvent peak. Gel permeation chromatography (GPC) was performed in tetrahydrofuran (THF) at a flow rate of 1.0 mL/min on a Waters chromatograph equipped with four 5 μm Waters columns (300 mm x 7.7 mm) connected in series. The Viscotek S3580 refractive index detector and Viscotek GPCmax autosampler were employed. Triple detectors (Viscotek, Houston, TX) include a light scattering detector and viscometer which were calibrated using monodisperse polystyrene standards (Polymer Laboratories). The right-angle light scattering (RALS) method was used to determine absolute molecular weights of polymers. Correction for any angular dissymmetry factor in the RALS data was performed in the TriSEC software using the viscometer signal. The angular dissymmetry correction is negligible because the polymers studied are relatively small compared to the laser wavelength (610 nm). The polymer solution (ca. 10 mg/mL) was prepared by dissolving the polymer in THF.

Materials. Toluene was distilled from sodium/benzophenone and degassed three times via freeze-pump-thaw cycles. ε-Caprolactone (CL) was purchased from Sigma-Aldrich and distilled from calcium hydride twice. Anhydrous methanol was purchased from Sigma-Aldrich and used as received. 4-Nitrophenol was purchased from Fluka and purified by recrystallization from toluene and sublimation. 1,3-bis(2,4,6-trimethylphenyl)imidazole-2-ylidene (IMes, 1), 1,3,4,5-tetramethyl-imidazol-2-ylidene (2), 1,3-diethyl-4,5-dimethylimidazol-2-ylidene (3), and 1,3-diisopropyl-4,5-dimethylimidazol-2-ylidene (4), and were prepared according to the literature procedure.[38] Linear PCL was prepared according to literature procedure[39]

Representative polymerization of ε-Caprolactone with 1,3,4,5-tetramethyl-imidazol-2-ylidene 2. Liquid ε-caprolactone (0.1433 g, 1.257 mmol) was weighed into a vial in the glovebox and dissolved in d_8-toluene (1.00 mL). This solution was placed in a J. Young NMR tube, sealed, and used to lock and shim the NMR used for acquisition (300 MHz). The NMR tube was returned to the glovebox and carbene 2 was added as a solution in d_8-toluene (1.575 mg in 0.25 mL toluene from stock solution, 0.0127mmol). The reaction was monitored by ^{1}H NMR overnight using mesitylene as an internal standard.

Kinetics Modeling Method: For a given reaction mechanism the concentrations of all the species as a function of time are obtained in this work using the Dynamic Monte Carlo (DMC) method[31, 32]. The implementation of the DMC method here is based on the Gillespie's algorithm[32] for which an original computer code has been created (see SI for details). The search for the set of the rate constants for a given mechanism that provides the best possible fit to data was carried out using the Nelder-Mead's (simplex) optimization method.[33]

REFERENCES

(1) Tezuka, Y., *Topological Polymer Chemistry: Progress of cyclic polymers in synthesis, properties and functions*. World Scientific Publishing: Singapore, 2013; p 352.

(2) Endo, K., Synthesis and Properties of Cyclic Polymers. *Adv. Polym. Sci.* **2008,** *217*, 121-183.

(3) Semlyen, J. A., *Cyclic polymers*. 2nd ed.; Kluwer Academic Publishers: Dordrecht 2000; p xx, 790 p.

(4) Kapnistos, M.; Lang, M.; Vlassopoulos, D.; Pyckhout-Hintzen, W.; Richter, D.; Cho, D.; Chang, T.; Rubinstein, M., Unexpected power-law stress relaxation of entangled ring polymers. *Nature Materials* **2008,** *7* (12), 997-1002; Pasquino, R.; Vasilakopoulos, T. C.; Jeong, Y. C.; Lee, H.; Rogers, S.; Sakellariou, G.; Allgaier, J.; Takano, A.; Brás, A. R.; Chang, T.; Gooßen, S.; Pyckhout-Hintzen, W.; Wischnewski, A.; Hadjichristidis, N.; Richter, D.; Rubinstein, M.; Vlassopoulos, D., Viscosity of Ring Polymer Melts. *ACS Macro Letters* **2013,** *2* (10), 874-878; Vlassopoulos, D.; Pasquino, R.; Snijkers, F., Progress in the Rheology of Cyclic Polymers. In *Topological Polymer Chemistry: Progress of cyclic polymers in synthesis, properties and functions*, Tezuka, Y., Ed. World Scientific Publishing: Singapore, 2013; pp 291-316; Halverson, J. D.; Lee, W. B.; Grest, G. S.; Grosberg, A. Y.; Kremer, K., Molecular dynamics simulation study of nonconcatenated ring polymers in a melt. II. Dynamics. *J. Chem. Phys.* **2011,** *134* (20), 204905; Hur, K.; Jeong, C.; Winkler, R. G.; Lacevic, N.; Gee, R. H.; Yoon, D. Y., Chain Dynamics of Ring and Linear Polyethylene Melts from Molecular Dynamics Simulations. *Macromolecules* **2011,** *44* (7), 2311-2315.

(5) Halverson, J. D.; Lee, W. B.; Grest, G. S.; Grosberg, A. Y.; Kremer, K., Molecular dynamics simulation study of nonconcatenated ring polymers in a melt. I. Statics. *J. Chem. Phys.* **2011,** *134* (20), 204904.

(6) Brown, H. A.; Waymouth, R. M., Zwitterionic Ring-Opening Polymerization for the Synthesis of High Molecular Weight Cyclic Polymers. *Acc. Chem. Res.* **2013,** *46* (11), 2585-2596.

(7) Laurent, B. A.; Grayson, S. M., Synthetic approaches for the preparation of cyclic polymers. *Chem. Soc. Rev.* **2009,** *38* (8), 2202-2213; Jia, Z. F.; Monteiro, M. J., Cyclic

Polymers: Methods and Strategies. *J. Polym. Sci., Part A: Polym. Chem.* **2012,** *50* (11), 2085-2097; Chisholm, M. H., Catalytic formation of cyclic-esters and -depsipeptides and chemical amplification by complexation with sodium ions. *J. Organomet. Chem.* **2008,** *693* (5), 808-818.

(8) Kricheldorf, H. R., Cyclic Polymers: Synthetic Strategies and Physical Properties. *J. Polym. Sci., Part A: Polym. Chem.* **2010,** *48* (2), 251-284.

(9) Xia, Y.; Boydston, A. J.; Yao, Y.; Kornfield, J. A.; Gorodetskaya, I. A.; Spiess, H. W.; Grubbs, R. H., Ring-Expansion Metathesis Polymerization: Catalyst-Dependent Polymerization Profiles. *J. Am. Chem. Soc.* **2009,** *131* (7), 2670-2677.

(10) Roovers, J., Organic Cyclic Polymers. In *Cyclic Polymers*, Second ed.; Semlyen, J. A., Ed. Kluwer Academic Publishers: Dordrecht, 2000; pp 347-384.

(11) Bielawski, C. W.; Benitez, D.; Grubbs, R. H., An "Endless" Route to Cyclic Polymers. *Science* **2002,** *297*, 2041-2044; Bielawski, C. W.; Benitez, D.; Grubbs, R. H., Synthesis of Cyclic Polybutadiene via Ring-Opening Metathesis Polymerization: The Importance of Removing Trace Linear Contaminants. *J. Am. Chem. Soc.* **2003,** *125*, 8424-8425; Boydston, A.; Xia, Y.; Kornfield, J., Cyclic Ruthenium-Alkylidene Catalysts for Ring-Expansion Metathesis Polymerization. *J. Am. Chem. Soc.* **2008**; Xia, Y.; Boydston, A. J.; Grubbs, R. H., Synthesis and Direct Imaging of Ultrahigh Molecular Weight Cyclic Brush Polymers. *Angew. Chem.* **2011,** *123* (26), 6004-6007; Kricheldorf, H. R., Biodegradable Polymers with Variable Architectures via Ring-Expansion Polymerization. *J.Polym. Sci., Part A: Polym. Chem.* **2004,** *42*, 4723-4742.

(12) Bielawski, C. W.; Grubbs, R. H., Living ring-opening metathesis polymerization. *Prog. Polym. Sci.* **2007,** *32* (1), 1-29.

(13) Brown, H. A.; De Crisci, A. G.; Hedrick, J. L.; Waymouth, R. M., Amidine-Mediated Zwitterionic Polymerization of Lactide. *ACS Macro Letters* **2012,** *1,* 1113-1115.

(14) Culkin, D.; Jeong, W.; Csihony, S.; Gomez, E.; Balsara, N.; Hedrick, J. L.; Waymouth, R., Zwitterionic Polymerization of Lactide to Cyclic Poly (Lactide) by Using N‐Heterocyclic Carbene Organocatalysts. *Angew. Chem., Int. Ed.* **2007,** *46,* 2627-2630.

(15) Jeong, W.; Hedrick, J. L.; Waymouth, R. M., Organic Spirocyclic Initiators for the Ring-Expansion Polymerization of β-Lactones. *J. Am. Chem. Soc.* **2007,** *129,* 8414-8415; Guo, L.; Li, J.; Brown, Z.; Ghale, K.; Zhang, D., Synthesis and characterization of cyclic and linear helical poly(α-peptoid)s by N-heterocyclic carbene-mediated ring-opening polymerizations of N-substituted N-carboxyanhydrides. *Biopolymers* **2011,** *96* (5), 596-603; Guo, L.; Zhang, D., Cyclic Poly (α-peptoid) s and Their Block Copolymers from N-Heterocyclic Carbene-Mediated Ring-Opening Polymerizations of N-Substituted N-Carboxylanhydrides. *J. Am. Chem. Soc.* **2009,** *131* (50), 18072-18074; Lahasky, S. H.; Hu, X.; Zhang, D., Thermoresponsive Poly(α-peptoid)s: Tuning the Cloud Point Temperatures by Composition and Architecture. *ACS Macro Letters* **2012,** *1* (5), 580-584; Lahasky, S. H.; Serem, W. K.; Guo, L.; Garno, J. C.; Zhang, D., Synthesis and Characterization of Cyclic Brush-Like Polymers by N-Heterocyclic Carbene-Mediated Zwitterionic Polymerization of N-Propargyl N-Carboxyanhydride and the Grafting-to Approach. *Macromolecules* **2011,** *44* (23), 9063-9074; Lee, C.-U.; Smart, T. P.; Guo, L.; Thomas H Epps, I.; Zhang, D., Synthesis and Characterization of Amphiphilic Cyclic Diblock Copolypeptoids from N-Heterocyclic Carbene-Mediated Zwitterionic Polymerization of N-Substituted N-Carboxyanhydride. *Macromolecules* **2011,** *44* (24), 9574-9585; Li, X. P.;

Guo, L.; Casiano-Maldonado, M.; Zhang, D. H.; Wesdemiotis, C., Top-Down Multidimensional Mass Spectrometry Methods for Synthetic Polymer Analysis. *Macromolecules* **2011,** *44* (12), 4555-4564; Zhang, D.; Lahasky, S. H.; Guo, L.; Lee, C.-U.; Lavan, M., Polypeptoid Materials: Current Status and Future Perspectives. *Macromolecules* **2012,** *45* (15), 5833-5841.

(16) Jeong, W.; Shin, E. J.; Culkin, D. A.; Hedrick, J. L.; Waymouth, R. M., Zwitterionic Polymerization: A Kinetic Strategy for the Controlled Synthesis of Cyclic Polylactide. *J. Am. Chem. Soc.* **2009,** *131* (13), 4884-4891.

(17) Shin, E. J.; Jeong, W.; Brown, H. A.; Koo, B. J.; Hedrick, J. L.; Waymouth, R. M., Crystallization of Cyclic Polymers: Synthesis and Crystallization Behavior of High Molecular Weight Cyclic Poly(epsilon-caprolactone)s. *Macromolecules* **2011,** *44* (8), 2773-2779.

(18) Shin, E. J.; Brown, H. A.; Gonzalez, S.; Jeong, W.; Hedrick, J. L.; Waymouth, R. M., Zwitterionic Copolymerization: Synthesis of Cyclic Gradient Copolymers. *Angew. Chem., Int. Ed.* **2011,** *50* (28), 6388-6391.

(19) Shin, E. J.; Jones, A. E.; Waymouth, R. M., Stereocomplexation in Cyclic and Linear Polylactide Blends. *Macromolecules* **2012,** *45* (1), 595-598.

(20) Guo, L.; Lahasky, S. H.; Ghale, K.; Zhang, D. H., N-Heterocyclic Carbene-Mediated Zwitterionic Polymerization of N-Substituted N-Carboxyanhydrides toward Poly(alpha-peptoid)s: Kinetic, Mechanism, and Architectural Control. *J. Am. Chem. Soc.* **2012,** *134* (22), 9163-9171.

(21) Johnston, D. S., Macrozwitterion Polymerization. *Adv. Polym. Sci.* **1982,** *42*, 51-106.

(22) Maji, B.; Breugst, M.; Mayr, H., N-Heterocyclic Carbenes: Organocatalysts with Moderate Nucleophilicity but Extraordinarily High Lewis Basicity. *Angew. Chem., Int. Ed.* **2011,** *50* (30), 6915-6919.

(23) Zhong, M.; Wang, Y.; Krys, P.; Konkolewicz, D.; Matyjaszewski, K., Reversible-Deactivation Radical Polymerization in the Presence of Metallic Copper. Kinetic Simulation. *Macromolecules* **2013,** *46* (10), 3816-3827; Albertsson, A. C.; Varma, I. K., Recent developments in ring opening polymerization of lactones for biomedical applications. *Biomacromolecules* **2003,** *4*, 1466-1486; Matyjaszewski, K.; Xia, J., Atom Transfer Radical Polymerization. *Chem. Rev.* **2001,** *101* (9), 2921-2990; Moscato, B. M.; Zhu, B. L.; Landis, C. R., GPC and ESI-MS Analysis of Labeled Poly(1-Hexene): Rapid Determination of Initiated Site Counts during Catalytic Alkene Polymerization Reactions. *J. Am. Chem. Soc.* **2010,** *132* (41), 14352-14354; Ding, K. Y.; Miranda, M. O.; Moscato-Goodpaster, B.; Ajellal, N.; Breyfogle, L. E.; Hermes, E. D.; Schaller, C. P.; Roe, S. E.; Cramer, C. J.; Hillmyer, M. A.; Tolman, W. B., Roles of Monomer Binding and Alkoxide Nucleophilicity in Aluminum-Catalyzed Polymerization of epsilon-Caprolactone. *Macromolecules* **2012,** *45* (13), 5387-5396; Zhang, Y. T.; Schmitt, M.; Falivene, L.; Caporaso, L.; Cavallo, L.; Chen, E. Y. X., Organocatalytic Conjugate-Addition Polymerization of Linear and Cyclic Acrylic Monomers by N-Heterocyclic Carbenes: Mechanisms of Chain Initiation, Propagation, and Termination. *J. Am. Chem. Soc.* **2013,** *135* (47), 17925-17941; Chisholm, M. H.; Eilerts, N. W.; Huffman, J. C.; Iyer, S. S.; Pacold, M.; Phomphrai, K., Molecular Design of Single-Site Metal Alkoxide Catalyst Precursors for Ring-Opening Polymerization Reactions Leading to Polyoxygenates. 1. Polylactide Formation by Achiral and Chiral Magnesium and Zinc Alkoxides, (η3-L)MOR, Where L

= Trispyrazolyl- and Trisindazolylborate Ligands. *J. Am. Chem. Soc.* **2000,** *122* (48), 11845-11854; Stridsberg, K.; Ryner, M.; Albertsson, A.-C., Dihydroxy-Terminated Poly(l-lactide) Obtained by Controlled Ring-Opening Polymerization: Investigation of the Polymerization Mechanism. *Macromolecules* **2000,** *33* (8), 2862-2869.

(24) Penczek, S.; Cypryk, M.; Duda, A.; Kubisa, P.; Slomkowski, S., Living ring-opening polymerizations of heterocyclic monomers. *Prog. Polym. Sci.* **2007,** *32* (2), 247-282.

(25) Novstrup, K. A.; Travia, N. E.; Medvedev, G. A.; Stanciu, C.; Switzer, J. M.; Thomson, K. T.; Delgass, W. N.; Abu-Omar, M. M.; Caruthers, J. M., Mechanistic Detail Revealed via Comprehensive Kinetic Modeling of [rac-C2H4(1-indenyl)2ZrMe2]-Catalyzed 1-Hexene Polymerization. *J. Am. Chem. Soc.* **2010,** *132* (2), 558-566.

(26) Penczek, S.; Biela, T.; Duda, A., Living polymerization with reversible chain transfer and reversible deactivation: the case of cyclic esters. *Macromol. Rapid Commun.* **2000,** *21* (14), 941-950.

(27) Kamber, N. E.; Jeong, W.; Gonzalez, S.; Hedrick, J. L.; Waymouth, R. M., N-Heterocyclic Carbenes for the Organocatalytic Ring-Opening Polymerization of Ɛ-Caprolactone. *Macromolecules* **2009,** *42* (5), 1634-1639.

(28) Kricheldorf, H. R.; Lomadze, N.; Schwarz, G., Cyclic polylactides by imidazole-catalyzed polymerization of L-lactide. *Macromolecules* **2008,** *41* (21), 7812-7816.

(29) Steelman, D. K.; Xiong, S. L.; Pletcher, P. D.; Smith, E.; Switzer, J. M.; Medvedev, G. A.; Delgass, W. N.; Caruthers, J. M.; Abu-Omar, M. M., Effects of Pendant Ligand Binding Affinity on Chain Transfer for 1-Hexene Polymerization Catalyzed by Single-Site Zirconium Amine Bis-Phenolate Complexes. *J. Am. Chem. Soc.* **2013,** *135* (16), 6280-6288;

Switzer, J. M.; Travia, N. E.; Steelman, D. K.; Medvedev, G. A.; Thomson, K. T.; Delgass, W. N.; Abu-Omar, M. M.; Caruthers, J. M., Kinetic Modeling of 1-Hexene Polymerization Catalyzed by Zr(tBu-(ONO)-O-NMe2)Bn-2/B(C6F5)(3). *Macromolecules* **2012,** *45* (12), 4978-4988.

(30) Similar induction periods were observed in the zwitterionic polymerization of acrylonitrile with phosphine initiators. Markevic, M. A.; Kochetov, E. V.; Ranogajec, F.; Enikolopyan, N. S. *J. Macromol. Sci., Part A, Pure Appl. Chem.* **1974**, *8*, 265-279.

.

(31) Xiong, S.; Steelman, D. K.; Medvedev, G. A.; Delgass, W. N.; Abu-Omar, M. M.; Caruthers, J. M., Selective Degenerative Benzyl Group Transfer in Olefin Polymerization. *ACS Catalysis* **2014,** *4* (4), 1162-1170.

(32) Gillespie, D. T., GENERAL METHOD FOR NUMERICALLY SIMULATING STOCHASTIC TIME EVOLUTION OF COUPLED CHEMICAL-REACTIONS. *J. Comput. Phys.* **1976,** *22* (4), 403-434.

(33) Nelder, J. A.; Mead, R., A SIMPLEX-METHOD FOR FUNCTION MINIMIZATION. *Computer Journal* **1965,** *7* (4), 308-313.

(34) Kricheldorf, H. R., Simultaneous Chain‐Growth and Step‐Growth Polymerization—A New Route to Cyclic Polymers. *Macromol. Rapid Commun.* **2009,** *30*, 1371-1381.

(35) Chisholm, M. H.; Gallucci, J. C.; Quisenberry, K. T.; Zhou, Z., Complexities in the Ring-Opening Polymerization of Lactide by Chiral Salen Aluminum Initiators. *Inorg. Chem.* **2008,** *47* (7), 2613-2624.

(36) Jacobson, H.; Stockmayer, W. H., Intramolecular Reactions in Polycondensations. 1. The Theory of Linear Systems. *J. Chem. Phys.* **1950,** *18*, 1600-1606; Moratti, S. C., Comment on "Macrocycles 21. Role of ring-ring equilibria in thermodynamically controlled polycondensations". *Macromolecules* **2005,** *38* (4), 1520-1522; Kricheldorf, H. R., Macrocycles. 21. Role of ring-ring equilibria in thermodynamically controlled polycondensations. *Macromolecules* **2003,** *36* (7), 2302-2308; Kricheldorf, H. R.; Lomadze, N., Cyclic and multicyclic polymers by thermodynamically controlled polycondensations-theory and experiments. *Polymer Science Series C* **2009,** *51* (1), 133-147.

(37) Nyce, G. W.; Lamboy, J. A.; Connor, E. F.; Waymouth, R. M.; Hedrick, J. L., Expanding the Catalytic Activity of Nucleophilic N-Heterocyclic Carbenes for Transesterification Reactions. *Org. Lett.* **2002,** *4* (21), 3587-3590.

(38) Arduengo III, A. J.; Dias, H. V. R.; Harlow, R. L.; Kline, M., ELECTRONIC STABILIZATION OF NUCLEOPHILIC CARBENES. *J. Am. Chem. Soc.* **1992,** *114* (14), 5530-5534; Kuhn, N.; Kratz, T., SYNTHESIS OF IMIDAZOL-2-YLIDENES BY REDUCTION OF IMIDAZOLE-2(3H)-THIONES. *Synthesis* **1993,** (6), 561-562.

(39) Storey, R. F.; Herring, K. R.; Hoffman, D. C., HYDROXY-TERMINATED POLY(EPSILON-CAPROLACTONE-CO-DELTA-VALEROLACTONE) OLIGOMERS - SYNTHESIS, CHARACTERIZATION, AND POLYURETHANE NETWORK FORMATION. *J. Polym. Sci., Part A: Polym. Chem.* **1991,** *29* (12), 1759-1777; Storey, R. F.; Hoffman, D. C., COPOLYMERIZATION OF EPSILON-CAPROLACTONE AND DELTA-VALEROLACTONE. *Makromolekulare Chemie-Macromolecular Symposia* **1991,** *42-3*, 185-193.

CHAPTER 8. NON-HEME MANGANESE CATALYSTS FOR ON-DEMAND PRODUCTION OF CHLORINE DIOXIDE IN WATER AND UNDER MILD CONDITIONS

This chapter contains published work. It is reproduced with permission from *J. Am. Chem. Soc.*, **2014**, *136* (9), pp 3680–3686; Copyright © 2014, American Chemical Society.

In this paper, I performed kinetics analysis on the catalyst systems. Scott D. Hicks did all the experimental work.

8.1 Introduction

The chlorine oxyanions (ClO_n^-, n = 1-4) spanning oxidation states of +1 to +7 have found diverse uses from bleaching agents to oxidizers in rocket fuels. As a result of their high solubility in water and wide range of applications, water sources have been severely contaminated by these toxic anthropogenic pollutants.[1] Perchlorate (ClO_4^-) is commonly used as an oxidant in rocket fuel, missiles, and fireworks.[2] Advances in perchlorate remediation using microbes[3] as well as chemical catalysts[4] have previously been discussed. Chlorate (ClO_3^-) is used as an herbicide and a source of chlorine dioxide (ClO_2). Chlorite (ClO_2^-) is primarily used as a source of ClO_2 in the pulp bleaching industry, and hypochlorite (ClO^-) is a widely used disinfectant. Of the aforementioned chlorine-containing species, the catalytic conversion of chlorite to either dioxygen and chloride or chlorine dioxide is of great interest. The reactivity of chlorite and chlorous acid, Cl^{III}, has been studied extensively.[5] The reactivity of aqua transition-metal ions towards Cl^{III} has

been reviewed by Fábián.[6] Collman and Braumann have shown that metalloporphyrins catalyze the electrochemical reduction of chlorite[7] as well as alkane oxidations using chlorite as an oxidant.[8] The Environmental Protection Agency has recently labeled chlorite as a major water contaminant as a result of suspected health risks such as childhood anemia.[9] Chlorite can also serve as an oxidizing or chlorinating agent when exposed to water pollutants and consequently enhance toxicity. Therefore, a method to remediate chlorite is of interest from an environmental standpoint.

The biological remediation of ClO_4^- occurs in three steps catalyzed by two enzymes.[10] Perchlorate reductase is a molybdopterin-dependent enzyme proposed to catalyze the reduction of ClO_4^- to ClO_2^- presumably via the intermediacy of ClO_3^- with the production of a water molecule at each step.[11] Despite a favorable reduction potential, perchlorate reductase does not further reduce ClO_2^-. Instead, it is further reduced to environmentally benign chloride (Cl^-) and dioxygen (O_2) in a reaction catalyzed by chlorite dismutase (Cld), a heme-containing enzyme.[12] This enzyme is of considerable interest since photosystem II is the only other known enzymatically catalyzed process for O–O bond formation. Dubois and co-workers have studied the mechanism of Cld and proposed that the resting Fe^{III}-heme reacts with ClO_2^- to form Compound I and ClO^-, which quickly rebounds to give O_2 and Cl^-.[13] Our group has also reported on the disproportionation of chlorite mainly to chloride and chlorate under physiological pH using water-soluble iron porphyrins as catalysts.[14]

Unlike their iron analogues, manganese porphyrin complexes have been shown, independently, by us and the Groves group to catalyze chlorine dioxide formation from chlorite.[15,16] Lau and co-workers have reported on a ruthenium bisphenanthroline complex

that produces ClO_2.[17] Industrially, there are several methods for the production of chlorine dioxide. Nonetheless, chlorine oxyanions (ClO_n^-) are the prevalent source of ClO_2 in every method. The majority of methods, however, involve highly corrosive conditions and harsh oxidants, which raise health and environmental/safety concerns.[18] Of the chlorine oxyanions used for ClO_2 production, ClO_3^- is the most common source via the reaction with methanol in the presence of concentrated sulfuric acid.[19] However, the one-electron electrochemical oxidation of chlorite offers an alternative route to ClO_2 but requires a substantial input of energy. The primary commercial use of chlorine dioxide is as an oxidizing agent for pulp bleaching and more recently for water disinfection/treatment.[19] Chlorine dioxide is preferred over chlorine gas (Cl_2) for water treatment as it exhibits superior antimicrobial activity and generates less harmful by-products (chlorinated species or trihalomethanes).[20] One major drawback is the instability of ClO_2 at high pressure, a fact that effectively prohibits its transport as a gas. Hence, on-site production of ClO_2 is a prerequisite for any practical application.

Our group communicated on the high reactivity of non-heme manganese–oxo complexes, $[Mn^{IV}(O)(Bn\text{-}TPEN)]^{2+}$ (Bn-TPEN = *N*-benzyl-*N*,*N'*,*N'*-tris(2-pyridylmethyl)-1,2-diaminoethane) and $[Mn^{IV}(O)(N4Py)]^{2+}$ (N4Py = *N*,*N*-bis(2-pyridylmethyl)-bis(2-pyridyl)methylamine) (see Figure 1), in oxidation reactions.[21] Herein, we provide a catalytic process for the generation of chlorine dioxide from chlorite using two non-heme manganese(II) complexes, $[Mn^{II}(N4Py)]^{2+}$ and $[Mn^{II}(Bn\text{-}TPEN)]^{2+}$. The reaction proceeds efficiently reaching completion within 30 min with as little as 0.1 mol% catalyst loading under ambient temperature and noncorrosive pH. The catalytic formation of chlorine dioxide is observed for both $[Mn^{II}(N4Py)]^{2+}$ and $[Mn^{II}(Bn\text{-}TPEN)]^{2+}$ with second-order

rate constants of 74 and 33 M^{-1} s^{-1}, respectively. For the non-heme manganese complexes in this report, catalysis initiates via OAT to generate a putative $Mn^{IV}(O)$ species. As chlorine dioxide is produced, a $Mn^{III}(OH)$ species accumulates and the ClO_2 product acts as an inhibitor of the reaction. A comprehensive mechanism that satisfies all experimental observations is obtained from quantitative kinetics modeling.

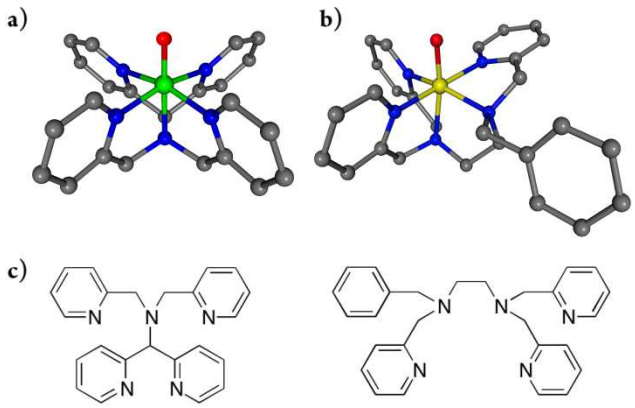

Figure 8-1. DFT-optimized structures of the complexes used as catalysts for the conversion of chlorite to chlorine dioxide. (a) $[Mn^{IV}(O)(N4Py)]^{2+}$ and (b) $[Mn^{IV}(O)(Bn\text{-}TPEN)]^{2+}$. (c) N4Py (left) and Bn-TPEN (right).

8.2 Results

Formation of ClO_2. The catalytic activity of $[Mn^{II}(N4Py)]^{2+}$ and $[Mn^{II}(Bn\text{-}TPEN)]^{2+}$ for ClO_2 production from ClO_2^- was examined at 25.0 °C in 50.0 mM acetate buffer at pH 5.00. Strikingly, if the pH of the buffer is increased then the production of ClO_2 is halted with the disproportionation of chlorite to chloride and chlorate instead being favored. This observation suggests the process for ClO_2 production is proton dependent. Additionally, when the buffer composition is changed from acetate to citrate, the production of ClO_2 is halted suggesting that the buffer is not innocent during catalysis. The formation of ClO_2 was monitored following its characteristic absorption band at λ_{max} = 360 nm (ε = 1250 M^{-}

^{1} cm^{-1}). The ClO_2 product can be extracted from the aqueous medium into diethyl ether. A typical spectrum of extracted ClO_2 from the catalytic reaction is shown in Figure 2a and is compared to an authentic sample of ClO_2. Negative mode electrospray ionization mass spectroscopy (ESI-MS) of the diethyl ether extract confirmed that ClO_2 (*m/z* = 67.0) and ClO_3^- (*m/z* = 83.0) were formed during the reaction. Chlorite is insoluble in diethyl ether, hence the peak at 67.0 m/z is that of ClO_2 and not ClO_2^- (Figure 2b). Dioxygen (O_2) was not observed in any of the reactions performed.

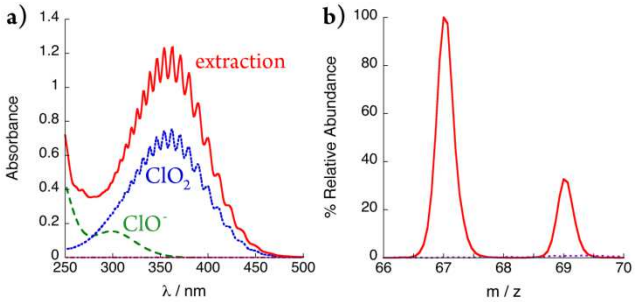

Figure 8-2. UV-vis spectroscopy and ESI-MS evidence for the formation of chlorine dioxide gas during catalysis. a) UV-vis spectra of an authentic sample of ClO_2 in diethyl ether (solid red), an extraction of ClO_2 from the catalytic reaction (dotted blue), difference spectrum/hypochlorite (dashed green), chlorite spectrum (dotted pink). b) ESI-MS of extracted ClO_2 from catalysis using 10.0 μM $[Mn^{II}(N4Py)]^{2+}$ and 8.00 mM ClO_2^- (solid red) and chlorite (dashed pink) in diethyl ether.

Products Analysis by Ion Chromatography (IC). Ion chromatography was used to identify and quantify chlorine containing anionic products. IC was performed on reaction mixtures upon maximum yield/concentration of ClO_2, confirming that the majority of the chlorite reactant was consumed and both Cl^- and ClO_3^- were also formed. When the concentration of chlorite or catalyst was increased, more chlorate was formed. Longer reaction times led to the complete decomposition of chlorite, while the concentration of chlorine dioxide remained relatively constant. The exact yields of anions of selected

reaction conditions are summarized in Table 1. Ion chromatograms and exact yields of anions for all reactions are provided in the Supporting Information (Figures S2 – S24 and Tables S1-5).

Table 8-1. Results for the Catalytic Conversion of Chlorite to Chlorine Dioxide in 50.0 mM Acetate Buffer (pH = 5.00)[a]

Catalyst	[cat]/ μM	$[ClO_2^-]_0$	$[ClO_2^-]_f$	$[Cl^-]$	$[ClO_3^-]$	$[ClO_2]$	% ClO_2[b]	% ox.[c]
Mn(N4Py)	10.0	10.0	4.24	2.24	1.79	1.68	29%	22%
Mn(N4Py)	10.0	4.00	1.10	1.10	0.88	0.91	31%	20%
Mn(N4Py)	100[d]	4.00	0.32	1.39	1.62	0.64	17%	16%
Mn(Bn-TPEN)	50.0	10.0	3.67	2.83	1.63	1.82	29%	34%
Mn(Bn-TPEN)	50.0	4.00	0.95	1.35	0.71	0.96	31%	34%
Mn(Bn-TPEN)	109[d]	4.00	0.86	1.49	0.64	1.01	35%	39%
Mn(N4Py)	10.0	-	-	0.01	0.12	0.61 – 0.47[e]	-	-
Mn(Bn-TPEN)	50.0	-	-	0.07	0.35	0.47 – 0.04[e]	-	-

[a] All concentrations are mM unless otherwise stated. Chlorine dioxide concentrations were quantified using UV-vis spectroscopy on the reaction mixture. Ion chromatography was used to quantify the concentrations of other chlorine containing species. Ion chromatograms were performed at 1 h unless otherwise stated. [b] Percentage calculated using the final concentration of chlorine dioxide divided by the concentration of reacted chlorite. [c] Percentage of oxidizing equivalence unaccounted for by chlorine containing species. [d] Ion chromatogram taken at maximum ClO_2 formation. [e] Chlorine dioxide prepared separately in acetate buffer. The range represents $[ClO_2]_0$ and 20 minutes after injection of catalyst.

Reactivity of Chlorine Dioxide with Manganese(II) and Manganese(III) Complexes. To test how the product affects the reaction, ClO_2 was collected in acetate buffer (pH 5) from a separate reaction and the reactivity of both catalysts with ClO_2 was examined. The reaction of ClO_2 with precatalyst, manganese(II) species, resulted in a rapid decrease in the absorption band for ClO_2 and the appearance of a Mn^{III}(OH) species for both manganese

complexes.[21] $[Mn^{II}(N4Py)]^{2+}$ was more reactive towards ClO_2 in comparison to $[Mn^{II}(Bn\text{-}TPEN)]^{2+}$ as shown in Figure 3. The reaction of ClO_2 with the resting state form of the catalyst, manganese(III) species, resulted in a slower decrease in absorption for ClO_2 relative to starting with $Mn^{II}(OH_2)$ (Figures S25-26). This observation implies that the decomposition of ClO_2 is dependent on the oxidation state of the catalyst.

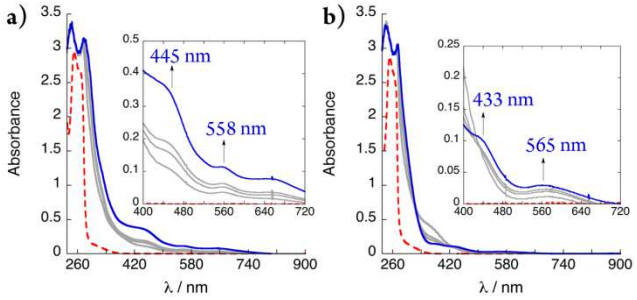

Figure 8-3. Examination of product inhibition by reacting ClO_2 with the manganese catalysts, $[Mn^{II}(N4Py)]^{2+}$ and $[Mn^{II}(Bn\text{-}TPEN)]^{2+}$. The dashed red spectrum is the starting catalyst. UV-vis scans at 2, 7, 12, 180 and 360 s. a) The reaction of $[Mn^{II}(N4Py)]^{2+}$ (500 μM) and chlorine dioxide (1.15 mM) results in the rapid disappearance of ClO_2 and the appearance of a $Mn^{III}(OH)$ species (see inset). b) The reaction of $[Mn^{II}(Bn\text{-}TPEN)]^{2+}$ (500 μM) and chlorine dioxide (1.15 mM) results in a slower disappearance of ClO_2 and the appearance of a $Mn^{III}(OH)$ species (see inset).

Absorption Spectroscopy and Kinetics. The consumption of chlorite can be monitored by the decrease in absorbance at 260 nm (ε = 154 M^{-1} cm^{-1}); however, both catalysts have a maximum absorption at this wavelength. Furthermore, the absorption of the catalyst increases as $Mn^{III}(OH)$ accumulates over the course of the reaction. Therefore, the reaction kinetics were studied following the formation of ClO_2 at 360 nm albeit the $Mn^{III}(OH)$ form of the catalyst also absorbs in this region but with minimal contribution due to its low extinction coefficient. While the time profiles at 360 nm (ClO_2) fit a single exponential equation to a first approximation, the time profiles exhibit features of more complex

kinetics (see Figures 4 and 5). Ion chromatography confirms that the majority of the chlorite is consumed (except for starting with high chlorite concentration of 10.0 mM) when the maximum concentration of ClO_2 is reached.

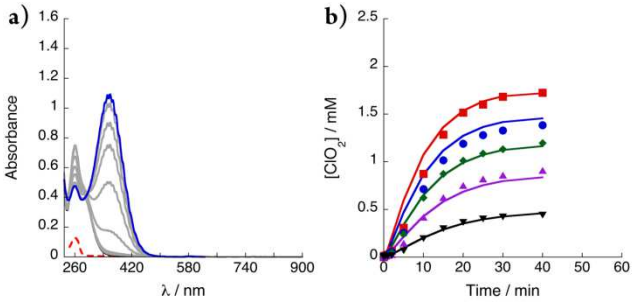

Figure 8-4. Kinetics of ClO_2 formation using $[Mn^{II}(N4Py)]^{2+}$ as a catalyst. a) UV-vis spectral changes of the reaction over 40 min. Initial catalyst (dashed), first and last scan (solid), others gray. Conditions: $[Mn^{II}(N4Py)]$ = 10.0 μM; $[ClO_2^-]$ = 4.05 mM. b) Changes in concentration of ClO_2 versus time. Solid lines represent kinetic modeling fits. Conditions: $[Mn^{II}(N4Py)]_0$ = 10.0 μM; $[ClO_2^-]_0$ = 9.85, 7.37, 6.00, 4.14, 1.95 mM (top to bottom).

The kinetics for $[Mn^{II}(N4Py)]^{2+}$ and $[Mn^{II}(Bn\text{-}TPEN)]^{2+}$ were examined. When a solution of chlorite (2.00–10.0 mM) was monitored in the presence of $[Mn^{II}(N4Py)]^{2+}$ (10.0 μM), an induction period was observed before the appearance of ClO_2. This induction period ranged from 5–300 s, depending on the initial catalyst concentration. When a solution of chlorite (2.00–10.0 mM) was monitored in the presence of $[Mn^{II}(Bn\text{-}TPEN)]^{2+}$ (50.0 μM), an induction period was not observed and ClO_2 followed approximately first-order kinetics. A five-fold increase in the concentration of $[Mn^{II}(Bn\text{-}TPEN)]^{2+}$ was necessary to achieve comparable reaction times as a result of its lower reactivity (Figures 4b and 5b).

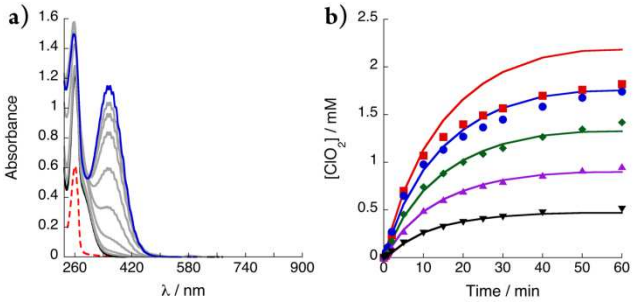

Figure 8-5. Kinetics of ClO_2 formation using $[Mn^{II}(Bn\text{-}TPEN)]^{2+}$ as a catalyst. a) UV-vis spectral changes of the reaction for 1 h. Initial catalyst (dashed), first and last scan (solid), others gray. Conditions: $[Mn^{II}(Bn\text{-}TPEN)]$ = 50.0 μM; $[ClO_2^-]$ = 4.00 mM. b) Change in concentration of ClO_2 versus time. Solid lines represent kinetic modeling fits. Conditions: $[Mn^{II}(Bn\text{-}TPEN)]_0$ = 50.0 μM; $[ClO_2^-]_0$ = 9.99, 7.93, 5.99, 4.02, 2.09 mM (top to bottom).

Preliminary inspection of the data shows dependence on $[ClO_2^-]$ and [Mn]. While the rate of reaction increases linearly with respect to the [Mn] (Figures S11a & S21a), the dependence on $[ClO_2^-]$, the limiting reagent, is more complex (Figures S11b & S21b). Furthermore, the amount of ClO_2 produced is dependent on $[ClO_2^-]$ in a nonlinear fashion (Table 1) with a maximum yield of ca. 31%. The sensitivity of ClO_2 yield indicates product inhibition or further decomposition of ClO_2 at high concentrations. It should also be noted that even with $[ClO_2^-]_0$ = 10.0 mM, ClO_2 production plateaus at ca. 1.82 mM. The effect of the product on the catalyst's state was investigated by performing successive additions of chlorite, which is described next.

Multiple Additions of ClO_2^-. The reactivity of both catalysts upon multiple additions of chlorite was examined. ClO_2^- (4.00 mM) was reacted with $[Mn^{II}(N4Py)]^{2+}$ (10.0 μM) or $[Mn^{II}(Bn\text{-}TPEN)]^{2+}$ (50.0 μM). Upon reaching the maximum concentration of ClO_2, the mixture was purged with argon gas for 5 minutes to remove the ClO_2 product. A second

aliquot of ClO_2^- (4.00 mM) was added to the catalyst solution and the kinetics of ClO_2 formation was monitored. A decrease in the observed rate was observed for both catalysts, $[Mn^{II}(N4Py)]^{2+}$ with a 40% decrease while $[Mn^{II}(Bn\text{-}TPEN)]^{2+}$ had a 66% decrease, as a result of catalyst deactivation (Figure 6).

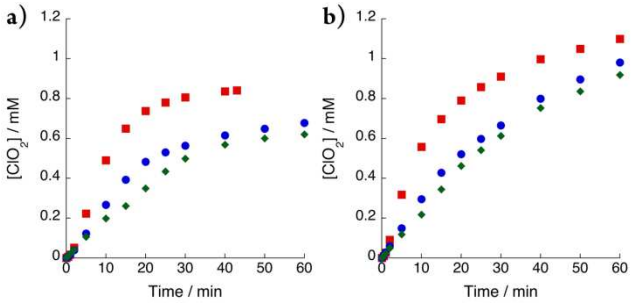

Figure 8-6. Further conversion to ClO_2 upon multiple additions of chlorite for manganese catalysts, $[Mn^{II}(N4Py]^{2+}$ and $[Mn^{II}(Bn\text{-}TPEN)]^{2+}$. Concentration of ClO_2 versus time for multiple additions of $[ClO_2^-] = 4.00$ mM upon purging the reaction mixture of ClO_2. First addition (squares), second addition (circles), third addition (diamonds). a) $[Mn^{II}(N4Py)] = 10.0$ μM. b) $[Mn^{II}(Bn\text{-}TPEN)] = 50.0$ μM.

Time-Dependent Product Distribution. To further elucidate the mechanism for chlorine dioxide formation, the concentrations of all chlorine-containing species were analyzed at 10 minute intervals by ion chromatography (ClO_2^-, Cl^-, ClO_3^-) and UV-vis spectroscopy (ClO_2) and fit by kinetic modeling. As expected, the reaction products chloride, chlorate, and chlorine dioxide are produced as chlorite is consumed (Figure 7). Chlorine dioxide reaches a plateau within 30 minutes while the concentration of both chloride and chlorate continue to increase over time.

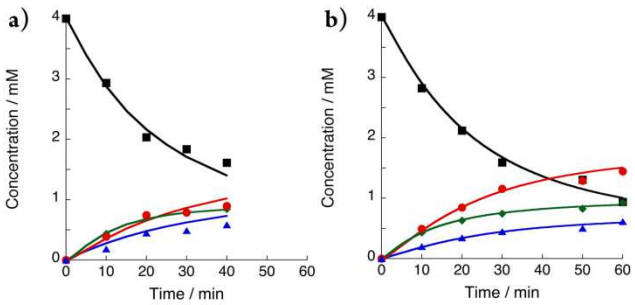

Figure 8-7. Time-dependent concentrations of chlorine containing species during catalysis. ClO_2^- (squares), Cl^- (diamonds), ClO_3^- (circles), and ClO_2 (triangles). Solid lines represent kinetic modeling fits. a) Reaction using $[Mn^{II}(N4Py)]^{2+}$ as catalyst. Conditions: $[Mn^{II}(N4Py)]$ = 10.0 μM; $[ClO_2^-]_0$ = 4.00 mM. b) Reaction using $[Mn^{II}(Bn\text{-}TPEN)]^{2+}$ as catalyst. Conditions: $[Mn^{II}(Bn\text{-}TPEN)]$ = 50.0 μM; $[ClO_2^-]_0$ = 4.00 mM.

Electron Paramagnetic Resonance (EPR). EPR spectroscopy was used to identify the change in oxidation state of the manganese catalysts. Both ClO_2^- (4.00 mM) and ClO_2 (1.00 mM) were reacted independently with $[Mn^{II}(N4Py)]^{2+}$ (500 μM) and $[Mn^{II}(Bn\text{-}TPEN)]^{2+}$ (500 μM) in acetate buffer (pH = 5.00). Figure 8 shows the EPR spectra for $[Mn^{II}(N4Py)]^{2+}$ and its reaction with ClO_2^- and ClO_2.The reactions with chlorite were allowed to react for 1 h, purged of ClO_2 using argon, then frozen. The same procedure was carried out for the reactions with ClO_2, except the reaction time was only 20 minutes. In these reactions, the characteristic signal for Mn^{II} is not observed and a feature that can be assigned to a $Mn^{III}(\mu\text{-}O)Mn^{IV}$ dinuclear complex emerges.[22] Both catalysts gave identical EPR spectra under reaction conditions. The EPR spectra for $[Mn^{II}(Bn\text{-}TPEN)]^{2+}$ can be found in the Supporting Information (Figure S1). Mn^{III} (S = 2) and Mn^{V} (S = 1 or 0) would not be observable in perpendicular mode EPR.

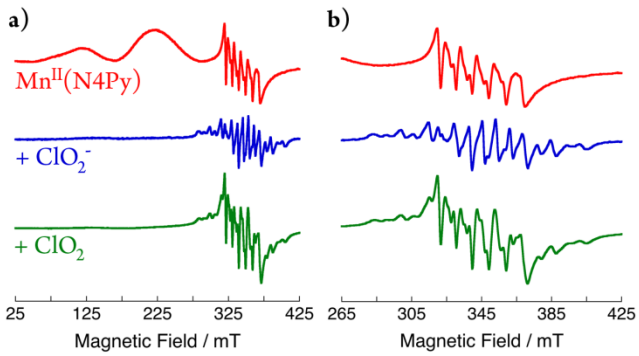

Figure 8-8. Formation of a $Mn^{III}(\mu\text{-}O)Mn^{IV}$ dinuclear species confirmed by EPR spectroscopy when the manganese catalyst $[Mn^{II}(N4Py)]^{2+}$ is reacted with chlorite and chlorine dioxide. Conditions: $[Mn^{II}(N4Py)]$ = 500 μM reacted with $[ClO_2^-]$ = 4.00 mM or $[ClO_2]$ = 1.15 mM. b) Expanded region of signals assigned to a $Mn^{III}(\mu\text{-}O)Mn^{IV}$ dinuclear species.

8.3 Discussion

Catalytic oxidation of ClO_2^- to ClO_2 by two water-soluble non-heme manganese complexes has been studied at 25.0 °C and pH = 5.00. To our knowledge, this is the first example of manganese non-heme complexes that catalyze this conversion. Good yields of ClO_2 were observed in less than 1 h using as little as 0.10 mol% $[Mn^{II}(N4Py)]^{2+}$ and 0.50 mol% $[Mn^{II}(Bn\text{-}TPEN)]^{2+}$. These catalyst loadings correspond to turnover frequencies (TOF), defined by $[ClO_2]$ versus catalyst loading versus time, of 1,000 and 200 h^{-1}, respectively. Since the production of ClO_2 in situ and on-site is important for industrial applications, these non-heme manganese catalysts offer a convenient route to ClO_2 production under reasonably mild and noncorrosive conditions.

Several manganese(III) porphyrin complexes have been examined for the catalytic formation of chlorine dioxide independently by our group and that of Groves.[15,16] The initial step for the heme complexes is oxygen atom transfer from chlorite to $[Mn^{III}]^+$ via either heterolytic or homolytic Cl–O bond cleavage of chlorite. Homolytic Cl–O bond

cleavage results in an $Mn^{IV}(O)$ species while heterolytic cleavage results in a $[Mn^{V}(O)]^{+}$ species. A proposed mechanism for the catalytic conversion of ClO_2^- to ClO_2 for manganese porphyrin catalysts is found in Scheme 1.

In contrast to the previously described manganese porphyrin systems, our non-heme catalysts described herein are present in the +2 oxidation state and are 5-coordinate. These catalysts also required higher catalyst loadings for comparable ClO_2 yields. Over the course of the reaction, the $Mn^{II}(OH_2)$ species is fully consumed giving rise to higher oxidation states of the manganese complexes as evident by UV-vis (Figure 3) and EPR spectroscopy (Figure 8). The relatively low stability of the $Mn^{IV}(O)$ species supported by N4Py and Bn-TPEN ligation in water solution suggests that this species does not accumulate at sufficient concentrations to be detected. These observations are in contrast to manganese porphyrin complexes where the precatalyst, $[Mn^{III}]^{+}$, remains the dominant form of the catalyst with $Mn^{IV}(O)$ and $[Mn^{V}(O)]^{+}$ species being proposed intermediates in the catalytic cycle. Another stark difference is the observed induction period when using $[Mn^{II}(N4Py)]^{2+}$ as a catalyst. The induction period indicates slower formation of the active species in comparison to $[Mn^{II}(Bn\text{-}TPEN)]^{2+}$ as a result of lower catalyst loading. The dominant observable form of the catalyst under catalysis is a $Mn^{III}(OH)$ species (UV-vis 440 and 560 nm). This complex has been prepared independently for the Bn-TPEN ligand.[21] The $Mn^{IV}(O)$ is expected to exhibit an absorption band at higher wavelength (ca. 1040 nm); furthermore, $Mn^{III}(OH)$ is also responsible for the increase in absorption at 260 nm (Figure 3). These observations as well as proposed reaction steps (Scheme 2) were used to predict the concentrations of these manganese species over the course of the reaction using a mathematical model as shown in Figure 9.

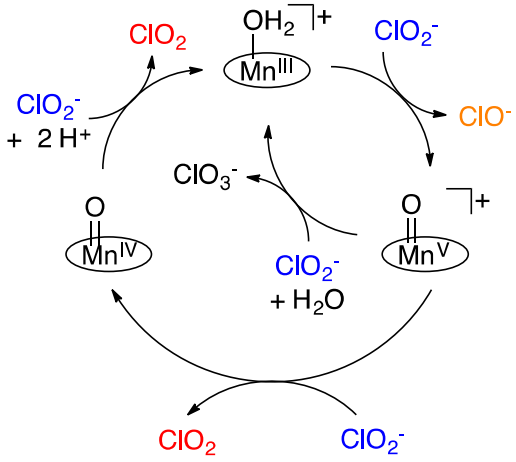

Scheme 8-1. General mechanism for the conversion of ClO_2^- to ClO_2 using water-soluble manganese porphyrin catalysts.

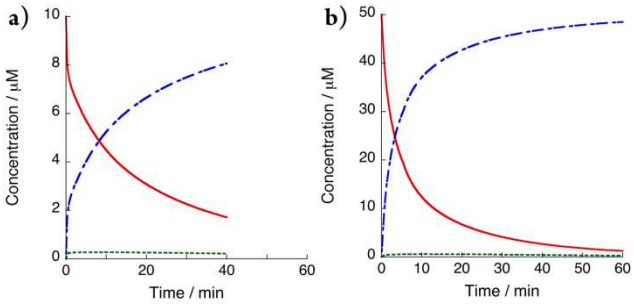

Figure 8-9. Predicted time-dependent concentrations of proposed manganese oxidation states versus reaction time. $Mn^{II}(OH_2)$ (solid red), $Mn^{III}(OH)$ (dashed blue), $Mn^{IV}(O)$ (dashed green). a) Using $[Mn^{II}(N4Py)]^{2+}$ as catalyst. Conditions: $[Mn^{II}(N4Py)]$ = 10.0 µM; $[ClO_2^-]$ = 4.00 mM. b) Using $[Mn^{II}(Bn\text{-}TPEN)]^{2+}$ as catalyst. Conditions: $[Mn^{II}(Bn\text{-}TPEN)]$ = 50.0 µM; $[ClO_2^-]$ = 4.00 mM.

Even though not observed directly, the putative $Mn^{IV}(O)$ and its participation is substantiated by the observation in the EPR spectra of a $Mn^{III}(\mu\text{-}O)Mn^{IV}$ dinuclear species.[22] The first-order dependence on [Mn] effectively rules out this dinuclear species as the active form of the catalyst, which would afford second-order kinetic dependence on catalyst. All of these observations are consistent with activation of the precatalyst via an OAT reaction with ClO_2^- forming $Mn^{IV}(O)$ and ClO^- (Eq. 1) to enter the proposed catalytic

cycle in Scheme 2. The hypochlorite formed does not rebound with the newly formed manganese–oxo species to form dioxygen but instead quickly reacts with excess chlorite to form chloride and chlorine dioxide (Eq. 7) with reaction kinetics provided in Figure S43. The high-valent manganese–oxo species then has three fates: 1) react via a PCET reaction with chlorite to give ClO_2 and $Mn^{III}(OH)$ (Eq. 2), 2) react via an OAT reaction with chlorite to form chlorate and precatalyst (Eq. 4), or 3) reacting with the dominant form of the catalyst, $Mn^{III}(OH)$, to form the dinuclear $Mn^{III}(\mu\text{-}O)Mn^{IV}$ species. The first pathway produces chlorine dioxide, which involves protonation of the oxo ligand on Mn^{IV} and hence accounts for the observed pH dependence for ClO_2 production. The second pathway results in the formation of chlorate and precatalyst, which quickly reacts with chlorine dioxide (Eq. 4) to form $Mn^{III}(OH)$ thus re-entering the catalytic cycle. The chlorate that is formed does not react with either of the catalysts under the conditions used. The dominant species, $Mn^{III}(OH)$, reacts with chlorite in the presence of protons via homolytic Cl–O bond cleavage to form [ClO] and regenerate the $Mn^{IV}(O)$ species (Eq. 3). This proposal has precedence in the iron heme systems based on DFT calculations.[23] The [ClO] radical byproduct is known to react with chlorite to make ClO^- and ClO_2.[24] [ClO] also reacts with ClO_2 to give $[Cl_2O_3]$, which disproportionates in water to HOCl, ClO_3^-, and H^+.[25] However, in our proposed reaction mechanism the [ClO] species reacts with buffer to form chloride and peracetic acid (Eq. 8). To account for the apparent slowing down and eventual cessation of the production of ClO_2 as well as other species, the deactivation reaction assumed to be either ligand oxidation or metal dissociation is included (Eq. 6). Rate constants, obtained from mathematical modeling, for the reaction steps described are given

in Table 2. The rate constant (k_8) for Eq. 8 is fast enough to be considered instantaneous relative to the other proposed reactions.

Table 8-2. Rate Constants for the Catalytic Conversion of Chlorite to Chlorine Dioxide in 50.0 mM Acetate Buffer (pH = 5.00).[a]

Catalyst	k_1	k_2	k_3	k_4	k_5	k_6	k_7 ($M^{-2/3}$ s^{-1}) [b]
Mn(N4Py)	19.2	207	21.0	500	74.2	0.3	1.8
Mn(Bn-TPEN)	3.0	265	6.3	173	33.3	0.5	1.8

[a] All rate constants are k * M^{-1} s^{-1} unless otherwise stated. See Scheme 2 or Equations 1-7 for reaction steps. [b] In Eq. 7, the reaction is 1st order in [ClO^-] and 2/3 order in [$ClO2^-$]. Determination of reaction order is described in SI.

The mathematical model accurately predicts the induction period observed for $[Mn^{II}(N4Py)]^{2+}$ where the reaction of precatalyst with chlorite is slow relative to subsequent reactions. An induction period was not observed for $[Mn^{II}(Bn\text{-}TPEN)]^{2+}$ as a result of higher catalyst loading. The model also predicts that the reactivity of chlorite with $Mn^{III}(OH)$ (k_5) is slower than $Mn^{IV}(O)$ (k_2) supporting the observation that $Mn^{III}(OH)$ is the dominant form during catalysis. The disappearance of the characteristic $Mn^{II}(OH_2)$ signal by EPR spectroscopy suggests that the precatalyst, if regenerated, is quickly converted to higher oxidation state species. According to the mathematical model the assumption that precatalyst is generated but quickly converted is validated by the observed product inhibition.

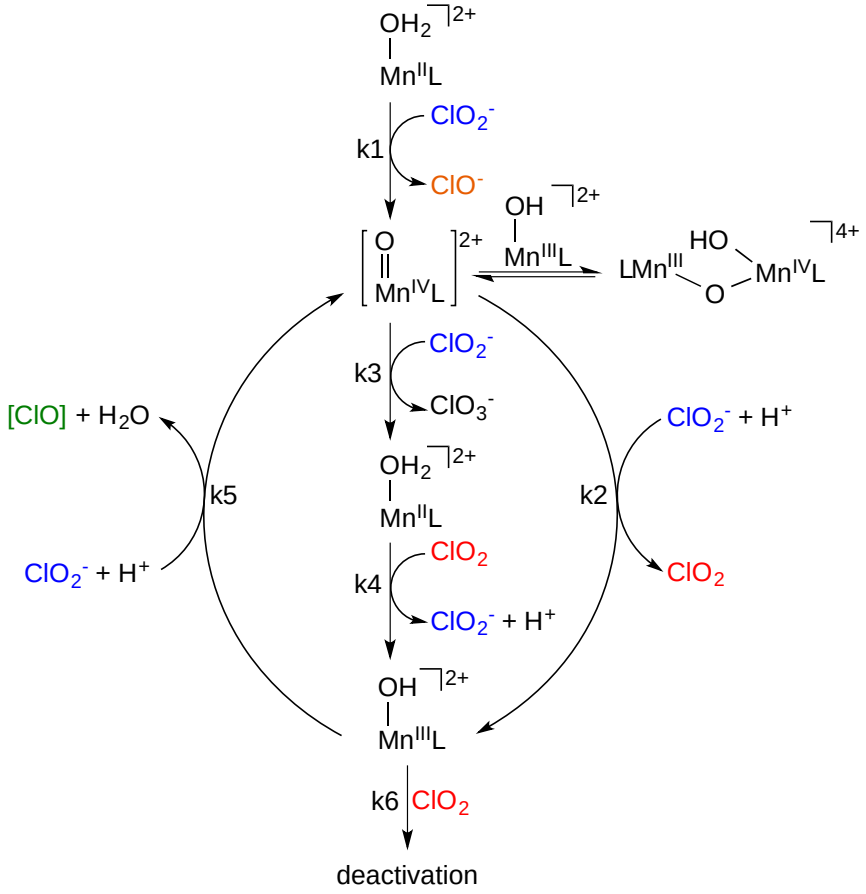

$$Mn^{II}(OH_2)L + ClO_2^- \xrightarrow{k_1} Mn^{IV}(O)L + ClO^- + H_2O \quad (1)$$

$$Mn^{IV}(O)L + ClO_2^- + H^+ \xrightarrow{k_2} Mn^{III}(OH)L + ClO_2 \quad (2)$$

$$Mn^{IV}(O)L + ClO_2^- + H_2O \xrightarrow{k_3} Mn^{II}(OH_2)L + ClO_3^- \quad (3)$$

$$Mn^{II}(OH_2)L + ClO_2 \xrightarrow{k_4} Mn^{III}(OH)L + ClO_2^- + H^+ \quad (4)$$

$$Mn^{III}(OH)L + ClO_2^- + H^+ \xrightarrow{k_5} Mn^{IV}(O)L + [ClO] + H_2O \quad (5)$$

$$Mn^{III}(OH)L + ClO_2 \xrightarrow{k_6} \text{deactivation} \quad (6)$$

$$2\,ClO_2^- + ClO^- + 2\,H^+ \xrightarrow{k_7} 2\,ClO_2 + Cl^- + H_2O \quad (7)$$

$$2\,[ClO] + 3\,C_2H_3O_2^- + H_3O^+ \xrightarrow{k_8} 2\,Cl^- + 3\,C_2H_4O_3 \quad (8)$$

Scheme 8-2. Proposed mechanism for the conversion of ClO_2^- to ClO_2 using two water-soluble non-heme manganese complexes.

A word is in order here regarding the overall stoichiometry of the reaction. The precatalyst enters the catalytic cycle by converting chlorite to hypochlorite via OAT (Eq.

1), which then reacts with chlorite to produce 2:1 equivalence of ClO_2:Cl^- (Eq. 7). Subsequent formation of ClO_2 from chlorite is expected to produce 1:1 equivalence of ClO_2:Cl^- for the outer cycle shown in Scheme 2. The inner reaction pathway results in a 1:1 equivalence of ClO_3^-:Cl^-. The resulting balanced equation results in a 2:1:1 equivalence of Cl^-:ClO_2:ClO_3^-, which is consistent with the product ratios when using $[Mn^{II}$(Bn-TPEN)$]^{2+}$ as the catalyst. All balanced reactions can be found in the Supporting Information. Our product ratios in Table 1 show variable values that depend on the starting concentrations of chlorite. All of the converted chlorite can be accounted for by the three products ClO_2, Cl^-, and ClO_3^-. However, a significant oxidizing equivalent is not accounted for in the chlorine containing products. For example, in the first entry of Table 1, 5.76 mM of ClO_2^- is converted. Based on Cl(III) oxidation state, this corresponds to a reactants overall oxidation state equivalent of +17.28. The products are 2.24 mM Cl^- (oxidation state equivalent of -2.24), 1.79 mM ClO_3^- (oxidation state equivalent of +8.95), and 1.68 mM ClO_2 (oxidations state equivalent of +6.72). While the total products comes to 5.76 mM, accounting nearly for all the chlorite conversion, the net oxidation state equivalent of the products is +13.43, leaving ca. 22% of the reactants oxidizing equivalents not accounted for. We probed for potential water oxidation by looking if O_2 is produced. The result was negative - no O_2 was observed. That limits the possibilities to the oxidation of the buffer. This theory is supported by the halt in ClO_2 formation when the buffer composition was changed from acetate to citrate with the same buffer capacity and pH. However, we were unable to detect acetate oxidation products in our system by mass spectrometry. It is noted that acetate buffer is frequently used in studying kinetics of ClO_2 reactions.[25]

Multiple additions of ClO_2^- for both catalysts were conducted to determine whether the catalysts were still active for the catalytic formation of ClO_2. Both manganese catalysts remained active for the production of ClO_2; however, slower reaction rates were observed with relatively comparable yields of ClO_2. This can be attributed to the relatively robust nature of the ligands and their manganese complexes under oxidizing conditions allowing for the observed high turnover numbers for ClO_2 formation of 2,160 and 560 for $[Mn^{II}(N4Py)]^{2+}$ and $[Mn^{II}(Bn\text{-}TPEN)]^{2+}$, respectively. These turnover numbers result from three successive additions of chlorite with a mild decrease in ClO_2 yield suggesting that even higher turnovers can be obtained.

8.4 Conclusions

Two non-heme coordination complexes of manganese, $[Mn^{II}(N4Py)]^{2+}$ and $[Mn^{II}(Bn\text{-}TPEN)]^{2+}$, catalyze the formation of chlorine dioxide from chlorite under ambient temperature at pH = 5.00. The catalysts are robust and stable enough to afford 1,000 turnovers per hour and still remain active in subsequent additions of chlorite. Kinetic and spectroscopic studies revealed that a $Mn^{III}(OH)$ species is the dominant form of the catalyst under reaction conditions. However, a $Mn^{III}(\mu\text{-}O)Mn^{IV}$ dinuclear species is observed by EPR spectroscopy, which supports the involvement of a putative $Mn^{IV}(O)$ species. The first-order kinetic dependence on the manganese catalyst precludes the $Mn^{III}(\mu\text{-}O)Mn^{IV}$ dinuclear species as the active form of the catalyst. Based on quantitative kinetic modeling, a mechanism has been put forth to explain the experimental observations (Scheme 2). The chlorine dioxide producing cycle involves formation of a $Mn^{IV}(O)$, which undergoes PCET reactions with chlorite to afford ClO_2. The proposed mechanism differs

from that of the manganese porphyrin systems as a result of the difference in ligand coordination to the metal (4 versus 5 coordinate) as well as the starting oxidation state. While the chlorine mass balance is excellent and the converted chlorite can be fully accounted for by the observed three products, ClO_2 Cl^-, and ClO_3^-, a significant oxidizing equivalent is not accounted for by the experimentally observed stoichiometric ratios of products. Nevertheless, the ClO_2 product can be efficiently removed from the aqueous reaction mixture via purging with an inert gas. These manganese non-heme catalysts offer a new method for the preparation of pure chlorine dioxide for on-site use, and further production of ClO_2.

REFERENCES

(1) a) EPA (2002 External Review Draft) “Perchlorate environmental contamination: toxicological review and risk characterization” 2001, Washington, D.C. b) Urbansky, E. T.; Schock, M. R. *J. Environ. Mangage.* 1999, *56*, 79-95.

(2) Motzer, W. E. *Environ. Forens.* 2001, *2*, 301-311.

(3) Coates, J. D.; Achenbach, L. A. *Perchlorate, Environmental Occurrence, Interactions and Treatment* (Eds.: Gu, B. and Coates, J. D.), Springer, New York, 2006, 279-291.

(4) Abu-Omar, M. M. *Chem. Commun.* 2003, *17*, 2102-2111.

(5) a) Deshwal, B. R.; Jo, H. D.; Lee, H. K.; *Can. J. Chem. Eng.* 2004, *82*, 619-623. b) Jia, Z.; Margerum, D. W.; Francisco, J. S. *Inorg. Chem.* 2000, *39*, 2614-2620. c) Furman, C. S.; Margerum, D. W. *Inorg. Chem.* 1998, *37*, 4321-4327. d) Cosson, H.; Ernst, W. R. *Ind. Eng. Chem. Res.* 1994, *33*, 1468-1475. e) Leitner, N. K. V.; Delaat, J.; Dore, M. *Water Res.* 1992, *26*, 1655-1664.

(6) Fábián, I. *Coord. Chem. Rev.* 2001, *216-217*, 449-472.

(7) Collman, J. P.; Boulatov, R.; Sunderland, C. J.; Shiryaeva, I. M.; Berg, K. E. *J. Am. Chem. Soc.* 2002, *124*, 10670-10671.

(8) Slaughter, L. M.; Collman, J. P.; Eberspacher, T. A.; Brauman, J. I. *Inorg. Chem.* 2004, *43*, 5198-5204.

(9) EPA 816-F-03-016, June 2003; available for download at http://www.epa.gov/safewater/mcl.html.

(10) a) Coates, J. D.; Achenbach, L. A. *Nat. Rev. Microbiol.*, 2004, *2*, 569-580. b) Thorell, H. D.; Stenklo, T. K.; Karlsson, J.; Nilsson, T. *Appl. Environ. Microbiol.* 2003, *69*, 5585-5592.

(11) a) Giblin, T.; Frankenberger, W. T. *Microbiol. Res.* 2001, *156*, 311-315. b) Kengen, S. W. M.; Rikken, G. B.; Hagan, W. R.; van Ginkel, C. G.; Stams, A. J. M. *Bacteriol.* 1999, *181*, 6706-6711. c) Okeke, B. C.; Frankenberger, W. T. *Microbiol. Res.* 2003, *158*, 337-344.

(12) a) Hagedoorn, P. L., de Geus, D. C.; Hagan, W. R. *Eur. J. Biochem.* 2002, *269*, 4905-4911. b) Thorell, H. D.; Karlsson, J.; Portelius, E.; Nilsson, T. *Biochim. Biophys. Acta* 2002, *1577*, 445-451. c) Stenklo, K.; Thorell, H. D.; Bergius, H.; Aasa, R.; Nilsson, T. *J. Biol. Inorg. Chem.* 2001, *6*, 601-607. d) Thorell, H. D.; Beyer, N. H.; Heegaard, N. H. H.; Ohman, M.; Nilsson, T. *Eur. J. Biochem.* 2004, *271*, 3539-3546. e) Xu, J. L.; Logan, B. E. *J. Microbiol. Met.*, 2003, *54*, 239-247. f) O'Connor, S. M.; Coates, J. D. *Appl. Environ. Microbiol.* 2002, *68*, 3108-3113.

(13) a) Streit, B. R.; DuBois, J. L. *Biochemistry* 2008, *47*, 5271-5280. b) Lee, A. Q.; Streit, B. R.; Zdilla, M. J.; Abu-Omar, M. M.; DuBois, J. L. *Proc. Natl. Acad. Sci. USA* 2008, *105*, 15654-15659.

(14) Zdilla, M. J.; Lee, A. Q.; Abu-Omar, M. M. *Inorg. Chem.* 2009, *48*, 2260-2268.

(15) Hicks, S. D.; Petersen, J. L.; Bougher, C. J.; Abu-Omar, M. M. *Angew. Chem., Int. Ed.* 2011, *50*, 699-702.

(16) a) Umile, T. P.; Wang, D.; Groves, J. T. *Inorg. Chem.* 2011, *50*, 10353-10362. b) Umile, T. P.; Groves, J. T. *Angew. Chem., Int. Ed.* 2011, *50*, 695-698.

(17) Hu, Z.; Du, H.; Man, W.-L.; Leung, C.-F.; Liang, H.; Lau, T.-C. *Chem. Commun.* 2012, *48*, 1102-1104.

(18) Alternative Disinfectants and Oxidants, Guidance Manual (EPA 815-R-99-014), 1999; available at http://www.epa.gov/ogwdw/mdbp/pdf/alter/chapt_4.pdf.

(19) Chlorine Oxides and Chlorine Oxygen Acids: Vogt, H.; Balej, J.; Bennett, J. E.; Wintzer, P.; Sheikh, S. A.; Gallone, P.; Vasudevan, S.; Pelin, K. in *Ullmann's Encyclopedia of Industrial Chemistry*, Wiley-VCH, Weinheim, 2010, 55.

(20) Ogata, N.; Shibata, T. *J. Gen. Virol.* 2008, *89*, 60-67.

(21) a) Wu, X.; Seo, M. S.; Davis, K. M.; Lee, Y.-M.; Chen, J.; Cho, K.-B.; Pushkar, Y. N.; Nam, W. *J. Am. Chem. Soc.* 2011, *133*, 20088-20091. b) Chen, J.; Lee, Y.-M.; Davis, K. M.; Wu, X.; Seo, M. S.; Cho, K.-B.; Yoon, H.; Park, Y. J.; Fukuzumi, S.; Pushkar, Y. N.; Nam, W. *J. Am. Chem. Soc.* 2013, *135*, 6388-6391.

(22) a) Huang, P.; Högblom, J.; Anderlund, M. F.; Sun, L.; Magnuson, A.; Styring, S. *J. Inorg. Biochem.* 2004, *98*, 733-745. b) Huang, P.; Magnuson, A.; Lomoth, R.;

Abrahamsson, M.; Tamm, M.; Sun, L.; van Rotterdam, D.; Park, J.; Hammarstrom, L.; Akermark, B.; Styring, S. *J. Inorg. Biochem.* 2002, *91*, 159-172.

(23) Keith, J. M.; Abu-Omar, M. M.; Hall, M. B. *Inorg. Chem.* 2011, *50*, 7928-7930.

(24) Buxton, G. V.; Subhani, M. S. *J. Chem. Soc. Faraday Trans. 1* 1972, *68*, 947 – 957.

(25) Cseko, G.; Horvath, A. K. *J. Phys. Chem. A* 2012, *116*, 2911-2919.

CHAPTER 9. CONCLUSION

Comprehensive kinetic studies of a family of single-site catalytic systems based on group IV amine bis-phenolate complexes have been completed, and the relevant rate constants and elementary reaction steps were robustly determined for each system. The mechanism usually includes initiation, normal propagation, misinsertion, recovery, and chain transfer. Correlations were found between the metal pendant ligand bond distance and the rate constants of chain transfer, and between the HOMO energy and the rate constants of propagation, misinsertion, and recovery from misinsertion. In the study of $Zr[tBu\text{-}ON^{THF}O]Bn_2/B(C_6F_5)_3$ system under sub-stoichiometric activator conditions, a Ligand Transfer Model was developed using quantitative kinetic analysis to describe the diverse data set. This mechanism includes the formation of the binuclear complex (BNC) consisting of the neutral catalytic species and an active site connected via degenerative transfer of benzyl ligand. In the study of $Zr[tBu\text{-}ON^{NEt2}O]Bn_2/B(C_6F_5)_3$ system, a new type of active site was discovered that was capable to polymerize branched high-MW polymers through the incorporation of vinyl terminated oligomers.

The kinetics analysis was also applied to the zwitterionic ring-opening polymerization. Our investigations revealed several key insights on the rate of zwitterionic ring-opening polymerization of caprolactone and the reaction steps responsible for the time evolution of molecular weights and polydispersities.

Finally the kinetics study of a non-polymerization system is provided: formation of chlorine dioxide from chlorite catalyzed by two non-heme coordination complexes. Based on quantitative kinetic modeling, a mechanism has been put forth to explain the experimental observations.

APPENDICES

Appendix A Modeling Methods

The goal of kinetic modeling of a complicated reaction such as polymerization is twofold: (1) to establish which elementary reaction steps and which intermediate species occur in the course of the reaction and (2) to obtain via fitting the kinetic data the values of the rate constants for each of these elementary reactions. In reality the available experimental data are always limited and therefore several different sets of elementary reactions i.e. different mechanisms, may fit the data equally well within the experimental error. In that case the result of the kinetic analysis should choose the minimal mechanism consistent with the data, i.e. the principal of Occam's Razor. Thus, the methodology (described in details elsewhere[2,3]) for determining the kinetic mechanism consists of (i) postulating the simplest possible set of elementary reactions (e.g. initiation and propagation) and (ii) then attempting to fit the multi-response data. If this initial model is unable to describe the data, then a new elementary reaction (e.g. monomer independent chain transfer) is added to the reaction mechanism and the fitting procedure is attempted a second time. This sequential model evolution and evaluation of its descriptive capabilities of the candidate kinetic model is continued until an adequate fit to the multi-response experimental data is achieved. The key issue during the evolution of the kinetic model is to critically evaluate the qualitative features of each model to determine what types of kinetic behavior results from the addition of new chemical steps, where this understanding guides the selection of the process that needs to be added to the next generation of the kinetic model.

Once a candidate mechanism is postulated, the set of the elementary reactions is fully defined and the time evolution of the concentrations of all the species participating in the reaction can be calculated and compared to the experimental data. The standard procedure consists of solving the system of ordinary differential equations (ODE) that define the time dependent concentration of the species; there are known as population balance equations. In case of a polymerization reaction this means that the polymeric species of all possible lengths are included so for example, if the maximum length chain has 10^3 repeat units then there are at least 10^3 species and, hence, there will be of order 10^3 equations in the ODE set. Knowing the concentrations of the chains of all lengths allows calculating the MWD at any time in the course of the reaction.

However, ODE methods are significantly more difficult when the number of chemical species is combinatorially large as is the case when the reaction evolves two polymeric species, e.g., there is the association/dissociation of two polymer species that occurs via a BNC mediated reaction. So for the above example where the maximum chain length is 10^3 there are of order 10^6 ODE terms. Although we have developed computational tools to automatically generate and repeatedly solve (as required in the course of the rate constant optimization) systems of this size,[5] this process is inefficient. Thus, an alternative approach based on the dynamic Monte Carlo (DMC) method[6] has been developed to calculate the time evolution of the concentrations of all the species participating in the reaction. A computer code has been developed to implement the DMC solution procedure, where further details are provided in the Appendix E.

Appendix B Supporting Information for Chapter 2

1. Estimation of Error Bounds

Here we give an example of how the error bounds were obtained for one of the systems (Catalyst **1**). First, the entire data set consisting of (1) monomer consumption, (2) MWD, (3) primary and secondary active site counts, and (4) vinyl terminated group counts was fit to the chosen mechanism as explained in the main text. The resulting values of the rate constants are shown in Table SI1. Fits are shown in Figure 2 in the main text.

The error due to uncertainty in the active site counts was estimated as follows: the upper bound of the active site counts is given by the upper end of the error bars in Figure 2(C) were chosen instead of the average values and the optimization procedure was carried out. The resulting values of the rate constants are shown in Table SI2 as upper bound values. Analogously, the lower bound of the active site counts were used to obtain the corresponding rate constants also shown in Table SI2 (lower bound values). The resulting fits to the active sites data are shown in Figure SI1.

Table B-SI1. Optimized rate constants based on measured data.

	k_i (M^{-1} s^{-1})	k_p (M^{-1} s^{-1})	k_{mis} (M^{-1} s^{-1})	k_{rec} (M^{-1} s^{-1})	$k_{vinylidene}$ (s^{-1})	$k_{vinylene}$ (s^{-1})
Average	.082	8.0	.054	.047	1.40e-4	5.1e-5

Table B-SI2. Optimized rate constants based on the estimated error in the active site counts.

	k_i (M^{-1} s^{-1})	k_p (M^{-1} s^{-1})	k_{mis} (M^{-1} s^{-1})	k_{rec} (M^{-1} s^{-1})	$k_{vinylidene}$ (s^{-1})	$k_{vinylene}$ (s^{-1})
Upper bound	.089	8.2	.058	.047	1.44e-4	4.9e-5
Lower bound	.076	7.8	.051	.047	1.38e-4	5.3e-5

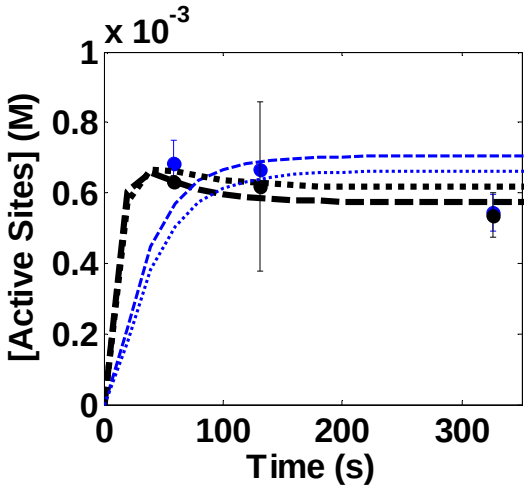

Figure B-SI1. Modeling fits of the active site counts using the upper bound (dashed lines) and the lower bound (dotted lines) sets of the rate constants given in Table SI2. The primary site counts are shown as black symbols, and the corresponding fits are shown as black lines. The secondary site counts are shown as blue symbols, and the corresponding fits are shown as blue lines. $[C]_0$ = 3.0 mM, $[M]_0$ = 0.60 M.

The error due to the uncertainty in the GPC measurements was estimated as follows: the MWD curve was shifted towards higher molecular weights by 0.04 on the log scale, and the entire data set was re-optimized giving rise to the rate constant values shown as upper bound values in Table SI3 (upper bound). Similarly, the MWD curve was shifted towards lower molecular weights by 0.05 on the log scale, and the entire data set was re-optimized giving rise to the lower bound rate constant, as shown in Table SI3 (lower bound). Figure SI2(B) illustrates the shift in the distributions.

Table B-SI3. Optimized rate constants based on the estimated error in the GPC measurements.

	k_i (M^{-1} s^{-1})	k_p (M^{-1} s^{-1})	k_{mis} (M^{-1} s^{-1})	k_{rec} (M^{-1} s^{-1})	$k_{vinylidene}$ (s^{-1})	$k_{vinylene}$ (s^{-1})
Upper bound	.098	8.8	.055	.045	1.54e-4	5.3e-5
Lower bound	.083	7.9	.080	.068	1.43e-4	4.8e-5

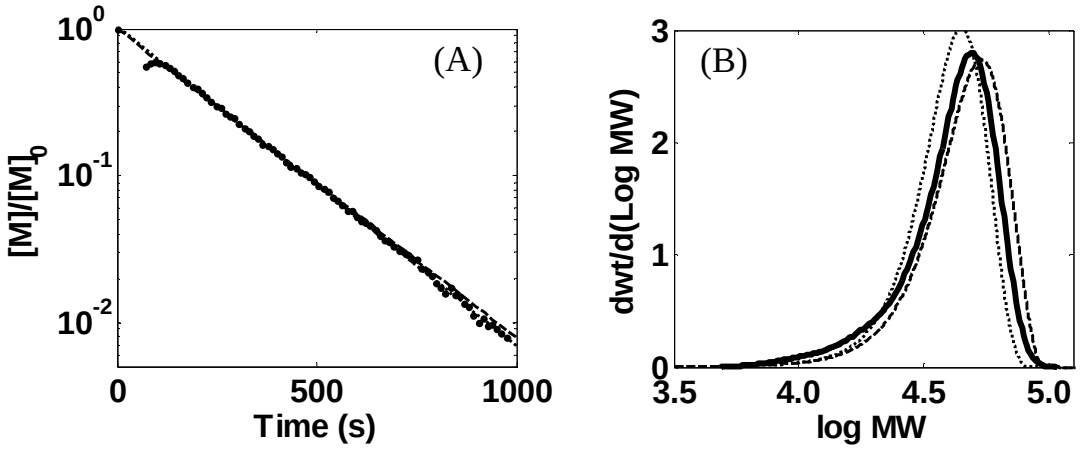

Figure B-SI2. Modeling Fits of (A) monomer consumption, (B) MWD using the upper bound (dashed lines) and the lower bound (dotted lines) sets of the rate constants given in Table SI3. $[C]_0$ = 3.0 mM, $[M]_0$ = 0.60 M.

Comparing rate constants in Tables SI2 and SI3, varying the MWD has the larger effect on the rate constants, and for this system, the error bars given in the main text are based on the error due to GPC measurements.

2. Detailed Kinetic Modeling

The modeling perspectives used in this communication (i) start with the simplest possible polymerization mechanism, (ii) determine if it fits the data, and (iii) if it does not fit the data within experimental error, postulate the next simplest mechanism. Using this procedure the simplest model consistent with the data is discovered.

2.1 Kinetic Modeling of Zr[tBu-ONTHFO]Bn2 Catalyst System

Mechanism I. Living polymerization.

We start by using the smallest model, i.e., the living polymerization model. A perfect fit of monomer consumption curve is obtained, however, the fit of MWD is

dramatically in error, where the experimental data exhibit both a higher molecular weight and a much broader distribution (Figure SI3).

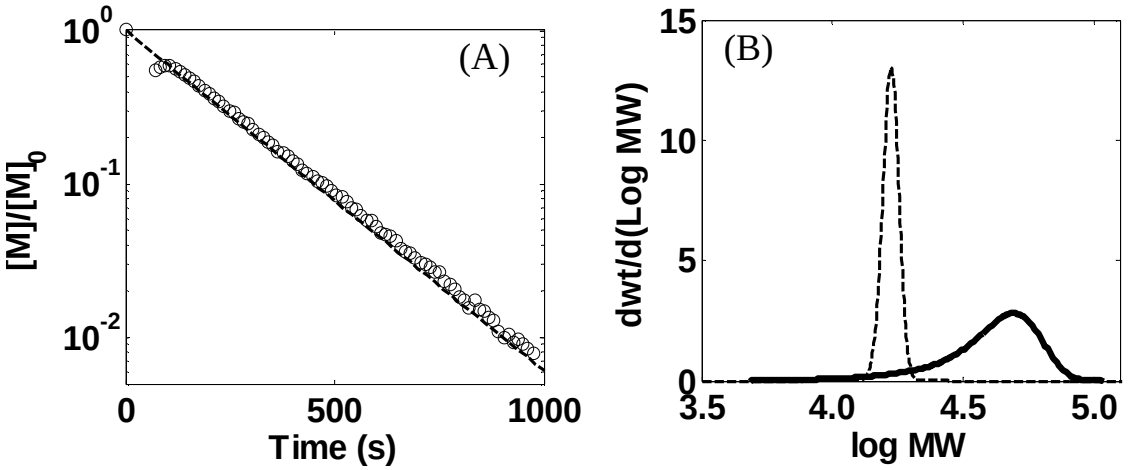

Figure B-SI3. Modeling using Mechanism I; data (A) monomer consumption (circles), (B) MWD (bold solid line); fits (dashed lines); rate constants: $k_i = k_p = 1.7\ M^{-1}\ s^{-1}$. $[C]_0 = 3.0$ mM, $[M]_0 = 0.60$ M.

Mechanism II. Slow initiation/incomplete catalyst participation.

There are two possible pathways to obtain higher molecular weight products: (1) slow initiation (red curves in Figure SI4), and (2) incomplete catalyst participation (blue curves in Figure SI4). Pathway 1 results in an apparent induction period, which does not exist in the experimental data. So pathway 2 is considered to be a better candidate to achieve the higher molecular weight observed experimentally for system **1**.

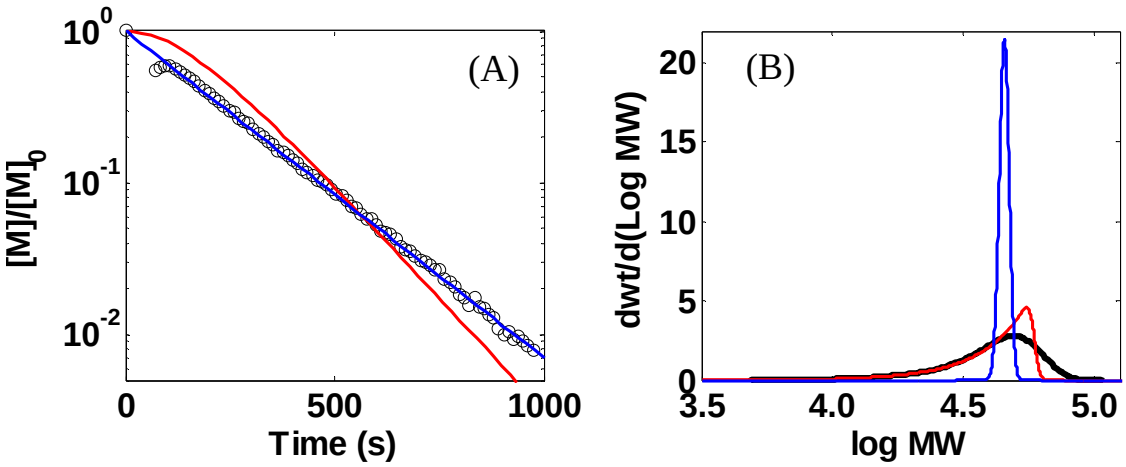

Figure B-SI4. Modeling using Mechanism II; data (A) monomer consumption data (circles), (B) MWD (bold solid line); fits (red and blue solid lines); rate constants: red: k_i = 0.0045 M^{-1} s^{-1}, k_p = 4.5 M^{-1} s^{-1}; blue: $k_i = k_p$ = 4.5 M^{-1} s^{-1}, active catalyst = 37%. $[C]_0$ = 3.0 mM, $[M]_0$ = 0.60 M.

Mechanism III. Monomer independent chain transfer.

The broadening of the MWD is commonly caused by chain transfer reaction, where a polymer chain leaves the metal center by forming a double bond (i.e. a vinyl terminated group). As a result of the monomer independent chain transfer via β-H elimination reaction, a metal hydride is formed, which in turn can be reinitiated to grow new chains. The monomer consumption curve is affected by this reinitiation rate (k_{reinit}). If k_{reinit} is fast (i.e. not slower than propagation), the total active site number in system **1** is conserved, and the monomer consumption curve is linear on log scale (red in Figure SI5). If k_{reinit} is slow, the monomer consumption curve is curved upward on log scale (blue in Figure SI5) at lower monomer concentrations, because chain transfer is monomer independent but reinitiation is monomer dependent. In the system **1**, we observe monomer consumption which is linear on log scale, so we assume a fast k_{reinit}.

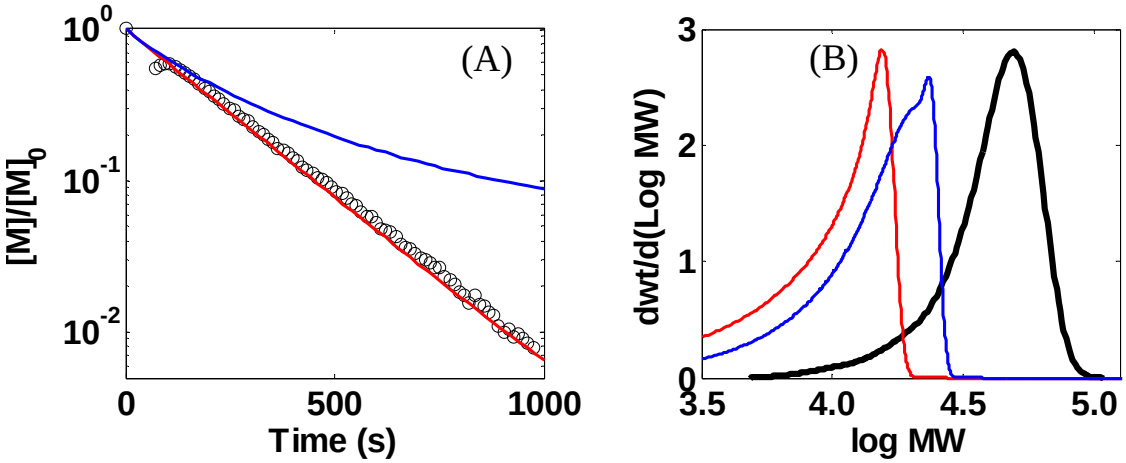

Figure B-SI5. Modeling using Mechanism III; data (A) monomer consumption data (circles), (B) MWD (bold solid line); fits (red and blue solid lines); rate constants: red: $k_i = k_p = k_{reinit} = 1.7\ M^{-1}\ s^{-1}$, $k_{ct} = 0.0038\ s^{-1}$; blue: $k_i = k_p = 1.7\ M^{-1}\ s^{-1}$, $k_{ct} = 0.003\ s^{-1}$, $k_{reinit} = 0.01\ M^{-1}\ s^{-1}$. $[C]_0 = 3.0$ mM, $[M]_0 = 0.60$ M.

Mechanism IV. Monomer independent chain transfer and incomplete catalyst participation.

To obtain an MWD which has a peak at high MW and is broad, we use a combined mechanism of monomer independent chain transfer and incomplete catalyst participation. The resulting fits are shown in Figure SI6, where the predicted MWD, although not perfect is qualitatively close to the data. To further validate this mechanism, we consider the vinyl terminated group counts. Significantly fewer (i.e. two orders magnitude lower by NMR) vinyl groups are experimentally observed than predicted by this mechanism in question (see Figure SI6(C)); thus chain transfer is ruled out as the cause for broadening of the MWD observed for system **1**.

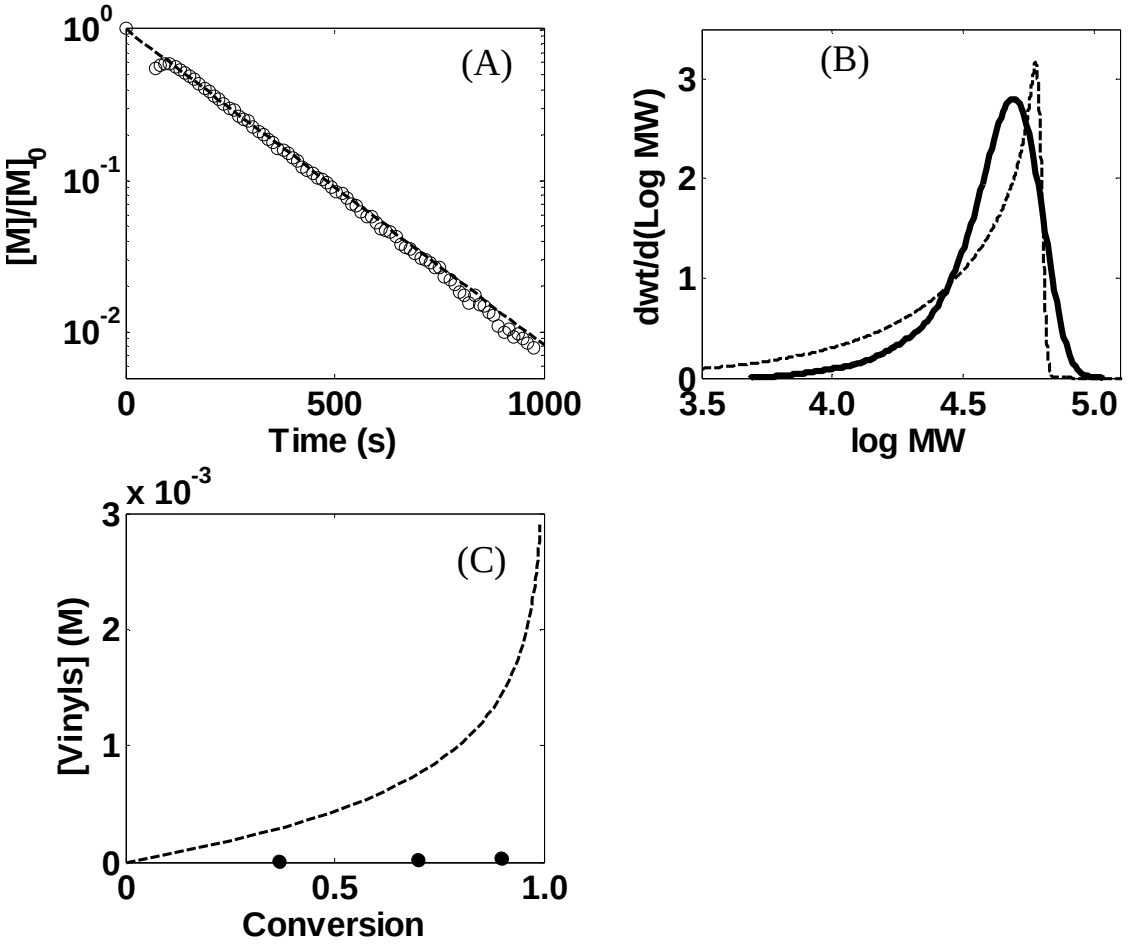

Figure B-SI6. Modeling using Mechanism IV; data (A) monomer consumption data (circles), (B) MWD (bold solid line), (C) vinyl terminated group counts (circles); fits (dashed lines); rate constants: $k_i = k_p = k_{reinit} = 6\ M^{-1}\ s^{-1}$, $k_{ct} = 0.0038\ s^{-1}$, active catalyst = 27%. $[C]_0 = 3.0$ mM, $[M]_0 = 0.60$ M.

Mechanism V. Misinsertion with slow recovery and incomplete catalyst participation.

If a misinsertion creates a specie that is significantly less reactive with monomer, such a catalytic site becomes dormant until recovery reaction occurs. The dormancy in conjunction with the slow recovery can also produce broad MWDs. This mechanism is supported by the experimental observation of vinyl counts and active site counts, where we observe two types of end groups and active sites. Depending on how the monomer is

inserted into the growing chain, there are primary active sites formed via 1,1-insertion and secondary sites formed via 1,2-insertion. Accordingly, chain transfer from primary site produces vinylidene terminated chain, chain transfer from secondary site produces vinylene terminated chain. The resulting fit is shown in (Figure SI7), where there is an excellent agreement with the exception of the last primary active site value at high conversion (i.e. longer time), which can be attributed to slight catalyst deactivation in the batch quench.

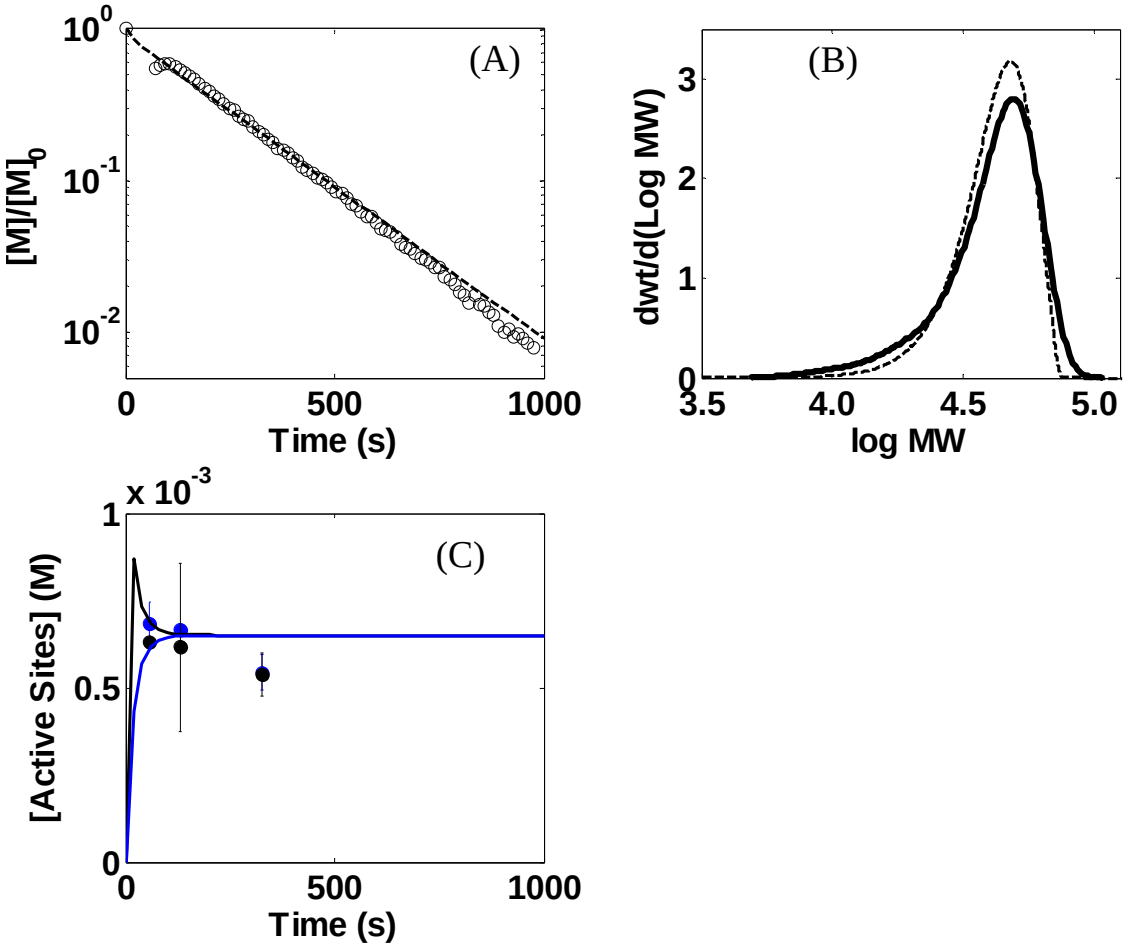

Figure B-SI7. Modeling using Mechanism V; data (A) monomer consumption data (circles), (B) MWD (bold solid line), (C) active site counts (black circles: primary site count, blue circles: secondary site counts); fits (dashed lines; fit of primary site count is shown in black; fit of secondary site count is shown in blue); constants: $k_i = k_p = 7\ M^{-1}\ s^{-1}$, $k_{mis} = k_{rec} = 0.05\ M^{-1}\ s^{-1}$, active catalyst = 43%. $[C]_0 = 3.0$ mM, $[M]_0 = 0.60$ M.

Mechanism VI. Misinsertion with slow recovery, incomplete catalyst participation, and little chain transfer.

Based on all our measurements and previous analysis, the minimal set of elementary steps are misinsertion with slow recovery, incomplete catalyst participation and little chain transfer. Typically, polymerizations at each initial condition are performed with multiple repeats, and the resulting data sets, including monomer consumption and MWD,

exhibit significant scatter (Figure SI8). The magnitude of the scatter exceeds the estimated experimental error of the NMR technique (based on 5% error in peak integration) used to obtain the data and conventional errors in measuring concentrations, etc. We believe that is because the amount of active catalyst can vary from experiment to experiment. Hence, the amount of active catalyst is allowed to be varied during the modeling of different data sets.

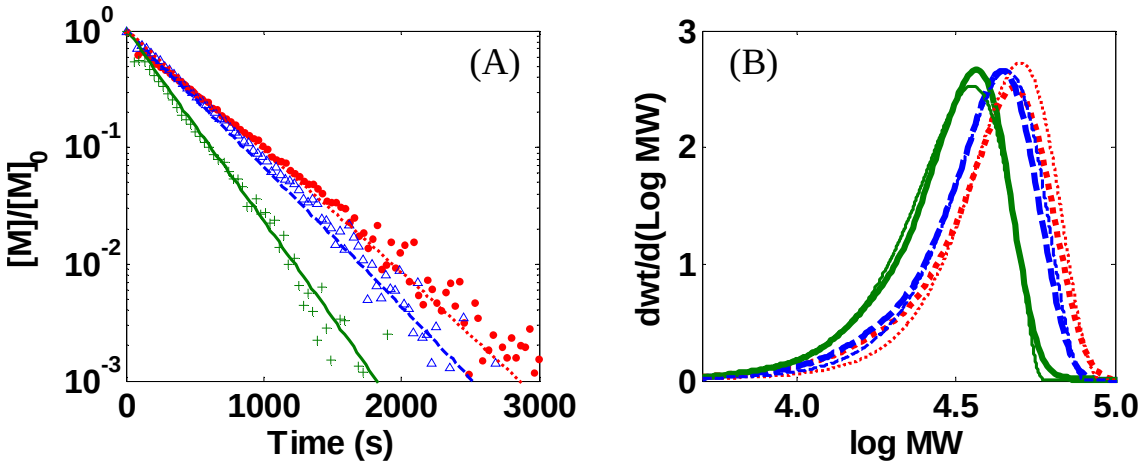

Figure B-SI8. Three repeats of NMR scale polymerizations ($[C]_0$ = 1.5 mM, $[M]_0$ = 0.30 M). (A) Monomer consumption. Modeling using Mechanism VI; Symbols are data, lines are fits. (B) MWDs of the polymer resulting from the reactions shown in (A). Bold lines are data, normal lines are fits. Modeled active catalyst percentage: 65% for green (pluses in monomer consumption, solid line in MWD), 47% for blue (triangles in monomer consumption, dashed line in MWD), 41% for red (dots in monomer consumption, dotted line in MWD). $[C]_0$ = 3.0 mM, $[M]_0$ = 0.60 M.

Finally, all the rate constants are optimized based on Mechanism VI. The fits of experimental data sets for various initial conditions are shown in Figure 2.

2.2 Kinetic Modeling of Zr[tBu-ONPyrO]Bn2 Catalyst System

Mechanism I. Living polymerization.

Here we start from the most basic model: living polymerization model. We achieve a good fit of monomer consumption curve. However, the fit of MWD is off dramatically. The experimental data exhibit much broader MWD (Figure SI9).

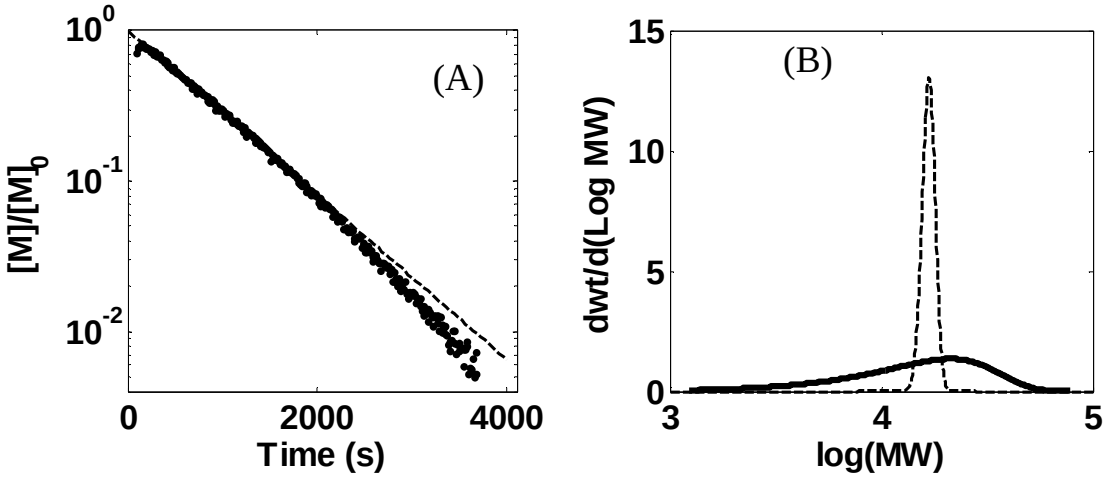

Figure B-SI9. Modeling using Mechanism I; data (A) monomer consumption data (dots), (B) MWD (bold solid line); fits (dashed lines); rate constants: $k_i = k_p = 0.42\ M^{-1}\ s^{-1}$. $[C]_0$ = 3.0 mM, $[M]_0$ = 0.60 M.

Mechanism II. Monomer independent chain transfer.

Monomer independent chain transfer mechanism was evaluated. If k_{reinit} is fast, the monomer consumption curve is linear on log scale (red in Figure SI10); in contrast, if k_{reinit} is slow, the monomer consumption curve is curved upward on log scale (blue in Figure SI10) at lower monomer concentrations. In the system **2**, the monomer consumption is nearly linear, with perhaps a small downward curve at the end on log scale; thus so we assume a fast k_{reinit}.

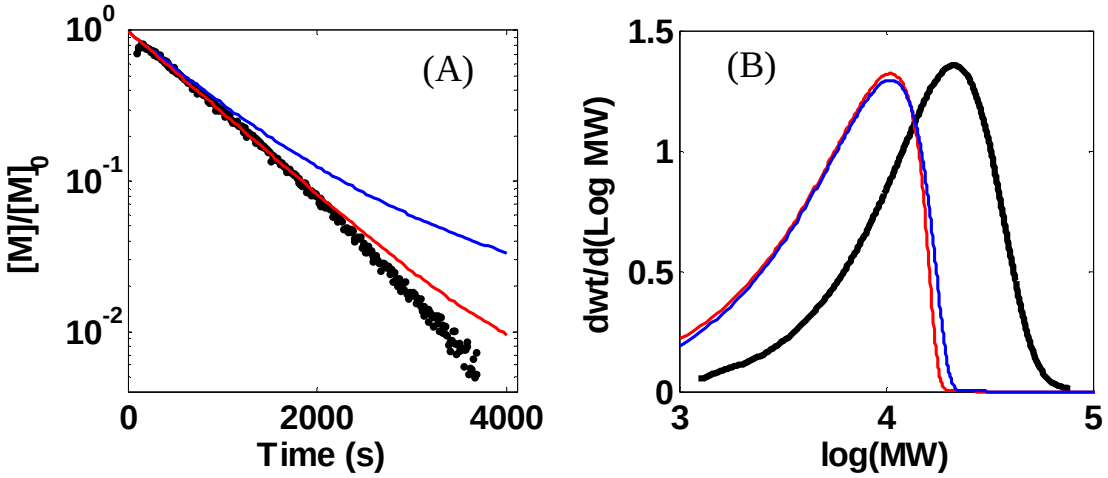

Figure B-SI10. Modeling using Mechanism II; data (A) monomer consumption data (dots), (B) MWD (bold solid line); fits (red and blue solid lines); rate constants: red: $k_i = k_p = k_{reinit} = 0.42\ M^{-1}\ s^{-1}$, $k_{ct} = 0.002\ s^{-1}$; blue: $k_i = k_p = 0.42\ M^{-1}\ s^{-1}$, $k_{ct} = 0.002\ s^{-1}$, $k_{reinit} = 0.042\ M^{-1}\ s^{-1}$. $[C]_0 = 3.0$ mM, $[M]_0 = 0.60$ M.

Mechanism III. Monomer independent chain transfer and slow initiation/ incomplete catalyst participation.

To increase the molecular weight of fits in Figure SI10(B), we examined the two mechanisms: (1) slow initiation (red curves in Figure SI11), (2) incomplete catalyst participation (blue curves in Figure SI11). Pathway 1 results in an apparent induction period, which is not seen in the experimental data; thus pathway 2 is considered to be a better candidate to achieve higher molecular weight experimentally observed in the system **2**.

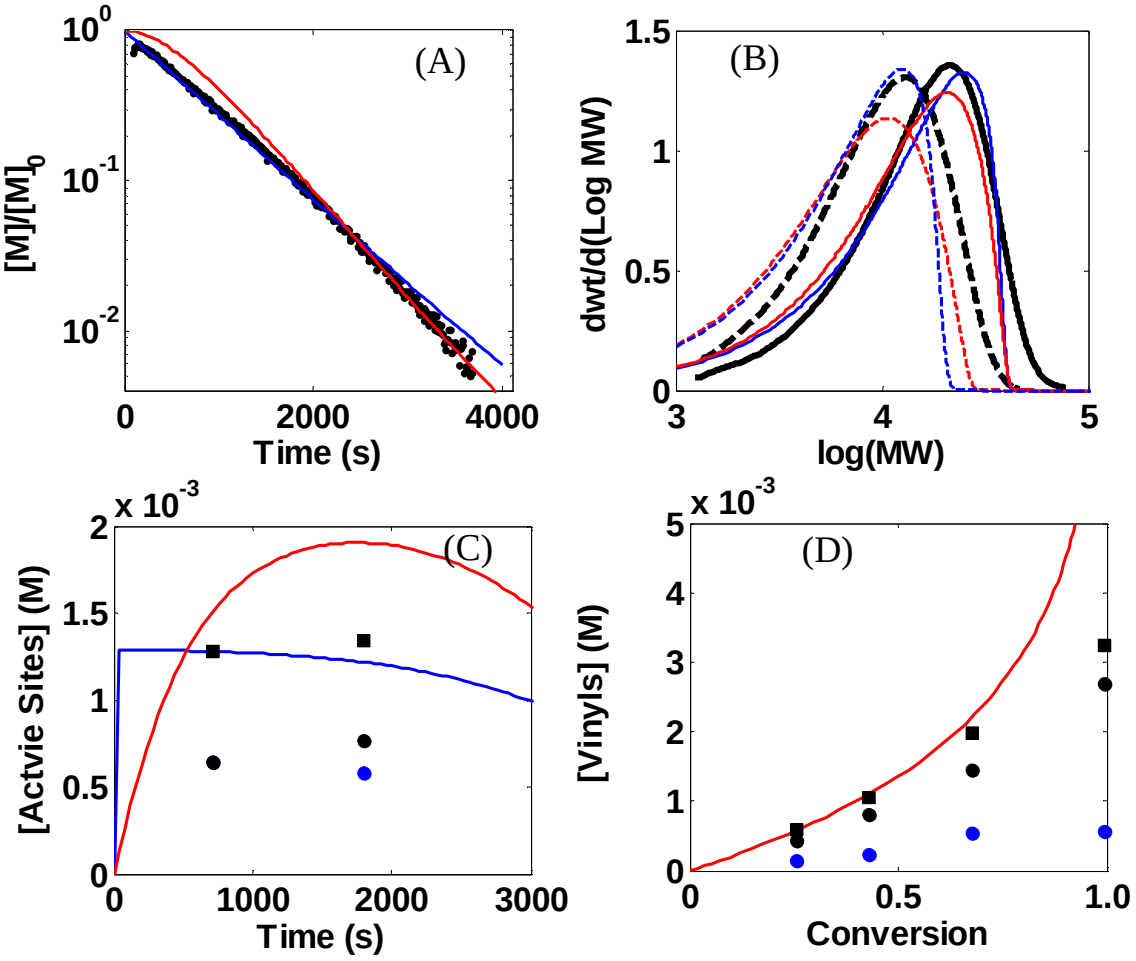

Figure B-SI11. Modeling using Mechanism III; data (A) monomer consumption data (dots), (B) MWD ($[C]_0$ = 3.0 mM, $[M]_0$ = 0.60 M for bold solid line, $[C]_0$ = 3.0 mM, $[M]_0$ = 0.30 M for bold dashed line), (C) active site counts (black circles: primary site count, blue circles: secondary site counts, black squares: total count; fits apply to the total count), (D) vinyl terminated group counts (black circles: vinylidene count, blue circles: vinylene count, black squares: total count; fits apply to the total count); fits (red and blue solid lines); rate constants: red: k_i = 0.002 M^{-1} s^{-1}, $k_p = k_{reinit}$ = 0.8 M^{-1} s^{-1}, k_{ct} = 0.0016 s^{-1}; blue: $k_i = k_p = k_{reinit}$ = 1 M^{-1} s^{-1}, k_{ct} = 0.002 s^{-1}, active catalyst = 43%. $[C]_0$ = 3.0 mM, $[M]_0$ = 0.60 M.

Mechanism IV. Monomer dependent chain transfer and incomplete catalyst participation.

β-H transfer to monomer is also a possible chain transfer pathway that produces vinyl terminated groups. This mechanism is evaluated in Figure SI12. Although a good fit

of monomer consumption, active site counts, and vinyl counts are obtained, the fit of the MWD is poor (red in Figure SI12). Alternatively, if the model parameters are adjusted to promote a better fit of MWD, the fit of active site counts is poor (green in Figure SI12). As a result, monomer dependent chain transfer is ruled out for system **2**.

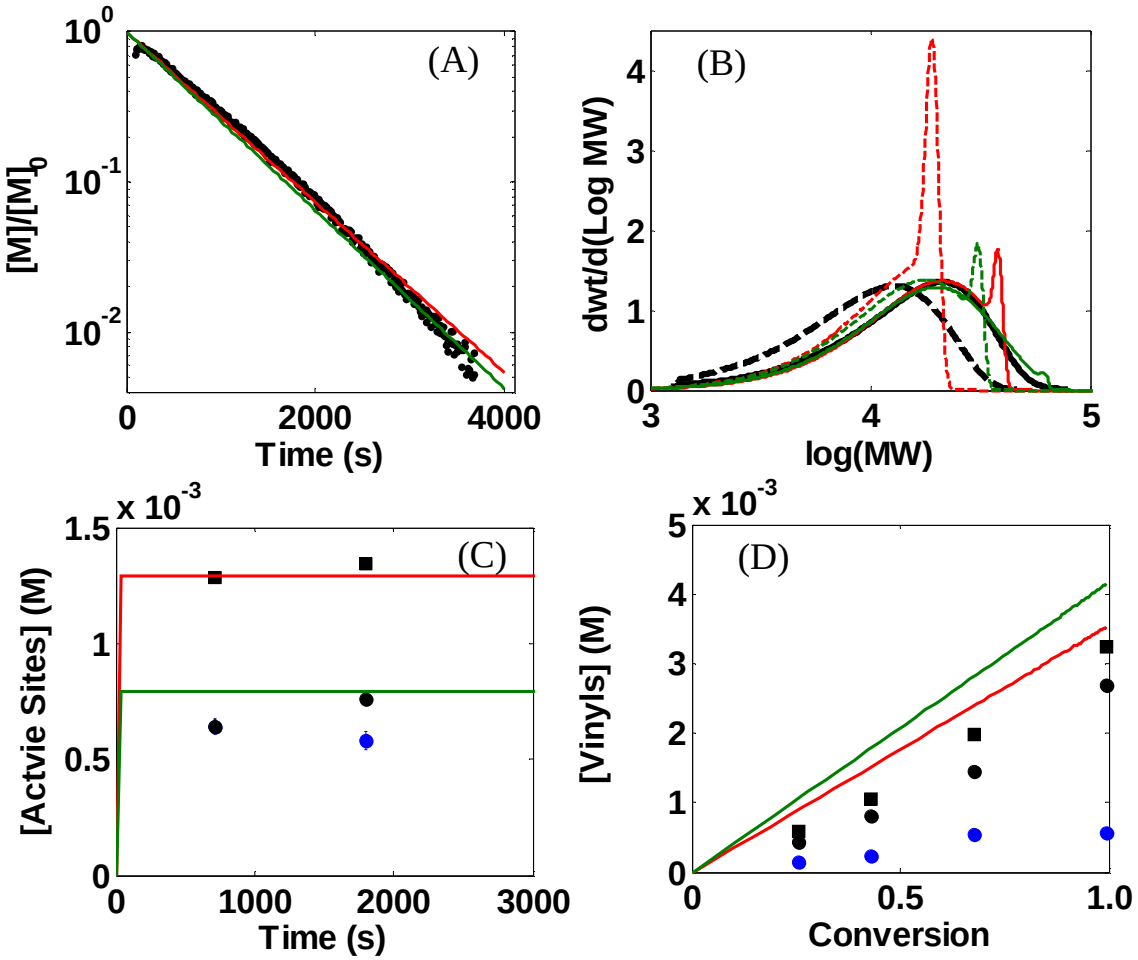

Figure B-SI12. Modeling using Mechanism IV; data (A) monomer consumption data (dots), (B) MWD ($[C]_0$ = 3.0 mM, $[M]_0$ = 0.60 M for bold solid line, $[C]_0$ = 3.0 mM, $[M]_0$ = 0.30 M for bold dashed line), (C) active site counts (black circles: primary site count, blue circles: secondary site counts, black squares: total count; fits apply to the total count), (D) vinyl terminated group counts (black circles: vinylidene count, blue circles: vinylene count, black squares: total count; fits apply to the total count); fits (red and green lines); rate constants: red: $k_i = k_p$ = 1 M^{-1} s^{-1}, k_{ct} = 0.006 M^{-1} s^{-1}, active catalyst = 43%; green: $k_i = k_p$ 1.7 M^{-1} s^{-1}, k_{ct} = 0.012 M^{-1} s^{-1}, active catalyst = 27%. $[C]_0$ = 3.0 mM, $[M]_0$ = 0.60 M.

Mechanism V. Monomer independent chain transfer, incomplete catalyst participation, and misinsertion with slow recovery.

Given that we observe two types of end groups and active sites in vinyl counts and active site counts experiments (Figure SI12(C, D)), we believe misinsertion with slow recovery also happens in the system **2**, together with monomer independent chain transfer and incomplete catalyst participation. All the rate constants are optimized based on Mechanism V. The fits of experimental data sets under different initial conditions are shown in Figure 3.

2.3 Kinetic Modeling of Zr[^{t}Bu-ON^{Furan}O]Bn$_2$ Catalyst System

Mechanism I. Living polymerization.

We start from the most basic model, i.e. the living polymerization model. The fits of both monomer consumption curve and MWD are poor. The monomer consumption data is curved; and the experimental data exhibit higher molecular weight where the distribution is also much broader (Figure SI13).

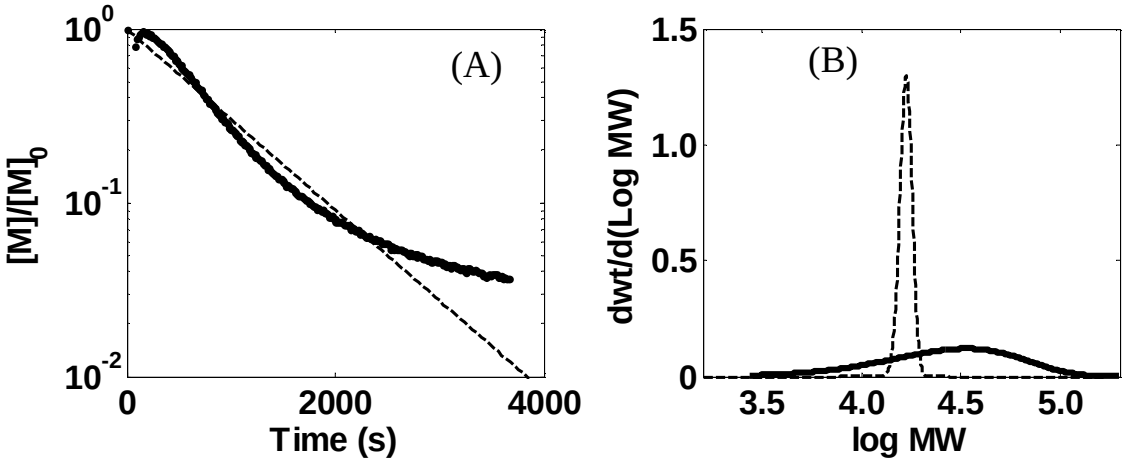

Figure B-SI13. Modeling using Mechanism I; data (A) monomer consumption data (dots), (B) MWD (bold solid line); fits (dashed lines); rate constants: $k_i = k_p = 0.4\ M^{-1}\ s^{-1}$. $[C]_0$ = 3.0 mM, $[M]_0$ = 0.60 M.

Mechanism II. Slow initiation and active site deactivation.

Since the monomer consumption curve exhibits an induction period, slow initiation is there. To model the slowdown of monomer consumption towards the end of the reaction, it is assumed that the active sites gradually deactivate. Based on mechanism II, we achieve an excellent fit of monomer consumption curve; but the fit of MWD needs to be improved (Figure SI14).

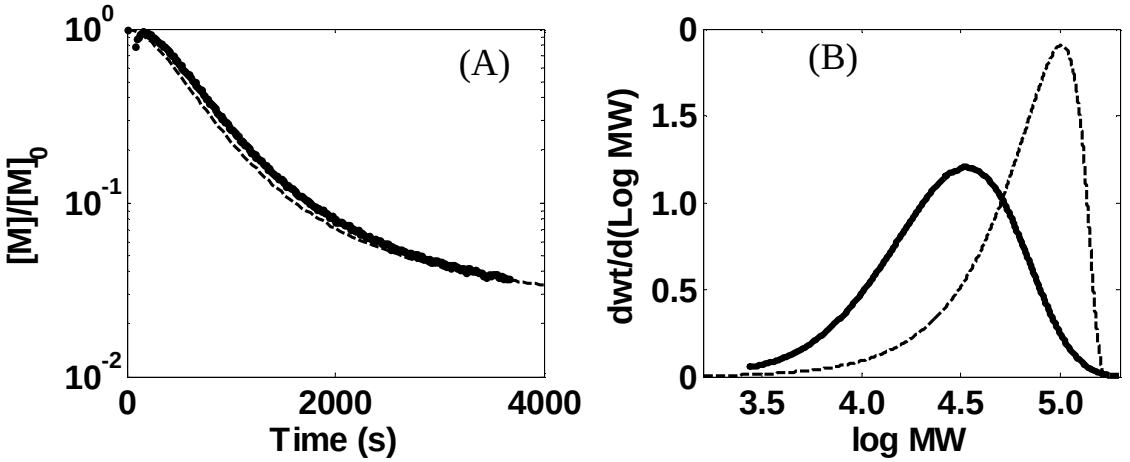

Figure B-SI14. Modeling using Mechanism II; data (A) monomer consumption data (dots), (B) MWD (bold solid line); fits (dashed lines); rate constants: k_i = 0.001 M^{-1} s^{-1}, k_p = 1.7 M^{-1} s^{-1}, k_d = 0.0013 s^{-1}. $[C]_0$ = 3.0 mM, $[M]_0$ = 0.60 M.

Mechanism III. Slow initiation and monomer independent chain transfer.

Monomer independent chain transfer via β-H elimination is evaluated here. If k_{reinit} is fast, the monomer consumption curve is linear on log scale (red in Figure SI15); in contrast, if k_{reinit} is slow, the monomer consumption curve is curved upward on log scale (blue in Figure SI15) at lower monomer concentrations. In the system **4**, we observe monomer consumption which is curved upward on log scale, so we assume a slow k_{reinit}. We achieve a good fit of experimental data obtained at $[C]_0$ = 3.0 mM, $[M]_0$ = 0.60 M. However, when the initial concentrations are changed, monomer independent chain transfer fails to model the MWDs under different initial concentrations (blue in Figure SI15(B)).

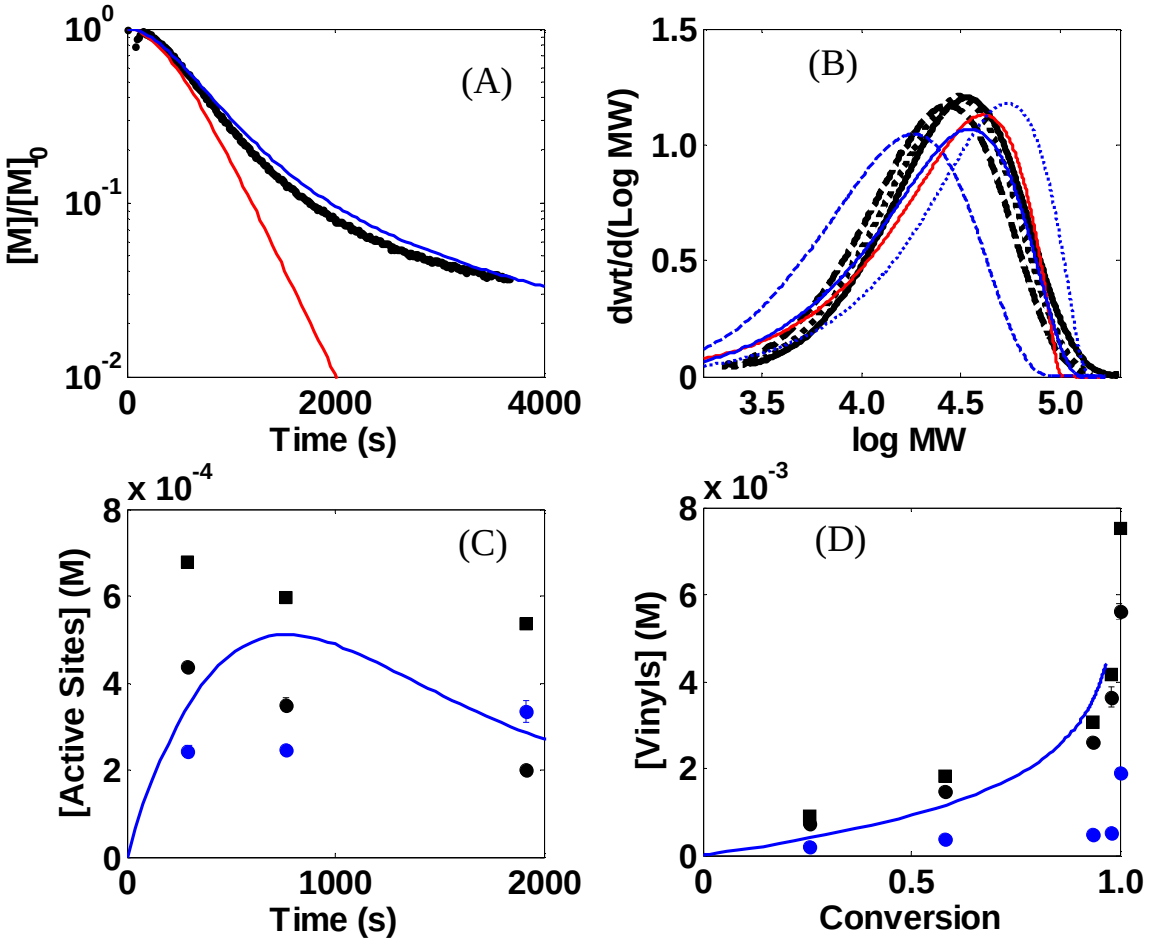

Figure B-SI15. Modeling using Mechanism III; data (A) monomer consumption data (dots), (B) MWD ($[C]_0$ = 3.0 mM, $[M]_0$ = 0.60 M for bold solid line, $[C]_0$ = 3.0 mM, $[M]_0$ = 0.30 M for bold dashed line, $[C]_0$ = 4.0 mM, $[M]_0$ = 1.0 M for bold dotted line), (C) active site counts (black circles: primary site count, blue circles: secondary site counts, black squares: total count; fits apply to the total count), (D) vinyl terminated group counts (black circles: vinylidene count, blue circles: vinylene count, black squares: total count; fits apply to the total count); fits (blue and red lines); rate constants: red: k_i = 0.001 M^{-1} s^{-1}, $k_p = k_{reinit}$ = 3 M^{-1} s^{-1}, k_{ct} = 0.003 s^{-1}; blue: k_i = 0.001 M^{-1} s^{-1}, k_p = 3 M^{-1} s^{-1}, k_{reinit} = 0.016 M^{-1} s^{-1}, k_{ct} = 0.004 s^{-1}. $[C]_0$ = 3.0 mM, $[M]_0$ = 0.60 M.

Mechanism IV. Slow initiation, monomer dependent chain transfer, and active site deactivation.

Monomer dependent chain transfer via β-H transfer to monomer pathway is evaluated in Figure SI16. As a result of the monomer dependent chain transfer, an initiated

chain with one repeat unit is formed, which is ready for propagation. The monomer consumption is linear with this mechanism (green in Figure SI16(A)). To model the curvature at lower monomer concentration, active site deactivation mechanism is also applied to system **4** (magenta in Figure SI16). In contrast to monomer independent chain transfer, monomer dependent chain transfer produces polymers of similar MWD even though the initial concentrations of monomer and catalyst are different (magenta in Figure SI16(B)), which correctly describes our experimental data. Mechanism IV gives a good fit of the experimental data with the exception of vinyl counts at the very end of the reaction (Figure SI16(D)).

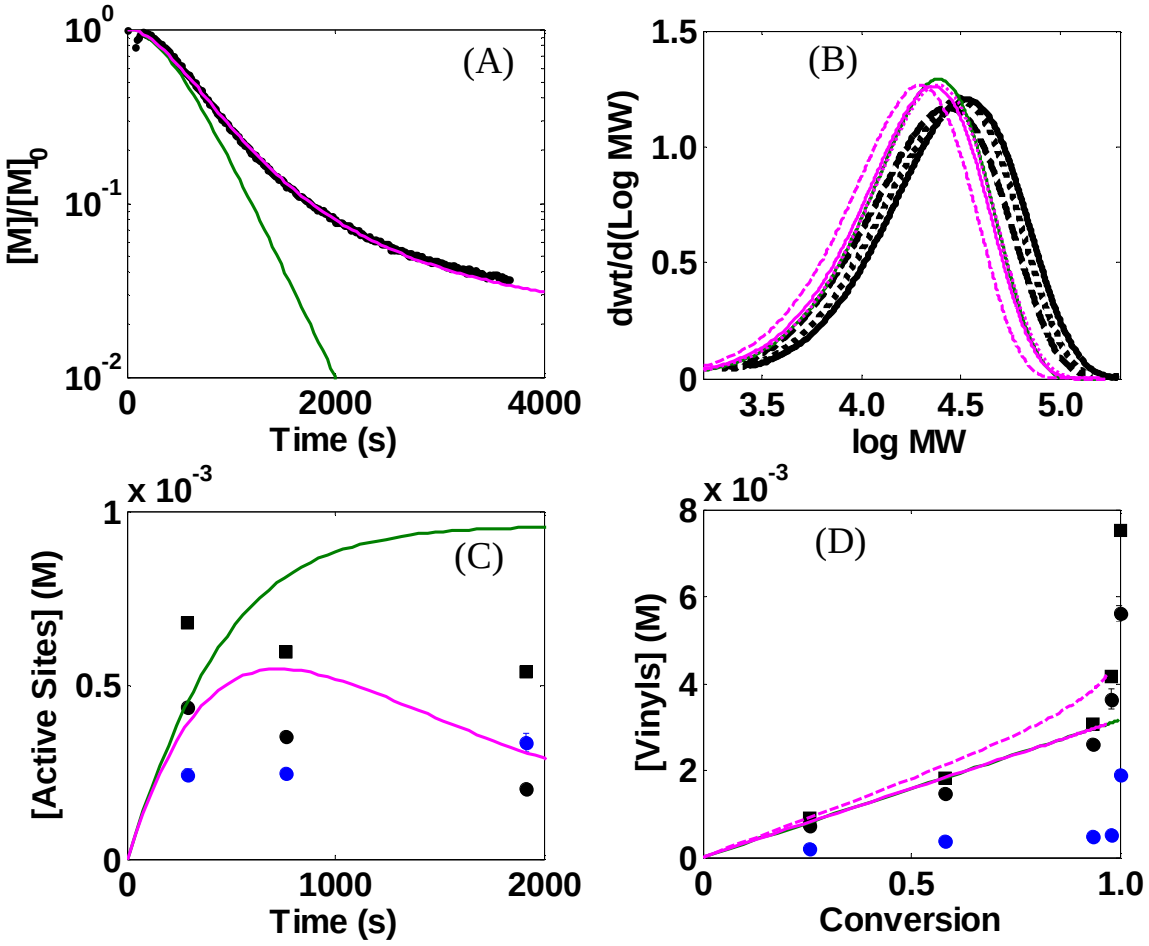

Figure B-SI16. Modeling using Mechanism IV; data (A) monomer consumption data (dots), (B) MWD ($[C]_0$ = 3.0 mM, $[M]_0$ = 0.60 M for bold solid line, $[C]_0$ = 3.0 mM, $[M]_0$ = 0.30 M for bold dashed line, $[C]_0$ = 4.0 mM, $[M]_0$ = 1.0 M for bold dotted line), (C) active site counts (black circles: primary site count, blue circles: secondary site counts, black squares: total count; fits apply to the total count), (D) vinyl terminated group counts (black circles: vinylidene count, blue circles: vinylene count, black squares: total count; fits apply to the total count); fits (green and magenta lines); rate constants: green: k_i = 0.001 M^{-1} s^{-1}, k_p = 3 M^{-1} s^{-1}, k_{ct} = 0.016 M^{-1} s^{-1}; magenta: k_i = 0.001 M^{-1} s^{-1}, k_p = 3 M^{-1} s^{-1}, k_{ct} = 0.016 M^{-1} s^{-1}, k_d = 0.001 M^{-1} s^{-1}. $[C]_0$ = 3.0 mM, $[M]_0$ = 0.60 M.

Mechanism V. Slow initiation, major monomer dependent chain transfer, minor monomer independent chain transfer with zero reinitiation, and misinsertion with zero recovery.

As a summary of mechanism III and IV, we believe chain transfer in the system **4** happens mainly via the β-H transfer to monomer pathway, which is monomer dependent. Also, monomer independent chain transfer is slowly happening at long times even when monomer is fully consumed, where the reinitiation rate is zero (which is an equivalent to active site deactivation), because we observe an apparent increase of vinyl counts when the reaction is allowed to run overnight (Figure SI16(D)). Also, two types of end groups and active sites were observed (Figure SI16(C, D)), which indicates misinsertion with zero slow or no recovery also happens in system **4.** With all these considerations, our final mechanism set V includes slow initiation, significant monomer dependent chain transfer, relatively minor monomer independent chain transfer with zero reinitiation, and misinsertion with slow/zero recovery. All the rate constants are optimized based on Mechanism V. The optimized value of the recovery rate turns out to be zero, because we observe the secondary sites are accumulating while the primary site count is decreasing. Incomplete catalyst participation is necessary to fit the full data set. The fits of experimental data sets under different initial conditions are shown in Figure 4.

2.4 Kinetic Modeling of Zr[tBu-ONSMeO]Bn2 Catalyst System

The results for system **5** were somewhat unique among the five systems studied as this was the only system where the data could be modeled with the assumption that 100% of the precatalyst is available for polymer growth. However, the data could also only be

reconciled with the introduction of a first order deactivation pathway. To demonstrate this, Figure SI17 shows the best possible fit by optimization of representative vinyl and MWD data from batch scale experiments quenched at different reaction times. While rate constants can be selected to satisfy the monomer consumption data reasonably well, there is a tradeoff in fitting the vinyl and MWD data. The model with slow initiation and fast chain transfer fits the MWDs moderately well but fits the vinyls poorly (cyan curves in Figure SI17), while the model with fast initiation and slow chain transfer does the opposite (red curves in Figure SI17). Neither of these model types matches the active site behavior well at the end of the reaction. Introducing a deactivation pathway, which seems intuitively reasonable based on the shape of the monomer consumption and active site data, allows a good fit of all data simultaneously (i.e. green curves in Figure SI17), where all of the catalysts is active.

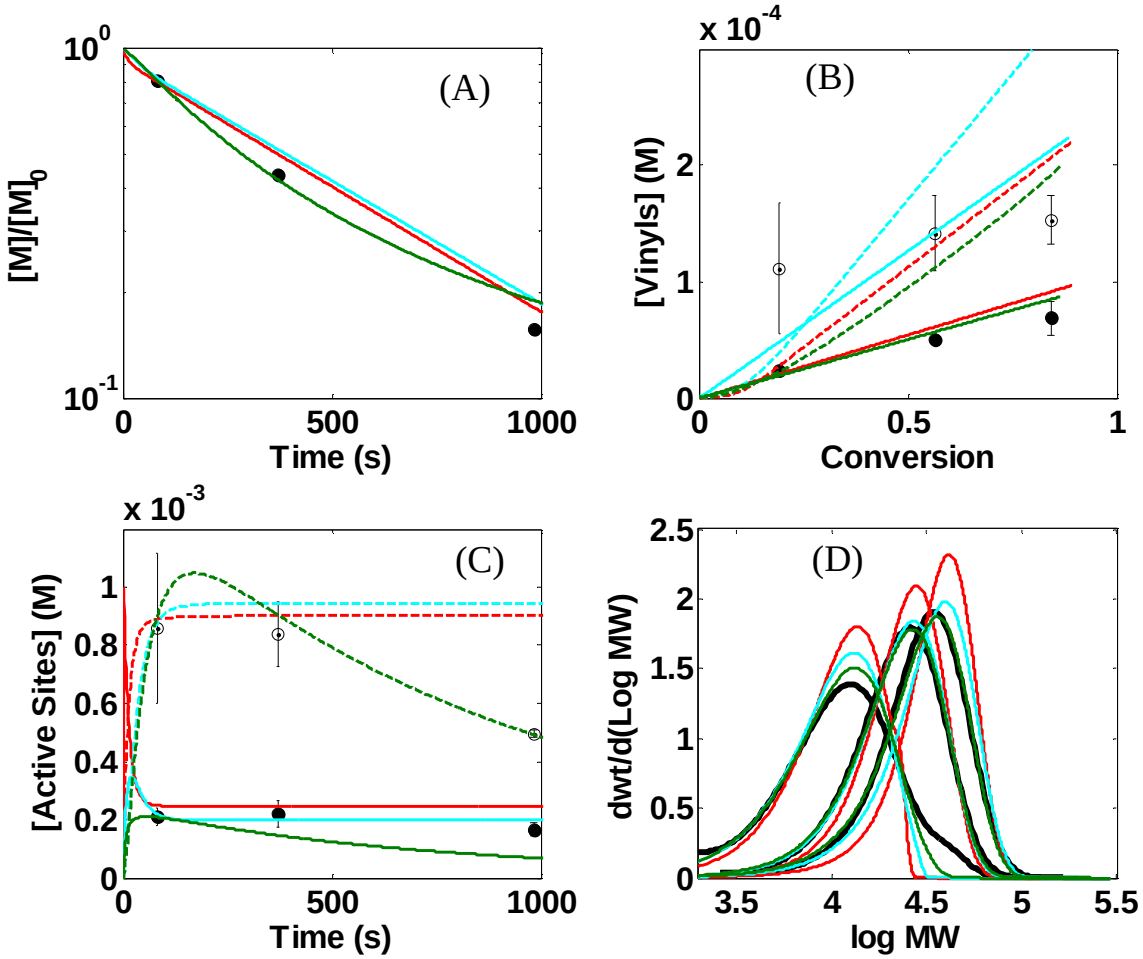

Figure B-SI17. Experimental data for three selected batch scale reactions, quenched at different reaction times. $[C]_0$ = 3.0 mM, $[M]_0$ = 0.60 M. Black: data. Colored lines represent kinetic modeling fits. Red: $k_i = k_p$ = 6.5 M^{-1} s^{-1}, k_{mis} = 0.11 M^{-1} s^{-1}, k_{rec} = 0.029 M^{-1} s^{-1}, k_{dene} = 0.0012 M^{-1} s^{-1}, k_{ene} = 0.0008 M^{-1} s^{-1}, active site fraction = 0.38; Cyan: k_i = 0.080 M^{-1} s^{-1}, k_p = 7.9 M^{-1} s^{-1}, k_{mis} = 0.12 M^{-1} s^{-1}, k_{rec} = 0.024 M^{-1} s^{-1}, k_{dene} = 0.0035 M^{-1} s^{-1}, k_{ene} = 0.0012 M^{-1} s^{-1}, active site fraction = 0.38; Green: k_d = 0.0079 s^{-1}, all other rates are in Table 1. (A) Monomer consumption data. (B) Vinyl measurements. Filled symbols/solid lines: vinylidene count; open symbols/dashed lines: vinylene count. (C) Active site measurements. Filled symbols/solid lines: primary site count; open symbols/dashed lines: secondary site count. (D) MWD data at (from left to right) 81 s, 371 s, 983 s.

One concern with determining a model for this catalyst system is predicting the vinylidene data. In one experiment where vinylene concentrations were measured (Figure 5D and SI17B), the vinylene concentration appears to be relatively high at the lowest monomer conversion, where there is minimal additional increase in vinylene concentration

as the polymerization proceeds. This implies that vinylene formation slows down later into the reaction, and therefore likely depends on monomer concentration. When plotted as vinylene concentration vs. monomer conversion a straight line is expected (in the absence of events that alter catalyst concentration, which do occur in this system), whereas when chain transfer is monomer independent the line would curve upwards. The behavior seen in the data is most closely modeled by monomer dependent vinylene formation (Figure SI18, green curve) rather than monomer independent vinylene formation (Figure SI18, blue curve), although no rate constants could be found that were completely satisfactory at fitting the initial measurement. One possible issue is the uncertainty in the NMR measurement of vinyl concentration at such low values, which may cause errors even larger than displayed in the figure.

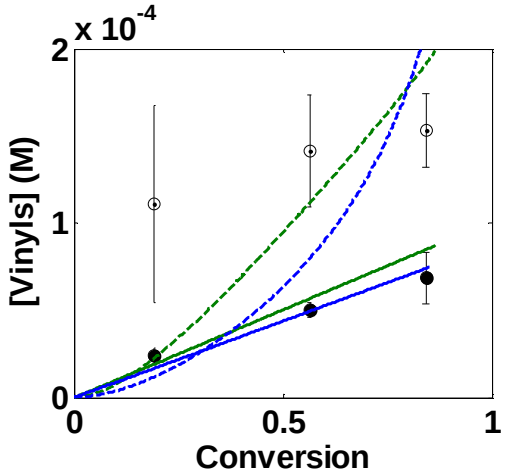

Figure B-SI18. Vinyl concentration data for three selected batch scale reactions, quenched at different reaction times. $[C]_0$ = 3.0 mM, $[M]_0$ = 0.60 M. Black: data. Colored lines represent kinetic modeling fits.; Green: Monomer dependent vinylene formation: k_d = 0.0079 s^{-1}, all other rates are in Table 1; Blue: Monomer independent vinylene formation: k_i = 0.018 M^{-1} s^{-1}, k_p = 11.9 M^{-1} s^{-1}, k_{mis} = 0.20 M^{-1} s^{-1}, k_{rec} = 0.038 M^{-1} s^{-1}, k_{dene} = 0.0018 M^{-1} s^{-1}, k_{ene} = 0.00026 s^{-1}, k_d = 0.0081 s^{-1}, active site fraction = 1.0. Filled symbols/solid lines: vinylidene count; open symbols/dashed lines: vinylene count.

3. Kinetic Model Equations

The mechanism from Scheme 1, which was used to fit the data in this report, is quantified as the series of chemical reactions given below.

List of Species

C	Precatalyst
A	Activator
C^*	Activated Catalyst
M	Monomer
R_n	Normal Propagating Chain
P_n	Misinserted Propagating Chain
C^*_H	Metal-Hydride
SR_n	Vinylidene Terminated Polymer Chain
SP_n	Vinylene Terminated Polymer Chain

List of Reactions

$C + A \xrightarrow{k_a} C^*$	Catalyst Activation	(S19)
$C^* + M \xrightarrow{k_i} R_1$	Initiation	(S20)
$R_n + M \xrightarrow{k_p} R_{n+1}, \quad 1 \le n \le L_{max}$	Normal Propagation	(S21)
$R_n + M \xrightarrow{k_{mis}} P_{n+1}, \ 1 \le n \le L_{max}$	2,1-Misinsertion of Monomer	(S22)
$P_n + M \xrightarrow{k_{rec}} R_{n+1}, \quad 2 \le n \le L_{max}$	Recovery of Normal Catalyst Site	(S23)
$R_n \xrightarrow{k_{vinylidene}} C^*_H + SR_n, \ 1 \le n \le L_{max}$	Vinylidene-forming β-H Elimination	(S24)
$P_n \xrightarrow{k_{vinylene}} C^*_H + SP_n, \ 2 \le n \le L_{max}$	Vinylene-forming β-H Elimination	(S25)

$$R_n + M \xrightarrow{k_{vinylidene}} R_1 + SR_n, 1 \le n \le L_{max}$$ Vinylidene-forming β-H transfer to monomer (S26)

$$P_n + M \xrightarrow{k_{vinylidene}} R_1 + SP_n, \quad 2 \le n \le L_{max}$$ Vinylene-forming β-H transfer to monomer (S27)

$$C^*_H + M \xrightarrow{k_{re\text{-}ininiation}} R_1$$ Initiation of Metal-Hydride (S28)

In these reactions, L_{max} represents the maximum number of monomers in the polymer chains. This parameter must be set sufficiently high to account for all polymer chains in the experiments, and it is usually set around 20% higher than the value determined from the highest molecular weight seen in the MWDs.

The mechanism given in S19 to S28 results in a set of ordinary differential equations (ODEs) that can be solved to determine the time dependent concentration of each of the chemical species for a given set of rate constants. These calculated concentrations are compared to the data using the objective function, and a Levenberg-Marquardt optimization routine is used to determine the rate constants so as to minimize the objective function. The ODEs are listed below (assuming chain transfer via β-H elimination).

List of ODEs

$$\frac{d[C]}{dt} = -k_a[C][A]$$ (S29)

$$\frac{d[A]}{dt} = -k_a[C][A]$$ (S30)

$$\frac{d[C^*]}{dt} = k_a[C][A] - k_i[C^*][M]$$ (S31)

$$\frac{d[M]}{dt} = \left(-k_i[C^*] - (k_p + k_{mis})\left(\sum_{n=1}^{L_{max}}[R_n]\right) - k_{rec}\left(\sum_{n=2}^{L_{max}}[P_n]\right) - k_{re-initiation}[C^*_H] \right)[M] \quad \text{(S32)}$$

$$\frac{d[R_1]}{dt} = \left(k_i[C^*] - k_p[R_1] - k_{mis}[R_1] + k_{re-initiation}[C^*_H]\right)[M] - k_{vinylidene}[R_1] \quad \text{(S33)}$$

$$\frac{d[R_n]}{dt} = \left(k_p([R_{n-1}] - [R_n]) - k_{mis}[R_n] + k_{rec}[P_{n-1}]\right)[M] - k_{vinylidene}[R_n], 2 \le n \le L_{max} \quad \text{(S34)}$$

$$\frac{d[P_n]}{dt} = \left(k_{mis}[R_{n-1}] - k_{rec}[P_n]\right)[M] - k_{vinylene}[P_n], 2 \le n \le L_{max} \quad \text{(S35)}$$

$$\frac{d[C^*_H]}{dt} = -k_{re-initiation}[C^*_H][M] + k_{vinylidene}\left(\sum_{n=1}^{L_{max}}[R_n]\right) + k_{vinylene}\left(\sum_{n=2}^{L_{max}}[P_n]\right) \quad \text{(S36)}$$

$$\frac{d[SR_n]}{dt} = k_{vinylidene}[R_n], 1 \le n \le L_{max} \quad \text{(S37)}$$

$$\frac{d[SP_n]}{dt} = k_{vinylene}[P_n], 2 \le n \le L_{max} \quad \text{(S38)}$$

Appendix C Supporting Information for Chapter 3

1. Estimation of Error Bounds

Here we give an example of how the error bounds were obtained for one of the systems (Catalyst **1b**). First, the entire data set consisting of (1) monomer consumption, (2) MWD, (3) primary and secondary active site counts, and (4) vinyl terminated group counts was fit to the chosen mechanism as explained in the main text. The resulting values of the rate constants are shown in Table 1. Fits are shown in Figure SI8.

The error due to the uncertainty in the GPC measurements was estimated as follows: the MWD curve was shifted towards higher molecular weights by 0.04 on the log scale, and the entire data set was re-optimized giving rise to a different set of rate constant values. Similarly, the MWD curve was shifted towards lower molecular weights by 0.05 on the log scale, and the entire data set was re-optimized giving rise to yet another set of rate constant values. Figure SI1 illustrates the shift in the distributions for Catalyst 1b.The summary of the results is in Table SI1.

Varying the MWD has the largest effect on the rate constants, and for this system, the error bars given in the main text are based on the error due to GPC measurements.

Table C-SI1. Optimized rate constants based on the estimated error in the GPC measurements.

Catalyst	k_i (M^{-1} s^{-1})	k_p (M^{-1} s^{-1})	k_{mis} (M^{-1} s^{-1})	k_{rec} (M^{-1} s^{-1})	$k_{vinylidene}$ (10^{-3} s^{-1})	$k_{vinylene}$ (10^{-3} s^{-1})
1b	0.03–0.06	0.47–0.59	0.0071–0.0083	0.05–0.08	0.80–0.86	0.21–0.34
2b	0.0016–0.0018	0.18–0.20	0.00028–0.00030	0–0.0002	3.6–4.1	0.9–1.1
3b	0.037–0.048	0.86–1.02	0.0012–0.0015	N/A	5.3–5.7	N/A

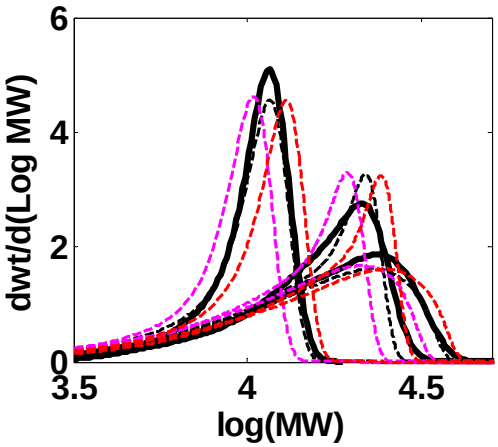

Figure C-SI1. Modeling Fits of MWDs from three batch quenches of catalyst 1b taken at 604, 1559, 3911 s using the upper bound (dashed lines) and the lower bound (dotted lines) sets of the rate constants given in Table SI3. $[C]_0$ = 3.0 mM, $[M]_0$ = 0.60 M.

2. Detailed Kinetic Modeling

The modeling perspectives used in this communication (i) start with the simplest possible polymerization mechanism, (ii) determine if it fits the data, and (iii) if it does not fit the data within experimental error, postulate the next simplest mechanism. Using this procedure the simplest model consistent with the data is discovered.

2.1 Kinetic Modeling of Hf[^{t}Bu-ON^{THF}O]Bn$_2$ Catalyst System (1b)

Mechanism I. Living polymerization.

We start by using the smallest model, i.e., the living polymerization model. A good fit of monomer consumption curve is obtained, however, the fits of MWDs are dramatically in error, where the experimental data exhibit both higher molecular weight and broader distributions (Figure SI2).

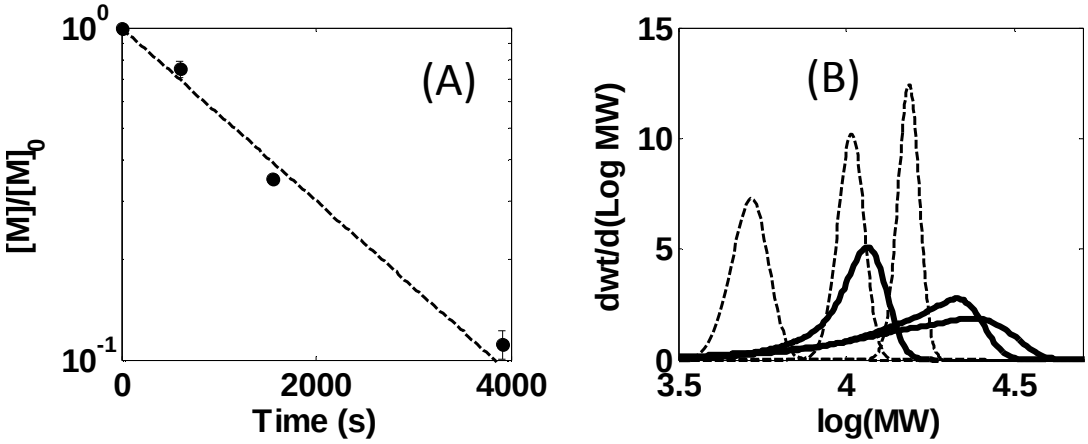

Figure C-SI2. Modeling using Mechanism I; data (A) monomer consumption from three batch quenches at 604, 1559, 3911 s (circles), (B) corresponding MWD of each quench (bold solid lines); fits (dashed lines); rate constants: $k_i = k_p = 0.2\ M^{-1}\ s^{-1}$. $[C]_0 = 3.0$ mM, $[M]_0 = 0.60$ M.

Mechanism II. Slow initiation/incomplete catalyst participation.

There are two possible pathways to obtain higher molecular weight products: (i) slow initiation (Figure SI3), and (ii) incomplete catalyst participation (Figure SI4). Pathway 1 results in an apparent induction period, which is not consistent with the experimental data. So pathway 2 is considered to be a better candidate to achieve the higher molecular weight observed experimentally for system **1b**.

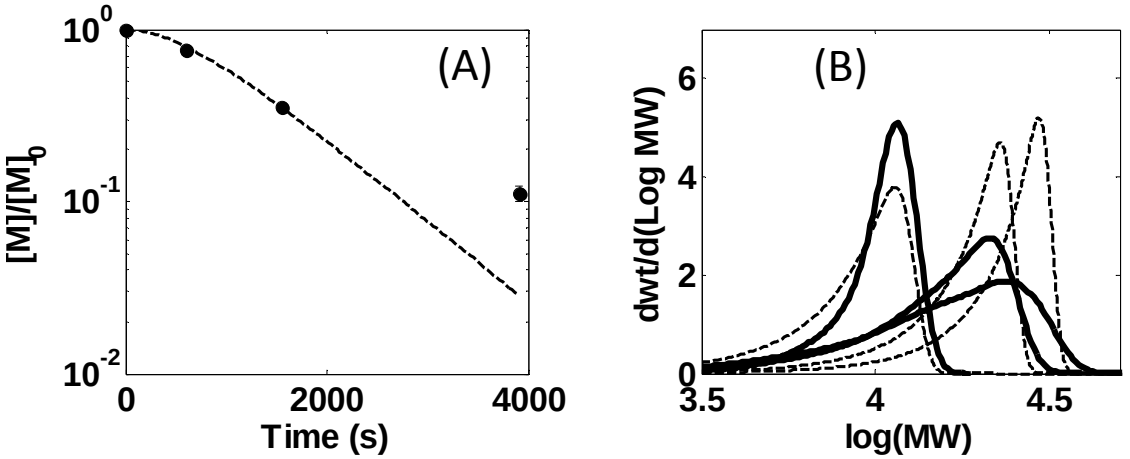

Figure C-SI3. Modeling using Mechanism II(i); data (A) monomer consumption from three batch quenches at 604, 1559, 3911 s (circles), (B) corresponding MWD of each quench (bold solid lines); fits (dashed lines); rate constants: k_i = 0.002 M^{-1} s^{-1}, k_p = 0.45 M^{-1} s^{-1}. $[C]_0$ = 3.0 mM, $[M]_0$ = 0.60 M.

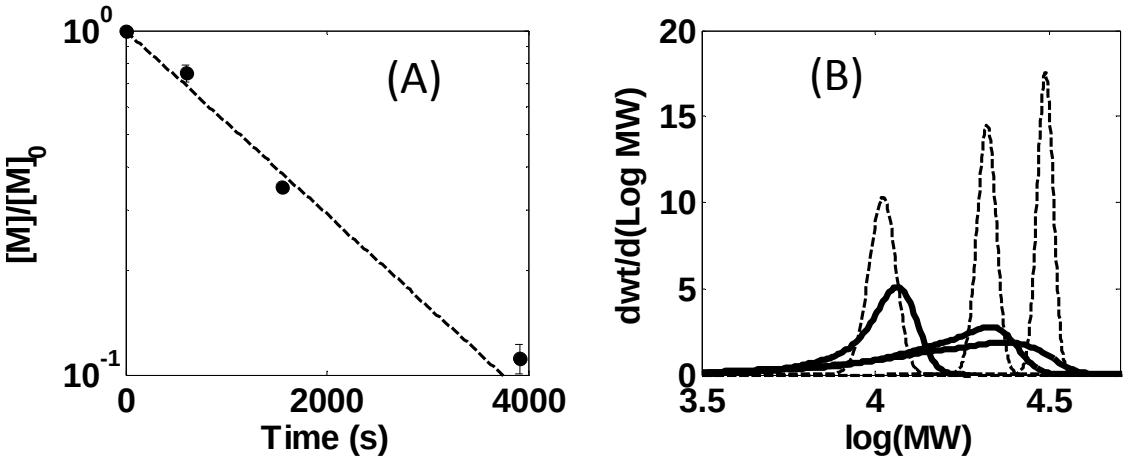

Figure C-SI4. Modeling using Mechanism II(ii); data (A) monomer consumption from three batch quenches at 604, 1559, 3911 s (circles), (B) corresponding MWD of each quench (bold solid lines); fits (dashed lines); rate constants: $k_i = k_p$ = 0.2 M^{-1} s^{-1}, active catalyst = 50%. $[C]_0$ = 3.0 mM, $[M]_0$ = 0.60 M.

Mechanism III. Monomer dependent chain transfer.

The broadening of the MWD is commonly caused by chain transfer reaction. β-H transfer to monomer is a possible chain transfer pathway that produces vinyl terminated groups. This mechanism is evaluated in Figure SI5. Although a good fit of monomer

consumption is obtained, the fit of the MWD is poor. Because both propagation and chain transfer are monomer dependent, the chain transfer to propagation ratio is a constant. As a result, if we try to achieve the broadness of MWD at earlier time (604 s) in the fitting, the fits to MWDs at later times (1559, 3911 s) are missed (Figure SI5B). If we increase the chain transfer rate, the MW will stop growing from the reaction middle time and the distribution is already very broad at early time (604 s) (Figure SI5C).

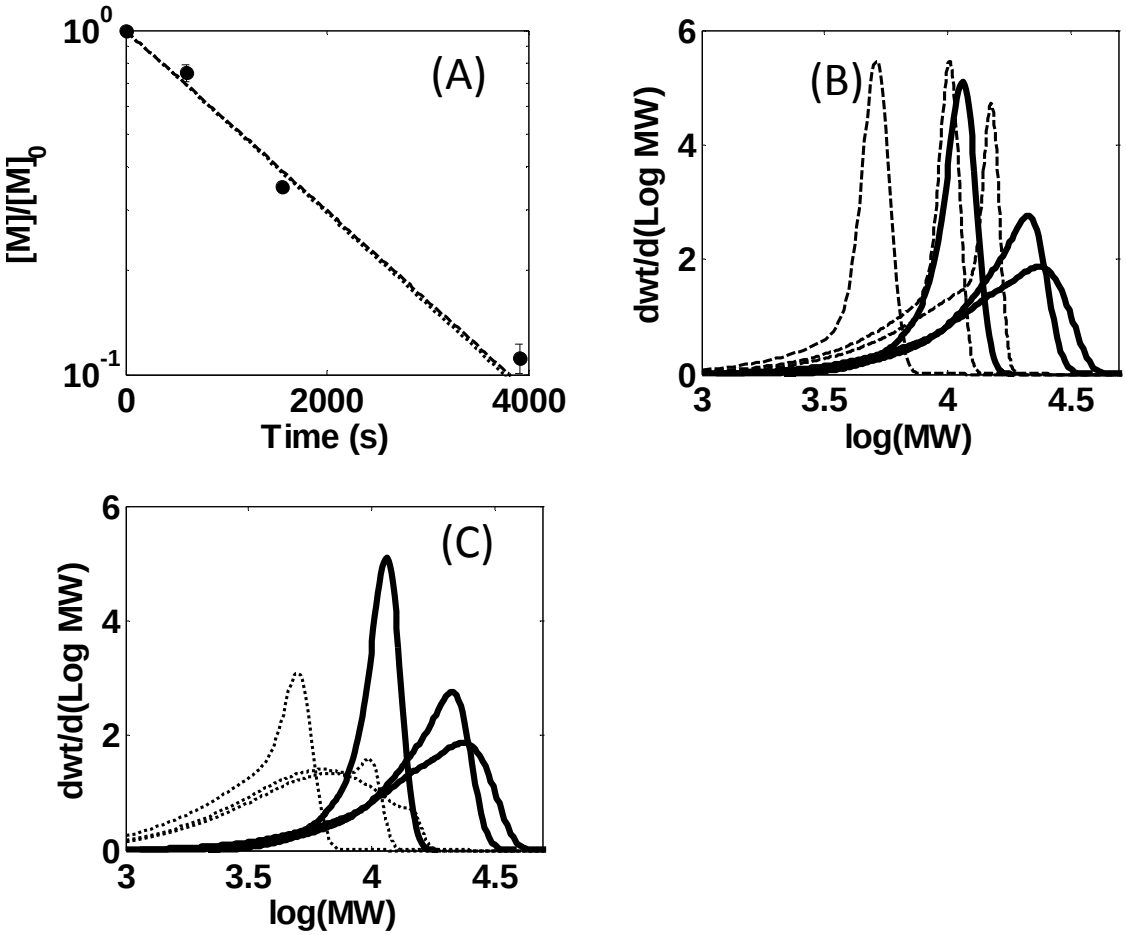

Figure C-SI5. Modeling using Mechanism III; (A) monomer consumption from three batch quenches at 604, 1559, 3911 s (circles), (B) and (C) corresponding MWD of each quench (bold solid lines) with different fits; fits (dashed and dotted lines); rate constants: dashed lines: $k_i = k_p = 0.2\ M^{-1}\ s^{-1}$, $k_{ct} = 0.0013\ M^{-1}\ s^{-1}$; dotted lines: $k_i = k_p = 0.2\ M^{-1}\ s^{-1}$, $k_{ct} = 0.004\ M^{-1}\ s^{-1}$. $[C]_0 = 3.0$ mM, $[M]_0 = 0.60$ M.

Mechanism IV. Monomer independent chain transfer.

Monomer independent chain transfer via β-H elimination reaction is also an effective way to produce broad MWD. A metal hydride is formed after the reaction happens, which in turn can be reinitiated to grow new chains. The monomer consumption curve is affected by this reinitiation rate (k_{reinit}). If k_{reinit} is fast (i.e. not slower than propagation), the total active site number in system **1b** is conserved, and the monomer consumption curve is linear on log scale. If k_{reinit} is slow, the monomer consumption curve is curved upward on log scale at lower monomer concentrations, because chain transfer is monomer independent but reinitiation is monomer dependent. In the system **1b**, we observe monomer consumption is linear on log scale especially from NMR scale reactions (Figure SI8E), so we assume a fast k_{reinit}. As shown in Figure SI6, we finally get the right shape and the right trend of MWDs, although the value of molecular weight is still lower than experimental data.

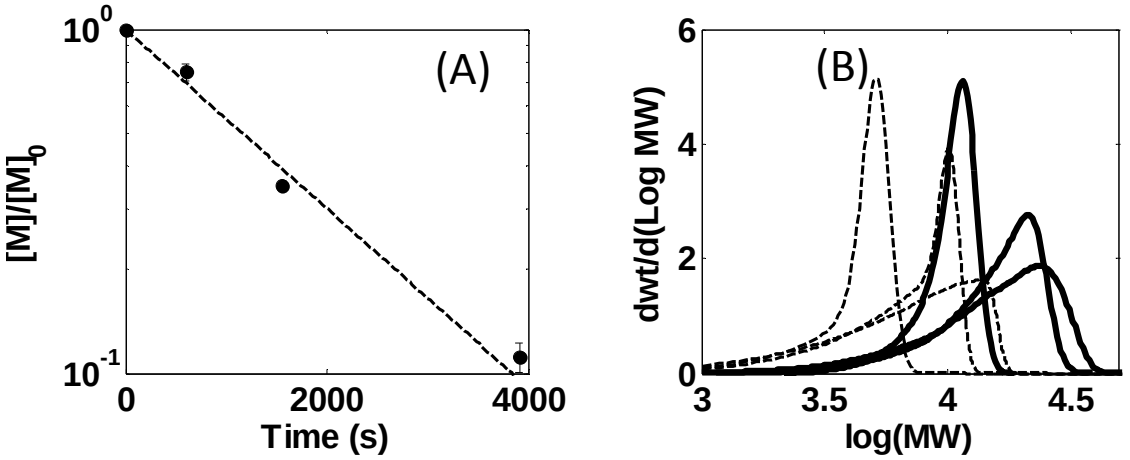

Figure C-SI6. Modeling using Mechanism IV; data (A) monomer consumption from three batch quenches at 604, 1559, 3911 s (circles), (B) corresponding MWD of each quench (bold solid lines); fits (dashed lines); rate constants: $k_i = k_p = k_{reinit} = 0.2\ M^{-1}\ s^{-1}$, $k_{ct} = 0.0008\ s^{-1}$. $[C]_0 = 3.0$ mM, $[M]_0 = 0.60$ M.

Mechanism V. Monomer independent chain transfer and incomplete catalyst participation.

To obtain an MWD which has a peak at high MW and is broad, we use a combined mechanism of monomer independent chain transfer and incomplete catalyst participation. The resulting fits are shown in Figure SI7, where the predicted MWD, although not perfect is qualitatively close to the data. To further validate this mechanism, we compare the active site counts and vinyl terminated group counts. They are basically correct. However, there are a small number of secondary sites existing, indicating misinsertion with slow recovery also participates in system **1b**.

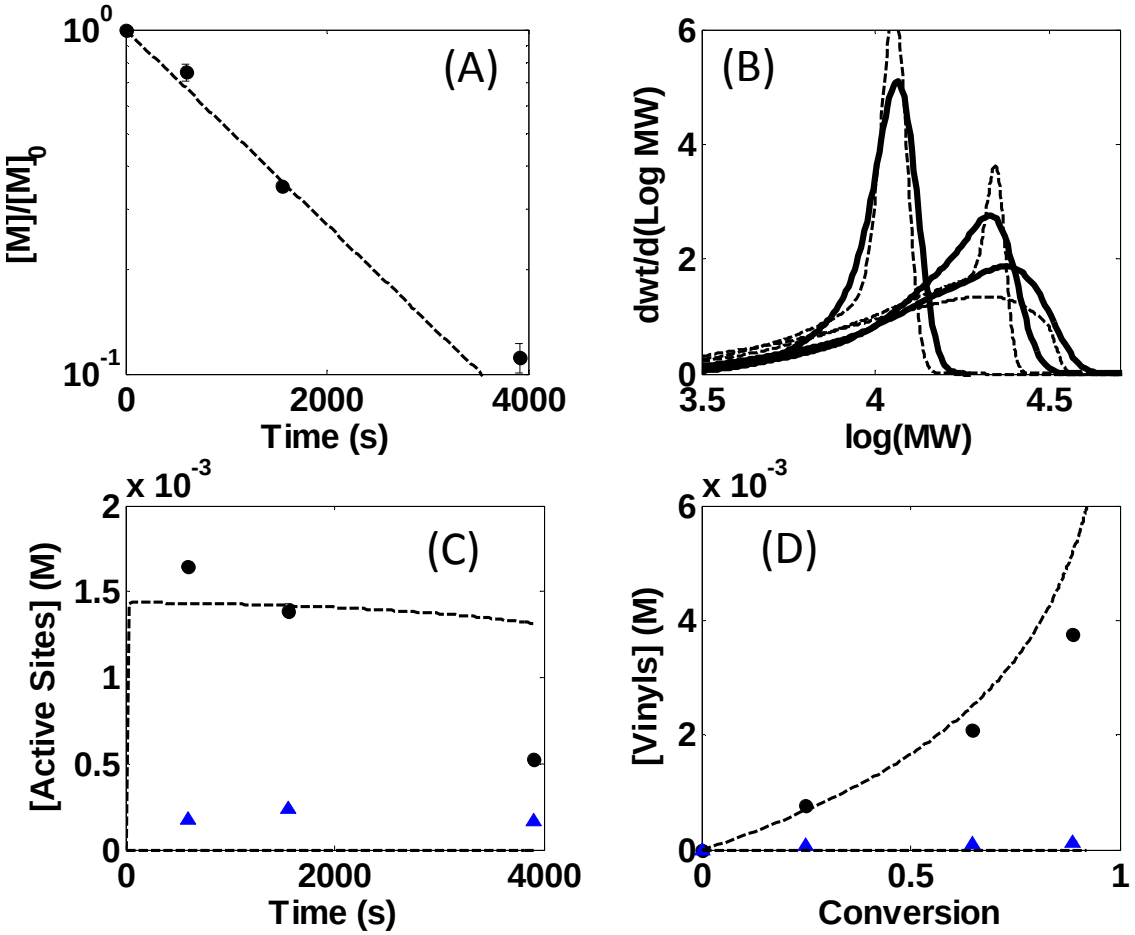

Figure C-SI7. Modeling using Mechanism V; data (A) monomer consumption from three batch quenches at 604, 1559, 3911 s (circles), (B) corresponding MWD of each quench (bold solid lines), (C) active site counts (black circles: primary site counts, blue triangles: secondary site counts), (D) vinyl terminated group counts (black circles: vinylidene counts, blue triangles: vinylene counts); fits (dashed lines); rate constants: $k_i = k_p = k_{reinit} = 0.45\ M^{-1}\ s^{-1}$, $k_{ct} = 0.0011\ s^{-1}$, active catalyst = 48%. $[C]_0 = 3.0$ mM, $[M]_0 = 0.60$ M.

Mechanism VI. Misinsertion with slow recovery, incomplete catalyst participation, and monomer independent chain transfer.

Based on all our measurements and previous analysis, the minimal set of elementary steps are misinsertion with slow recovery, incomplete catalyst participation and little chain transfer. To account for the slight curvature of the monomer consumption obtained from the batch quenches, as well as the drop on active site counts, we believe

there is a slight deactivation (k_d = 0.00023 s^{-1}) in the batch reaction, probably due to the experimental operations. The monomer consumptions of NMR scale experiments are perfectly linear (Figure SI8E), so we believe the deactivation is not intrinsic. Finally, all the rate constants are optimized based on Mechanism VI. The fits of the full experimental data sets for various initial conditions are shown in Figure SI8.

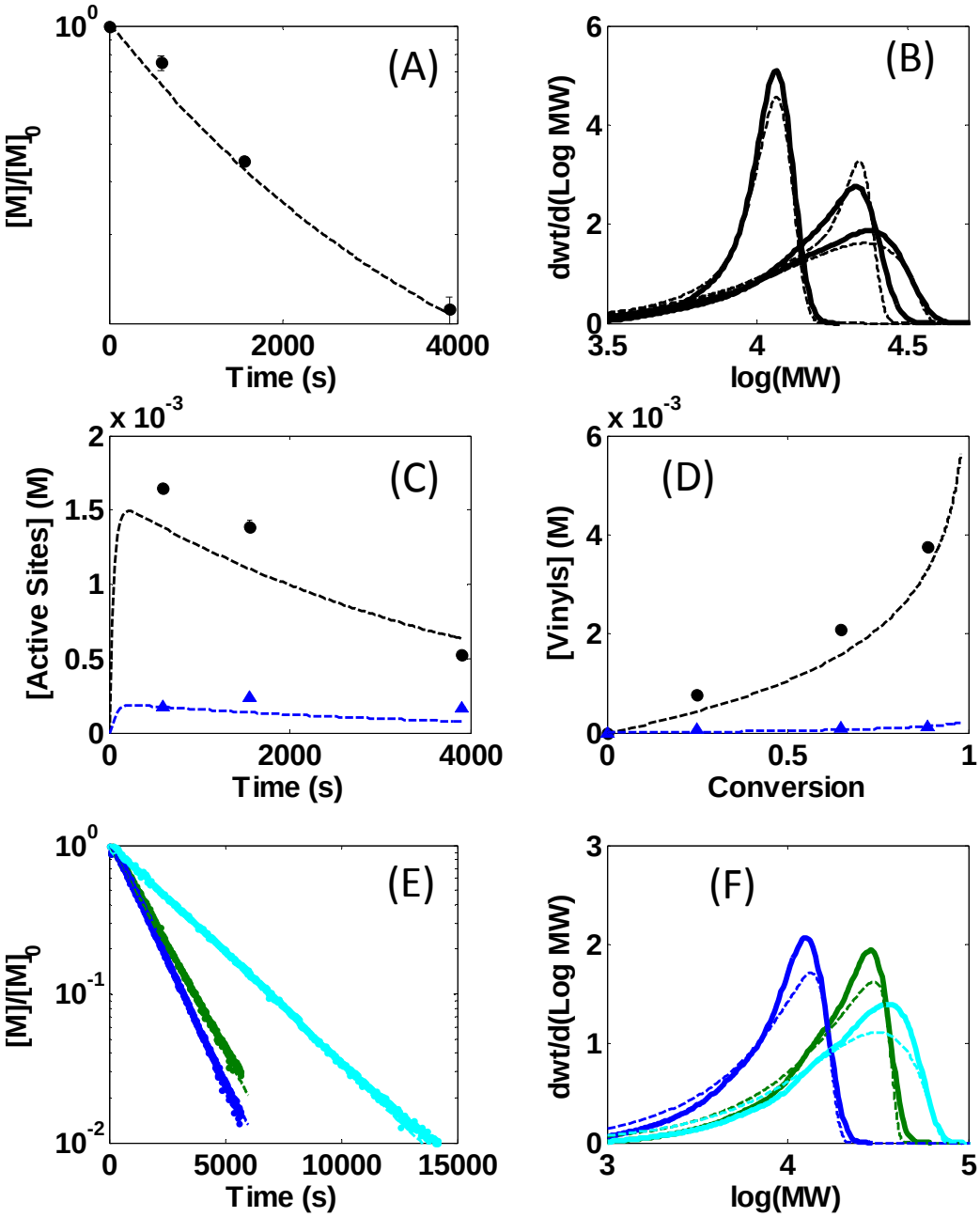

Figure C-SI8. Modeling using Mechanism VI; data (A) monomer consumption (circles), (B) corresponding MWD of each quench (bold solid lines), (C) black circles: primary site counts, blue triangles: secondary site counts, (D) black circles: vinylidene counts, blue triangles: vinylene counts, (E) monomer consumptions under different initial concentrations (symbols), (F) corresponding MWD of each NMR scale experiment (bold solid lines); fits (dashed lines); rate constants are shown in Table 1, active catalyst = 48% for black fits. Initial conditions: black: $[C]_0$ = 3.0 mM, $[M]_0$ = 0.60 M, blue: $[C]_0$ = 3.0 mM, $[M]_0$ = 0.30 M, green: $[C]_0$ = 3.0 mM, $[M]_0$ = 0.60 M, cyan: $[C]_0$ = 1.5 mM, $[M]_0$ = 0.60 M.

2.2 Kinetic Modeling of Hf[^{t}Bu-ON^{pyr}O]Bn$_2$ Catalyst System (2b)

Mechanism I. Living polymerization.

Again, we start by using the living polymerization model. It is immediately apparent from the monomer consumption data (Figure SI9A) that the logarithm of monomer consumption is not linear. It is therefore not surprising that this simplified model is inadequate to fit the data. The MWD fits are also poor (Figure SI9B), predicting higher MW than expected MWDs.

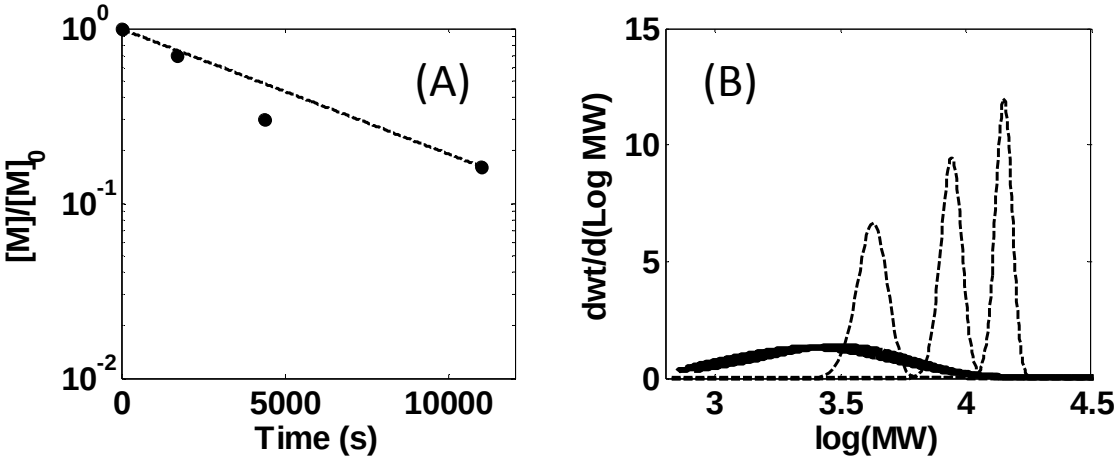

Figure C-SI9. Modeling using Mechanism I; data (A) monomer consumption from three batch quenches at 1694, 4352, 10963 s (circles), (B) corresponding MWD of each quench (bold solid lines); fits (dashed lines); rate constants: $k_i = k_p = 0.55\ M^{-1}\ s^{-1}$. $[C]_0 = 3.0$ mM, $[M]_0 = 0.60$ M.

Mechanism II. Vinylidene formation via chain transfer.

Vinyl end groups were measured during polymerization of this system, indicating that chain transfer is likely present. Inclusion of a chain transfer pathway into the kinetic mechanism will also produce the smaller MW chains that we expect compared with Mechanism I, and it will also produce broader distributions. We start with only vinylidene

formation because it is the dominant vinyl species. Vinylidene may form in a unimolecular reaction, i.e. β-H elimination (Mechanism II(i)), or it may form in a bimolecular reaction with monomer, i.e. β-H transfer (Mechanism II(ii)). The elimination reaction results in the formation of Hf-H species. For the current mechanism it is assumed that these species enchain monomer at a rate equal to the propagation rate. Results of the model fits are in Figure SI10. One additional comment is that the active sites reported in Figure SI10C only represent long chain active sites, that is, chains longer than two repeat units. Smaller chains are lost in polymer workup, and so the active site prediction of the model corrects for this.

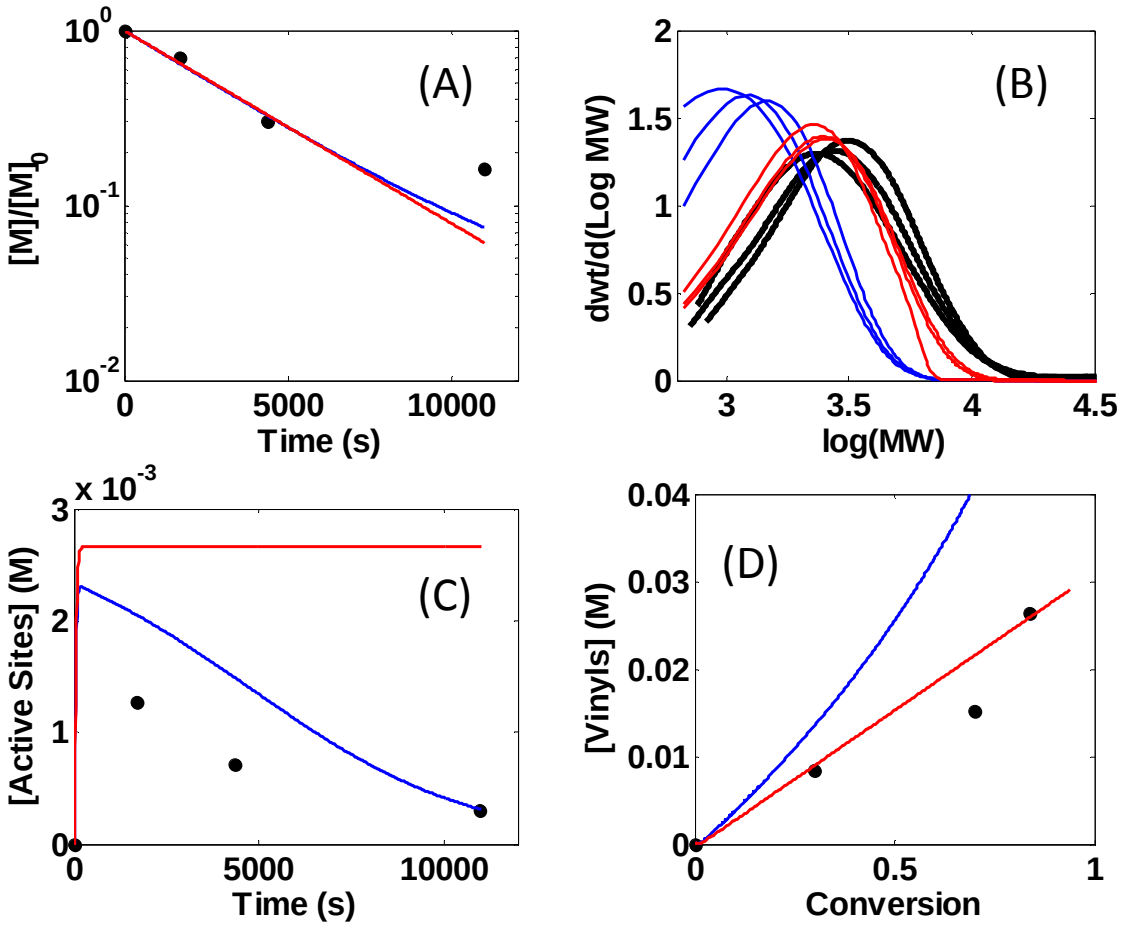

Figure C-SI10. Modeling using Mechanism II; data (A) monomer consumption from three batch quenches at 1694, 4352, 10963 s (circles), (B) corresponding MWD of each quench (bold solid lines); fits (colored lines), (C) primary active site concentration; circles: data; solid lines: fit, (D) vinylidene concentration vs. monomer conversion; circles: data; lines: fit. $[C]_0$ = 3.0 mM, $[M]_0$ = 0.60 M. Blue: Mechanism II(i), rate constants: k_p = 0.087 M^{-1} s^{-1}, $k_{vinylidene}$ = 0.0046 s^{-1}. Red: Mechanism II(ii), rate constants: k_p = 0.08 M^{-1} s^{-1}, $k_{vinylidene}$ = 0.005 M^{-1} s^{-1}.

Both mechanisms shown in SI10 have advantages and disadvantages. The elimination mechanism (blue) captures the drop in active site concentration and the curvature of the vinyl concentration, but the transfer mechanism (red) has a better absolute fit to the distributions and vinyl data. In either case, additional refinement to the mechanism is necessary.

Mechanism III. Misinsertion with slow recovery and monomer independent chain transfer.

Additional data was collected for this system that shows that secondary Hf-alkyls are present during polymerization. To account for such a species, a monomer misinsertion reaction has been added to the mechanism, along with a slow recovery rate, which allows for secondary site accumulation. (The absence of a recovery rate altogether would lead to an ever increasing concentration of secondary sites over the course of the reaction, which is not supported by the data.) These reaction steps, along with monomer independent chain transfer, were used to predict the data, and the result is in Figure SI11. The fit does an excellent job at fitting all the data shown except for the secondary active sites. Also, this model does not have the capability to fit vinylene data (not shown in Figure SI11). An alternate mechanism is therefore required.

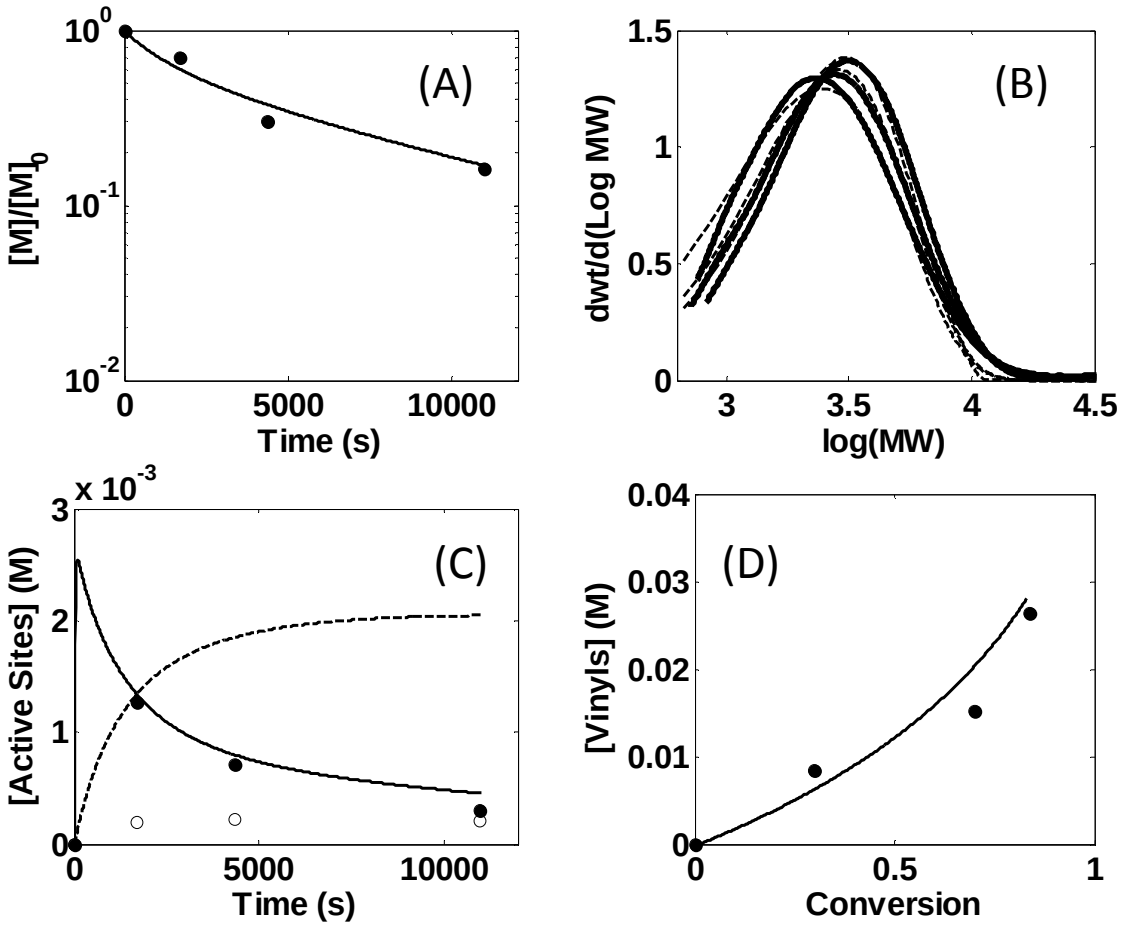

Figure C-SI11. Modeling using Mechanism III; (A) monomer consumption from three batch quenches at 1694, 4352, 10963 s (circles), (B) corresponding MWD of each quench (bold solid lines) with different fits; fits (dashed lines), (C) active site concentrations; filled circles: primary sites, open circles: secondary sites; solid line: primary site fit; dashed line: secondary site fit, (D) vinylidene concentration vs. monomer conversion; circles: data; line: fit. Rate constants: $k_i = k_p = 0.14\ M^{-1}\ s^{-1}$, $k_{vinylidene} = 0.0029\ s^{-1}$, $k_{mis} = 0.00097\ M^{-1}\ s^{-1}$, $k_{rec} = 0.00024\ M^{-1}\ s^{-1}$. $[C]_0 = 3.0$ mM, $[M]_0 = 0.60$ M.

Mechanism IV. Slow initiation and chain transfer.

The overprediction of the active site concentrations and the underprediction of the MWD peaks in Mechanism II suggest that chain initiation may be slow relative to propagation. If this mechanism is amended by a slow initiation process (in the absence of misinsertion) the resulting model prediction can be improved, as shown in Figure SI12. As

in Mechanism II, Mechanism IV(i) uses β-H elimination (monomer independent), while Mechanism IV(ii) uses β-H transfer.

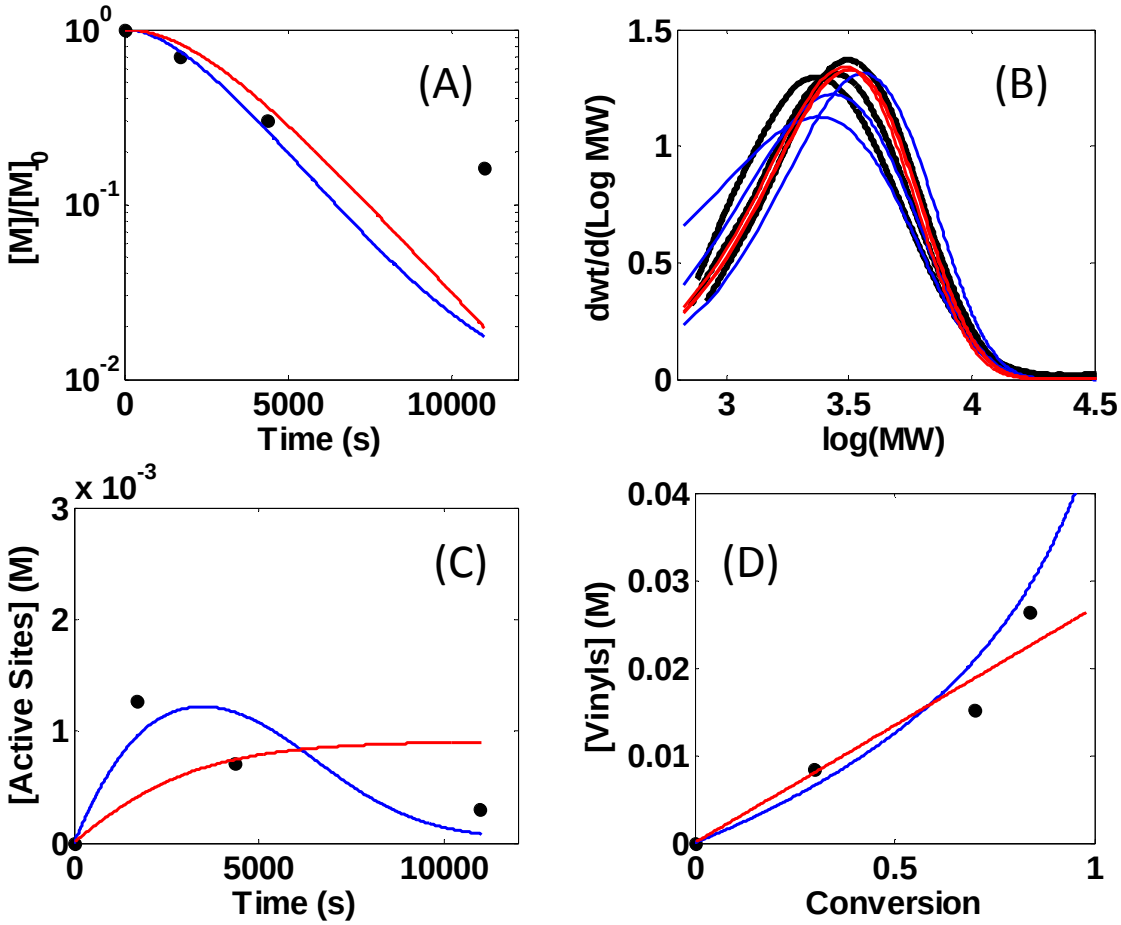

Figure C-SI12. Modeling using Mechanism IV; data (A) monomer consumption from three batch quenches at 1694, 4352, 10963 s (circles), (B) corresponding MWD of each quench (bold solid lines); fits (colored lines), (C) primary active site concentration; circles: data; solid lines: fit, (D) vinylidene concentration vs. monomer conversion; circles: data; lines: fit. $[C]_0$ = 3.0 mM, $[M]_0$ = 0.60 M. Blue: Mechanism IV(i), rate constants: k_p = 0.27 M^{-1} s^{-1}, k_i = 0.00049 M^{-1} s^{-1}, $k_{vinylidene}$ = 0.0057 s^{-1}. Red: Mechanism IV(ii), rate constants: k_p = 0.44 M^{-1} s^{-1}, k_i = 0.00017 M^{-1} s^{-1}, $k_{vinylidene}$ = 0.023 M^{-1} s^{-1}.

Relative to Mechanism II, the elimination mechanism (blue) is much improved compared to the transfer mechanism (red). Nonetheless, there is still the need for a model that can predict secondary active sites, which have not yet been shown due to clarity.

Mechanism V. Slow initiation, chain transfer, and misinsertion with slow recovery.

To account for all observed species, the additions to all previous mechanisms are here considered simultaneously. Monomer independent vinylidene formation is preferred to monomer dependent formation due to its ability to predict the curvature in the vinylidene data. In addition, chain transfer following misinsertion of monomer is added due to the vinylene groups that are observed. Vinylene may potentially form via monomer independent β-H elimination or monomer dependent β-H transfer to monomer. Both are presented in Figure SI13, with blue representing elimination and red representing transfer. The vinylene fits in Figure SI13D show that the monomer dependent transfer reaction is preferred due to its linear behavior, similar to the data. However, neither series of pathways is able to capture the late reaction monomer concentration behavior. Additional changes to the model are necessary.

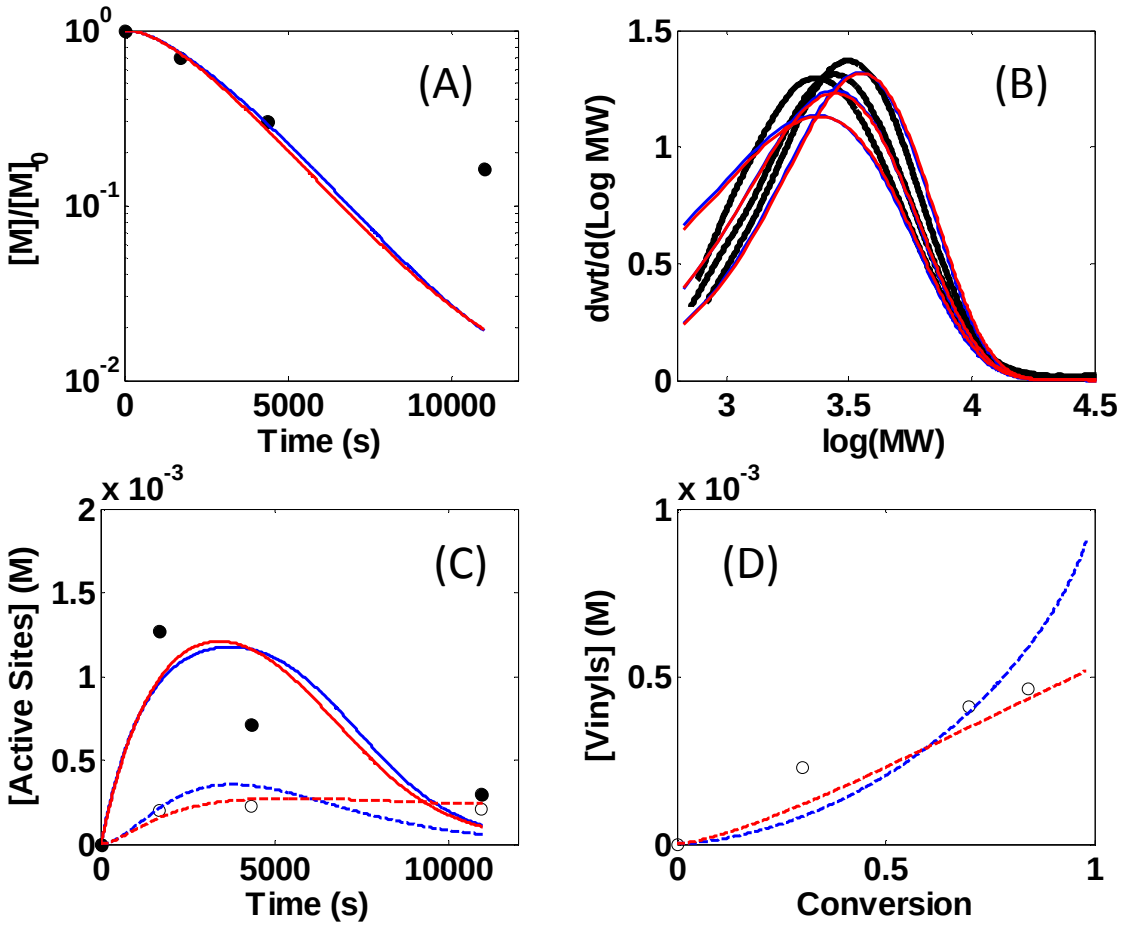

Figure C-SI13. Modeling using Mechanism V; data (A) monomer consumption from three batch quenches at 1694, 4352, 10963 s (circles), (B) corresponding MWD of each quench (bold solid lines); fits (colored lines), (C) active site concentrations; filled circles: primary sites, open circles: secondary sites; solid line: primary site fit; dashed line: secondary site fit, (D) vinylene concentration vs. monomer conversion; open circles: data; dashed lines: fit. $[C]_0$ = 3.0 mM, $[M]_0$ = 0.60 M. Blue: Mechanism V(i), rate constants: k_p = 0.25 M^{-1} s^{-1}, k_i = 0.00064 M^{-1} s^{-1}, $k_{vinylidene}$ = 0.0052 s^{-1}, $k_{vinylene}$ = 0.0004 s^{-1}, k_{mis} = 0.0005 M^{-1} s^{-1}, k_{rec} = 0. Red: Mechanism V(ii), rate constants: k_p = 0.26 M^{-1} s^{-1}, k_i = 0.00062 M^{-1} s^{-1}, $k_{vinylidene}$ = 0.0053 s^{-1}, $k_{vinylene}$ = 0.0016 M^{-1} s^{-1}, k_{mis} = 0.00056 M^{-1} s^{-1}, k_{rec} = 0.00087 M^{-1} s^{-1}.

Mechanism VI. Slow initiation, chain transfer, misinsertion with slow recovery, and deactivation.

In order to account for the monomer consumption behavior, a deactivation reaction is assumed to occur. This reaction in first order in active catalyst concentration and does

not involve monomer. This reaction may be due to air sensitivity of the catalyst or a poison introduced during the experiment. When this pathway is added to Mechanism V, the result is much improved. This model is reported in the main text, and the rate constants are reported in Table 1, along with the values: $k_{vinylene}$ = 0.00097 M^{-1} s^{-1} and $k_{deactivation}$ = 0.00020 s^{-1}. This model also provides a good fit of data collected in smaller NMR-scale experiments, which were performed at different initial concentrations (Figure SI14).

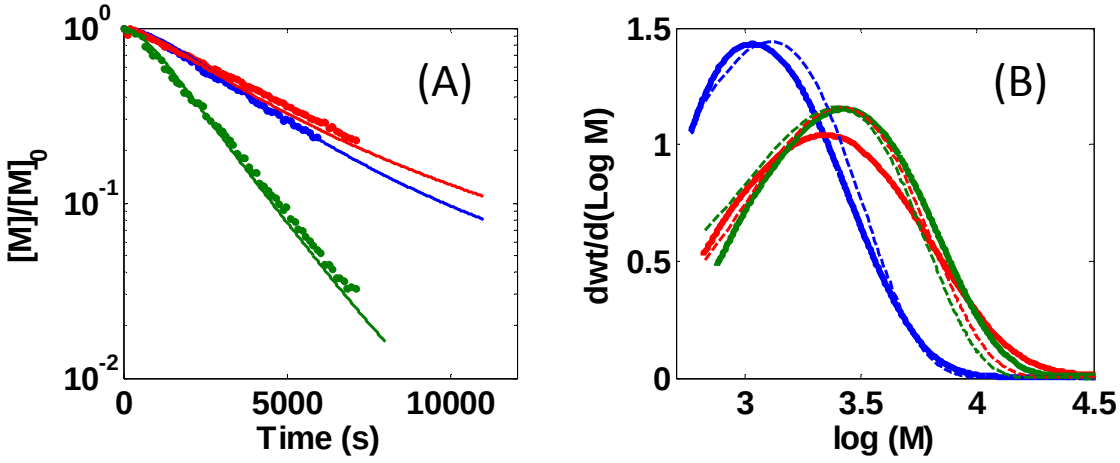

Figure C-SI14. Modeling using Mechanism VI; data (A) monomer consumption from three NMR trials (circles), (B) corresponding endpoint MWD (bold solid lines); fits (dashed lines). Blue: $[C]_0$ = 3.0 mM, $[M]_0$ = 0.30 M, Red: $[C]_0$ = 3.0 mM, $[M]_0$ = 0.60 M, Green: $[C]_0$ = 6.0 mM, $[M]_0$ = 0.60 M. Rate constants: reported in Table 1.

2.3 Kinetic Modeling of Hf[^{t}Bu-ON^{NMe_2}O]Bn_2 Catalyst System (3b)

Mechanism I. Living polymerization.

As before, we start by using the living polymerization model with the initiation rate constant equal to the propagation rate. The monomer consumption data (Figure SI15A) is somewhat accurate, but the MWD fits are very poor (Figure SI9B), predicting distributions that are much narrower than the data and have incorrect peak MWs.

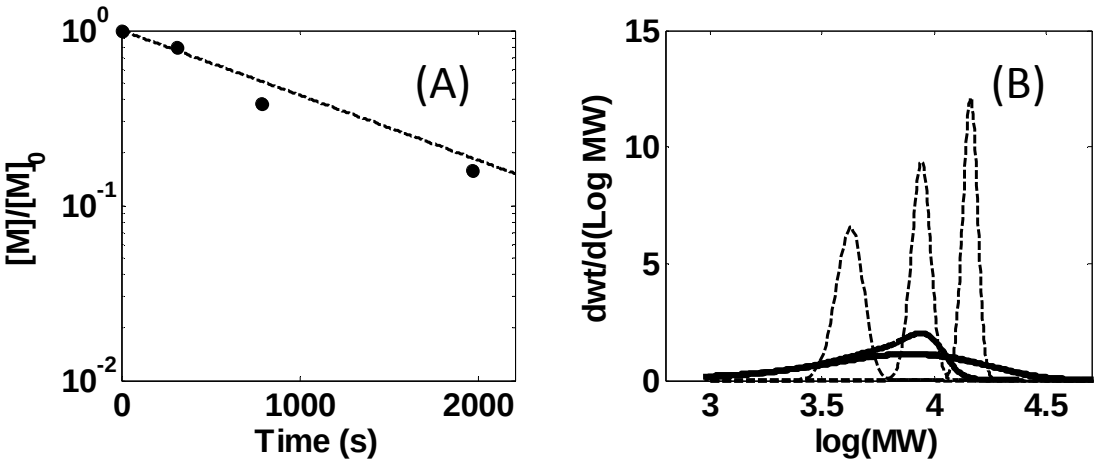

Figure C-SI15. Modeling using Mechanism I; data (A) monomer consumption from three batch quenches at 310, 788, 1961 s (circles), (B) corresponding MWD of each quench (bold solid lines); fits (dashed lines); rate constants: $k_i = k_p = 0.30\ M^{-1}\ s^{-1}$. $[C]_0 = 2.85$ mM, $[M]_0 = 0.60$ M.

Mechanism II. Vinylidene formation via chain transfer.

To account for the broader distributions and vinyl species measured by experiment, chain transfer will also be included in the mechanism. Vinylidene groups may once again be formed through either a β-H elimination (monomer independent; Mechanism II(i)) pathway or a β-H transfer to monomer (mechanism II(ii)) pathway. Both are compared in Figure SI16. The elimination pathway (blue) seems to provide a better fit of the vinylidene data due to its ability to predict an upward curve at higher monomer conversion.

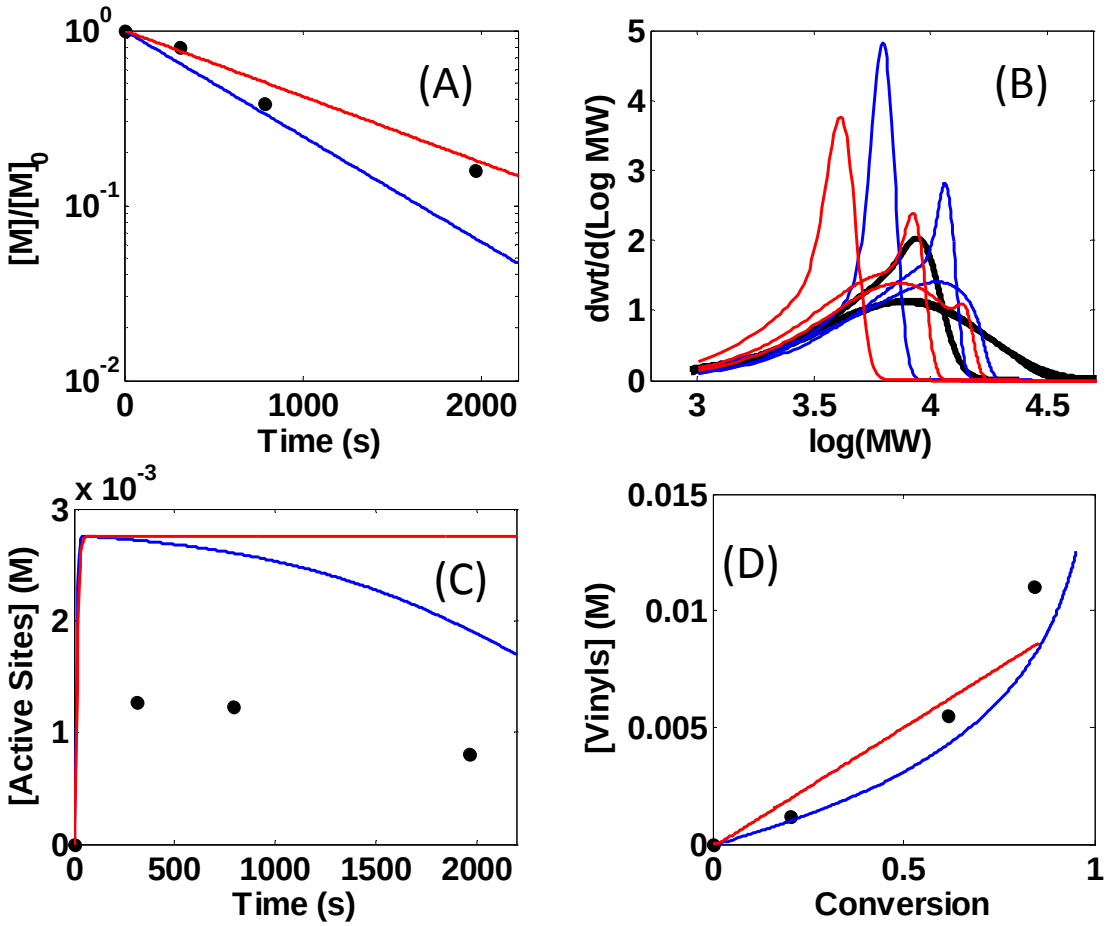

Figure C-SI16. Modeling using Mechanism II; data (A) monomer consumption from three batch quenches at 310, 788, 1961 s (circles), (B) corresponding MWD of each quench (bold solid lines); fits (colored lines), (C) primary active site concentration; circles: data; solid lines: fit, (D) vinylidene concentration vs. monomer conversion; circles: data; lines: fit. $[C]_0$ = 2.85 mM, $[M]_0$ = 0.60 M. Blue: Mechanism II(i), rate constants: k_p = 0.49 M^{-1} s^{-1}, $k_{vinylidene}$ = 0.0023 s^{-1}. Red: Mechanism II(ii), rate constants: k_p = 0.30 M^{-1} s^{-1}, $k_{vinylidene}$ = 0.0054 M^{-1} s^{-1}.

Mechanism III. Slow initiation and chain transfer.

A slow initiation rate constant may be present in this system. Its effect can be seen in the initial points of the monomer consumption data. Furthermore, a slow initiation rate would push the early MWDs to higher molecular weights. When this model is fit to the data, an improved fit can indeed be seen (Figure SI17). This mechanism is an improvement

over Mechanism II, but it still lacks the ability to predict vinylene end groups (not shown in Figure SI17), and it over predicts the concentration of active sites late in the reaction.

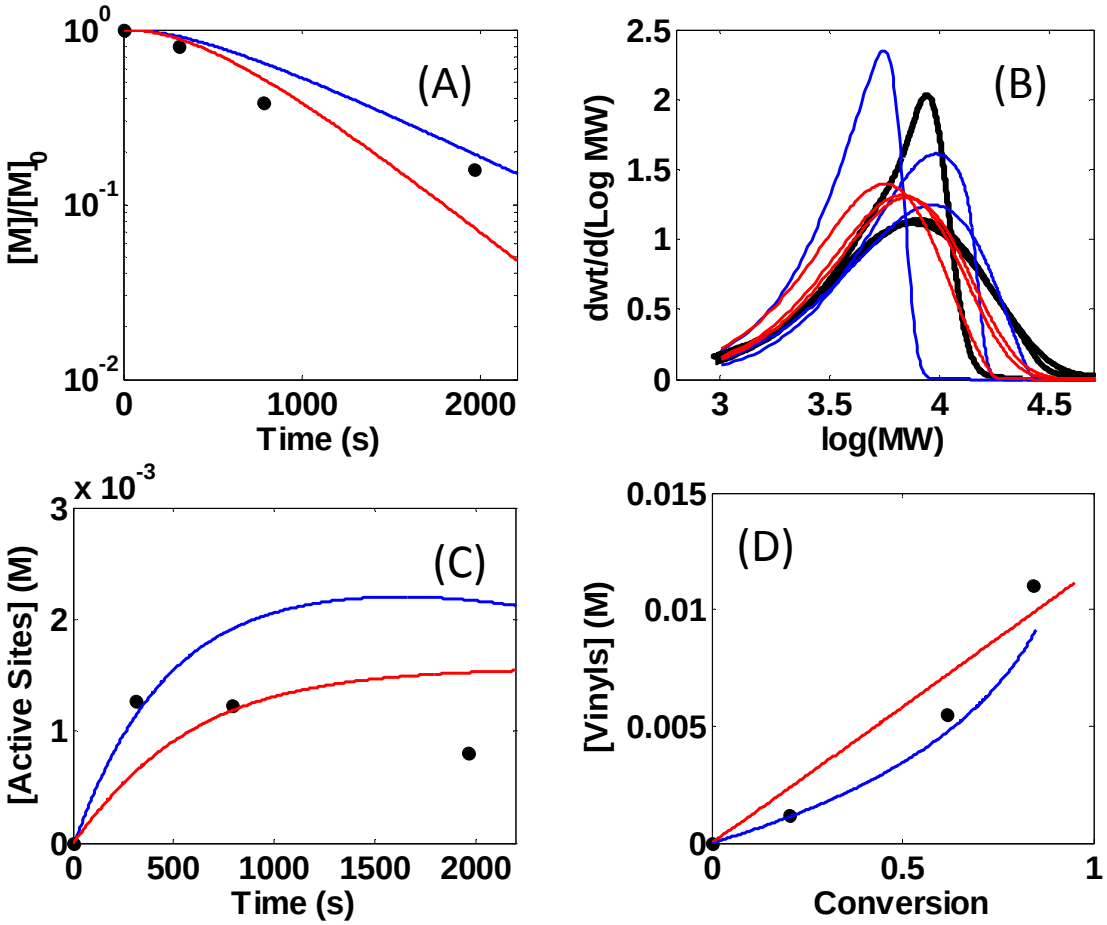

Figure C-SI17. Modeling using Mechanism IV; data (A) monomer consumption from three batch quenches at 310, 788, 1961 s (circles), (B) corresponding MWD of each quench (bold solid lines); fits (colored lines), (C) primary active site concentration; circles: data; solid lines: fit, (D) vinylidene concentration vs. monomer conversion; circles: data; lines: fit. $[C]_0$ = 2.85 mM, $[M]_0$ = 0.60 M. Blue: Mechanism III(i), rate constants: k_p = 0.44 M^{-1} s^{-1}, k_i = 0.0030 M^{-1} s^{-1}, $k_{vinylidene}$ = 0.0023 s^{-1}. Red: Mechanism III(ii), rate constants: k_p = 1.1 M^{-1} s^{-1}, k_i = 0.0015 M^{-1} s^{-1}, $k_{vinylidene}$ = 0.023 M^{-1} s^{-1}.

Mechanism IV. Slow initiation, chain transfer, and incomplete catalyst participation.

Mechanism III(i) is preferable to Mechanism III(ii) due to its ability to capture the curve in the vinylidene data (Figure SI17D). However, this mechanism over predicts the

primary active site concentration (Figure SI17C). In addition, the early time MWD has a higher MW than predicted. Both of these differences may be accounted for with the assumption that not all of the catalyst actively participates in the reaction. This new assumption is used to predict the data in Mechanism IV, along with a monomer-dependent reaction that will generate vinylene species. No secondary active sites were detected, so the model predicts that vinylene is formed from a reaction involving a primary active site and a monomer even though the true reaction may involve a two step process of monomer misinsertion followed by fast chain transfer. The result for this model is in Figure SI18.

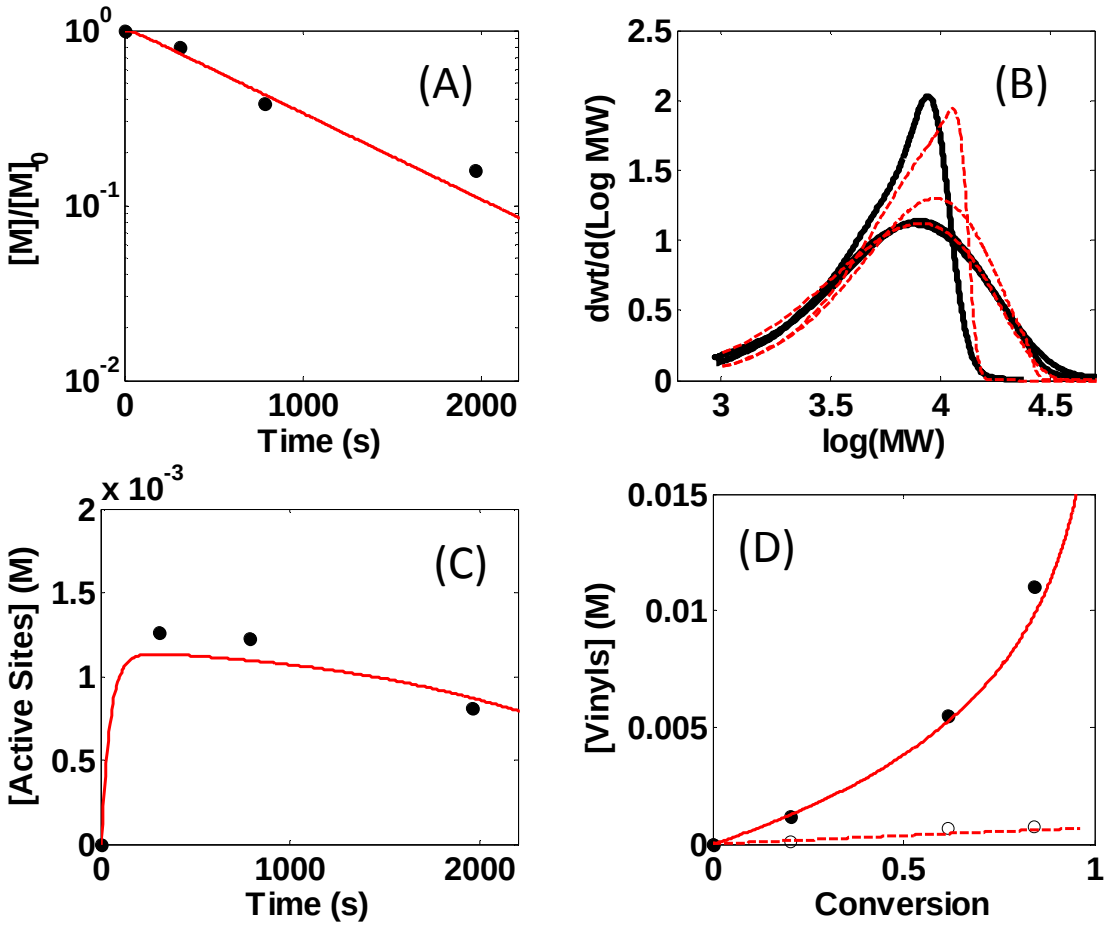

Figure C-SI18. Modeling using Mechanism IV; data (A) monomer consumption from three batch quenches at 310, 788, 1961 s (circles), (B) corresponding MWD of each quench (bold solid lines); fits (red lines), (C) active site concentrations; circles: primary sites; solid line: fit, (D) vinyl concentration vs. monomer conversion; filled circles: vinylidene concentration, open circles: vinylene concentration, solid line: vinylidene fit, dashed line: vinylene fit. $[C]_0$ = 2.85 mM, $[M]_0$ = 0.60 M. Red: Mechanism IV, rate constants: k_p = 0.95 M^{-1} s^{-1}, k_i = 0.037 M^{-1} s^{-1}, $k_{vinylidene}$ = 0.0055 s^{-1}, k_{mis} = 0.0012 M^{-1} s^{-1} (forms vinylene), active catalyst = 42%. Rates also reported in main text.

Additional data was collected for this catalyst in NMR scale reactions with different initial catalyst and monomer concentrations. The fit using Mechanism IV and the rate constants in the main text (also in the Figure SI18 caption) to these data are in Figure SI19.

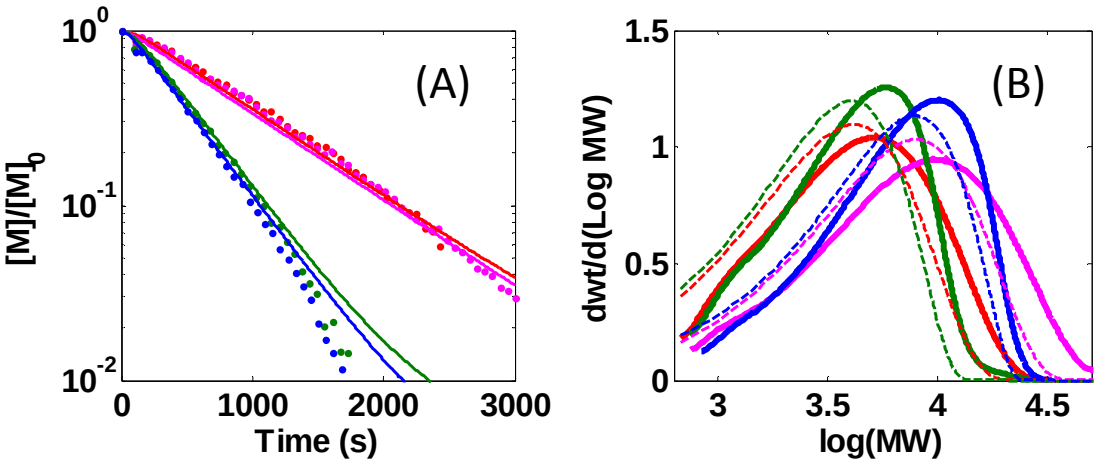

Figure C-SI19. Modeling using Mechanism IV; data (A) monomer consumption from four NMR trials (circles), (B) corresponding endpoint MWD (bold solid lines); fits (dashed lines). Blue: $[C]_0$ = 6.0 mM, $[M]_0$ = 0.60 M, Green: $[C]_0$ = 6.0 mM, $[M]_0$ = 0.30 M, Magenta: $[C]_0$ = 3.0 mM, $[M]_0$ = 0.60 M. Red: $[C]_0$ = 3.0 mM, $[M]_0$ = 0.30 M. Rate constants: reported in Figure SI18 caption.

Appendix D Supporting Information for Chapter 4

1. Experimental Procedure

Gel Permeation Chromatography (GPC) Analysis. The procedure used to analyze polymer samples using GPC methods was taken from Novstrup et al.,[2] and it is summarized below. Poly(1-hexene) samples were added to THF at room temperature and allowed to dissolve for 4 h. Solutions were then passed through a 0.2 μm filter to remove any particulate matter. The GPC analysis was performed on a Viscotek GPCmax VE 2001. On the Viscotek GPCmax VE 2001, samples were injected through a 200 μL injection loop and passed through three Viscotek T6000M 10 μm General Mixed Org columns in series in a 35 °C oven at a flow rate of 1.0 mL min^{-1}. The analysis made use of the differential RI detector, a viscometer and both high angle and low angle light scattering detectors. Molecular weights were assigned by way of a triple-detector curve created with polystyrene standard of 99 kg mol^{-1} (ref).

2. Estimation of Error Bounds

Here we give an example of how the error bounds were obtained for one of the systems (Catalyst **1b**). First, the entire data set consisting of (1) monomer consumption, (2) MWD, (3) primary and secondary active site counts, and (4) vinyl terminated group counts was fit to the chosen mechanism as explained in the main text. The resulting values of the rate constants are shown in Table 1. Fits are shown in Figure SI8.

The error due to the uncertainty in the GPC measurements was estimated as follows: the MWD curve was shifted towards higher molecular weights by 0.04 on the log

scale, and the entire data set was re-optimized giving rise to a different set of rate constant values. Similarly, the MWD curve was shifted towards lower molecular weights by 0.05 on the log scale, and the entire data set was re-optimized giving rise to yet another set of rate constant values. Varying the MWD has the largest effect on the rate constants, and for this system, the error bars given in the main text are based on the error due to GPC measurements.

3. Additional Kinetic Modeling Results of Systems 1-4

The modeling perspectives used in this paper (i) start with the simplest possible polymerization mechanism, (ii) determine if it fits the data, and (iii) if it does not fit the data within experimental error, postulate the next simplest mechanism. Using this procedure the simplest model consistent with the data is discovered. Examples of how to proceed through these steps has been detailed described in previous publications.[1] The final fits to the monomer consumptions and MWDs of systems **1-4** have been included in the main text, as well as the end-group counts and active site counts for system **2**. Below are the additional fits of the end-group counts and active site counts for system **1, 3,** and **4**.

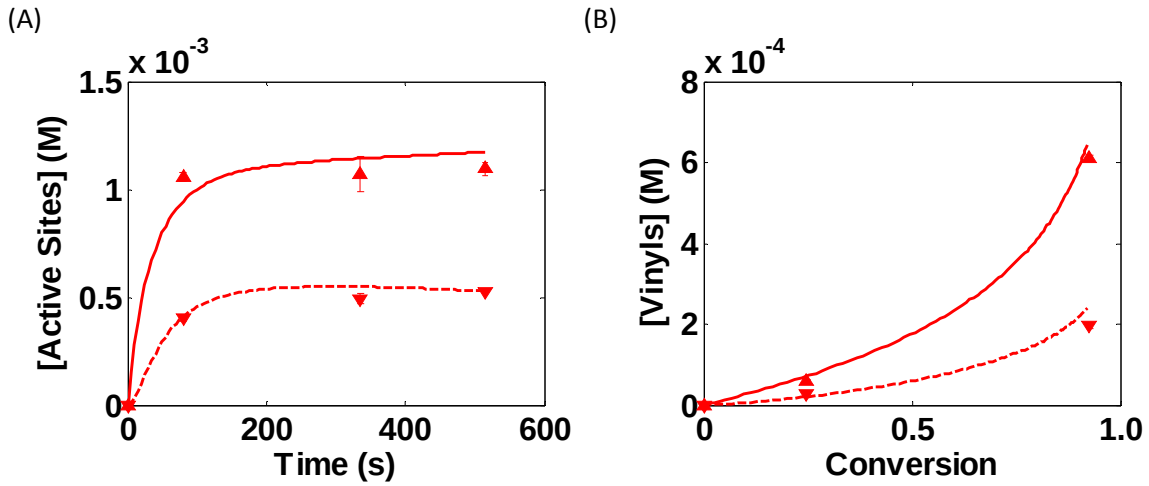

Figure D-SI1. Additional fits to the data of system **1**. (A) Active site counts. Primary – up triangles (data)/solid line (fit); secondary – down triangles (data)/dashed line (fit). (B) End group analysis. Vinylidene - up triangles (data)/solid line (fit); vinylene - down triangles (data)/dashed line (fit).

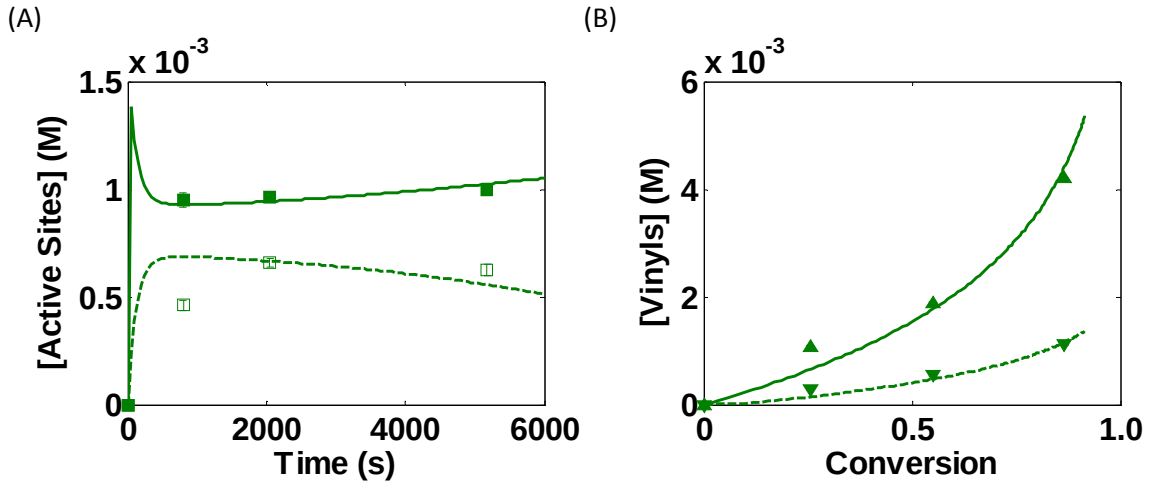

Figure D-SI2. Additional fits to the data of system **3**. (A) Active site counts. Primary – up triangles (data)/solid line (fit); secondary – down triangles (data)/dashed line (fit). (B) End group analysis. Vinylidene - up triangles (data)/solid line (fit); vinylene - down triangles (data)/dashed line (fit).

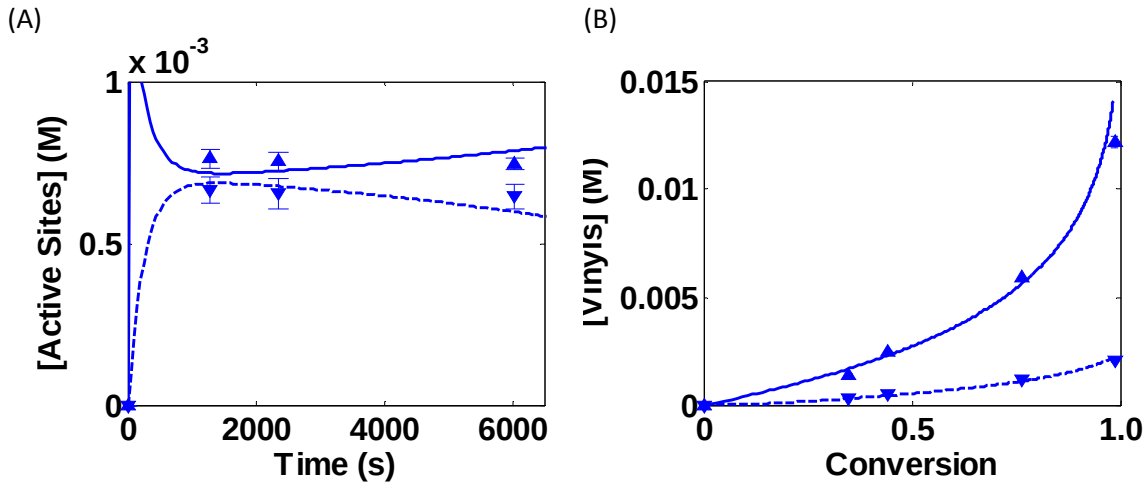

Figure D-SI3. Additional fits to the data of system **4**. (A) Active site counts. Primary – up triangles (data)/solid line (fit); secondary – down triangles (data)/dashed line (fit). (B) End group analysis. Vinylidene - up triangles (data)/solid line (fit); vinylene - down triangles (data)/dashed line (fit).

Appendix E Supporting Information for Chapter 5

1. EXPERIMENTAL PROCEEDURES

Gel Permeation Chromatography (GPC) Analysis. The procedure used to analyze polymer samples using GPC methods was taken from Novstrup et al.,[4] and is summarized as follows: Poly(1-hexene) samples were dissolved in THF at room temperature for 2 hours. Solutions were then passed through a 0.2 μm filter to remove any particulate matter. The GPC analysis was performed on a Viscotek GPCmax VE 2001. Samples were injected through a 200 μL injection loop and passed through three Viscotek T6000M 10 μm General Mixed Org columns in series in a 35 °C oven at a flow rate of 1.0 mL min^{-1}. The analysis made use of the differential RI detector, a capillary viscometer, a low-angle and a high angle light scattering detectors. Molecular weights were assigned by way of a multi-detector calibration curve created with polystyrene standards of 99 kg mol^{-1}.

2. KINETIC MODELING

Model 1. Base model including initiation, propagation, misinsertion and recovery.

As described in detail a the previous publication,[2] the set of elementary reactions needed to predict the experimental data in the case of the stoichiometric amount of the activator (case **1**) consists of initiation, propagation, misinsertion and recovery, with the associated rate constants k_i, k_p, k_{mis} and k_{rec}. Chain transfer for this system is shown to be negligible.[2] The set of elementary reactions are:

$$C^* + M \xrightarrow{k_i} R_1 \qquad \text{S1}$$

$$R_i + M \xrightarrow{k_p} R_{i+1} \qquad \text{S2}$$

$$R_i + M \xrightarrow{k_{mis}} P_{i+1} \quad \text{S3}$$

$$P_i + M \xrightarrow{k_{rec}} R_{i+1} \quad \text{S4}$$

where the following notation is used:

M monomer

C precatalyst (see Scheme 1 in main text)

C* activated catalyst, i.e. the ion pair including pre-catalyst with activator (see Scheme 1 in main text)

R_i primary active site with a growing polymer chain of length i, where the most recent repeat unit is normally inserted; this is an ion pair including the catalytic site and activator (see Scheme 1 in main text)

P_i secondary (misinserted) active site with a growing polymer chain of length i, where the most recent repeat unit is misinserted; this is an ion pair including the catalytic site and activator (see Scheme 1 in main text)

The defining differential equations for the mass action kinetics of the Base Model are given in reactions S1 though S4. The model was fit to the experimental monomer consumption and MWD data shown in Figure S1, where the values of the rate constants are given in the figure caption. The monomer consumption is adequately fit. However, in the Base Model each activator molecule forms a single active site and, hence, the amount of active sites cannot exceed the initial amount of activator. This is not consistent with the active site counts shown in Figure 2. Also, because the Base Model under predicts the number of active sites, the Base Model predicts much higher molecular weights under sub-stoichiometric activator conditions than the MWD observed experimentally. This analysis clearly shows the need for the presence of more active sites than the stoichiometric amount

of activator. Although more chain transfer reactions can lower the molecular weight distribution, the predicted MWD would then be much broader than with a PDI much larger than the experimental PDI of 1.1, and the predicted M_n will not grow with monomer conversion as shown in Figure 7.

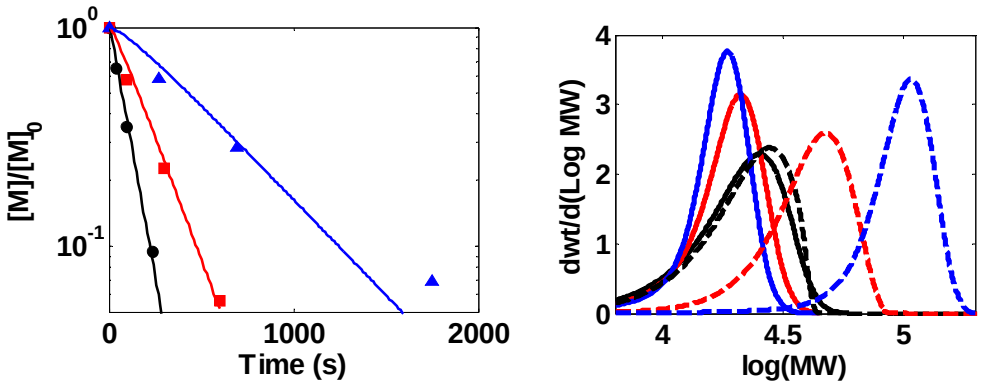

Figure E-SI1. Base Model predictions of reactions **1** (black), **2** (red), **3a** (blue).. (A) Monomer consumption; data: symbols, predictions: lines. (B) End-point MWD; data: solid, predictions: dashed. Rate constants: k_i = 0.08 M^{-1} s^{-1}, k_p = 8.0 M^{-1} s^{-1}, k_{mis} = 0.054 M^{-1} s^{-1}, k_{rec} = 0.040 M^{-1} s^{-1}.

Model 2 Reversible Activation Model.

Model 2.1 Reversible activation of both primary and secondary active sites

How can there be more active sites than the nominal amount of activator as observed under sub-stoichiometric activator conditions? One possible kinetic postulate is to make the activation reversible. In a reverse reaction the benzyl ligand (Bn) would transfer from the counterion of an active catalyst (R_i or P_i), resulting in a free activator and an inactive catalytic complex which is denoted as Bn-R_i or Bn-P_i (i.e., neutral catalyst with a polymer chain and a benzyl ligand attached, but no active site). In addition to reactions S1 through S4 the elementary reaction steps also include:

$$C + A \xrightleftharpoons{K_{act}} C^* \quad \text{S5}$$

$$Bn\text{-}R_i + A \xrightleftharpoons{K_{act}} R_i \quad \text{S6}$$

$$Bn\text{-}P_i + A \xrightleftharpoons{K_{act}} P_i \quad \text{S7}$$

The reversible activation process is assumed to be fast compared to k_p; otherwise, the propagation of R_i will be interrupted when the it is converted into Bn-R_i, resulting in increased dormancy and broader MWD of polymer chains, which would contradict the experimentally observed MWD with a PDI of 1.1. Thus, an equilibrium constant is employed instead of explicit forward and reverse reactions. Based upon fitting the experimental data $K_{act} = 10^3$ M^{-1} and the forward reaction rate $k_{act} > 10^4$ $M^{-1}s^{-1}$. Moderate changes in these rate constants will not have significant effect on the prediction; thus, it is reasonable to assume that the same rate constant controls the reversible activation process independent of the chemical moieties to which the activator is associated. As described in Eqns. S5 through S7 all the pre-catalyst can be activated even with sub-stoichiometric amounts of activator, although not all the catalyst is activated at the same time. In the active site count experiments (Figure 2), both R_i and Bn-R_i species are counted as primary sites and both P_i and Bn-P_i species are counted as secondary sites, which explains how the measured amount of active sites can exceed the initial amount of the activator consistent with the data shown in Figure 2.

The defining differential equations for the mass action kinetics for Model 2.1 are given by reactions S1 though S7. The model was fit to the experimental monomer consumption, MWD, and active site counts data shown in Figure S2, where the rate constants are given in the caption. Since additional reactions take place under both sub-stoichiometric and stoichiometric activator conditions, the other rate constants (i.e. k_i, k_p,

etc.) for the Model 2.1 differ slightly from those for Base Model. The equilibrium constant is large, indicating that the forward (i.e. activation) reaction is strongly favored. An important observation is that, since in the Model 2.1 reversible activation occurs for both primary and secondary sites, the ratio of primary and secondary sites is constant and independent of the activator amount. However, since the reversible activation is fast, normal propagation is not interrupted and consequently the predicted MWD is unaffected by the change by the ratio of activator concentration to catalyst concentration, which clearly contradict with the experimental data shown in Figure S2.

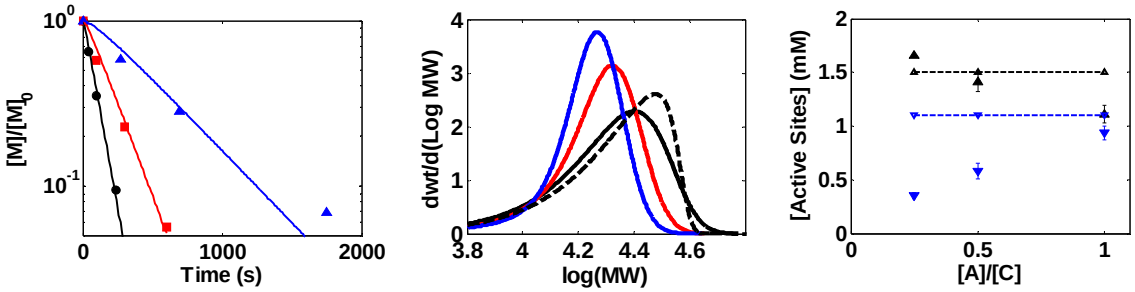

Figure E-SI2. Predictions of Model 2.1. A) Monomer consumption of reactions **1** (black), **2** (red), **3a** (blue). Data: symbols, predictions: lines. B) End-point MWDs of reactions **1** (black), **2** (red), **3a** (blue). Data: solid; predictions: dashed (the predictions for all three condition, i.e. **1**, **2** and **3a** are the same and are shown as the single dashed black line). C) Active site counts of quenched NMR scale reactions **1**, **2**, **3a**. Data: black up-pointing triangles: primary active-site count; blue down-pointing triangles: secondary active-site count, predictions: dashed lines with unfilled triangles. Rate constants: $K_{act} = 10^3$ M^{-1}, $k_i =$ 0.08 M^{-1} s^{-1}, $k_p = 10$ M^{-1} s^{-1}, $k_{mis} = 0.045$ M^{-1} s^{-1}, $k_{rec} = 0.033$ M^{-1} s^{-1}.

Model 2.2. Selective reversible activation of primary active site

An obvious way to rectify the problem in Model 2.1 as described above is to postulate that only the primary site can undergo the reversible activation; thus, Eqn. S7 is eliminated in Model 2.2. The defining mass action differential equations for Model 2.2 are given by Eqns. S1 through S6. The model was fit to the experimental monomer

consumption, MWD at the end of reaction and active site counts data, where the predictions are shown in Figure S3. The values of the rate constants are given in the figure caption. The monomer consumption data are adequately fit. The prediction of the variation in the relative amounts of primary and secondary active sites with the amount of activator is much improved as compared with Model 2.1, where the primary sites count increases and the secondary sites counts decreases as the amount of activator decreases. However, the prediction of the MWDs under sub-stoichiometric activator conditions, although improved, is not completely successful as shown in Figure S3A. The MWDs for the cases **2** and **3a** are narrower than for the stoichiometric case **1** in agreement with the experimental data, but the position of the peak does not shift toward lower MW as observed experimentally.

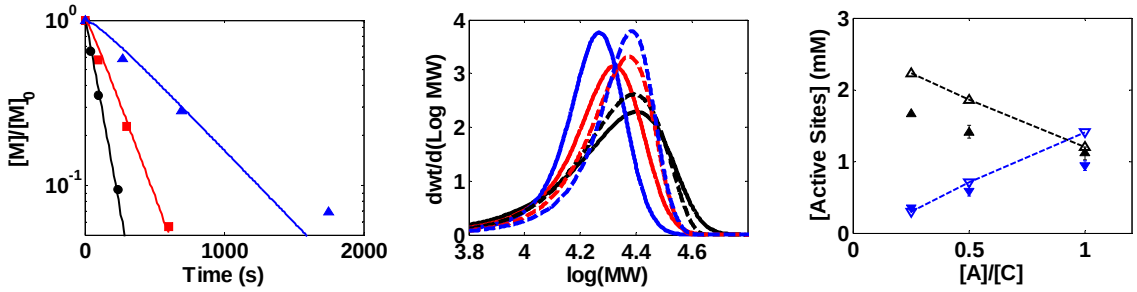

Figure E-SI3. Predictions of Model 2.1. A) Monomer consumption of reactions **1** (black), **2** (red), **3a** (blue). Data: symbols, predictions: lines. B) End-point MWDs of reactions **1** (black), **2** (red), **3a** (blue). Data: solid, predictions: dashed. C) Active site counts of quenched NMR scale reactions **1**, **2**, **3a**. Data: black up-pointing triangles: primary active-site count; blue down-pointing triangles: secondary active-site count, predictions: dashed lines with unfilled triangles. Rate constants: $K_{act} = 10^4$ M^{-1}, $k_i = 0.08$ M^{-1} s^{-1}, $k_p = 10$ M^{-1} s^{-1}, $k_{mis} = 0.045$ M^{-1} s^{-1}, $k_{rec} = 0.033$ M^{-1} s^{-1}.

The major positive result in Models 2.1 and 2.2 is that the MWDs now do not shift to higher molecular weights with sub-stoichiometric amounts of activator. The MWDs are not perfect, but perhaps the fits could be improved with additional modifications of the

Reversal Activation Model. However, the fluorine NMR results described in the Results section strongly argue against Model 2. According to reactions S5 through S7, the reversible activation takes place at both stoichiometric and sub-stoichiometric amounts of activator, where broadening of the benzyl signals in the ^{1}H NMR spectra is expected due to the exchange of the benzyl group. However, broadening of the benzyl ligand peaks is only observed experimentally under the sub-stoichiometric conditions as shown in Figure S4, where the corresponding peaks under stoichiometric conditions are sharp.

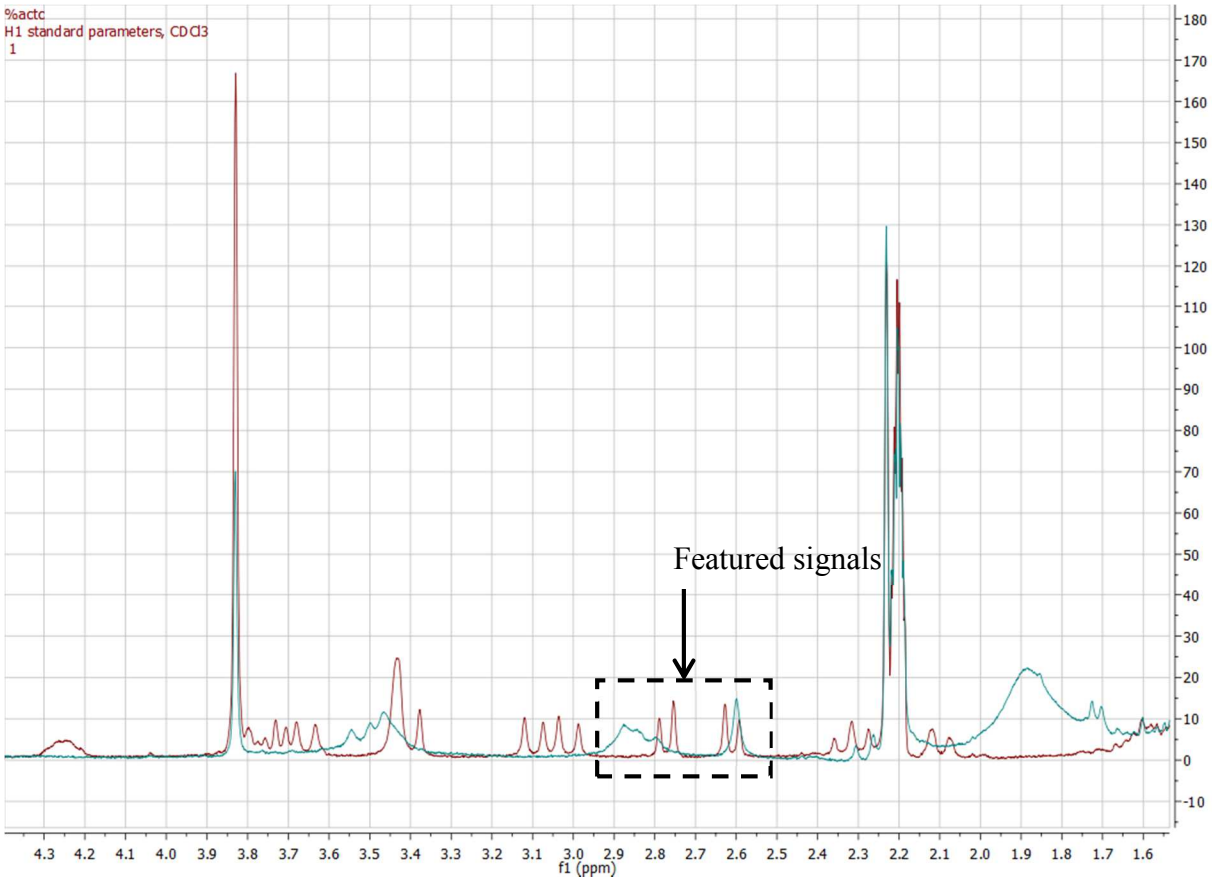

Figure E-SI4. ^{1}H NMR spectra of activation. Initial Conditions: red: $[C]_0$ = 3.0 mM, $[A]_0$ = 3.3 mM; blue: $[C]_0$ = 3.0 mM, $[A]_0$ = 1.5 mM.

Model 3. Ligand Transfer Model.

The difference between stoichiometric and sub-stoichiometric activator conditions is the presence of the inactivated pre-catalyst in the latter case. So it is natural to assume that there may be an activation of pre-catalyst via direct ligand transfer from pre-catalyst to active catalyst. In this process, the two catalysts need to be close proximity, thus we assume the formation of a BNC consisting of one active catalytic complex (R_i or P_i) and one inactive catalytic complex (either Bn-R_i or Bn-P_i). When the bridge ligand in the BNC shifts from the inactive catalyst to the active one, the inactive catalyst becomes active and

vice versa. This specific Ligand Transfer Model preserves useful features of the Model 2. In addition, in this new kinetic mechanism the exchange between the active and inactive catalyst complex will not take place under stoichiometric condition, when there is no free pre-catalyst; thus, for stoichiometric activator conditions the BNC will not form and consequently Model 1 will be recovered as desired. The formation/dissociation reaction of the BNC is given by

$$R_i + Bn\text{-}R_j \overset{K_{ex}}{\rightleftharpoons} R_i\text{-}Bn\text{-}R_j \qquad \text{S8A}$$

Eq. S8A is a compact notation that includes both activated catalyst and pre-catalyst, where we denote the activated precatalyst C* as R_0, and the unactivated precatalyst C as Bn-R_0.

Introduction of the BNC complex in the kinetic mechanism leads to several questions that need to be addressed: Are both primary and secondary active sites capable of forming the BNC (Model 3.1)? Is the BNC formation reversible (Model 3.2)? Does the BNC propagate and what is the propagation rate constant? And, can a BNC that consists of the activated catalyst and a pre-catalyst (i.e. C-C*) be initiated and, if possible, what is the rate constant of this initiation? The answer to each of these questions will result in different versions of the Model 3. In addition to the model description in the paper, here we address the first two questions.

Model 3.1 Both primary and secondary active catalyst complexes can from the BNC.

When both primary and secondary active catalytic complexes form the BNC, there is an additional reaction in Eq. S8; specifically,

$$P_i + Bn\text{-}P_j \overset{K'_{ex}}{\rightleftharpoons} P_i\text{-}Bn\text{-}P_j \qquad \text{S8B}$$

The mechanism included in Eq. S8-B can be dismissed for the same reason Model 2.1 was been dismissed in the previous section. Specifically, the mechanism is not selective with respect to the primary and secondary sites and, thus, cannot predict experimentally observed change in the ratio of primary and secondary active sites with change in the amount of activator (see Figure S2B).

Model 3.2a Ligand transfer via BNC with no dissociation.

If one assumes that the BNC once formed will never decompose, S8A is replaced with

$$R_i + Bn\text{-}R_j \xrightarrow{k_{ex}} R_i\text{-}Bn\text{-}R_j \qquad \text{S9}$$

The main difficulty with this assumption is that one activator can activate at most two pre-catalysts. As shown in Figure S5 when the [A]:[C] ratio is 1:4 (i.e. the blue dashed line), only one half of the catalyst can grow chains, resulting in the predicted MWD being much higher than the experimentally observed MWD. Thus, the BNC formation has to be reversible.

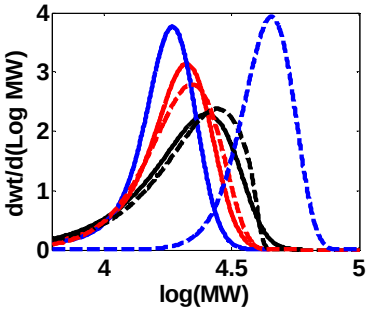

Figure E-SI5. Model 3.2a predictions of the MWD at the end NMR scale reactions for the following conditions: **1** (black), **2** (red), **3a** (blue) based on Model 3.1. Data: solid, predictions: dashed.

Model 3.2b Ligand transfer via BNC followed by instant dissociation of BNC.

In contrast to the previous assumption, In Model 3.3 we assume that the BNC is an unstable intermediate, where the Bn-ligand is immediately transferred to the originally inactive chain followed by dissociation of BNC as defined by

$$R_i + Bn\text{-}R_j \overset{k_{ex}}{\rightleftharpoons} Bn\text{-}R_i + R_j \qquad \text{S10}$$

The Ligand Transfer Model is defined by reactions S1 through S4 and S10. This mechanism is characterized by the following important features:

1. Since the ligand transfer does not change the concentrations of any reactive species, the reaction rate does not affect the monomer consumption.
2. The Bn-R_i species are inactive. Thus, if k_{ex} is small, the ligand transfer results in a formation of dormant species similarly to how the misinsertion results in formation of the secondary active sites. Dormancy causes broadening of the MWD as illustrated in Figure S6B by the blue dotted line corresponding to the case of the k_{ex}, which is 10 times smaller than the model value of the dashed line. If the exchange happens much faster than propagation, varying k_{ex} will no longer have any effect on the reaction system.
3. Model 3.2B still does not provide a fully satisfactory answer to how the molecular weight becomes lower with decreased amount of activator. Specifically, there is a narrowing of the MWD as shown in Figure S6B with a small decrease in the MWD peak maximum with sub-stoichiometric amounts of activation, where the data shows a more substantial decrease with sub-stoichiometric amounts of activator.

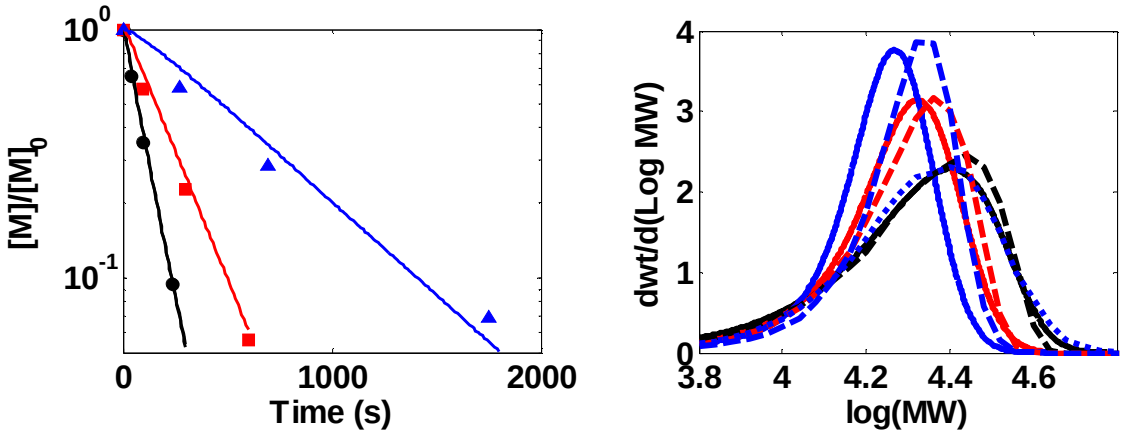

Figure E-SI6. Model 3.2b predictions of NMR scale reactions for the following conditions: **1** (black), **2** (red), **3a** (blue) based on Model 3.2b. A) Monomer consumptions. Data: symbols, predictions: lines. B) End-point MWDs. Data: solid, predictions: dashed. k_{ex} = 500 M^{-1} s^{-1}.

Model 3.3 Ligand Transfer Model via BNC with fast initiation

Model 3.3 involves the same basic mechanics described above, but not with fast initiation. Model 3.3 is described fully in the main text as described by Schemes 1 and 2, and it is the minimal model that is capable of describing the experimental data.

3. KINETIC ANALYSIS OF THE Cp*ZrMe2[N(tBu)C(Me)N(Et)]/[B(C6F5)4] SYSTEM

The Ligand Transfer Model defined in Scheme 1 and 2 was used to analysis the sub-stoichiometric polymerization data reported by Zhang and Sita[1] for the polymerization of 1-hexene using a Cp*$ZrMe_2$[N(tBu)C(Me)N(Et)]/[$B(C_6F_5)_4$] catalyst. DMCP simulation is also applied to this system. Because of the simplicity of the "living system", in which there is no misinsertion or recovery, some of the Model 3.3 parameters, including catalyst participation and rate constants, can be obtained by analytical solving the rate

equations instead of doing unconstrained optimization. In the following we will show the analysis needed to obtain these parameters, which are then used in the Discussion section of the main paper.

3.1. Determination of catalyst participation

Because the system is "living" (PDI ≤ 1.05), the M_n of the polymer at the end of the reaction is determined by $[M]_o/[Zr]_{total}$. Ideally, if the catalyst participation is 100%, the slope of the M_n vs. $[M]_o/[Zr]_{total}$ plot equals to the molecular weight of the monomer, which is 84. However, as shown in Figure S7, the slope is fit to be 123.2 (dashed line), indicating that the actual catalyst participation is 68%.

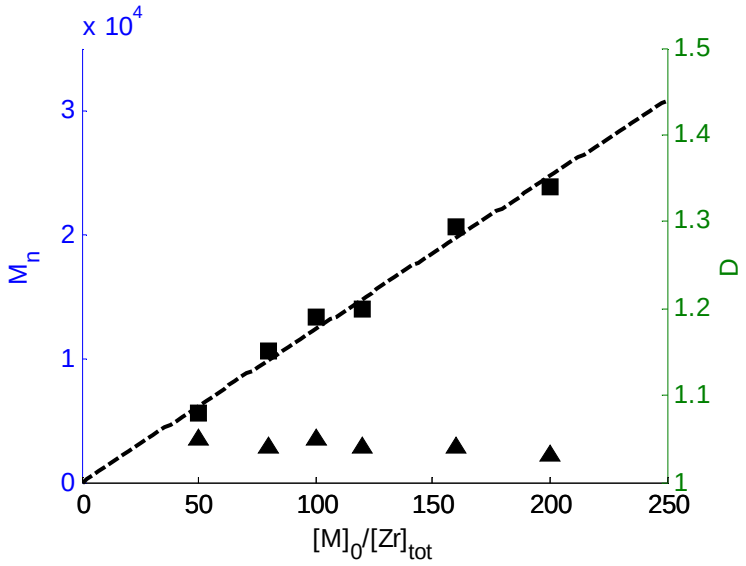

Figure E-SI7. $[M]_o/[Zr]_{total}$ dependence of the number average molecular weight M_n (squares) and the polydispersity PDI (D) (triangles) for 1-hexene polymerization using a Cp^*ZrMe_2 $[N(tBu)C(Me)N(Et)]/[B(C_6F_5)_4]$ catalyst. Data from Zhang and Sita. $[M]_o$ = 0.50 M and $[A]_o$ = 2.5 mM. All data are obtained from reference paper.[1] Dashed line is an experimental fit based on reactions in Scheme 1 and 2 with a catalyst participation of 68%.

3.2. Determination of the rate constant of propagation k_p

As reported in the paper, the monomer consumption is strictly first order in monomer concentration as expected for a living system. Without an excess precatalyst no BNC formed and, thus, the concentration of active site R_n equals to the concentration of the active catalyst participating in the polymerization. Using Eq. S15, k_p is determined to be 19.6 M^{-1} s^{-1}.

Table E-SI1. Experimental data used in determine k_p

$[C]_0$ (mM)	$[A]_0$ (mM)	k_{app} (s^{-1})	R^2
1.56	1.56	0.0208	0.999

3.3. Determination of the equilibrium constant of BNC formation

Based on the assumption that both the rates of formation and dissociation of BNC are very fast, the concentration of BNC is in equilibrium with the concentration of active site and neutral catalytic species. Hence, we will have following equation:

$$[BNC] = K_{ex}[R_n][Cl\text{-}R_n] \quad \text{S11}$$

Where R_n is defined as active site, and Cl-Rn is defined as inactive catalytic complex. At any time of the reaction, the sum of the concentration of BNC and that of Rn is equal to the initial concentration of active catalyst C*, and the sum of the concentration of BNC and that of inactive catalytic complex is equal to the initial concentration of excess precatalyst C:

$$[BNC] = [C^*]_0 - [R_n] \quad \text{S12}$$

$$[Cl\text{-}R_n] = [C]_0 - [BNC] = [C]_0 - [C^*]_0 + [R_n] \quad \text{S13}$$

Hence Eq. S11, S12, S13 can be solved as

$$[R_n] = \frac{-([C]_0 - [C^*]_0 + 1/K_{ex}) + \sqrt{([C]_0 - [C^*]_0 + 1/K_{ex})^2 - 4[C^*]_0/K_{ex}}}{2} \quad \text{S14}$$

Also, knowing that

$$k_{app} = k_p [R_n] \quad \text{S15}$$

We can predict the dependence of k_{app} vs. excess amount of precatalyst with a fixed amount of active catalyst, which is shown in Figure S8 (dashed curve). Notice that based on this equilibrium equation, the predicted dependence is non-linear.

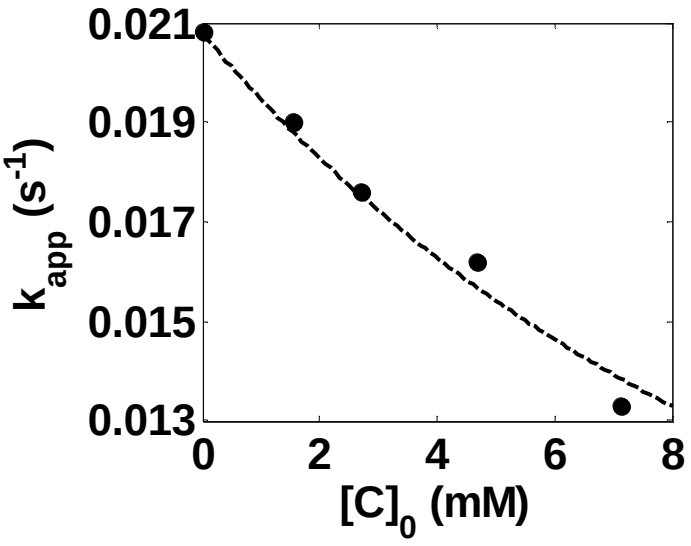

Figure E-SI8. Dependence of k_{app} vs. $[C]_0$ with $[C^*]_0$ held constant at 1.56 mM. Symbols are data from Zhang and Sita[1] and the curve is prediction of Ligand Transfer Model defined by reactions S1, S2, and S8A.

3.4. Determination of the rate constant of BNC formation

As Zhang and Sita[1] pointed out, the PDI of the products barely changes and remains narrow with increasing excess of precatalyst. Using our Monte Carlo simulation, we are able to predict the changes on the PDI for the different initial conditions of sub-stoichiometric activator. As shown in Figure S9 the Ligand Transfer Model shows that

when the formation rate of BNC $k_{ex}^{+} > 3000\ \mathrm{M^{-1}s^{-1}}$, the PDI will no longer be affected by the ligand transfer reactions.

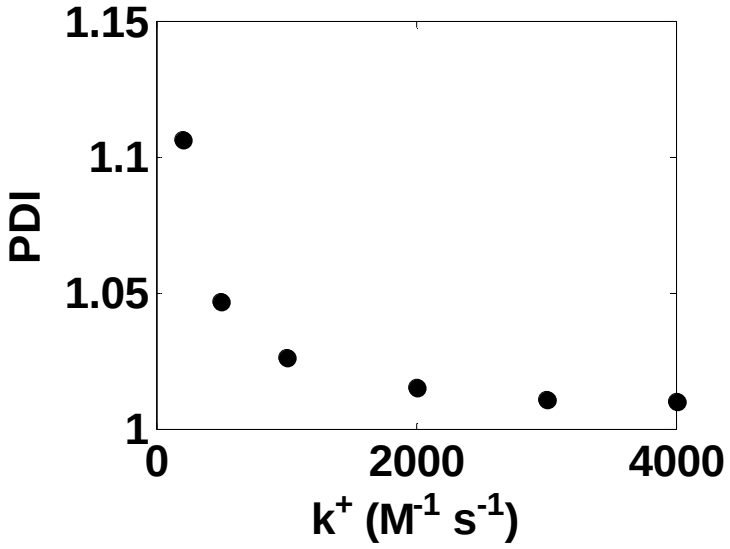

Figure E-SI9. Predicted dependence of PDI vs. the rate constant of BNC formation k_{ex}^{+}. K_{ex} = 111.5 M^{-1}.

4. DYNAMIC MONTE CARLO ALGORITHM

For a given reaction mechanism the time dependent concentrations of various the species were obtained using the Dynamic Monte Carlo (DMC) method,[2] which is different than the more traditional analysis method based on solving a set of coupled ordinary differential equations.[7] Although the traditional method is more than adequate for many kinetic mechanisms, it becomes inefficient when the number of reacting species is combinatorially large. As will be shown below such a situation arises when ligand transfer reaction is considered, where for example an active site attached by a growing chain of length *n* (i.e. consisting of *n* repeat units) can react with neutral catalytic species attached by a chain of length *m*.

The implementation of the DMC method here is based on the Gillespie's algorithm[6] for which an original C++ computer code was written. The model is concerned with a finite set of molecules contained in a control volume *V*. The initial number of molecules of species *I* in the V is X_{i0} as given by

$$X_{i0} = [x_i]_0 V \quad \text{S16}$$

where $[x_i]_0$ is the initial concentration of each species in for the experimental conditions under consideration. The probability that the reaction will occur given that the collision of the reactant molecules has happened is characterized by reaction parameter c_μ. The relationship between the reaction parameter c_μ and macroscopic reaction rate constant k_μ is given by $k_\mu = c_\mu$ for unimolecular reaction and $k_\mu = V c_\mu$ for bimolecular reactions. The number of reactant combinations for a particular reaction is denoted as h_μ , where h_μ for every elementary step employed in the main text are defined by:

Initiation:

$$C^* + M \xrightarrow{k_i} R_1 \qquad h_1 = X_{C*} X_M \quad \text{S17}$$

Propagation:

$$R_n + M \xrightarrow{k_p} R_{n+1} \qquad h_2 = X_M \left(\sum_{n>0} X_{R_n} \right) \quad \text{S18}$$

Misinsertion:

$$R_n + M \xrightarrow{k_{mis}} P_{n+1} \qquad h_3 = X_M \left(\sum_{n>0} X_{R_n} \right) \quad \text{S19}$$

Recovery:

$$P_n + M \xrightarrow{k_{rec}} R_{n+1} \qquad h_4 = X_M \left(\sum_{n>1} X_{P_n} \right) \qquad \text{S20}$$

Ligand transfer:

$$R_n + Bn - R_m \xrightarrow{k_{ex}^{+}} R_n - Bn - R_m \qquad h_5 = \sum_{n\geq 0} X_{R_n} \sum_{m\geq 0} X_{Bn-R_m} \qquad \text{S21}$$

$$R_n - Bn - R_m \xrightarrow{k_{ex}^{-}} R_m + Bn - R_n \qquad h_6 = \sum_{n\geq 0} \sum_{m\geq 0} X_{R_n-Bn-R_m} \qquad \text{S22}$$

Initiation through BNC:

$$R_n - Bn - C^{*} + M \xrightarrow{k_{i\_BNC}} R_n - Bn - R_1 \qquad h_7 = X_M \sum_{n\geq 0} X_{R_n-Bn-R_0} \qquad \text{S23}$$

X_i is the number of molecules of species i, e.g., X_M is the number of molecules of monomer (M), X_{R_n} is the number of molecules of primary active site with chain length n (R_n). When n = 0, R_0 is the unitiatiated activated site (C*), and Bn-R_0 is the precatalyst (C).

The reaction between two molecules is the result of a random collision which may or may not result in formation of the product. The probability of such reaction occurring during time interval δt is $a_\mu \delta t$, where $a_\mu \equiv h_\mu c_\mu$. The probability at time t that 1) no reactions take place between t and $t + \tau$, and 2) the reaction will occur between $t + \tau$ and $t + \tau + \delta t$, and will be a R_μ reaction is defined as $P(\tau, \mu)\delta t$. The probability density function $P(\tau, \mu)$ can be written as a product of two one variable probability density functions,

$$P(\tau, \mu) = P(\tau)P(\mu|\tau) \qquad \text{S24}$$

where $P(\tau)\delta t$ is the probability that the next reaction will occur within time interval $(t + \tau, t + \tau + \delta t)$, irrespective of which reaction it might be; and $P(\mu|\tau)\delta t$ is the probability

that the next reaction will be an R_μ reaction, given that the next reaction occurs at time $t + \tau$. According to Gillespie's method,[6]

$$P(\tau) = a \exp(-a\tau) \quad \text{S25}$$

$$P(\mu|\tau) = \frac{a_\mu}{a} \quad \text{S26}$$

$$a \equiv \sum_{\mu=1}^{M} a_\mu \quad \text{S27}$$

These expressions allow generating a random pair (τ, μ) according to the probability density $P(\tau, \mu)$ by using the random number generator. τ is generated by drawing a random number r_1 from the uniform distribution in the unit interval and taking

$$\tau = \left(\frac{1}{a}\right) \ln\left(\frac{1}{r1}\right). \quad \text{S28}$$

μ is generated by drawing another independent random number r_2 from the uniform distribution in the unit interval and taking μ to be that integer for which

$$\sum_{\nu=1}^{\mu-1} a_\nu < r_2 a \leq \sum_{\nu=1}^{\mu} a_\nu. \quad \text{S29}$$

The algorithm of DMCP Simulation described above is shown in Figure S10.

The maximum chain length observed experimentally is approximately 10^4. The choice of the control volume must be such that there is initially enough monomer to at least in principle form chains of such length, in practice the control volume here contains 10^5 molecules which was verified to give a good compromise between the numerical efficiency and accuracy of the MWD prediction. Each run containing 10^5 molecules is repeated 10^3 times in order to obtain relatively smooth MWD curves, thus the total number of simulated

molecules is 10^8. At the end of the Monte Carol simulation the numbers of molecules are converted back to the concentrations reported in this communication using

$$[x_i] = \frac{\sum_{repeats} X_i}{V \cdot N_{repeat}} \qquad \text{S30}$$

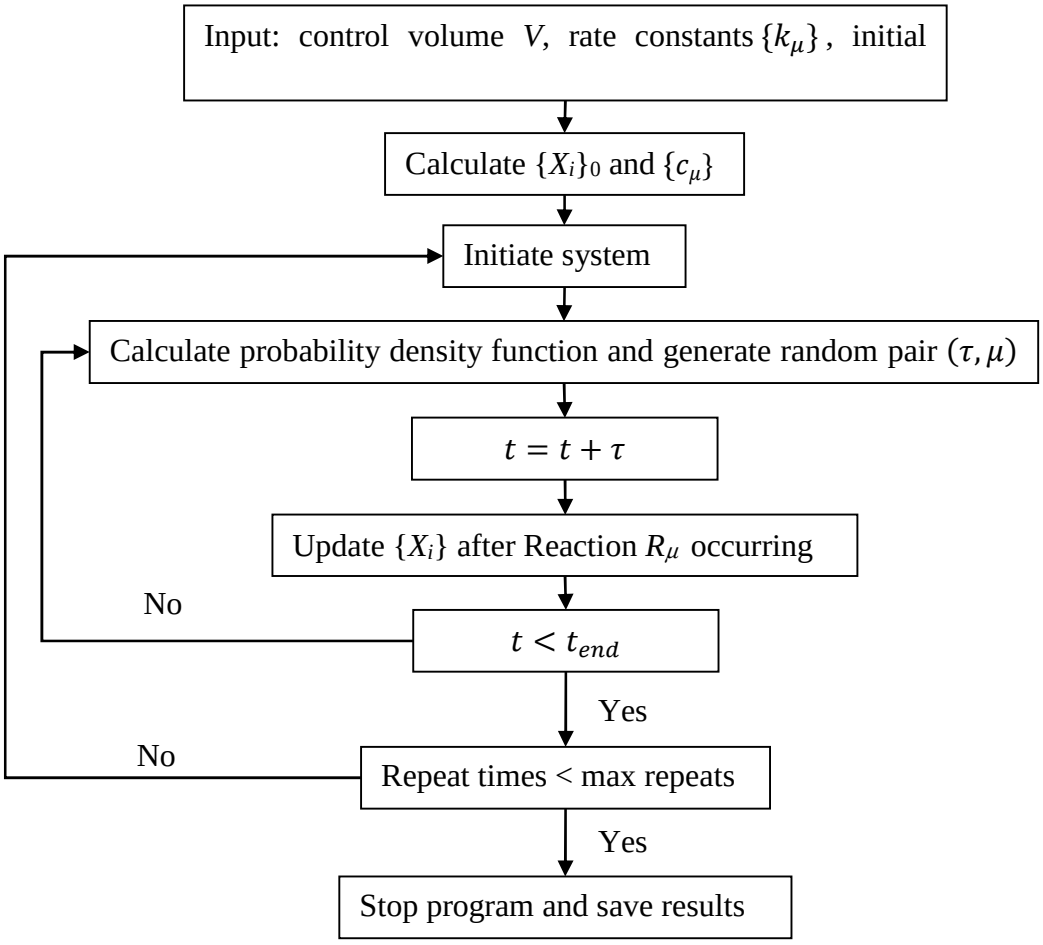

Figure E-SI10. Schematic of dynamic Monte Carlo algorithm for simulation of polymerization

REFERENCES

(1) Zhang, Y.; Sita, L. *Journal of the American Chemical Society* **2004**, *126*, 7776.
(2) Steelman, D. K.; Xiong, S.; Pletcher, P. D.; Smith, E.; Switzer, J. M.; Medvedev, G. A.; Delgass, W. N.; Caruthers, J. M.; Abu-Omar, M. M. *Journal of the American Chemical Society* **2013**, *135*, 6280.
(3) Switzer, J.; Travia, N.; Steelman, D.; Medvedev, G.; Thomson, K.; Delgass, W.; Abu-Omar, M.; Caruthers, J. *Macromolecules* **2012**, *45*, 4978.
(4) Novstrup, K.; Travia, N.; Medvedev, G.; Stanciu, C.; Switzer, J.; Thomson, K.; Delgass, W.; Abu-Omar, M.; Caruthers, J. *Journal of the American Chemical Society* **2010**, *132*, 558.
(5) Cao, J.; Goyal, A.; Novstrup, K.; Midkiff, S.; Caruthers, J. *International Journal of Parallel Programming* **2009**, *37*, 127.
(6) GILLESPIE, D. *Journal of Computational Physics* **1976**, *22*, 403.
(7) Novstrup, K. A.; Travia, N. E.; Medvedev, G. A.; Stanciu, C.; Switzer, J. M.; Thomson, K. T.; Delgass, W. N.; Abu-Omar, M. M.; Caruthers, J. M. *Journal of the American Chemical Society* **2009**, *132*, 558.

Appendix F Supporting Information for Chapter 7

1. Stochastic simulations using DMC

For a given reaction mechanism the concentrations of all the species as a function of time are obtained in this work using the Dynamic Monte Carlo (DMC) method[4]. It should be noted that the more traditional analysis method[5] is based on solving a set of coupled ordinary differential equations (ODE)s for species concentrations. Although adequate in most cases, the traditional method fails when the number of reacting species is combinatorially intractable. As will be shown below such a situation arises when attack of a growing chain end on dormant cyclic chains or other growing chains is considered, where for example a growing chain of length *n* (i.e. consisting of *n* repeat units) can react with another chain of length *m* resulting in creation of the two new chains of lengths *n'* and *m'* (where *n*+*m*=*n'*+*m'*).

The implementation of the DMC method here is based on the Gillespie's algorithm[4] for which an original computer code has been created. We model a finite set of molecules contained in a control volume *V*. Hence the initial number of molecules of species *i*, X_{i0} can be calculated via

$$X_{i0} = [x_i]_0 V$$

, where $[x_i]_0$ is the initial concentration of each species in an experimental run. The probability that the reaction will occur given that the collision of the reactant molecules has happened is characterized by reaction parameter c_μ. The conversion between the reaction parameter c_μ and macroscopic reaction rate constant k_μ is given by

$$k_\mu = c_\mu$$

for unimolecular reaction, and

$$k_\mu = Vc_\mu$$

for bimolecular reactions between different molecules. The number of reactant combinations for a particular reaction is denoted as h_μ. h_μ for every elementary step (shown in the main text) are listed below:

(1) initiation (Scheme 2): $h_1 = X_I X_M$

(2) reverse initiation (Scheme 2): $h_2 = X_{Z_1}$

(3) propagation (Scheme 2): $h_3 = X_M \left(\sum_n X_{Z_n} \right)$

(4) cyclization (Eq. 1): $h_4 = \sum_n X_{Z_n}$

(5) carbene attack (Eqs. 2 and 3): $h_5 = X_I \left(\sum_n nX_{Z_n} + \sum_n nX_{C_n} \right)$

(6) back-biting (Eq. 4): $h_6 = \sum_n X_{Z_n}$

(7) intermolecular chain transfer (Eqs. 5 and 6): $h_7 = \left(\sum_m X_{Z_m} \right) \left(\sum_n nX_{Z_n} + \sum_n nX_{C_n} \right)$

where X_i is the number of molecules of species i, e.g., X_I is the number of molecules of carbene initiator I, $X_{Z_n}$is the number of molecules of growing zwitterion Z_n, and nX_{Z_n} is the number of repeat units in Z_n.

The maximum chain length observed in the experiment is approximately 10^4. The choice of the control volume must be such that there is initially enough monomer to at least in principle form chains of such length, in practice the control volume here contains 10^5 molecules which was verified to give a good compromise between the numerical efficiency and accuracy of the MWD prediction. Each run containing 10^5 molecules is repeated 10^3

times in order to get relatively smooth MWD curves, thus the total number of simulated molecules is 10^8. In the end numbers of molecules are converted back to concentrations according to:

$$[x_i] = \frac{\sum_{repeats} X_i}{V \cdot N_{repeat}}$$

2. Additional Simulations.

Inclusion of these reactions into Model III will result in changes in the optimized values of the rate constants present in Table 4. To access the extent to which cyclization reaction (Eq 1) may be present, we do the following: (1) the cyclization step is added to Model III. As seen in Figure S1a, this results in an effective deactivation of zwitterions via the mechanism described in Model II section. Even at the rate constant value of k_c = 0.001 min^{-1}, the deviation of the model prediction from the data is beyond the experimental uncertainty for the lowest concentration of initiator and monomer (run 5). At the higher value of k_c (e.g., k_c = 0.05 min^{-1}, dashed in Figure S1a), the discrepancy becomes even more dramatic. (2) If both cyclization and attack of the carbene on growing zwitterions or macrocycles, i.e., entire Model II is combined with Model III, the performance of the model improves; however, as illustrated in Figure S2bc, only relatively small amount of kc and kca reactions can be accomodated. Specifically, at the values of k_c = 0.007 min^{-1}, k_{ca} = 0.001 $M^{-1}min^{-1}$, the rate of monomer consumption at the highest $[I]_0$ (run 1, red curve) is too fast compared to the data and the rate of monomer consumption at the lowest $[I]_0$ (run 5, green curve) is too slow. Larger kc values result in even bigger deviations. Note that in the presence of cyclization reaction, the rate of back-biting (k_{bb}) had to be adjusted to

preserve the fit to the MWD. The estimate for the rate of cyclization obtained here is an upper bound which can be made tighter with more experimental data becoming available. Another conclusion is that the optimized set of rate constants for the Model III is only slightly affected (k_{bb} was changed by 10%).

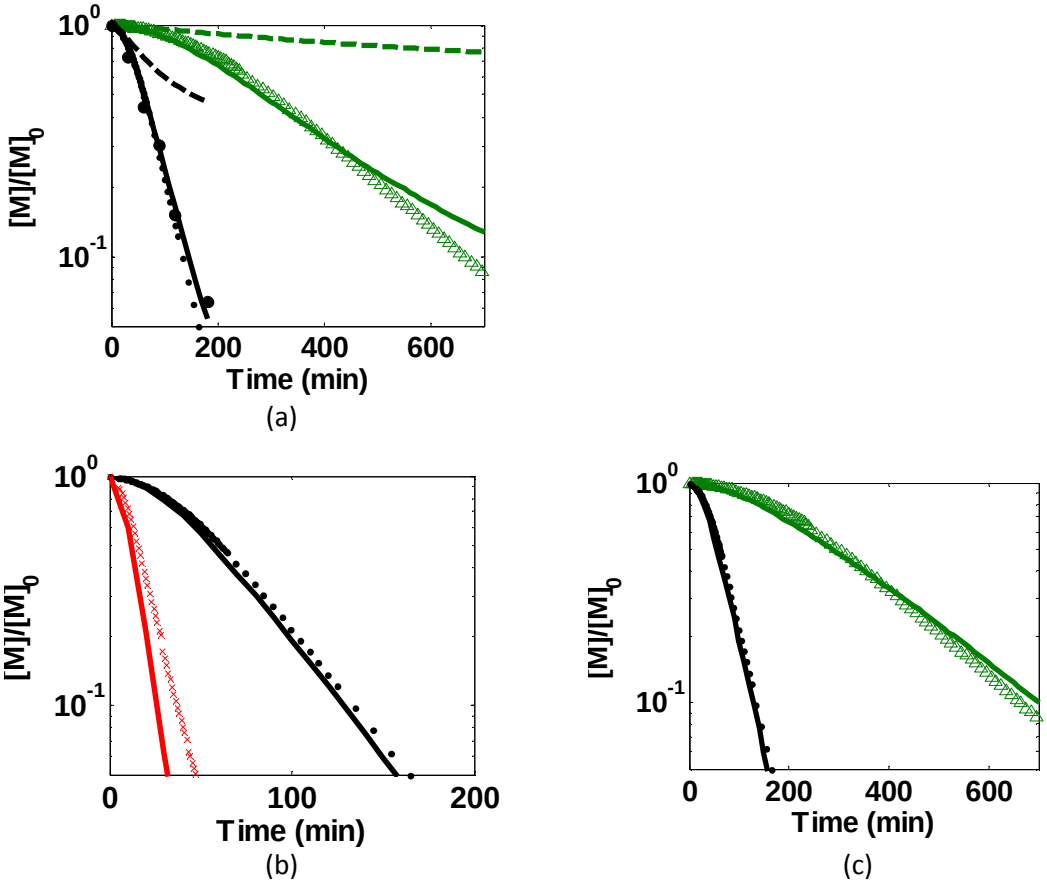

Figure F-SI1. Simulation results of monomer consumption data of run **1** (red), **3a** (black), and **5** (green) ($[I]_0$ = 0.05, 0.01, 0.006 M, respectively). Symbols are data, lines are fits. Rate constants for optimized Model III (Table 4 in the paper) were used unless mentioned: (a) Model III with added step of cyclization (eq 1 of text) dashed lines: k_c = 0.05 min^{-1}, solid lines: k_c = 0.001 min^{-1}, and Xcarbene = 30% for both. (b, c) Model III with added steps of cyclization (eq 1) and chain attack (eqs 2 and 3) k_c = 0.007 min^{-1}, k_{ca} = 0.001 $M^{-1}min^{-1}$, for Xcarbene = 40%. (b) and (c) use the same set of rate constants but are plotted in different time scale.

Appendix G Supporting Information for Chapter 8

1. Reaction order for equation 7

Table G-SI1. Initial conditions of three runs of chlorite react with hypochlorite at pH = 5.00.

Run	$[ClO_2^-]$ / mM	$[HClO/ClO^-]$ / mM
1	1.0	0.187
2	2.0	0.270
3	4.0	0.482

This is consistent with our catalytic reaction environment where chlorite is of much higher concentration and ClO^- is quickly consumed once generated. Hence, for Eq. 7, the differential rate equation can be written as:

$$\frac{\mathrm{d}[\mathrm{ClO_2}]}{\mathrm{dt}} = \left(2\mathrm{k}[\mathrm{ClO_2^-}]_0^{n_2}\right)[\mathrm{ClO^-}]^{n_1}$$

By examining the data, the growth of ClO_2 can be simulated by assuming 1st order dependency on $[ClO^-]$ using function

$$\mathrm{y} = \mathrm{m}_1 * (1 - e^{-\mathrm{m}_2 * x})$$

where

$$\mathrm{m}_1 = 2[\mathrm{ClO^-}]_0$$

$$\mathrm{m}_2 = 2\mathrm{k}[\mathrm{ClO_2^-}]_0^{n_2}$$

m_1 and m_2 are obtained by fitting experimental data and the values are listed in Table SI1. The rate constant and reaction order in $[ClO_2^-]$ is obtained subsequently by linearly fitting *ln*(m_2) vs. *ln*($[ClO_2^-]_0$).

Table G-SI2. Simulated values of m_1 and m_2 based on experimental data.

Run	m_1	m_2
1 (red)	0.327	0.204
2 (blue)	0.644	0.374
3 (black)	0.923	0.555

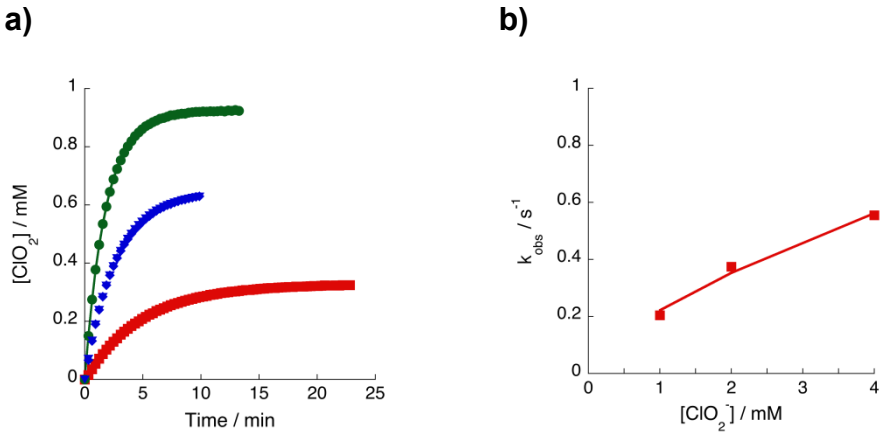

Figure G-SI1. Determination of reaction order for Equation 7. a) Chlorine dioxide versus time for the reaction of chlorite with hypochlorite in acetate buffer at pH 5.00. Run 1 (red), run 2 (blue), run 3 (green) where symbols are experimental data and solid lines are mathematical fits. b) Plot of $\ln(m_2)$ versus $\ln([ClO_2^-]_0)$. Reaction order n_2 = slope = 0.67, rate constant (k) = intercept/2 = 0.11 $mM^{-2/3}$ min^{-1}.

2. Mechanism

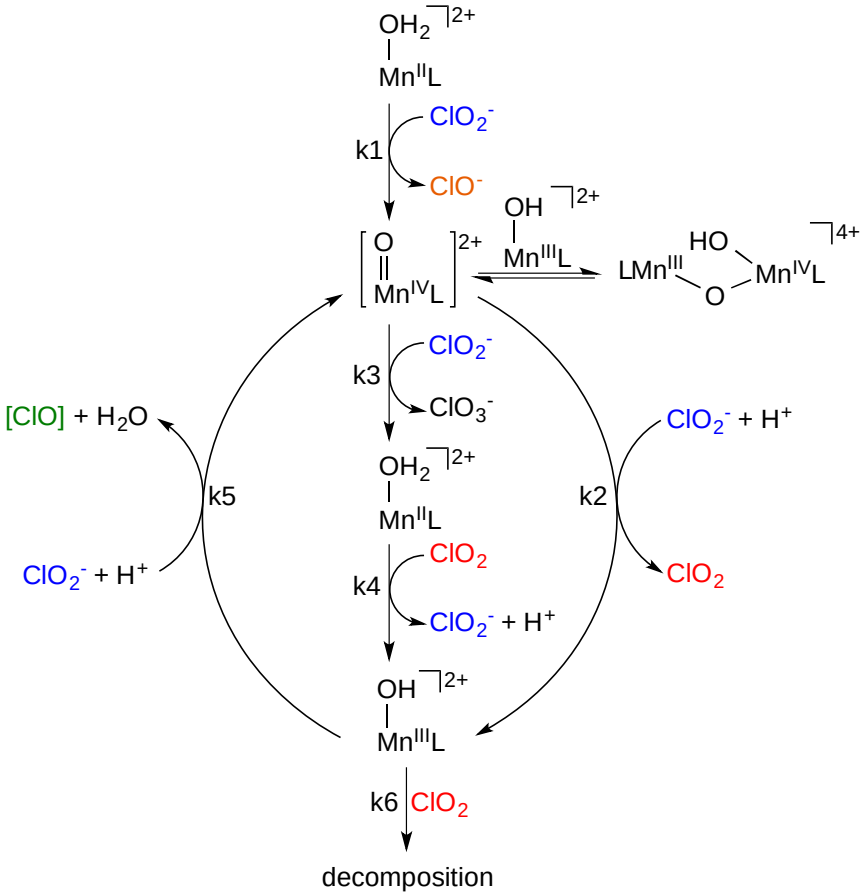

Potential reactions independent of catalyst

$[ClO] + ClO_2^- \longrightarrow ClO_2 + ClO^-$

$2\ ClO_2^- + ClO^- + 2\ H^+ \longrightarrow 2\ ClO_2 + Cl^- + H_2O$

$[ClO] + ClO_2 \longrightarrow [Cl_2O_3]$

$[Cl_2O_3] + H_2O \longrightarrow ClO^- + ClO_3^- + 2\ H^+$

$2\ [ClO] + 3\ C_2H_3O_2^- + H_3O^+ \longrightarrow 2\ Cl^- + 3\ C_2H_4O_3$

Manganese Species

$-d[Mn^{II}]/dt = k_1[Mn^{II}][ClO_2^-] + k_4[Mn^{II}][ClO_2] - k_5[Mn^{IV}][ClO_2^-]$

$d[Mn^{III}]/dt = k_2[Mn^{IV}][ClO_2^-] + k_4[Mn^{II}][ClO_2] - k_5[Mn^{III}][ClO_2^-] - k_6[Mn^{III}][ClO_2]$

$d[Mn^{IV}]/dt = k_1[Mn^{II}][ClO_2^-] - k_2[Mn^{IV}][ClO_2^-] - k_3[Mn^{IV}][ClO_2^-] + k_5[Mn^{III}][ClO_2^-]$

Chlorine Species

$-d[ClO_2^-]/dt = k_1[Mn^{II}][ClO_2^-] + k_2[Mn^{IV}][ClO_2^-] + k_3[Mn^{II}][ClO_2^-] - k_4[Mn^{II}][ClO_2] + k_5[Mn^{III}][ClO_2^-]$

$d[ClO^-]/dt = k_1[Mn^{II}][ClO_2^-] - k_7[ClO_2^-]^{2/3}[ClO^-]$

$d[Cl^-]/dt = k_7[ClO_2^-]^{2/3}[ClO^-] + k_8[ClO][C_2H_3O_2^-]$

$d[ClO_3^-]/dt = k_4[Mn^{IV}][ClO_2^-]$

$d[ClO_2]/dt = k_2[Mn^{IV}][ClO_2^-] - k_5[Mn^{II}][ClO_2] - k_6[Mn^{III}][ClO_2] + k_7[ClO_2^-]^{2/3}[ClO^-]$

Peroxyacetic Acid

$d[C_2H_4O_3]/dt = k_8[ClO]^2[C_2H_3O_2^-]$

VITA

VITA

Silei Xiong

EDUCATION

Ph.D., Chemical Engineering, 2015, Purdue University, West Lafayette, IN

B.S., Polymer Materials and Engineering, 2009, Tsinghua University, Beijing, China

RESEARCH EXPERIENCE

Single-Site Olefin Polymerization

- Structure-Activity Relationships
    - Effect of metal-pendant distance on chain transfer rate
    - Comparison of Zirconium and Hafnium Amine Bis(phenolate) Catalysts
    - Effect of electronic perturbations on 1-hexene polymerization
- New reaction pathways
    - Selective Degenerative Benzyl Group Transfer in Olefin Polymerization
    - Polymer Chain Growth by Incorporation of Active Site Oligomer

Ring-Opening Polymerization

Catalytic Oxidation of ClO_2^- to ClO_2

PUBLICATIONS

PUBLICATIONS

D. Keith Steelman, **Silei Xiong**, Grigori A. Medvedev, W. Nicholas Delgass, James M. Caruthers, and Mahdi M. Abu-Omar, *"Effects of Pendant Electronic Perturbations on the Polymerization of 1-Hexene Catalyzed by Single-Site Zirconium Amine Bis-Phenolate Complexes"*, ***ACS Catalysis***, 2014, 4 (7), pp 2186–2190

Hayley A. Brown, **Silei Xiong**, Grigori A. Medvedev, Young A. Chang, Mahdi M. Abu-Omar, James M. Caruthers, Robert M. Waymouth, *"Zwitterionic Ring-Opening Polymerization: Kinetic Models for the Synthesis of Cyclic Poly(caprolactones)"*, ***Macromolecules***, 2014, 47 (9), pp 2955–2963

Silei Xiong, D. Keith Steelman, Grigori A. Medvedev, W. Nicholas Delgass, Mahdi M. Abu-Omar and James M. Caruthers, *"Selective Degenerative Benzyl Group Transfer in Olefin Polymerization"*, ***ACS Catalysis***, 2014, 4, pp 1162–1170

Scott D. Hicks, Doyeon Kim, **Silei Xiong**, Grigori A. Medvedev, Seungwoo Hong, Wonwoo Nam, and Mahdi M. Abu-Omar, *"Non-Heme Manganese Catalysts for On-Demand Production of Chlorine Dioxide in Water and Under Mild Condition"*, ***J. Am. Chem. Soc.***, 2014, 136 (9), pp 3680–3686

D. Keith Steelman, **Silei Xiong**, Paul D. Pletcher, Erin Smith, Jeffrey M. Switzer, Grigori A. Medvedev, W. Nicholas Delgass, James M. Caruthers, and Mahdi M. Abu-Omar, *"Effects of Pendant Ligand Binding Affinity on Chain Transfer for 1-Hexene*

Polymerization Catalyzed by Single-Site Zirconium Amine Bis-Phenolate Complexes”, ***J. Am. Chem. Soc.***, **2013**, *135* (16), pp 6280–6288

D. Keith Steelman, Paul D. Pletcher, Jeffrey M. Switzer, **Silei Xiong**, Grigori A. Medvedev, W. Nicholas Delgass, James M. Caruthers, Mahdi M. Abu-Omar, *“Comparison of Selected Zirconium and Hafnium Amine Bis(phenolate) Catalysts for 1-Hexene Polymerization”*, ***Organometallics***, 2013, 32 (17), pp 4862–4867